Università degli Studi di Parma

Dipartimento di Ingegneria Civile, dell'Ambiente, del Territorio e Architettura

Dottorato di Ricerca in Ingegneria Civile - XXVIII Ciclo

Curriculum: Protezione Idraulica del Territorio (ICAR /02)

Fausto Cupola

Theory and application of inverse problems in groundwater: numerical, laboratory and field studies.

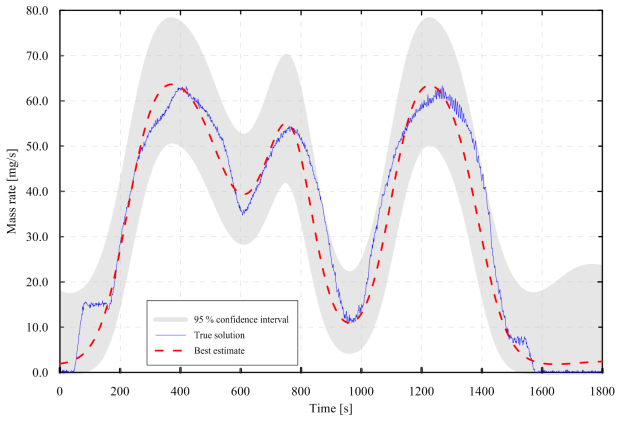

Dissertazione per il conseguimento del titolo di Dottore di Ricerca

Tutore: Prof. Ing. Andrea Zanini

Co-Tutori: Prof. Ing. Maria Giovanna Tanda, Dott. Michael Cardiff

Coordinatore del Dottorato: Prof. Ing. Gianfranco Forlani

Parma, Gennaio 2016

...stay hungry, stay foolish...
Steve Jobs

Acknowledgements

This dissertation contains the results of the research activity performed during the PhD course (XXVIII cycle) regarding different approaches for inverse problems in groundwater and not only.

First of all I would thank my advisor Prof. Andrea Zanini, who gave me the opportunity of this Phd and who spent a lot of energy for sending me abroad to increase my knowledge and to live awesome experiences. I thank my co-advisor Prof. Maria Giovanna Tanda for her kidness and helpfulness: she helped me during the activities and she gave me a valuable guidance. I would like to express my gratitude to Prof. Michael Cardiff for giving me the opportunity of visiting the University of Wisconsin and involving me in his researches. I thank YaoQuan for her collaboration.

Thanks to all guys of University of Parma, with whom I shared the office and the laboratory.

A really big thank to Rikki and Ryan and their beautiful families, who made my experience in the US unbelievable and unforgettable. Thanks for all the adventures, both in the US and Italy. Thanks also to Robert and Dante.

Last but not least I thank Natascia, my wife soon, to whom I dedicate this work.

Contents

List of Figures

List of Tables

Introduction

Aquifers are a vital water resource whose quality characteristics must be safeguarded or, if damaged, restored. The extent and complexity of aquifer contamination is related to characteristics of the porous medium, the influence of boundary conditions, and the biological, chemical and physical processes. After the nineties, the efforts of the scientists have been increased exponentially in order to find an efficient way for estimating the hydraulic parameters of the aquifers, and thus, recover the contaminant source position and its release history. To simplify and understand the influence of these various factors on aquifer phenomena, it is common for researchers to use numerical and controlled experiments. This work presents some of these methods, applying and comparing them on data collected during laboratory, field and numerical tests. The work is structured in four parts which present the results and the conclusions of the specific objectives.

The **first part** concerns the laboratory activities carried out at Department of Civil, Environmental, Land Management Engineering and Architecture (DICATeA) of the University of Parma. At first, an overview of the experimental equipment and a brief literature review of laboratory strategies for investigating the contaminant phenomenon is presented. This work allowed to develop an efficient laboratory tool for estimating the dispersion properties of a porous medium (*Citarella et al.*, 2015) and for testing and validating numerical procedures (*Cupola et al.*, 2015a).

Then, the Numerical-Imaging Dispersivity Evaluation (N-IDE) procedure for estimating the dispersivity coefficients, by using images which follow the contaminant process in the sandbox, is presented. This method is along the way traced by several authors like *Silliman et al.* (1987), *Sternberg* (2004) and by Grathwohl's research group, and it allows to estimate the dispersivity coefficients punctually and it works also with heterogeneous porous media.

Then, the results of the application of two different methods (Simultaneous release function and source location (SRSI) and Backward location model based on adjoint state method (BPM-ASM)) on the data collected during laboratory tests is reported. The first method uses the geostatistcal approach proposed by *Snodgrass and Kitanidis* (1997) and implemented by *Butera et al.* (2013). It is the first time that it has been applied on real data. The second method, instead, has been developed by *Neupauer and Wilson* (1999, 2001), who showed that the backward location and travel time probability density functions are related to adjoint states of concentration. Performing the tests in a laboratory, allows to control all the variables and so, to verify the reliability of the methods.

The **second part** is focused on the laboratory activities performed at the University of

Wisconsin - Madison. The goal of the work presented in this part (published in *Zhou et al.* (submitted) and *Zhou et al.* (2014)) is to provide an experimental confirmation of the theory of oscillatory hydraulic tomography (OHT) originally presented by *Cardiff et al.* (2013). In the past numerous methods have been suggested for estimating spatially variable hydraulic properties: only for example, *Kolterman and Gorelick* (1996) processed data through geostatistical analysis while incorporating geologic, hydrogeologic, and geophysical information to create images of aquifer properties; *Yeh and Liu* (2000) originally performed a numerical hydraulic tomography study by applying a geostatistical inverse approach - the sequential successive linear estimator (SSLE) - to characterize 3-D spatial heterogeneity. In this study an instrumented laboratory sandbox, filled with material of known hydraulic properties has been used. Applying the OHT approach, several periodic pumping signals of different frequencies have been used for stimulation, and the responses have been analyzed tomographically, using a fast "steady-periodic" groundwater flow model.

The **third part** presents the field activities and the analysis carried out on the well field of the Department of Physics and Geosciences (DiFeST) of the University of Parma. Partial results have been presented in *Cupola et al.* (2015e). Initially, that well field was created for educational purposes, but it represents a very good research site for its location. Initially, some constant pumping tests have been performed and analyzed through traditional methods like Theis, Bierchenk and Hantush. This has allowed to understand the behavior of the well field and its defects. After this first part, some oscillatory pumping tests have been performed in order to collect data for applying the Oscillatory Hydraulic Tomography and compare its results with those obtained through the traditional analysis. A numerical model based on the MODFLOW 2005 code, able to reproduce the observed values at the same locations and times for each pumping tests, have been produced.

The **fourth part** concerns about the numerical studies. In particular, the Minimum Relative Entropy (MRE) method, proposed by *Woodbury and Ulrych* (1993, 1996) has been applied and extended to a non-linear flow field. The results of this work is presented in *Cupola et al.* (2014, 2015b). The principle of this method has been introduced by *Kullback* (1959) and has been used in several different fields. *Woodbury and Ulrych* (1993, 1996) applied the MRE approach for recovering the contaminant release history in aquifers. In this work the MRE procedure has been extended considering a synthetic 2-D non-uniform flow field and several observation points at a given time and considering uniform and non-uniform flow field starting from observations collected at two monitoring points only at different monitoring times. For computing the sensitivity matrix, the Stepwise Input Function (SIF) (*Butera and Tanda*, 2006) procedure has been used, which allows to calculate the transfer matrix even in the more complex cases, where an

analytically formulation is not possible. In this part a discussion of the results obtained modifying the input parameters is presented. At the end a study for determining the minimum information required for estimating a reliable release history with a partially known flow field has been carried out. A numerical model of a 2-D confined aquifer with rectangular shape characterized by a heterogeneous hydraulic conductivity field was built. The conductivity field was estimated through a kriging interpolation starting from values sampled on a regular grids of different density. Starting from that partially known field the pollutant release history was estimated. Preliminary results of this work have been presented in *Cupola et al.* (2015d).

Part 1

Laboratory studies at DICATeA

1 Fundamentals of Hydraulics of Groundwater

§

The basic governing equations[1] (for fully saturated soil) of flow and transport in groundwater are summarized in this section to better clarify the following chapters.

1.1 Flow

Darcy's experimental results concluded that the rate of flow Q [L^3T^{-1}] is proportional to a cross-sectional area A [L^2] and to the difference of head $\left(h_1 - h_2\right)$ [L] and inversely proportional to the length L [L]:

$$Q = \frac{K \cdot A(h_1 - h_2)}{L} \tag{1.1}$$

where K [LT^{-1}] is the hydraulic conductivity that represents the ability of the aquifer material to transport water under hydraulic gradients. Considering infinitesimal length the relationship $\frac{(h_1 - h_2)}{L}$ tends to $i = -\frac{dh}{dx}$ that represents the hydraulic gradient (the minus sign means that the flow goes from high head to low head). So Eq. (1.1) can be written as $Q = K \cdot i \cdot A$ and $v = Q/A = K \cdot i$ represents the velocity of the fluid. This expression is valid for one dimensional motion; considering three dimensional flux, the velocity is represented by $\mathbf{v} = -\mathbf{K} \cdot \nabla h$, so the Darcy's law becomes:

$$Q = -\mathbf{K} \cdot \nabla h \cdot A$$

[1] This section is based on *Bear* (1972), *Bear and Bachmat* (1990) and *Domenico and Schwartz* (1998)

where $\mathbf{K}$ is the symmetric tensor of the hydraulic conductivity

$$\mathbf{K} = \begin{bmatrix} k_{xx} & k_{xy} & k_{xz} \\ & k_{yy} & k_{yz} \\ & & k_{zz} \end{bmatrix}$$

The velocity along the three main Cartesian directions results:

$$\begin{aligned} v_x &= -k_{xx}\frac{\partial h}{\partial x} - k_{xy}\frac{\partial h}{\partial y} - k_{xz}\frac{\partial h}{\partial z} \\ v_y &= -k_{yx}\frac{\partial h}{\partial x} - k_{yy}\frac{\partial h}{\partial y} - k_{yz}\frac{\partial h}{\partial z} \\ v_z &= -k_{zx}\frac{\partial h}{\partial x} - k_{zy}\frac{\partial h}{\partial y} - k_{zz}\frac{\partial h}{\partial z} \end{aligned}$$

i.e.

$$\mathbf{v} = -\mathbf{K}\nabla h \tag{1.2}$$

The continuity equation (conservation of mass) for a porous medium saturated with water is the following:

$$div\,(\rho\mathbf{U}) + \frac{\partial \phi\rho}{\partial t} \pm \rho q = 0 \tag{1.3}$$

where $\mathbf{U}$ [LT^{-1}] represents the Darcy's velocity, ρ [ML^{-3}] is the density of the fluid, ϕ [-] is the effective porosity and q [T^{-1}] is a term of source/sink per unit of volume. Substituting the Darcy velocity in the Eq. 1.3 it results:

$$div\,[\rho\,(-\mathbf{K}\nabla h)] + \frac{\partial \phi\rho}{\partial t} \pm \rho q = 0$$

that is the diffusion equation. Considering that the density ρ is constant in the space but variable in time with few approximation

$$\frac{1}{\rho}\frac{\partial \phi\rho}{\partial t} \simeq S_s\frac{\partial h}{\partial t}$$

where S_s [L^{-1}] represents the specific storativity. Eq. 1.3 can be rewritten as:

$$div\,(\mathbf{K}\nabla h) = S_s\frac{\partial h}{\partial t} \pm q$$

In steady state condition $\frac{\partial h}{\partial t} = 0$ and without source or sinks the Eq. 1.3 collapses to $div(\mathbf{K}\nabla h) = 0$. Expanding this equation it results:

$$\frac{\partial}{\partial x}\left(K_{xx}\frac{\partial h}{\partial x}\right) + \frac{\partial}{\partial y}\left(K_{yy}\frac{\partial h}{\partial y}\right) + \frac{\partial}{\partial z}\left(K_{zz}\frac{\partial h}{\partial z}\right) = 0$$

in a homogeneous domain it is reduced to

$$K_{xx}\frac{\partial^2 h}{\partial x^2} + K_{yy}\frac{\partial^2 h}{\partial y^2} + K_{zz}\frac{\partial^2 h}{\partial z^2} = 0 \tag{1.4}$$

In isotropic medium $K_{xx} = K_{yy} = K_{zz}$ so Eq. 1.4 becomes

$$\frac{\partial^2 h}{\partial x^2} + \frac{\partial^2 h}{\partial y^2} + \frac{\partial^2 h}{\partial z^2} = 0$$

that is the Laplace's equation: $\nabla^2 h = 0$. If the flow can be considered horizontal the transmissivity (T [L^2T^{-1}]) indicates the ability of the aquifer to transmit water through its entire thickness, and it is equal to the integral (over a vertical line) of the product of the hydraulic conductivity and the aquifer's thickness dz:

$$T = \int_0^b k_{xx} dz \tag{1.5}$$

The aquifer's storativity S [-] is defined as the volume of water released from (or added to) the aquifer per unit horizontal area and per unit decline (or rise) of the average (over the vertical) piezometric head in the aquifer.

$$S = \int_0^b S_s dz \tag{1.6}$$

1.2 Transport of Contaminants

Eq. 1.7 describes the transport process in an aquifer corresponding to the injection of a non-sorbing, non-reactive solute in a point source (*Bear and Verruijt*, 1987):

$$\phi\frac{\partial(C(\mathbf{x},t))}{\partial t} = \nabla[\phi\mathbf{D}(\mathbf{x})\cdot\nabla C(\mathbf{x})] - \nabla[\phi\mathbf{u}(\mathbf{x},t)\cdot\nabla C(\mathbf{x})] + s(\mathbf{x}_0,t)\cdot\delta(\mathbf{x}-\mathbf{x}_0) + \sum R_n \tag{1.7}$$

where ϕ [-] is the effective porosity (taken as spatially variable, but constant in time), $\mathbf{u}(\mathbf{x},t)$ [$L\cdot T^{-1}$] is the effective velocity at location $\mathbf{x}$ and time t [T], $\mathbf{D}(\mathbf{x})$ [$L^2\cdot T^{-1}$] the dispersion tensor, $C(\mathbf{x},t)$ [$M\cdot L^{-3}$] the concentration at location $\mathbf{x}$ and time t, $s(\mathbf{x}_0,t) =$

$C_0(\mathbf{x}_0, t) \cdot q_0(\mathbf{x}_0, t)$ [M·T^{-1}] is the amount of pollutant per time unit injected into the aquifer through the source located at $\mathbf{x}_0$, $C_0(\mathbf{x}_0, t)$ is the concentration injected and $q_0(\mathbf{x}_0, t)$ [L^3·T^{-1}] is the injection flow rate at $\mathbf{x}_0$ at time t [T]. The solution of 1.7, by considering uniform porosity, when associated with the initial and boundary conditions $C(\mathbf{x}, 0) = 0$; $C(\infty, t) = 0$, is given by the following integral (*Jury and Roth*, 1990):

$$C(\mathbf{x}, t) = \int_0^t s(\mathbf{x}_0, \tau) f(\mathbf{x}, t - \tau) d\tau \tag{1.8}$$

where $f(\mathbf{x}, t-\tau)$ [L^{-p}] is the transfer function that describes the effect at $\mathbf{x}$ at time t [T] by an impulse injection occurring at $\mathbf{x}_0$ at time $t - \tau$ (p is the dimension of the problem).

For many field-scale contaminant transport problems, the advection term dominates over other terms. To measure the degree of advection dominance, a dimensionless Peclet number is usually used; it is defined as

$$P_e = \frac{|\mathbf{u}|\, L}{D} \tag{1.9}$$

where $|\mathbf{u}|$ [LT^{-1}] is the magnitude of the effective velocity vector, L [L] is the characteristic length and D [L^{2}T^{-1}] is the dispersion coefficient. For pure advection problems, the Peclet number approaches infinity.

Dispersion in porous media refers to the spreading of contaminants over a region greater than the one predicted from the advection process. Dispersion is caused by mechanical dispersion, a result of deviations of actual velocity on a microscale from the average groundwater velocity and by molecular diffusion driven by concentration gradients. Molecular diffusion is generally secondary and negligible, compared with the effects of mechanical dispersion, and only becomes important when groundwater velocity is very low. The sum of mechanical dispersion and molecular diffusion is termed hydrodynamic dispersion. The hydrodynamic dispersion tensor (D_{ij}) for a porous medium, is defined

(*Scheidegger*, 1961) in the following component form:

$$\begin{aligned}
D_{xx} &= \alpha_L \frac{u_x^2}{|u|} + \alpha_T \frac{u_y^2}{|u|} + \alpha_T \frac{u_z^2}{|u|} + D^* \\
D_{xy} &= \left(\alpha_L - \alpha_T\right) \frac{u_x u_y}{|u|} + D^* = D_{yx} \\
D_{xz} &= \left(\alpha_L - \alpha_T\right) \frac{u_x u_z}{|u|} + D^* = D_{zx} \\
D_{yy} &= \alpha_L \frac{u_y^2}{|u|} + \alpha_T \frac{u_x^2}{|u|} + \alpha_T \frac{u_z^2}{|u|} + D^* \\
D_{yz} &= \left(\alpha_L - \alpha_T\right) \frac{u_y u_z}{|u|} + D^* = D_{zy} \\
D_{zz} &= \alpha_L \frac{u_z^2}{|u|} + \alpha_T \frac{u_x^2}{|u|} + \alpha_T \frac{u_y^2}{|u|} + D^*
\end{aligned} \tag{1.10}$$

where D_{xx}, D_{yy}, D_{zz}, $[\mathrm{L}^2\mathrm{T}^{-1}]$ are the principal component of the dispersion tensor; α_L [L] is the longitudinal dispersivity; α_T [L] is the transverse dispersivity; D^* $[\mathrm{L}^2\mathrm{T}^{-1}]$ represents the effective molecular diffusion coefficient; u_x, u_y, u_z $[\mathrm{LT}^{-1}]$ are the components of the effective velocity vector u, $|u| = \sqrt{u_x^2 + u_y^2 + u_z^2}$.

The fluid sink/source term of the governing equation, $s(\mathbf{x}_0, t) \cdot \delta(\mathbf{x} - \mathbf{x}_0)$, represents solute mass entering the model domain through sources or leaving the model domain through sinks. Sinks or sources may be classified as areally distributed sinks or sources or as point sinks or sources. The areally distributed sinks or sources include recharge and evapotranspiration. The point sinks or sources include wells, drains, and rivers.

The reactive terms, can be described, in general, as:

$$\sum R_n = -\rho_b \frac{\partial \bar{C}^k}{\partial t} - \lambda_1 n C^k - \lambda_2 \rho_b \bar{C}^k$$

where ρ_b $[\mathrm{ML}^{-1}]$ is the bulk density of the subsurface medium; $\bar{C}^k$ $[\mathrm{MM}^{-1}]$ is the concentration of species k sorbed on the subsurfaces solid; λ_1 $[\mathrm{T}^{-1}]$ is the first order reaction rate for the dissolved phase; and λ_2 $[\mathrm{T}^{-1}]$ is the first order reaction rate for the sorbed (solid) phase. In the applications of the present thesis only non reactive pollutants have been considered such that the term $\sum R_n = 0$.

2 Experimental installation

§

2.1 Introduction

The importance of properly accounting for the heterogeneous makeup of aquifers has been known for over thirty years (e.g., *Freyberg*, 1986; *Sudicky*, 1986; *Gelhar et al.*, 1992). Important consequences of that are recognized in the theoretical description of groundwater flow and transport as well as in the proper design and application of technical actions aimed at the quantitative evaluation, management, protection and remediation of groundwater resources. Understanding the role of heterogeneity in groundwater flow and transport processes continues to pose open questions. A key challenge is the scale-dependent nature of the porous medium and our ability to transfer estimates of hydraulic parameters determined at one scale (i.e., the core or field scale) to another scale of interest. In this sense, it is relevant to collect high quality information on hydraulic parameters coming from different measurement scales within a variety of observation windows (e.g., laboratory, field, or regional scale) and heterogeneous conditions. Substantial research has focused on theoretical and numerical frameworks. However, the verification of these developments in real applications (as laboratory and field experiments) is limited (*Sudicky*, 1986; *Woodbury and Sudicky*, 1991; *Tidwell et al.*, 1999; *Dai et al.*, 2005) and these experiments still give rise to different explanations and new research suggestions. The need for experimental work in this field has been recognized; for instance *Butera et al.* (2013)

stated the necessity of datasets to validate a numerical procedure aimed at recovering the contaminant release history and the relative sources in groundwater. It is very important that experiments are performed in rigorously controlled domain with specified boundary conditions, known structure of the porous medium and high precision experimental protocols and measurements. Laboratory experimental equipments (sand-boxes) have recently been adopted with the aim of studying two dimensional (on the vertical plane) heterogeneous porous media (e.g., *Liu et al.*, 2002; *Goswami and Clement*, 2007; *Illman et al.*, 2007; *Liu et al.*, 2007; *Yin and lllman*, 2009). The laboratory sandbox allows the development of experiments with a well-known medium structure, defined boundary conditions and accurate hydraulic (or transport) measurements. Moreover, recent works (*Jose et al.*, 2004; *Catania et al.*, 2008) have shown that good results could be achieved collecting transport data by means of photographic surveys during sandbox experiments. Building on this background, in the hydraulic laboratory of the Department of Civil, Environmental and Land Engineering and Architecture (DICATeA) of the University of Parma, an experimental device to perform groundwater transport tests has been set up. The collected data will be useful to validate numerical procedures oriented to the solution of groundwater transport problems as, for examples, the identification of the contamination source and the pollutant release history that some of the authors of *Cupola et al.* (2015a) have recently developed (*Butera et al.*, 2013). The objectives of the experimental activity are:

1. to develop a noninvasive detection system in respect of the flow and concentration field;

2. to analyze whether the present potential of digital photography (color camera with high resolution) improves the detection of concentration in terms of reading and of spatial detail;

3. to realize the experimental runs adopting substances and methodologies harmless for the people and the environment;

4. to develop a method that monitors the experimental errors aimed at validating the collected data;

5. to validate different methodologies for detecting the source position and the contaminant release history;

6. to develop and test a new procedure for estimating the dispersivity coefficients, starting from different images representing the evolution of the dispersion phenomenon.

2.2 Previous works

The use of laboratory models in order to simulate and study aquifers has been widely applied by researchers for nearly 80 years; for instance, *Taylor and Uppal* (1934) developed a model to evaluate the groundwater flow under a dam. *Bernard and Wilhelm* (1950) studied turbulent diffusion using a physical model. *Grane and Gardner* (1961) continued the work of Bernard and Wilhelm studying transverse dispersion in granular media using x-rays. *Bruch* (1970) performed laboratory experiments to evaluate the dispersion of porous media using conductivity probes and sodium chloride as tracer. More recently, *Silliman et al.* (1987) and *Silliman and Simpson* (1987) studied the effect of anisotropy on dispersion. The authors evaluated the concentration using sodium chloride as tracer and monitoring the salt concentration with a network of electric probes. *Yeh and Liu* (2000) developed an aquifer model to test a new methodology aimed at evaluating the hydraulic conductivity field. They gauged the pressure in several points by means of pressure transducers. *Silliman and Zheng* (2001) compared the data collected on a physical model to the results of stochastic theory. In the above-mentioned paper the photographic technique eventually was used as a tool for a qualitative description of the studied phenomenon, but only after the development of the digital image acquisition systems, the opportunity to detect crucial information (such as anisotropy, concentration, etc.) from pictures was caught by the Researchers.

Ursino et al. (2001) performed tracer experiments in a laboratory model to estimate, by image analysis, the macroscopic anisotropy of the conductivity and the dispersive behavior based on the spatial moments of small solute plumes. *Aeby et al.* (2001) presented a method that detect small scale mixing processes and compared local distribution of differently mobile compounds using an imaging technique to estimate the concentrations of the tracers. The images were stored in gray scale and the intensity of the fluorescence was converted into concentration. *Huang et al.* (2002) developed a 2-D confined aquifer model, in which the authors injected sodium fluorescein as a fluorescent tracer. The model was illuminated by ultraviolet (UV) light to excite the fluorescein, which emits green light in proportion to the concentration of the solute. The concentrations were evaluated through a photographic technique that records the emitted fluorescence with a Charge-Coupled Device (CCD) Black and white camera. The gray scale images were decoded and converted into concentration values.

The resulting method was efficient and low cost. *Sternberg* (2004) evaluated the dispersion in a highly heterogeneous porous medium using a laboratory column. He evaluated the concentration using electrodes and potassium chloride as a tracer. *Gimmi and Ursino* (2004) mapped a model aquifer's heterogeneities by means of image analysis. They took 16 bit gray scale digital pictures and decoded them with appropriate tools that filter images and correct the inhomogeneity of the illumination. *Persson* (2005) presented

a method to estimate dye tracer concentration using image analysis. The Red, Green and Blue (RGB) images were acquired with a digital camera and successively processed and converted in concentration values. *McNeil et al.* (2006) applied an image technique to determine concentration maps on intermediate scale flow experiments with heterogeneous porous media. *Rahman* (2005) used an image technique in order to evaluate transverse dispersion in a porous medium.

Catania et al. (2008) built a 2-D confined aquifer model with a thickness of 1 cm; the porous media consists of glass beads. The medium was illuminated with a fluorescent lamp and the evolution of a tracer injected in the aquifer was studied by means of gray scale images. *Sánchez Fuster et al.* (2008) constructed a laboratory equipment, able to observe flow and transport in porous media under controlled conditions. The authors estimated the concentration field due to a tracer injection through digital photography. *Barrero et al.* (2010) studied anomalous transport behavior by means of a laboratory tank and monitored the concentration distribution in time through an imaging technique. *Capilla Roma et al.* (2012) analyzed the spatial variability of the dispersivity carrying out a series of tracer tests on a laboratory tank also using an imaging technique. *Castro-Alcala et al.* (2012) made use of a vertical sandbox, representing an unconfined 2D aquifer, with the aim of studying the mixing process in heterogeneous porous media. The authors evaluate the process through an imaging technique.

The work described in this chapter differs from the others above referred in many aspects: Fluorescein sodium salt was used, because unlike other tracers (Methyl Blue (*Aureli et al.*, 2011) or Rhodamine B (*McNeil et al.* (2006); *Castro-Alcala et al.* (2012)), it is harmless to people and to the environment (according to EU directive 67/548/CEE) and it can be handled and disposed off in the sewage system without any treatment; the Fluorescein has been excited with blue light LEDs (Light Emitting Diode), avoiding the use of UV that requires special precautions: the light source consists of 8 LEDs, which, according to *Castro-Alcala et al.* (2012), are more stable than the fluorescent lamps (used for instance by *Huang et al.* (2002) and *Catania et al.* (2008)).

The pictures were taken at a higher resolution (10.1 Megapixels with a resolution of 14 bits for each RGB color) than previous studies; this allowed to analyze the RGB channels individually and in combinations and highlighted the necessity of developing filtering techniques in order to manage the great amount of data collected by the camera. Furthermore, in the previous studies (e.g. *Huang et al.* (2002); *Catania et al.* (2008)) the validation of the experiments was performed only at single times or comparing experimental data with simplified analytical solutions at a certain time. In the present study the performance of the experimental procedure has been verified through the analysis of the mass balance for the entire time of the test; with this control the reliability of the methodology has been validated with continuity in order to assure that the experimental conditions remain regular and coherent with the main hypothesis of operation of the ex-

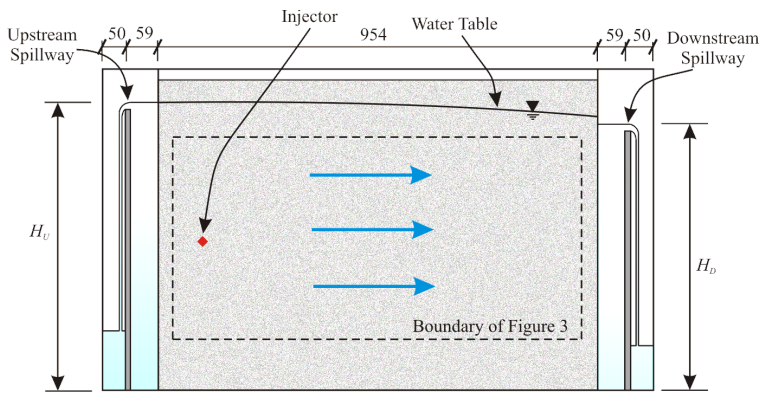

Figure 2.1: Sketch of the sandbox. Distances in mm.

perimental device (e.g. 2D flow in the vertical plane, steady background flow and tracer injection and so on). In this chapter we describe materials and methods of the laboratory experiments, the results of a meaningful experimental test case, and its numerical modeling.

2.3 Sand box

Sand box is built with plexiglas plates with 2 and 3 cm thickness for, respectively, the lateral and the bottom sides (see Fig. 2.1). The external dimensions of the sand box are 73 x 120 x 14 cm^3. The experimental device has been divided along the maximum direction in three parts: two tanks (upstream and downstream) and a central chamber (height $H = 70$ cm, thickness $T_H = 10$ cm, length $L = 94.5$ cm) which contains the porous medium. The division between the tanks and the porous medium is realized using pierced iron plates covered by brass wire gauze. A weir controls the water in the upstream and downstream tanks in order to maintain the same boundary conditions without oscillations. A small tank (70 L) and a centrifugal pump, which circulates the water discharge is monitored with a flow rate meter, which presents an output display and works in the range 6.6 - 250 mL/s with an accuracy of $\pm$ 0.4% of the full-scale value (Fig. 2.2). In order to prevent excessive deformation and to strengthen the structure, an iron bar was installed on the top of the box. However, the tests have shown that they aren't negligible, so they were measured with the photogrammetric technique.

2.4 Porous medium

The porous medium has been chosen to be inert and to allow the total reset of the system at the end of a transport experiment; it is built with glass beads with diameter in the

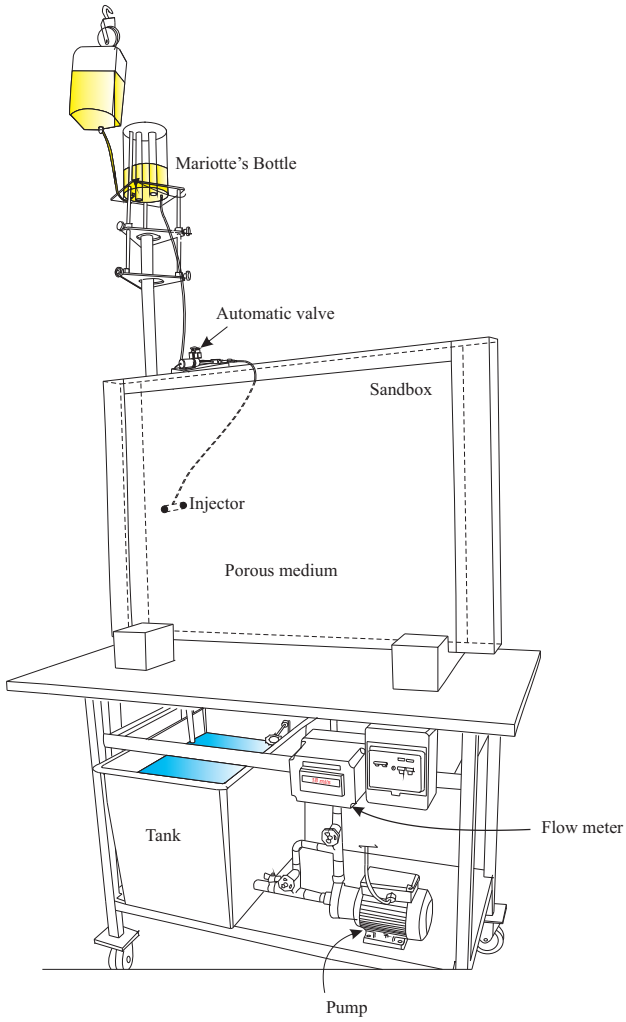

Figure 2.2: Experimental device. The Mariotte's bottle and the automatic valve are represented. The point of view is external at the opposite side respect the camera.

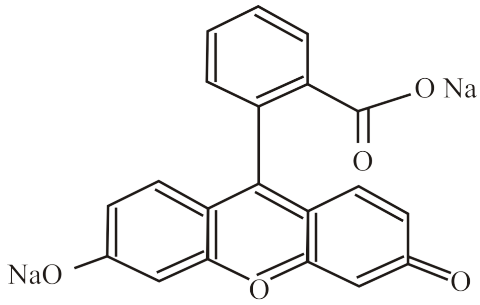

Figure 2.3: Chemical structure of Fluorescein.

range between 0.75 and 1 mm with density of 1480 kg/m^3 and the composition: 72% SiO_2, 13% Na_2O, 9% CaO. The central tank of sand box was packed under fully saturated conditions layer by layer to avoid trapping of air and minimize segregation. The porosity was estimated by means of laboratory test at 37% and the hydraulic conductivity K [L/T] has been assessed after a series of tests as a calibration of the Dupuit Forcheimer formula (*Bear*, 1972):

$$q = \frac{K\left(H_U^2 - H_D^2\right)}{2L} \tag{2.1}$$

which gives the total discharge q [L^2/T] per unit width flowing trough an unconfined aquifer between two reservoirs at distance D [L] with constant head H_U [L] and H_D [L] at the upstream and downstream boundary. A very important step of tests is the introduction of the porous medium in the sandbox: it is crucial to avoid bubbles air inside the pores. In fact, it can modify the flow and it can represent an important source of noise in the analysis of the images acquired during the transport experiments. With the aim of avoiding these phenomena, the glass beads have been introduced only when the sandbox is full of water.

2.5 Tracer and injection system

A colored fluid was chosen as tracer in order to optimize the photographic survey; in particular, the fluorescein sodium salt ($C_{20}H_{10}Na_2O_5$) (Fig. 2.3) was chosen after an analysis of the substances available (cochineal red, methyl blue, and others). It is a non-toxic compound and consequently easy to handle; after use it can be disposed of and the porous medium can be cleaned without difficulty between experiments. The fluorescein sodium salt mixed with water and excited with UV rays ($\lambda = 256$ nm) or with blue light ($\lambda = 490$ nm) irradiates at longer wavelength (green light, $\lambda = 520$ nm). Moreover, when evaluating the properties of several dye tracers, *Smart and Laidlaw* (1977) showed that

the fluorescein presents moderately high resistance to sorption and may be regarded as a conservative tracer under neutral or moderately basic pH. A preliminary assessment of the photo-bleaching phenomenon (*Imamura and Koizumi*, 1955) was carried out; the loss of brightness, observed during 12 hours, was less than 1%, representing a non-relevant problem for the present tests. The registration of all RGB channels allowed the control of the quenching effects (*Lakowicz*, 2006),which were reduced using softened water (2 °f). The tracer solution, with known concentration, was introduced into the porous medium by using an injector made up of a brass cylinder with 32 holes located on the line of the downstream stagnation. The injector is supplied with a pipe (1 mm diameter) connected to a Mariotte's bottle (*McCarthy*, 1934) that guarantees a constant head; an automated valve located in the supply pipe is able to adjust the tracer discharge in the range 0 to $5{\cdot}10^{-6}$ m^3/s, and also to manage the start and the end of the injection precisely. A vent pipe is connected at the top of the system to allow air discharge in order to avoid a non-uniform supply of the injection. The Mariotte's bottle was equipped with an inductive level gauge (0.5% relative instrument error) to monitor the change in the solution level.

2.6 Lighting system and dark room

The experimental device was placed in a darkroom to avoid all external light contamination. Previous literature indicated that UV light is ideal to induce fluorescence but, in order to realize harmless experimental conditions and because the PMMA of the experimental equipment walls is impervious to UV, a blue light source was chosen. After preliminary tests carried out with blue neon lights, which gave a partially unsatisfactory performance (*Citarella et al.*, 2010), monochromatic blue LED lights were used. The system was composed of 8 blue LED lights, each requiring 2.5 W of power, mounted on a rectangular frame that surrounded the digital camera (see Fig. 2.4). These LEDs irradiate in the wavelength from 460 to 490 nm with the peak at 470 nm and require a 600 mA Direct Current. The high power requirement necessitated a cooling system. In the first version of the experimental equipment, there were some problems regarding some reflections on the wall of the sandbox: in the new version, all these problems were avoided building a bigger dark room. The camera Canon Eos 40D, which is used for recording the evolution of the tracer during the tests is anchored to a block of concrete and the position is fastened at 1.6 m far from the sandbox. Inside the darkroom a webcam takes place: it permits to follow in real-time the phenomenon.

2.7 Data acquisition

As shown in Fig. 2.5, several data have been managed in order to control and to acquire all the variables during the tests. For doing that, the software *LabView*® has been used

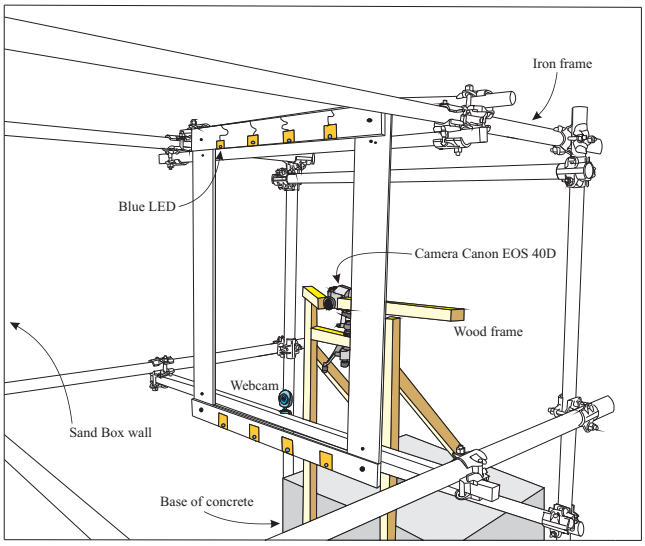

Figure 2.4: Structure of the dark room with the lighting system and the structure for susteining the camera.

together with an acquisition card *SC* 2345 made by *National Instrument* ($\pm$10V, 16 bit). Briefly, all the data acquisition system allows to:

- manage the camera in order to shoot the frames at fixed time intervals and to record the time shoot;
- control and record when the injection starts and finishes;
- record the fluorescein solution level in the Mariotte's bottle, and indirectly the flow rate injected;
- record the temperature at the outlet of the sandbox;
- record the background discharge flowing in the sandbox.

2.8 Spatial reference of the frames

Even though the camera is always in the same position, eight markers have been attached at the wall of the sandbox with the aim of having a known reference equal in every experiment and in every photo. The coordinates of the markers have been evaluated in a local system through a topographic survey (see Fig. 2.6).

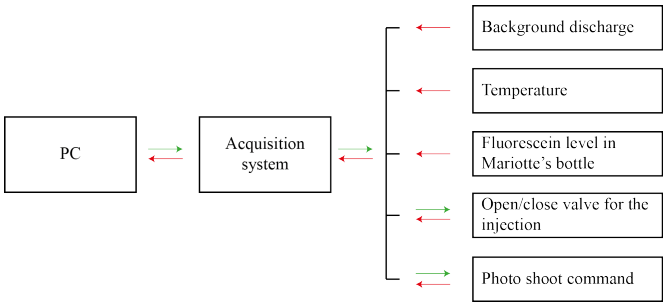

Figure 2.5: Variables managed and acquired during the tests.

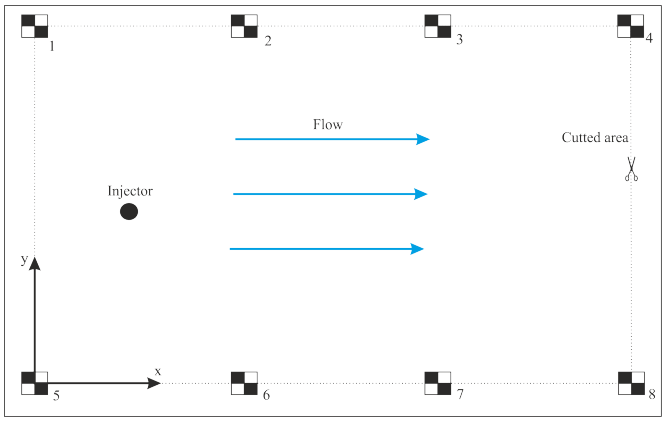

Figure 2.6: Markers used for spatially referencing the photos acquired during the tests.

2.9 Wall effects

Despite the iron bar installed on the top of the sandbox, the topographic survey for calculating the coordinates of the markers denoted a not-negligible deformation of the walls of the sandbox. For studying this phenomenon in a deeper way, an analytical and a photogrammetric technique have been adopted for knowing in detail the magnitude of the deformation, and, in that way, for calculating more precisely the inner volume of the sandbox.

2.9.1 Analytical study

With the aim of estimating the magnitude of the deformation, the coordinates of the markers have been used for calculating the mutual distances between the markers in the direction orthogonal to the wall of the sandbox. For doing that, three markers have been used for calculating the equation of the plane containing them, then the distances between the

other five markers and that plane have been calculated. The equation of a plane in the $\mathbb{R}^3$ is:

$$ax + by + cz = 0$$

in which a, b, c are the parameters of the plane. They can be estimated knowing three points out of line: $P_1 = (x_1, y_1, z_1)$, $P_2 = (x_2, y_2, z_2)$, $P_3 = (x_3, y_3, z_3)$. In particular

$$a = \begin{vmatrix} y_2 - y_1 & z_2 - z_2 \\ y_3 - y_1 & z_3 - z_1 \end{vmatrix}$$

$$b = -\begin{vmatrix} x_2 - x_1 & z_2 - z_2 \\ x_3 - x_1 & z_3 - z_1 \end{vmatrix}$$

$$c = \begin{vmatrix} x_2 - x_1 & y_2 - y_2 \\ x_3 - x_1 & y_3 - y_1 \end{vmatrix}$$

Thus, the distance between a plane π and a generic point $P = (x_0, y_0, z_0)$ can be calculated as

$$d(\pi, P) = \frac{| ax_0 + by_0 + cz_0 |}{\sqrt{a^2 + b^2 + c^2}}$$

where d is the distance. Adopting this procedure, the maximum deformation has been estimated equal to 5 mm at each part of the sandbox.

2.9.2 Photogrammetric technique

The analytical estimation does not allow to estimate precisely the deformation of the sandbox. At this aim the photogrammetric technique has been adopted: this has required of shooting several photos to the sandbox and then the software *Photo Modeler Pro* 5 has been used for estimating the coordinates of a big number of points identified on the frame by several markers. Preliminary, two steps are required:

1. calibration of the camera: this step is fundamental and it allows to estimate the distortion of the sensor of the camera. Several photos of a poster representing a grid of black points having known coordinates have been shooted (Fig. 2.7). In

that way the software *Photo Modeler Pro* 5 can automatically compare the true distances between the points and those estimated by using the frames.

2. the design of the photogrammetric block: in particular, knowing the characteristic of the camera (Table 2.1) and the maximum error accepted σ_z [L], the distance z [L] between the camera and the object and the distance between the camera at two consecutive position b [L] have to be defined. Starting from

$$\begin{cases} \sigma_z = \frac{z}{c} \cdot \frac{z}{b} \cdot \sigma_{px} \\ \frac{z}{b} = \frac{c}{0.4 \cdot w} \end{cases}$$

where c is the focal length adopted for shooting the photos, σ_{px} [L] is the uncertainty associated at the collimation of a point on the frame ($\sqrt{2} \cdot d_{px}$ where d_{px} is the dimension of a pixel) and w [L] is the biggest dimension of the sensor of the camera. So,

$$z = \frac{\sigma_z}{\sigma_{px}} \cdot 0.4w$$

and

$$b = \frac{z}{c} \cdot 0.4w$$

3. the choice of some points having known coordinates: these points are necessary for orientating, in a fixed reference system (local in this case), all the coordinates obtained through the photogrammetric technique. At this aim, the coordinates of some points have been estimated by using a very accurate theodolite.

Once the position of several points are known in the same local reference system, the coordinates of other points disposed at the nodes of a regular grid have been estimated through the Kriging method. Thus, the surface of the sandbox (Figs. 2.8, 2.9 and 2.10) has been reproduced by using the software *Surfer* 6.

2.10 Images properties and post-processing

The objective of the experimental device is to follow the evolution of the tracer at different time during a test. At this aim, several photos are taken and then they are post-processed

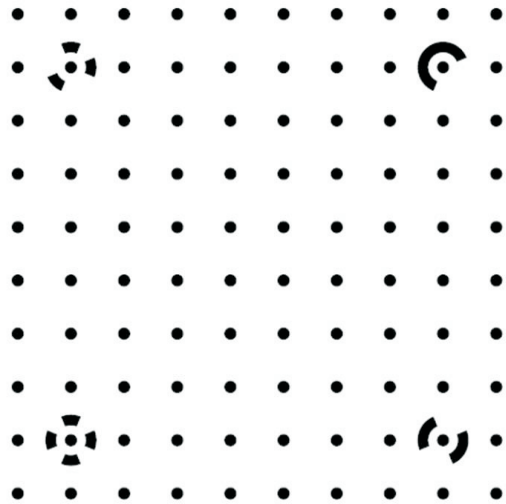

Figure 2.7: Poster used for calibrating the camera. It is a standard poster, so the coordinates of the points are already known by *Photo Modeler Pro* 5.

Table 2.1: Properties of the camera used in the tests.

Camera	Canon EOS 40D
Sensor dimension	$22.2 \cdot 14.8$ mm
Focal length f	16 mm
Precision required σ_z	0.5 mm
Pixel dimension d	$22.2/3888 = 0.0057$ mm
Precision of the collimation σ_{px}	$\sqrt{2} \cdot d = 0.008$ mm
Bigger sensor dimension w	22.2 mm
Frame scale	$S = b/f = 34$

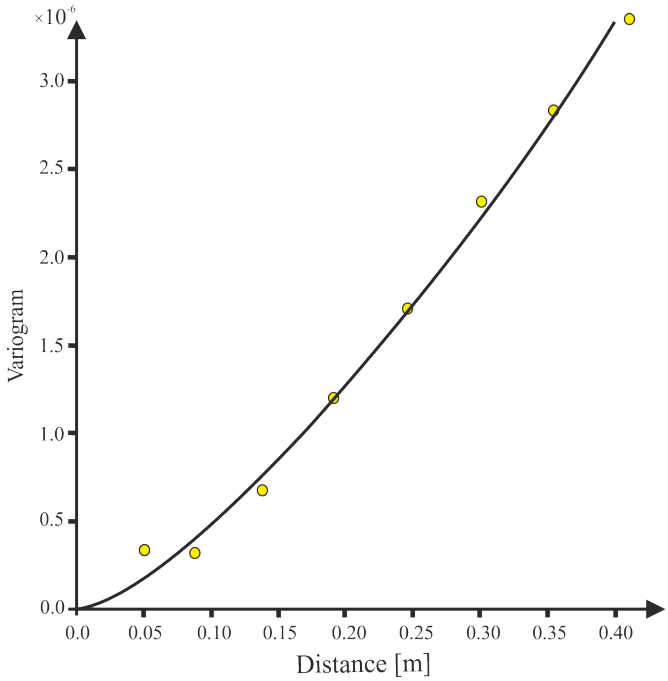

Figure 2.8: Variogram of experimental deformation measured by using the theodolite.

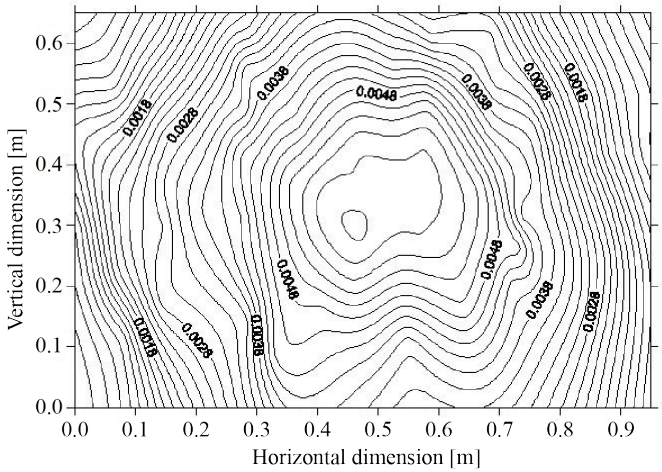

Figure 2.9: Surface of the sandbox reproduced using *Surfer*.

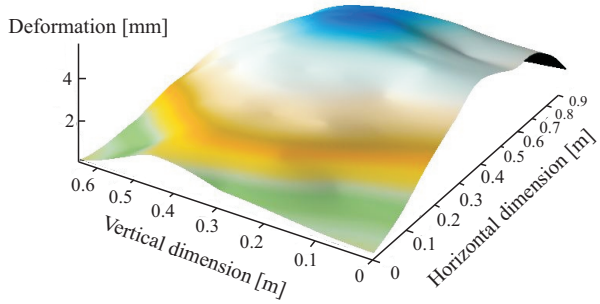

Figure 2.10: Surface of the sandbox reproduced using *Surfer*.

for knowing the concentration map. All these elaborations will be described in the next sections. Moreover, preliminary studies have been carried out with the aim of optimizing the procedure.

2.10.1 Setting of the camera parameters

The camera Canon EOS 40D, used for shooting the frames during the tests, allows of setting several parameters, such as the shutter speed, the sensibility ISO, the focal lenght and the aperture. Different combinations of these parameters give different results. With the aim of maximizing the gain of the concentration of the tracer respect to the luminosity value and for avoiding the saturation of the color channels, several preliminary tests have been carried out. In particular 80 frames have been taken changing the ISO value and the shutter speed. Instead, the aperture and the focal length have been fixed at $f2.8$ and 35 mm respectively. Fig. 2.11 shows the value of the dR, dG and LoB at two points of Fig. 2.12 for different values of ISO and shutter speed and adopting an uniform tracer concentration equal to 30 mg/L. The circles are the measurement points, the circles with a cross inside indicate that the luminosity channel reached the saturation and the filled circles represent the points corresponding to the chosen values of ISO and shutter speed.

2.10.2 Image processing

The images collected were oriented by using two rows of 4 markers affixed to the detection side of the sandbox and utilized as reference system. All images were corrected with the projective transformation in Matlab®(*Mathworks*, 2010), which performs an optimization process on the 16 coordinates of the markers available previously computed by means of a topographic survey. Then the processed images were cutted by deleting the outer side of the markers in order to keep only the most significant area; consequently, the size of

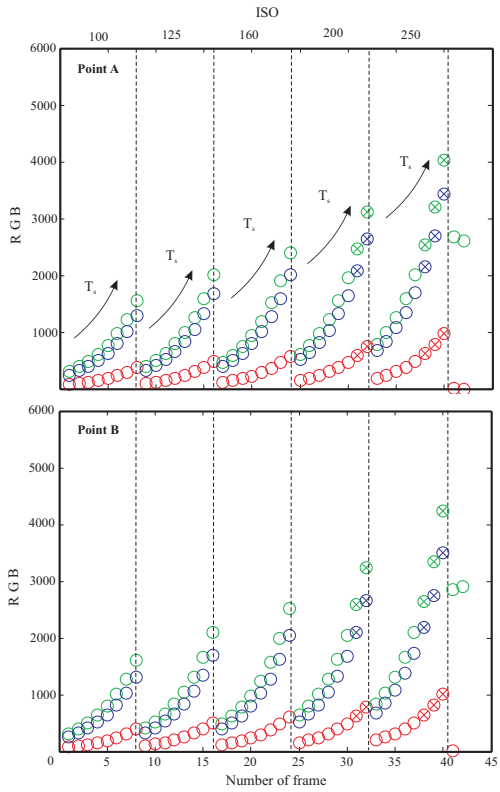

Figure 2.11: Luminosity values for different ISO and the shutter speed at Point A and Point B of Fig. 2.12.

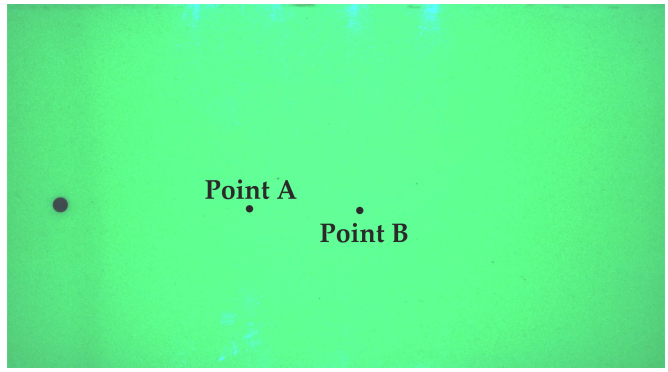

Figure 2.12: Points used for investigating the influence of the camera parameters on the luminosity values.

the image became 3380×1750 pixels. The minimum meaningful volume of the porous matrix must contain a cluster of grains and the relative interstitial space, thus its dimension must be several millimeters on each side. In fact, a preliminary analysis carried out with increasing dimensions of the computation volume showed that irregular luminosity values are obtained with very small sizes. Therefore, the image was down-sampled: the RGB values were averaged over a fixed number of pixels ($n \times n$) covering an Aggregated pixel Area (in short ApA) of $(0.252 \cdot n)^2$ mm^2.

Another step in the image processing was the removal of background noise. An image of the sandbox prior to the tracer injection (background image) was acquired and the color quantities in subsequent images were modified through the relationships:

$$\bar{F}_{ij}^{k} = F_{ij}^{k} - F_{ij}^{0} \tag{2.2}$$

for the Red, Green and Gray (calculated as Gray $= 0.2989 \cdot$ Red $+ 0.5870 \cdot$ Green $+$ $0.1140 \cdot$ Blue) channels, and

$$\bar{F}_{ij}^{k} = F_{ij}^{0} - F_{ij}^{k} \tag{2.3}$$

for the Blue channel, where F_{ij}^{k} is the luminosity value of the pixel located in the i, j position of the picture matrix k, and F_{ij}^{0} is the luminosity in the same location detected in the background image. According to Eq. 2.2 the Red and Green luminosity are reduced to cut off the background noise only; Eq. 2.3, however, computes the loss of the Blue color due to the fluorescein emission. In fact in the absence of fluorescein injection, the sand box appears, obviously, almost totally blue; the green tracer irradiation reduces the quantity of blue, so the "loss of Blue" can be also used to detect the presence of fluorescein. In the following of the thesis the values of Eqs. 2.2 and 2.3 will called as depurated Red (dR), Green (dG), Gray (dGray) and Loss of Blue (LoB) for the Red, Green, Gray and Blue respectively.

2.10.3 Choise of the ApA dimension

The concept of ApA has been showed in Section 2.10.2. Preliminary studies have been aimed at identifying the optimal dimension of ApA. In fact, a small dimension doesn't mean enough luminosity variability between different pixels, but on the other hand, a big dimension doesn't allow to punctually investigate the concentration values and in that way some information could be lost. For this study, the luminosity has been investigated around some fixed points for different values of tracer concentration and for different dimensions of ApA (around those points). Fig. 2.13 reports the results of the investigation at points A and B of Fig. 2.12. The first and the second row refer to the absence and the

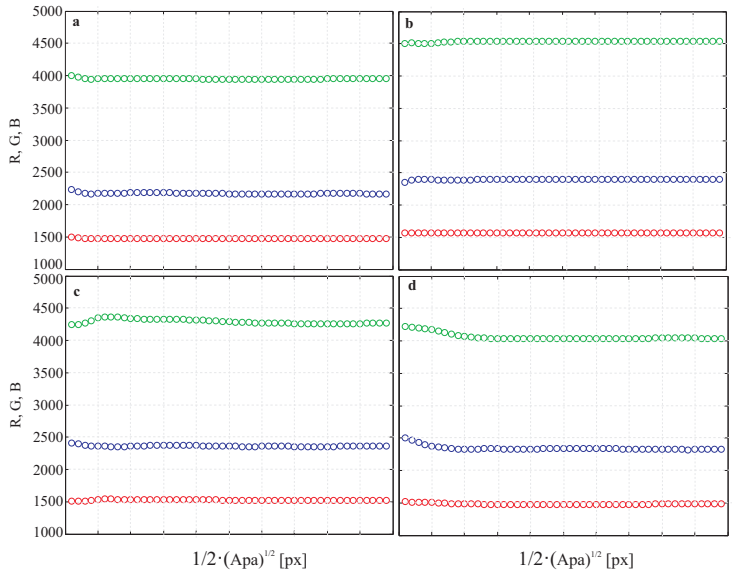

Figure 2.13: Trend of the depurated luminosity channels for different ApA dimension. The first and the second row refer to the absence and the presence of air in the porous medium for points A and B of Fig. 2.12 respectively.

presence of air in the porous medium respectively. The luminosity values become stable for ApA side equal or bigger than 5 pixels in the absence of air, while the second row denotes how the presence of air makes necessary a bigger ApA for mitigating the noise due to the air bubbles.

2.11 System calibration

The preliminary work needed for the calibration of the device was a difficult step. Following the suggestion of *Catania et al.* (2008), a "pixel by pixel" calibration has been performed: the analysis of each pixel allows to identify a calibration relationship between the intensity of each color band and the concentration, taking into account the different light conditions, the local heterogeneity of the porous medium and the possible defects of the PMMA panel. The calibration procedure consisted in the following steps:

1. complete the saturation of the porous medium with a solution of fluorescein at a known concentration;

2. activation of the re-circulation system to maintain a uniform and steady distribution of the solution in the porous medium;

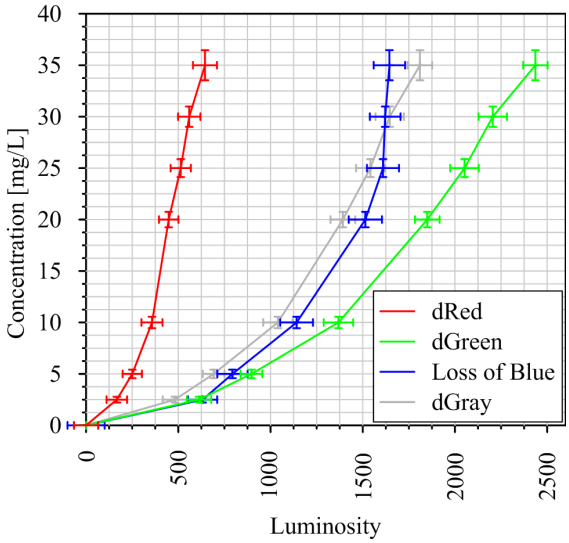

Figure 2.14: Calibration curves of the monitoring point A depicted in Fig. 2.12. The error bars represent the 95% confidence interval.

3. acquisition of the images;

4. restart from step 1 with a new solution concentration.

This procedure has been performed for different concentrations (C = 0; 2.5; 5; 10; 20; 25; 30; 35 mg/L) in order to obtain an adequate calibration curve. Fig. 2.14 shows the trend of dR, dG and dGray values versus the fluorescein concentration for the monitoring point A depicted in Fig. 2.12. Color quantities increase non linearly with increasing concentration. The LoB color quantities are plotted in the same Fig. 2.14, and they too show an increasing trend with increasing concentration. The analysis in gray scale was performed in addition to the single color-tracer concentration trend. The experimental data of Fig. 2.14, and the others relevant to all ApAs, are linearly interpolated between each concentration, for dR, dG, LoB and dGray colors. Several interpolation laws were considered, such as exponential, power, and cubic, but it was impossible to identify a unique function suitable for all ApAs; for this reason the piecewise linear law was chosen. As a conclusion of the calibration process, we obtained four luminosity–concentration relationships, which will be referred to in the following as the dR, dG, LoB, dGray concentration laws for each ApA. In Fig. 2.14 the calibration relationships are depicted together with the band confidence interval (less than 6.4%).

2.12 Analysis of the results

Some preliminary tests have been carried out in order to verify the reliability of the results obtained through the experimental equipment. At first the influence of the air in the porous medium has been evaluated carrying out some experiments with the presence of air bubbles. They clearly showed that the results are strongly affected by the presence of the air: in fact it isn't uni formally distributed in the flow domain and the luminosity at a certain point could change in time even though the concentration value remains the same. These studies have allowed to conclude that the absence of air is of crucial importance at the aim of obtaining reliable results. For each experiment, the measured data have been compared with those obtained analytically through the elaboration of the images acquired during the evolution of the dispersion phenomenon.

2.12.1 Mass rate evaluation

Through the inductive level gauge installed in the Mariotte's bottle it is possible to know the volume of tracer solution injected in the sandbox, i.e. it is possible to calculate the solution flow rate as:

$$Q_{inj}(t_{i+1}) = \frac{-(V_{i+1} - V_i)}{dt}$$

where $Q_{inj}(t_{i+1})$ [$L^3 \cdot T^{-1}$] is the volume of solution injected in the time interval between t_i and t_{i+1}, while V_{i+1} and V_i are the volume of solution resident in the Mariotte's bottle at time t_{i+1} and t_i. Knowing the injected flow rate, the injected mass rate can be calculated as:

$$\dot{M}_{inj} = Q_{inj} \cdot C_{inj} \tag{2.4}$$

where C_{inj} [$M \cdot L^{-3}$] is the known solute concentration. The data obtained through Eq. 2.4 has been compared with those calculated evaluating the mass rate which flows through a sandbox cross section. In particular, the mass rate $\dot{M}^J(t)$ [$M \cdot T^{-1}$] crossing a vertical section J can be computed by analyzing the concentration field by means of the relationship:

$$\dot{M}^J(t) = \sum_Z v_{i,J} \cdot T_H \cdot \Delta z_{i,J} \cdot C_{i,J}(t) = \bar{v} \cdot T_H \cdot \Delta z \cdot \sum_{i=1}^{N_{row}} C_{i,J}(t) \tag{2.5}$$

where J [-] is the position index of the cross section (i.e. the column index), $v_{i,J}$ [$L \cdot T^{-1}$] is the specific discharge at the cell location i, J and the other symbols denote known

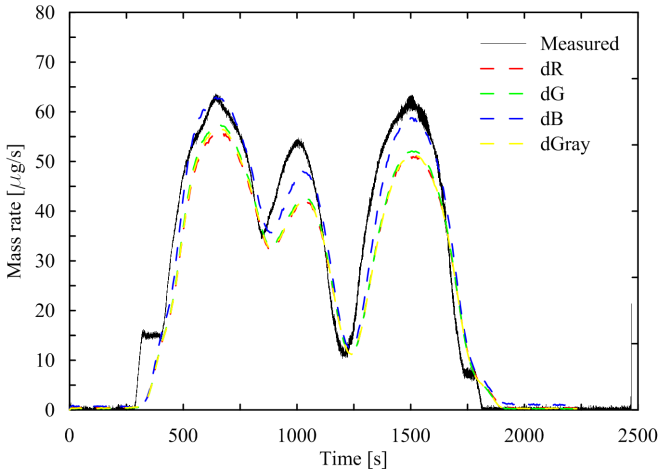

Figure 2.15: Measured and calculated (Eq. 2.5) injected mass rate at a distance from the source equal to 35 cm.

quantities. With a certain approximation $v_{i,J}$ has been considered constant and equal to:

$$v_{i,J} = \bar{v} = \frac{Q_s}{T_H \cdot Z} \tag{2.6}$$

where $Z = N_{row} \cdot \Delta z$ [L] is the length of the cross section in the vertical direction, and $\bar{v}$ [$L \cdot T^{-1}$] is the average velocity computed by the ratio of the water discharge flowing across the sandbox Q_s [$L^3 \cdot T^{-1}$] on the cross section area equal to $T_H \cdot Z$.

2.12.2 Integration in the whole domain: resident mass versus time

A meaningful evaluation of the experimental system's reliability can be obtained by checking the mass balance of the injected tracer and comparing the mass released by the injector and the mass estimated through the image processing. Such proof is necessary also to check if undesirable wall effects occur. At a certain time t the fluorescein quantity $M_{rc}(t)$ [M] resident in the sandbox, through image analysis, can be computed by:

$$M_{rc}(t) = \int_{Volume} C(\mathbf{x},t) \cdot \phi \cdot d\mathbf{x} \cong \sum_{Area} C_{i,j}(t) \cdot \phi \cdot T_H \cdot \Delta x \cdot \Delta z = \phi \cdot T_H \cdot l^2 \sum_{i=1}^{N_{row}} \sum_{j=1}^{N_{col}} C_{i,j}(t) \tag{2.7}$$

where $C_{i,j}(t)$ [$M \cdot L^{-3}$] is the average concentration in the ApA with centroid location

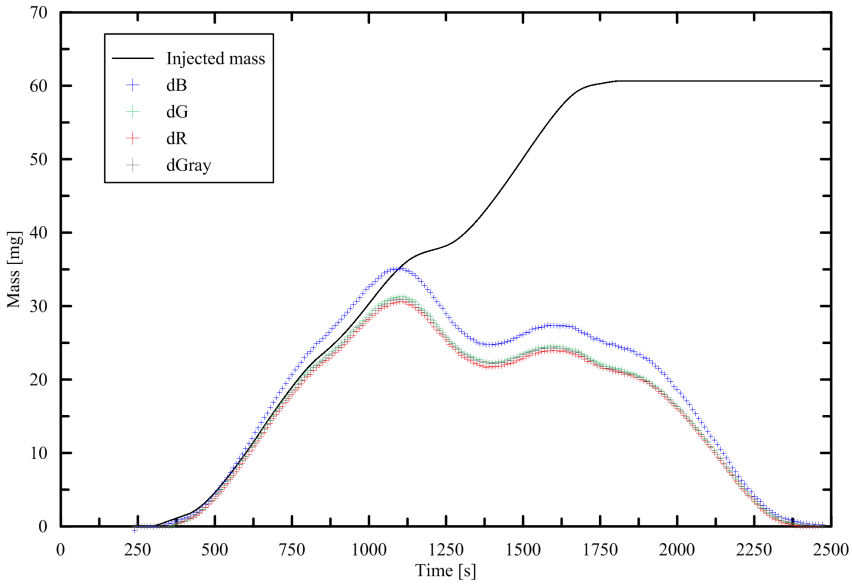

Figure 2.16: Cumulative injected mass and resident mass versus time. Before that the plume reaches the outlet they are very similar. After that, the resident mass decreases according to the plume evolution which has reached the outlet.

i, j at time t, by assuming that the concentration is homogeneously distributed along the tank thickness. T_H [L], ϕ [-] is the effective porosity of the glass beads, $\Delta x = l$ [L] is the dimension of the pixel in x direction, and $\Delta z = l$ [L] is the pixel dimension in z direction. N_{row} and N_{col} [pxs] are the number of rows and columns of the investigated area. The total resident fluorescein mass $M_{rc}(t)$ [M] can be compared to the injected mass at the same time $M_{inj}(t)$ [M]:

$$M_{inj}(t) = Q_{inj} \cdot C_{inj} \cdot t \tag{2.8}$$

where Q_{inj} [$L^3 \cdot T^{-1}$] is the solution flow rate from the injector, C_{inj} [$M \cdot L^{-3}$] is the fluorescein solution concentration, and t [T] is the time elapsed from the beginning of the test.

2.13 Example of the results of a test

In this section, the results of the test carried out on July 11^{th} 2013 is shown. This test has been used for the analyses of Chapter 4. In Table 2.2 the boundary conditions and the properties of the test are reported. The test had a time length of 2200 s. The injection started at time $t_{start} = 310$ s and finished at $t_{end} = 1800$ s considering a constant concen-

Table 2.2: Boundary condition and properties of the test explained in this section.

Variable	Value
Date	July 11th, 2013
Upstream head	59.9 cm
Downstream head	53.6 cm
Duration of the test	2470 s
Start of the injection	310 s
End of the injection	1800 s
Time of the first image	240 s
Total number of images acquired	494
Time interval between images	5 s
Concentration of the tracer solution	20 mg/L
x-position of the injector	14.5 cm
z-position of the injector	32.5 cm
Dimension of the cutted image	3380×1750 pxs
Real dimension of the cutted image	85.28×44.15 cm

tration of 20 mg/L and a variable injection rate (from 0 to about 3 mL/s); consequently the mass rate varied in a range between 0 and approximately 60 µg/s (see Fig. 2.15).

During the test, the water discharge is monitored with a flow meter that works in the range $6.5{\cdot}10^{-3}$ to $250{\cdot}10^{-3}$ L/s with an accuracy of $\pm 0.4\%$ of the full-scale value. As shown in Fig. 2.17 the background discharge is influenced by the injection and, in the test showed here, it detected the three different peaks.

Also the test the temperature of the water at the outlet has been monitored. As shown in Fig. 2.18 the temperature remains pretty constant: this indicates that the injection of the tracer solution does not change the temperature of the water appreciably.

In Fig. 2.15 the mass rate measured and estimated through the three color-channels are compared. One can note the the estimation is satisfactory and that the blue channel is more reliable for this analyses.

In Fig. 2.16 the comparison between the mass resident in the sandbox (estimated through the image processing, Eq. 2.7) and that injected is shown. Until the plume reaches the outlet, the comparison is very good, then this analyses can not be used.

2.14 Numerical modeling

Several attempts were carried out to represent the experimental conditions with analytical formulation. The results of such computations were unsatisfactory for different reasons: the flow field where the tracer transport occurs is not strictly steady, and the source dimen-

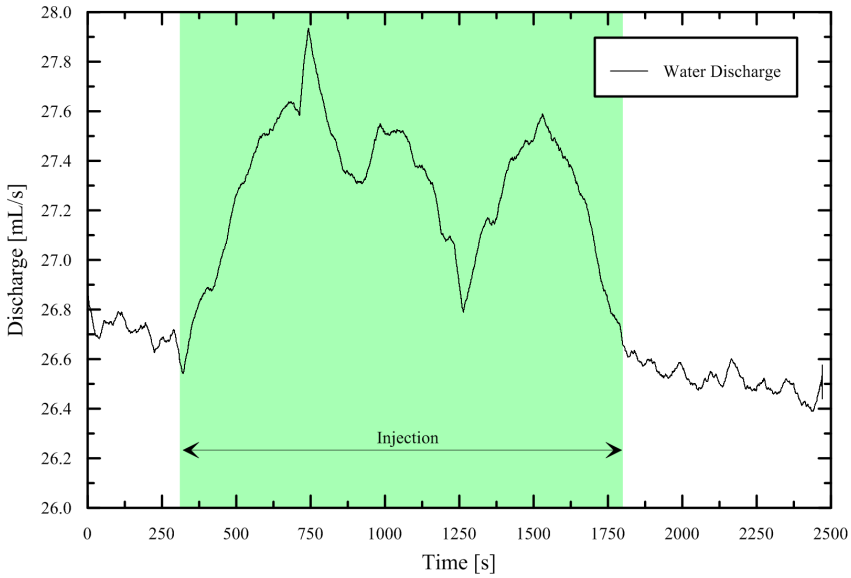

Figure 2.17: Background discharge measured by the flow meter. Its trend is influenced by the injection.

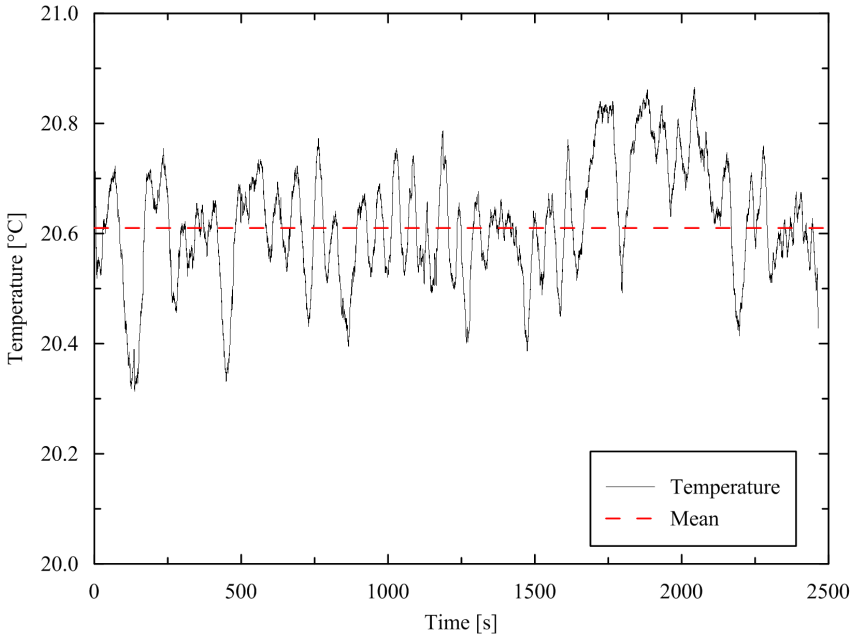

Figure 2.18: Temperature of the water at the outlet.

sions are neither negligible nor well defined. A numerical model of the flow and transport processes was implemented since the analytical solutions refer to steady background flow and point or known area source (*Bear*, 1972; *Domenico and Robbins*, 1985).

The main assumptions the model is based on are that the flow and transport phenomena are uncoupled and that the flow can be studied in a vertical plane; the porous medium was considered homogeneous and isotropic. The groundwater flow was reproduced with MODFLOW2000 (*Harbaugh et al.*, 2000), and the transport process by using MT3DMS with TVD as advection solver package (*Zheng and Wang*, 1999). The model reproduced the sandbox taking into account lateral deformations by using a finite difference grid of 192 columns (representing the longitudinal size), 140 layers (describing the sandbox height) and one row only (the depth size), resulting in 26880 computation nodes. On the vertical plane the size of the cells was 0.5×0.5 cm^2, while along the thickness, the dimension was fixed according to the photogrammetric survey. The hydraulic conductivity of the porous medium in the numerical flow model was set up after a calibration process based on the experimental results of the runs. In particular the calibration consisted in: 1. building the grid and performing a simulation in steady state condition; 2. using PEST (Parameter Estimation) (Doherty, 2008) for estimating the hydraulic conductivity in order to obtain the experimental background discharge; 3. introducing the injector as well with an injected flow rate equal to the measured one. This simulation has been performed in stationary state condition, so, the result has been assumed as initial condition of the transient model; 4. finally, the transport phenomenon has been simulated and the dispersion parameters have been adjusted in order to fit the measured concentration data.

Several tests were performed to calibrate the experimental equipment by considering different concentrations, background flow rates, injection positions and discharges, but, for illustration purposes, one test case only will be presented here. This test has been used also for testing a new procedure for estimating the dispersivity coefficients (see Chapter 3). The test case has a mean groundwater flow rate of about 26 mL/s, obtained with a hydraulic gradient of 7.6% and a mean specific discharge of about $4.6 \cdot 10^{-4}$ m/s. In such conditions the Darcy law is valid because the Reynolds Number does not exceed 1. During the test, the water exiting the sandbox was conveyed to the sewage system. During the entire test 660 images were acquired with a 5 s time interval (total duration equal to 3300 s). Two injections have been performed: the first from 30 and 670 s and the second from 1800 and 2400 s. The detailed analysis of the images taken during the test allows an accurate description of the transport process. The image processing carried out on the plume images provides the concentration field in the study area at each monitoring time. Fig. 2.19 shows, as an example, the concentration field computed on the basis of the dGray law at time 500 s after the beginning of the test; each pixel represents an ApA and it is colored in agreement with the reported color concentration scale; each ApA has a own calibration curve. As shown in Fig. 2.23 the agreement between the numerical

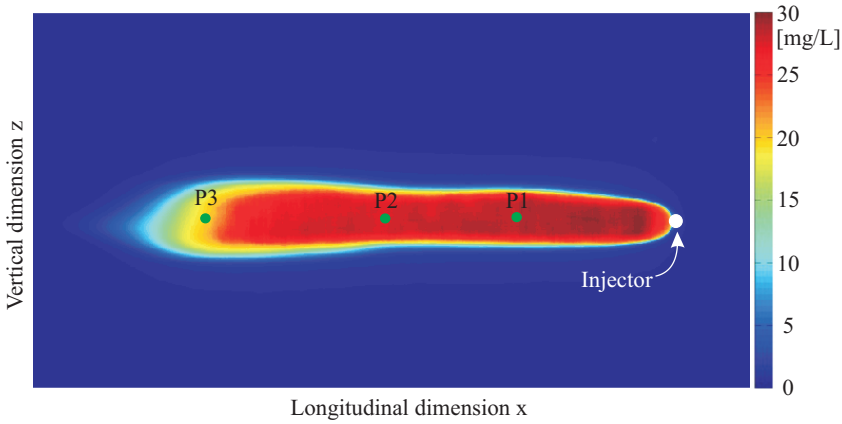

Figure 2.19: Concentration estimated through the analysis of the dGray at time T=550 s after the beginning of the test.

model and the Gray-law image evaluated mass is satisfactory. Fig. 2.22 shows the tracer concentration versus time at the monitoring points P1, P2 and P3 of Fig. 2.19; the concentration values were obtained applying dR-, dG-, LoB-, and dGray-Concentration laws plotted. Fig. 2.23 shows the concentration profile (at time 500 s) of the ApA column where the monitoring point P2 of Fig. 2.19 is located. All channels give similar results and experimental data are well represented by the numerical model.

The numerical model results are generally centered within the scatter of the image-processing results. Fig. 2.23 compares the actual, the numerical model (black line) and the image evaluated injected mass calculations over time.

Finally, in Fig. 2.20 the numerical results (5 mg/L concentration contour level) are superimposed on the image captured during the experiment at different times. The 5 mg/L contour level includes the precise plume contour suggesting that the implemented numerical model represents corresponds closely with the flow and transport in the sandbox. The best results were obtained using the calibrated hydraulic conductivity value (K = 6.52·10^{-3} m/s), an effective porosity of 0.37, a longitudinal dispersivity of $\alpha_L = 1.8 \cdot 10^{-4}$ m and a transverse dispersivity of $\alpha_T = 1/10\ \alpha_L$.

2.15 Conclusions

The detection of physical parameters in laboratory by means of image processing is known as a very powerful system: it is cheap, not invasive and able to collect information in infinity of locations. Other methods for the concentration detection require point measurements, by means of physical contact with the solution or sampling; the number of measurements has to be restricted by economic considerations and the need of reducing

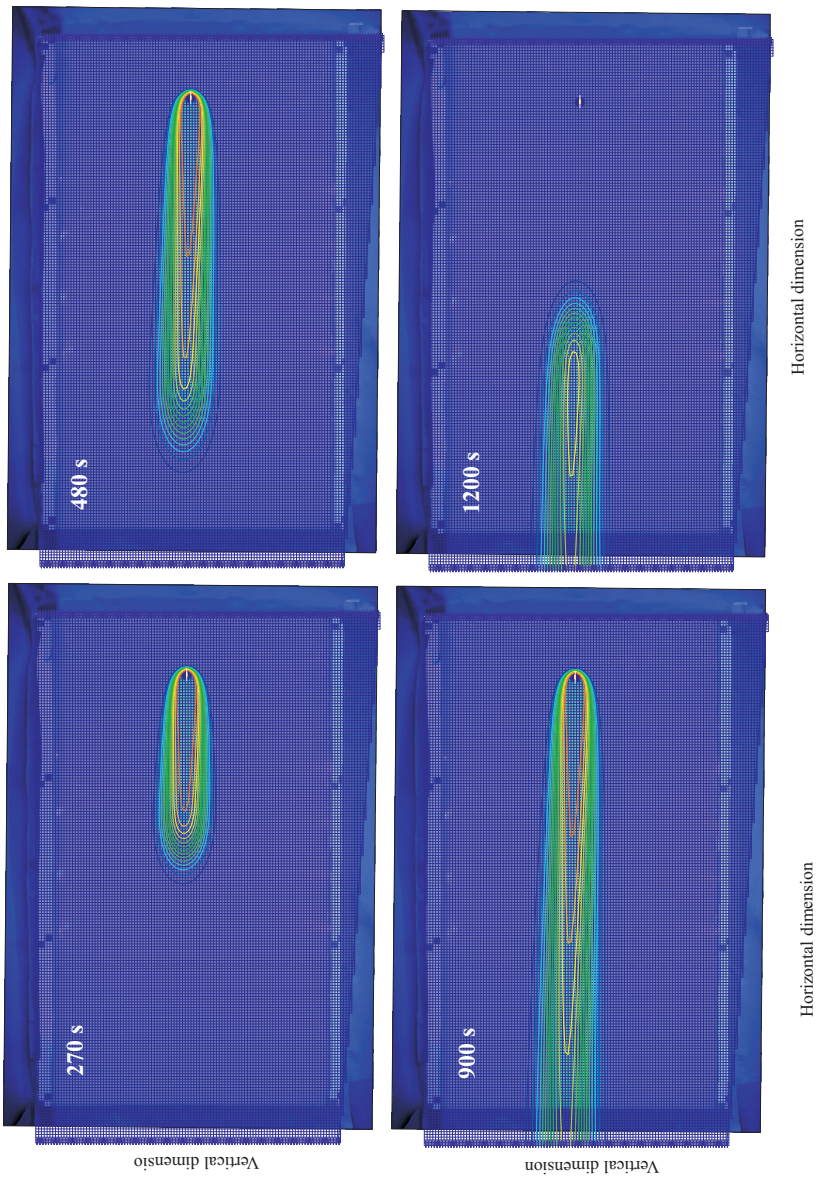

Figure 2.20: Numerical model superimposed on raw images at different times.

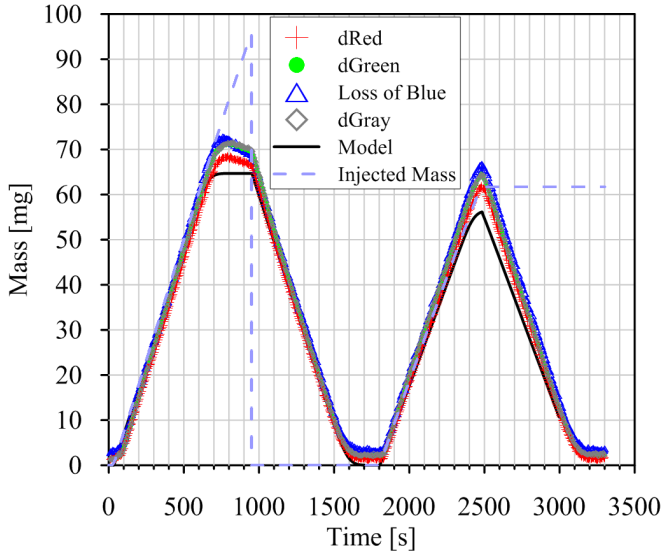

Figure 2.21: Injected and observed mass in the sandbox versus time. Eq. 2.7 has been used for estimating the mass resident in the sandbox through the color analyses.

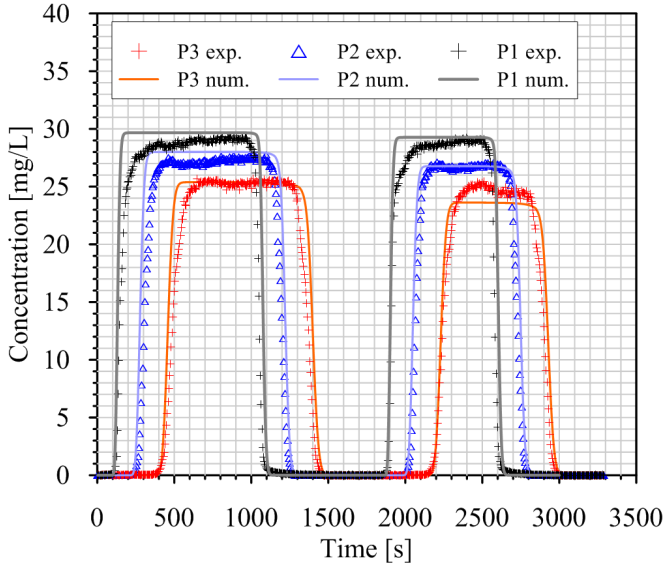

Figure 2.22: Comparison between numerical and experimental breakthrough curves at three different points of Fig. 2.19. For experimental breakthrough curve, the dGray law was used.

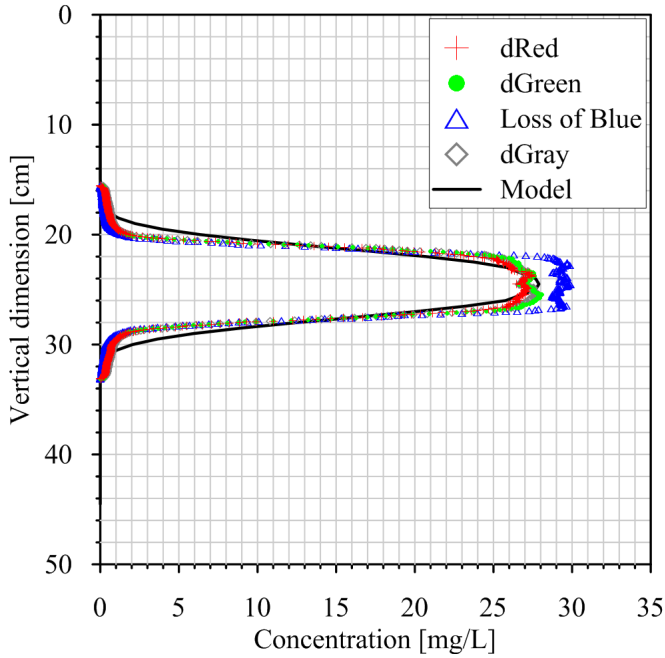

Figure 2.23: Concentration at time $T = 500$ s in the vertical cross section of the monitoring point P2.

the flow interference. The technique tested in this work uses, instead, the information coming from the face view of the sandbox that has to be, obviously, transparent and in the same side of the lighting. No noise can derive to the flow and transport process. It is possible to apply this photographic technique also for experimental devices that present a rear wall not transparent where piezometer or pressure transducer inlets can be located as described, for example, in *Jose et al.* (2004). It represents a change in perspective in comparison with other experiments such as *Huang et al.* (2002) and *Catania et al.* (2008) that detected the light after the transit through the sandbox (on the opposite side with respect to the illumination).

The main issue about the detection from the side view is that the wall concentration field is considered representative of the entire depth of the porous medium and, due to the wall effect discussed above; it can lead to errors in the tracer transport detection. However, it is possible to inspect if the errors are remarkable or not by checking the mass balance. In the experimental runs so far completed, the mass balance errors are very restrained; we cannot rule out that in the future experiments, with heterogeneous porous medium and coarse particles, the wall effect can be more serious but, anyway, it can be evaluated. The calibration process was a very delicate step; moreover the present photographic re-

sources that can produce information on the different color channel add potentialities and complexities. Our work shows that it is possible to infer color quantity-concentration relationships for the different RGB channels but they can lead to not consistent concentration estimations. In agreement to *Persson* (2005) and *Aureli et al.* (2011) we found better results converting the RGB information to gray color through the weighting average relationship that preserve the luminance (brightness) of the image. Again the mass balance computation was the tool that oriented our opinion. Several future improvements and developments can be outlined. The injection conditions have to be optimized in order to limit the moderate initial noise observed in the breakthrough curves. It can be very interesting to enlarge the injecting area in order to involve a greater portion of the porous medium. The best performance can be achieved using as injecting chamber the upstream tank: it can be crucial in the experiments with the heterogeneous medium also in presence of connectivity channels.

3 Evaluation of dispersivity coefficients by means of a laboratory image analysis

§

3.1 Introduction

Aquifers are a vital water resource whose quality characteristics must be safeguarded or, if damaged, restored. The extent and complexity of aquifer contamination is related to characteristics of the porous medium, the influence of boundary conditions, and the biological, chemical, and physical processes. To simplify and understand the influence of these various factors on aquifer contamination, it is common for researchers to use controlled laboratory conditions. For example, contaminant transport has been studied in aquifer models constructed in sandboxes; these allow control of porous medium structure, boundary conditions and reactions (e.g. *Bruch*, 1970; *Yeh and Liu*, 2000; *Yin and Illman*, 2009; *Silliman and Zheng*, 2001; *Sternberg*, 2004; *Goswami and Clement*, 2007). One very important physical process that affects contaminant transport and has been studied extensively in sandboxes is contaminant dispersion.

By using the aquifer sandbox model described in Chapter 2, a new procedure for estimating the dispersivity coefficients has been developed. In previous efforts, longitudinal dispersivity was determined from one-dimensional transport experiments (*Silliman et al.*, 1987; *Sternberg*, 2004) and transverse dispersivity has been determined by assuming a fixed ratio of longitudinal to transverse dispersivity (*Kim et al.*, 2004; *Aksoy and Guney*, 2010; *Capilla Roma and Sánchez Fuster*, 2012a and 2012b). In other efforts, transverse dispersivity was determined from experiments (*Klenk and Grathwohl*, 2002; *Benekos et al.*, 2006; *Cirpka et al.*, 2006; *Olsson and Grathwohl*, 2006; *Chiogna et al.*, 2010; *Rolle*

et al., 2012) making assumptions on the longitudinal dispersivity. None of the aforementioned procedures simultaneously estimated both longitudinal and transverse dispersivities. All the previous studies, except *Capilla Roma and Sánchez Fuster* (2012a and 2012b) that used a numerical discretization of the advection dispersion equation, estimated the dispersivity coefficients by fitting the experimental data to analytical solutions available in literature. In the literature of the imaging systems, there is very little documentation on strategies for monitoring negative effects of the experimental limitations, such as photobleaching, quenching, side-walls effects, local heterogeneities, non-homogeneous lightening etc., that cannot be totally eliminated but, at least, they can be quantified. In the present chapter the efforts to test a new procedure for estimating the dispersivity coefficient values by means of the experimental equipment described in Chapter 2, is reported. The work presented in this chapter has been published in *Citarella et al.* (2014) and *Cupola et al.* (2015c) and presented at 7^{th} Groundwater Symposium of IAHR (*Cupola et al.*, 2014) and at IDRA Congress (*Cupola et al.*, 2014).

3.2 Numerical-Imaging Dispersivity Evaluation (N-IDE)

3.2.1 Mathematical Statements

Eq. 1.7 describes the transport process in an aquifer responding to the injection of a non-sorbing, non-reactive solute in a point source (*Bear and Verruijt*, 1987). Considering a homogeneous porous medium and a uniform flow in a vertical plane, it becomes:

$$\phi\frac{\partial C}{\partial t} = -u\phi\frac{\partial C}{\partial x} + \phi D_L\frac{\partial^2 C}{\partial x^2} + \phi D_T\frac{\partial^2 C}{\partial z^2} + s(\mathbf{x}_0, t)\cdot\delta(\mathbf{x}-\mathbf{x}_0) \tag{3.1}$$

where u is the effective velocity that has component only along x, D_L [$L^2{\cdot}T^{-1}$] and D_T [$L^2{\cdot}T^{-1}$] are the longitudinal and the transverse dispersion coefficients respectively, x is the Cartesian coordinate oriented in the average flow direction, and z is the transverse (vertical) one (see Fig. 3.1). In general, dispersion is a phenomenon whereby the solute spreads out in the longitudinal and transverse direction originating a dilution effect. Theoretical developments, together with experimental evidence, have shown that for negligible molecular diffusion, the dispersion coefficients can be approximated with

$$D_L = \alpha_L\cdot u\ ,\ D_T = \alpha_T\cdot u \tag{3.2}$$

where α_L [L] and α_T [L] are the longitudinal and transverse dispersivity coefficients of the porous medium. Eq. 3.1 is discretized with the aim of determining the dispersivity coefficients by applying a leap-frog finite difference method (Fig. 3.2); for the generic

function f the time derivatives are computed at time $t = n \cdot \Delta t$ with the following formulation:

$$\frac{\partial f_{i,j}^{n}}{\partial t} \approx \frac{f_{i,j}^{n+1} - f_{i,j}^{n-1}}{2 \cdot \Delta t} \tag{3.3}$$

where $f_{i,j}^{n}$ refers to the value of the generic function f (for instance the concentration) in the grid node with location described by the indexes i and j at time n. The spatial derivatives at time n are computed with the following formulation:

$$\frac{\partial f_{i,j}^{n}}{\partial x} \approx \frac{f_{i+1,j}^{n} - f_{i-1,j}^{n}}{2 \cdot \Delta x} \, , \, \frac{\partial f_{i,j}^{n}}{\partial z} \approx \frac{f_{i,j+1}^{n} - f_{i,j-1}^{n}}{2 \cdot \Delta z} \tag{3.4}$$

The experimental device, described in Chapter 2, allows to detect the concentration of the tracer at each point of the domain, at different times. Starting from the concentration distributions, it is possible to estimate the spatial and time derivatives with Eqs. 3.3 and 3.4 and then the dispersivity coefficients (α_L [L] and α_T [L]) under the hypothesis that the plume evolves according to Eq. 3.1. The estimation of the dispersivities can be done in each ApA (N computation nodes) at each monitoring time under different hypotheses:

1. the ratio $r = \alpha_L/\alpha_T$ between the dispersivities is assumed to be fixed at a known value (N equations are needed);

2. the ratio r is constant but unknown ($N + 1$ equations are necessary) (as shown in *Sanchez Fuster*, 2011);

3. the ratio r is unknown and variable at each grid node ($2N$ equations are required). In this work this third case has been considered.

For each ApA, two equations are therefore required to estimate longitudinal and transverse dispersivities, so two consecutive time steps (n and $n+1$) were considered. At each time step, the partial derivatives in Eq. 3.1 were evaluated according to Eqs. 3.3 and 3.4 obtaining:

$$CT_n = \left(\frac{\partial C}{\partial t}\right)_n = \frac{C_{i,j}^{n+1} - C_{i,j}^{n-1}}{2 \cdot \Delta t} \tag{3.5}$$

$$CX_n = \left(\frac{\partial C}{\partial x}\right)_n = \frac{C_{i+1,j}^{n} - C_{i-1,j}^{n}}{2 \cdot \Delta x} \tag{3.6}$$

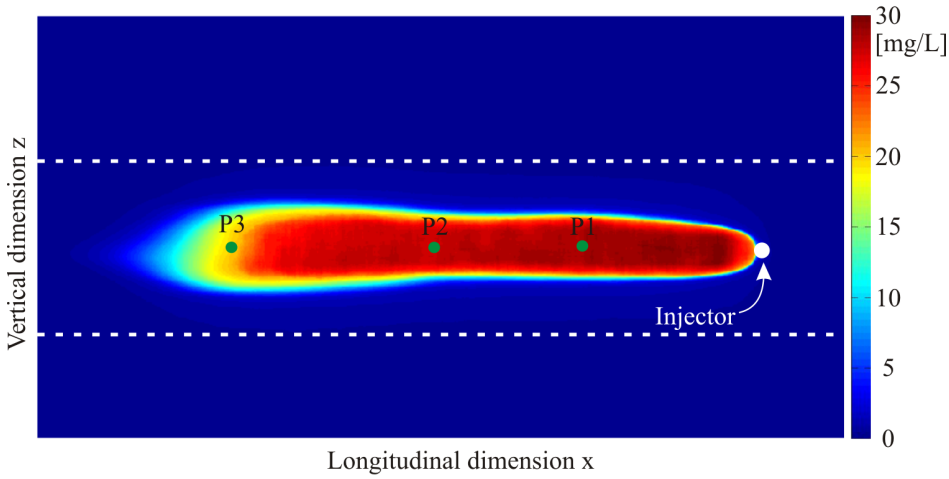

Figure 3.1: Concentration estimated through the analysis of the dGray at time T=550 s after the beginning of the test.

$$CXX_n = \left(\frac{\partial^2 C}{\partial x^2}\right)_n = \frac{CX^n_{i+1,j} - CX^n_{i-1,j}}{2 \cdot \Delta x} \tag{3.7}$$

$$CZ_n = \left(\frac{\partial C}{\partial z}\right)_n = \frac{C^n_{i,j+1} - C^n_{i,j-1}}{2 \cdot \Delta z} \tag{3.8}$$

$$CZZ_n = \left(\frac{\partial^2 C}{\partial z^2}\right)_n = \frac{CZ^n_{i,j+1} - CZ^n_{i,j-1}}{2 \cdot \Delta z} \tag{3.9}$$

where $i = 1 : N_{row}$ is the row index and $j = 1 : N_{col}$ is the column index. Using the symbolism of Eqs. 3.5 to 3.9, in a location different from the source and dividing for ϕ, Eq. 3.1 could be rewritten as:

$$CT_n = -u \cdot CX_n + u\alpha_L \cdot CXX_n + u\alpha_T \cdot CZZ_n \tag{3.10}$$

By considering two time steps, under the hypotheses of steady state flow and known mean velocity in the x-direction, a system of two equations in two unknowns can be

written for each ApA:

$$\begin{cases} CT_n = -u \cdot CX_n + u\alpha_L \cdot CXX_n + u\alpha_T \cdot CZZ_n \\ CT_{n+1} = -u \cdot CX_{n+1} + u\alpha_L \cdot CXX_{n+1} + u\alpha_T \cdot CZZ_{n+1} \end{cases} \tag{3.11}$$

in matrix form it results:

$$\underbrace{u \cdot \begin{bmatrix} CXX_n & CZZ_n \\ CXX_{n+1} & CZZ_{n+1} \end{bmatrix}}_{\mathbf{A}} \underbrace{\begin{bmatrix} \alpha_L \\ \alpha_T \end{bmatrix}}_{\lambda} = \underbrace{\begin{bmatrix} CT_n + u \cdot CX_n \\ CT_{n+1} + u \cdot CX_{n+1} \end{bmatrix}}_{\mathbf{b}} \tag{3.12}$$

At the domain border a rectangular frame, of 1 ApA size, must be used only for the computation of the derivatives (Eqs. 3.3 to 3.4) without evaluating the dispersivity coefficients. The solution of the system 3.12 ($\lambda = \mathbf{A}^{-1} \cdot \mathbf{b}$) for each grid node (ApA) provides the dispersivity values; we will refer to this procedure in the following with the acronym N-IDE, i.e. Numerical-Imaging Dispersivity Evaluation. The proposed N-IDE has been applied for solving an analytically problem in order to quantify the influence of the numerical dispersion due to the discretization of the differential equation.

3.3 Test case

The test case used for validating the N-IDE procedure is that described in Section 2.14, however, for clarity, the details of the test case is reported here in detail. The test case has a mean groundwater flow rate of about 26 mL/s (see Fig. 3.4), obtained with a hydraulic gradient of 7.6% and a mean specific discharge of about $4.6 \cdot 10^{-4}$ m/s. In such conditions the Darcy law is valid because the Reynolds Number does not exceed 1. During the test, the water exiting the sandbox was conveyed to the sewage system. The test (Fig. 3.4) could be summarized in the following phases:

- (1) start of the first injection (I) of $Q_{injI} = 3.5$ mL/s with constant concentration $C_{inj} = 30$ mg/L; the plume developed increasing its length and width;
- (2) the plume reached the outlet and appeared in steady state inside the sandbox;
- (3) end of injection I;
- (3-4) the plume, being no longer fed, reduced its extension and moved to the outfall;
- (4) the sandbox was completely clean;

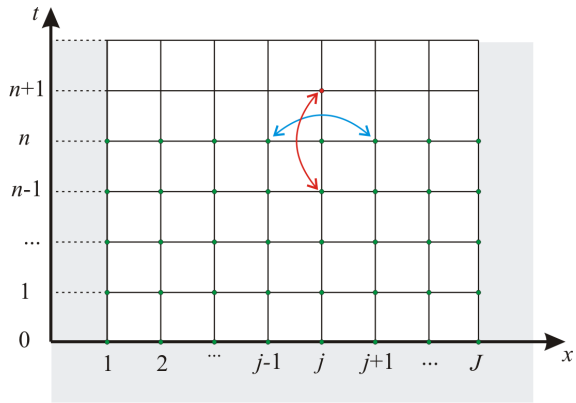

Figure 3.2: Scheme adopted for calcultating derivatives (Eqs. 3.3 to 3.4).

- (5) start of the second injection (II) of $Q_{injII} = 3.0$ mL/s with constant concentration $C_{inj} = 30$ mg/L; the plume developed increasing its length and width;
- (6) the plume reached the outlet and appeared in steady state inside the sandbox;
- (7) end of injection II;
- (7-8) the plume, being no longer fed, reduced its length and moved to the outfall;
- (8) the sandbox was completely clean;
- (9) end of the test. During the entire test 660 images were acquired with a 5s time interval.

3.4 N-IDE results

In this test case $\Delta t = 5$ s, Δx=$\Delta z = 0.5$ mm, $\phi = 0.37$, $u = \bar{v}/\phi = 1.23 \cdot 10^{-3}$ m/s and, following the considerations reported in the previous chapters, only the concentrations estimated through the analysis of the dGray signal were taken into consideration. In the plume steady state condition (phases 2-3 and 6-7), time and spatial derivatives along x direction are null and consequently the system in Eq. 3.12 allowed infinite solutions (det$\mathbf{A}$ = 0). Similar considerations can be made for the ApA inside the plume's core, where the concentration does not vary spatially ($CX \sim 0$ and $CZ \sim 0$). In order to limit the estimation of dispersivity coefficients in these areas, the ApAs in which the quantity CZ (Eq. 3.12) was less than a specific value CZ_{MIN} were discarded. CZ_{MIN} was evaluated after the analysis of preliminary results and it was chosen as 5% of the maximum derivative possible (i.e. $CZ_{MAX} = \Delta C/2\Delta z$ with $\Delta C = 30$ mg/L, $\Delta z = 1$ mm). Therefore the zones

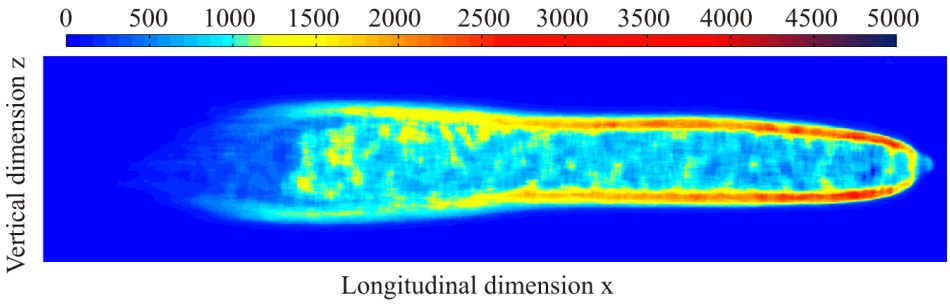

Figure 3.3: Spatial z derivative of the concentration computed with Eq. 3.4 at time 500 s in the area inside the white dashed lines of Fig. 3.1.

effectively useful for the evaluation of the dispersivity coefficients are the plume boundaries only (see Fig. 3.3), for this reason only the area inside the white dashed line of Fig. 3.1 was considered. The computed dispersivity coefficients appears to vary from ApA to ApA and from time to time; with the aim of describing such variability in Fig. 3.5 we plotted the mean and the standard deviations of the longitudinal and transverse dispersivity coefficients as obtained from the numerical process described in Section 3.2.1. The mean dispersivities values resulting from the N-IDE were $\alpha_L = 1.06$ mm and $\alpha_T = 0.45$ mm. These values are very close to the ones estimated by *Benekos et al.* (2006) ($\alpha_L = 1.0$ mm and $\alpha_T = 0.38$ mm) for similar porous media (glass beads 0.75 – 1.0 mm diameter) but under different experimental conditions (helix motion). By analyzing Fig. 3.5 one can see that the confidence interval of the estimated value of the longitudinal dispersivity coefficient depends on the phase of the test:

- Phase (1-2, 5-6) during the first stages of the injection process the standard deviation is high and shows a decreasing trend with the development of the plume; this behavior can be explained by considering that at the initial stage of plume development the computations are limited to a small area close to the injector where the velocity differs from an uniform value. Eq. 3.1, where the velocity is assumed constant and in the x direction only, does not fit the real flow conditions; or, from another point of view, the computed coefficients can be defined as macro-dispersivity coefficients since their values provide an evaluation of both the transport dispersion and the velocity uncertainty;

- Phase (3-4, 7-8): the mean values are rather constant and the confidence interval presents small variability. The transverse dispersivity coefficient assumes an approximately constant value during the entire experiment and its standard deviation is quite small.

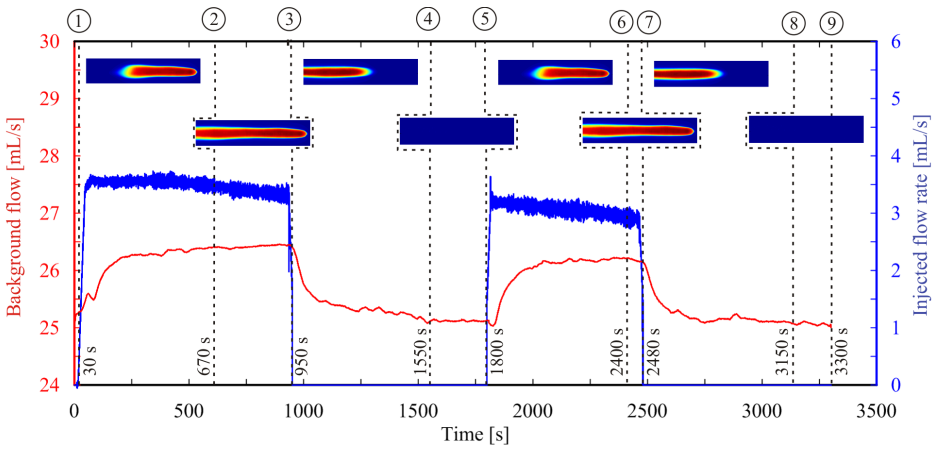

Figure 3.4: Observed background discharge (red line) and observed injected (blue line) flow rates. 1 start of injection I at Q_{inj1} with constant concentration C_{inj}; 2 the plume reaches the outlet and it is in steady state inside the sandbox; 3 end of injection I; 3–4 the plume moves out the porous media; 4 the sandbox is completely clean; 5 start of injection II at Q_{injII} with constant concentration C_{inj}; 6 the plume reaches the outlet and it is in steady state inside the sandbox; 7 end of injection II; 7–8 the plume moves out the porous media; 8 the sandbox is completely clean; and 9 end of the test.

This approach could be applied also in non-homogeneous porous media if the flow field is well known at each grid node. This can be possible if there is perfect knowledge of the hydraulic conductivity field, at this aim several procedures have been reported in literature (*Yeh et al.*, 2000; *Fienen et al.*, 2009; *Zanini and Kitanidis*, 2009; *Cardiff et al.*, 2013). After the identification of the medium conductivity and the proper application of the boundary conditions the flow field can be obtained with a numerical modeling, then the application of the N-IDE will give the dispersivity coefficients. Moreover, considering that it is very difficult to reach a complete description of the flow in heterogeneous field, we think that the N-IDE analysis can be useful for the computation of the macrodispersivity coefficients, the dispersion coefficients and for a detailed study of the scale effect in dispersion. Since the procedure is based on finite differences it could be affected by approximation errors that could lead to inaccuracy of the dispersivity coefficients that are related to the space-time discretization grid adopted. In order to quantify this error, a comparison test with an analytical solution was carried out: at first considered a 2-D analytical solution (*Butera and Tanda*, 2003) with a uniform effective velocity ($u = 1.23 \cdot 10^{-3}$ m/s) and dispersivity values ($\alpha_L = 1.06$ mm, $\alpha_T = 0.45$ mm) equal to the experimetnal test case was considered. A contaminant (at mass rate 0.105 mg/s) was injected for 980 s and the plume evolution was simulated for a total of about 1600 s. Then, taken a window with the same dimension of the sandbox, different "images" were created, at different times, of the analytically determined concentration field on a grid with density

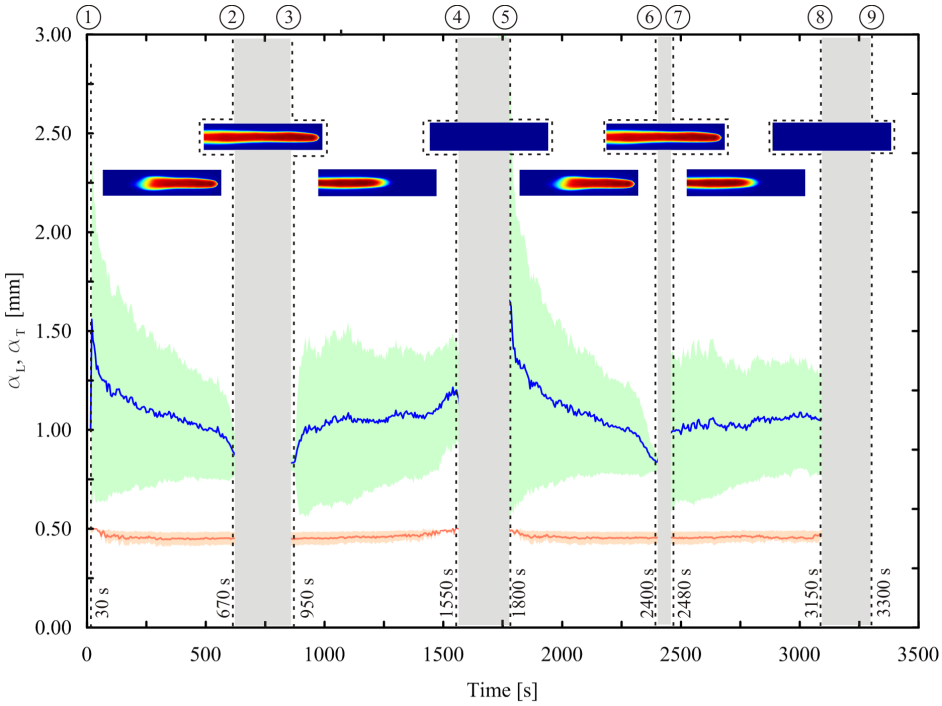

Figure 3.5: Longitudinal and transverse dispersivities computed by the N-IDE procedure. The blue line represents the average longitudinal dispersivity. The red lines represent themean transverse dispersivity. The green and red areas represent the longitudinal and transverse dispersivities' 95% confidence interval.

equal to that of the images processed in the experimetal test case. Finally, we applied the N-IDE procedure to estimate the dispersivities and compared the results to the true ones. The outcomes of this analysis are reported in the Fig. 3.6 with the same style adopted in Fig. 3.5; at the beginning of the plume development, the longitudinal coefficient shows moderate oscillation with a decreasing average value that tends to the true one. The transverse coefficient results pretty constant without remarkable oscillations. The average dispersivity estimates ($\alpha_L = 1.065 \pm 0.038$ mm, $\alpha_T = 0.452 \pm 0.007$ mm) are very close to the true one, and the difference could be quantified to 0.5%, a quantity that suggests a negligible influence of the numerical dispersion of the N-IDE procedure on the space-time discretization grid adopted.

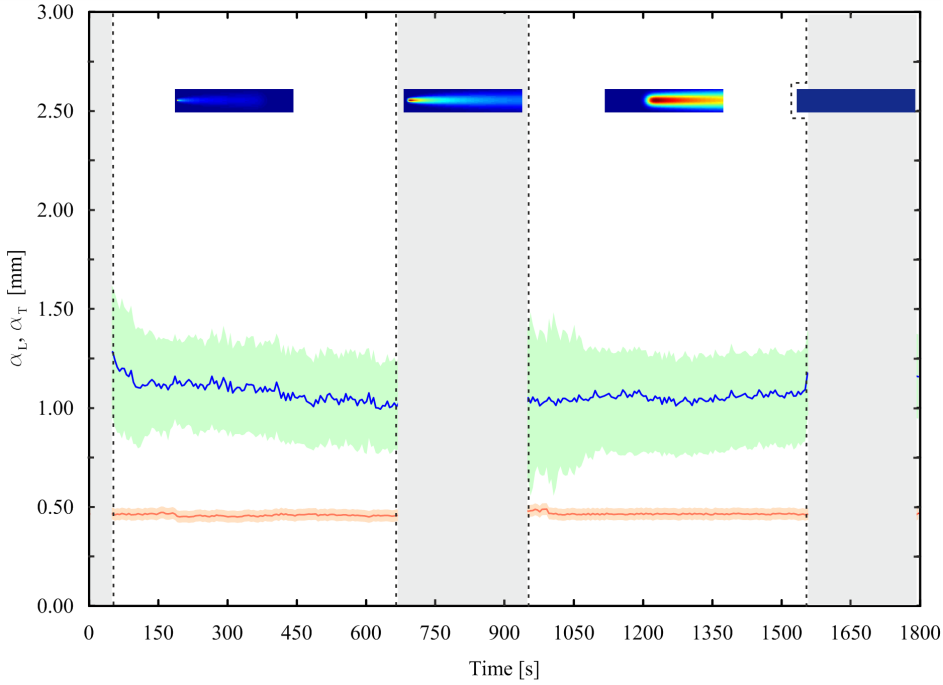

Figure 3.6: Longitudinal and transverse dispersivities computed by the N-IDE procedure on analytical concentration field. The blue line represents the average longitudinal dispersivity. The red lines represent the mean transverse dispersivity. The green and red areas represent the longitudinal and transverse dispersivities' 95% confidence interval.

3.5 Evaluation of dispersivity by calibration of the numerical modeling

The experimental run reported above was reproduced with the numerical model calibrated in steady state conditions. A transient flow simulation was carried out mimicking the experimental test described above. The computation had a total duration of 3300 s; the results were recorded with a time interval of 5 s. In the cell corresponding to the injector position a water discharge was introduced with the same procedure as the experimental test (Fig. 3.4). The results were assumed as the base transient flow for the transport simulation. The transport simulation with MT3DMS (*Zheng and Wang*, 1999) was carried out by introducing the non-reactive solution with concentration equal to 30 mg/L in the injector location. The numerical and experimental results were compared with attention to the breakthrough curve at three different observation points (Fig. 2.22). Initially the mean square root has been minimized manually adjusting the dispersion parameters. Then, with the aim of obtaining very robust assessments, the dispersivity values have been estimated by means of the software PEST (*Doherty*, 2008). The effective porosity was fixed at 0.37.

The best results were obtained using longitudinal dispersivity of $\alpha_L = 1.06$ mm and transverse dispersivity of $\alpha_T = 0.41$ mm. Fig. 2.22 shows the numerical breakthrough curves (continuous lines) at the monitoring points shown in Fig. 3.1 and the observed values obtained through the image processing by means of the dR, dG, LoB and dGray laws. The modeled breakthrough curves are very close to the experimental ones. Comparing the dispersivity estimation of the numerical modeling and of the N-IDE one can notice that there is perfect agreement for the values of the transverse dispersivity (0.41 mm and 0.45 mm respectively). The average value in phases 3-4 and 7-8 (1.06 mm) corresponds to the α_L calibrated value. Another validation of the numerical model is reported in Chapter 4 where, thanks to the numerical model, the source position and the fluorescein release history have been estimated on the basis of the concentration values detected at few points in the sand box.

3.6 Discussion and Conclusions

The investigation on transport phenomena in laboratory by means of image processing is known as a very powerful system: it is cheap, not invasive and able to collect information at an infinity of locations. Other methods for concentration detection require point measurements by means of physical contact with the solution or sampling (*Kim et al.*, 2004; *Aksoy and Guney*, 2010); the number of measurements must be restricted by economic considerations and the need to reduce flow interferences. The procedure tested in this work instead uses the information coming from the face view of the sandbox, which must obviously be transparent and on the same side as the lighting. No noise can derive from the flow and transport process. This photographic technique can also be applied to experimental devices, which present a non-transparent rear wall where piezometer or pressure transducer inlets can be located as described, for example, in *Jose et al.* (2004). It represents a change in perspective, compared to other experiments (such as *Huang et al.*, 2002 and *Catania et al.*, 2008), which detected the light after the transit through the sandbox (on the opposite side with respect to the illumination).

The main issue about the detection from the side view is that the wall concentration field is considered representative of the entire depth of the porous medium; it can lead to errors in the tracer transport detection. However, it is possible to verify whether the errors are remarkable by checking the mass balance. The estimation of the dispersivity coefficients was carried out after several tests aimed at verifying the reliability of the experimental device. In particular, by assuming a homogeneous porous medium and a uniform flow in the vertical plane, the 2-D advection-dispersion equation was applied to the images collected using a leap-frog scheme. The results show that the longitudinal dispersivity presents the same order of magnitude as the pore dimension and the transverse dispersivity is constant through the entire domain for all the times. The estimated disper-

sivity coefficients are very close to the one evaluated by *Benekos et al.* (2006) using a completely different procedure. The N-IDE procedure was tested even on an analytical concentration field to verify that the numerical dispersion does not affect the estimation of the dispersivity coefficients. The results of this test have shown that the numerical dispersion is negligible. An interesting consideration comes out from the results of the study: even though the dispersivities can be estimated for each pixel of the figures, only a few provide reliable information; in fact, a significant variation in concentration could be detected on the plume boundaries only. For this reason a selection criterion has been developed for the reliability of the results. The results of the N-IDE have been checked by comparison with the transport parameters obtained by calibration of the detailed numerical model of the sandbox. The values are in good agreement. Future developments can be the application of the N-IDE in experimental tests carried out in a sandbox filled with heterogeneous porous media; they can lead to a detailed analysis of the dispersion phenomena with investigations about the apparent dispersivity coefficients (macro-dispersivity) and their scale characteristics.

4 Recovery of the source position and of the contaminant release history

§

4.1 Introduction

Source identification and recovery of the pollutant release history in groundwater have received muchattention in recent years. The identification of a source location could allow to identify the true cause of the contamination and to foresee the future pollution spread, while the release time, the duration, and the maximum value of the released solute concentration could allow to apportion remediation costs among the responsible parties. The problems in recovering the release history and/or the source location were studied extensively in the past. In this chapter two different approaches are compared with respect to the same test case (Table 2.2): simultaneous release function and source location (in short SRSI) (*Butera et al.*, 2013) and backward location model based on adjoint state method (briefly BPM-ASM) (*Neupauer and Wilson*, 1999). Both methodologies were tested on experimental data collected in the laboratory sandbox described in Section 2.13. This allows to validate the methodologies in a real test case, in which all variables are measured and controlled. This is the first time that a well-known experimental dataset is used to test and validate these kinds of procedures.

The first method, developed by *Butera et al.* (2013), is based on the geostatistical approach proposed by *Snodgrass and Kitanidis* (1997) for the one-dimensional uniform flow. Several improvements and applications of the geostatistical methodology were proposed (*Michalak and Kitanidis* 2002, 2003, 2004a, 2004b), also by *Butera and Tanda*

(2003) and *Butera et al.* (2006, 2013). Given the linearity of the governing differential equation the approach uses the transfer functions (TF) to describe the effect in time, at a certain location of the aquifer, of an impulse release of a pollutant at a known source. Although TFs can be analytically determined if the problem has a simple flow field, in many practical applications, the characteristics of the groundwater flow field do not allow this solution. To overcome this difficulty, a numerical procedure to compute TFs was developed by *Butera et al.* (2004) and applied to homogeneous and weakly heterogeneous aquifers (*Butera at al.*, 2006). The source identification procedure requires a preliminary delineation of an area where the pollutant source is most likely to be present, but it allows to obtain the simultaneous identification of the release history and the source location. An application of this methodology, in a complex real case study, has been made by *Gzyl at al.* (2014).

The second methodology is developed by *Neupauer and Wilson* (1999, 2001). In these works, the authors showed that the backward location and travel time probabilities density functions (PDF) are related to adjoint states of concentration, and they developed a technique for obtaining the governing equation of the backward model using the adjoint theory. The backward location PDF describes the possible former positions of the observed contamination at a certain time before the detection, while the backward travel time PDF describes the possible travel time of the contaminant from a selected upgradient position to the observation location. Using an adjoint model, an instantaneous point source of an adjoint state (related to the PDFs) is released at the observation location at observed time. The adjoint state is thus transported upgradient and backward in time, following the same processes that occur in forward contaminant transport modeling. The resulting spatial distribution in the domain is related to the backward location PDF. The work of *Neupauer and Wilson* (1999, 2001) was improved considering non-uniform flow field (*Neupauer and Wilson*, 2002), sorbing solutes (*Neupauer and Wilson* 2004a, 2004b, 2009), multiple observations (*Neupauer and Wilson*, 2005), measured concentration (*Neupauer and Lin*, 2006) and sorption and decay phenomena (*Neupauer et al.*, 2007). Using a numerical model, previously calibrated, the single-observation and multiple-observation backward location PDF can be computed. Then this PDF was conditioned on the concentration measurement, reducing the variance and improving the results. However, this methodology was developed to manage plumes originates from single instantaneous point source; nevertheless, it seems an interesting approach and in this work its performance has been tested on a continuous release source.

The chapter is organized in three parts: first the mathematical statements concerning the two approaches are presented, then a brief description of the experimental equipment is reported. Finally, the results of the application of the two methodologies are presented and discussed. The work presented in this chapter has been published in *Cupola et al.* (2015a) and presented at AGU Fall Meeting (*Zanini et al.*, 2013) and at IDRA Congress

(*Cupola et al.*, 2014).

4.2 SRSI methodology

The source position was estimated through the procedure developed by *Butera et al.* (2013). The method, called simultaneous release function and source location identification (SRSI), allows not only to identify the source position but also its release history in time. The SRSI procedure can be summarized with the following steps:

- collect a set of concentration measurements in space and/or time;
- delineate the suspect area (SA) for the source location and discretize it into J sub-areas assuming the origin of the possible sources in the centroid of any sub-area;
- compute the transfer functions at the monitoring points for each possible source (J runs of the numerical transport model);
- recover the release histories performing the geostatistical procedure that simultaneously considers all the possible point sources (superposition effect) by means of $C(\mathbf{x}, t) = \sum_{j=1}^{J} \int_0^t s_j(\eta) \cdot f_j(\mathbf{x}, t-\eta) \cdot d\eta$ where $C(\mathbf{x}, t)$ [M $\cdot$ L$\cdot^{-3}$] is the concentration at location $\mathbf{x}$ and time t, $f_j(\mathbf{x}, t-\eta)$ [L^{-p}] (p is the dimension of the problem) is the transfer function (TF) that describes the effects at $\mathbf{x}$ at time t by an impulse injection occurring at the jth potential source position at time η [T] (j is one of J generic sub-areas inside the SA);
- identify the source location as the location from which the highest amount of released pollutant is estimated.

TFs can be determined easily in simple flow conditions (such as homogeneous and isotropic porous media in absence of interferences) by means of analytical formulations (*Bear and Verruijt*, 1987). Considering non-uniform flow field (for instance heterogeneous porous media, or presence of a withdrawal) it is necessary to develop numerical strategies. *Butera et al.* (2006, 2013) developed the Stepwise Input Function procedure (SIF) for TF calculation. The procedure, in brief, consists of making the time derivative of convolution integral considering a constant and known input function , where $H_{SF}(t)$ is the Heaviside step function and $F_0 = C_0 \cdot q_0$ is the amount of pollutant injected into the aquifer with constant and known concentration C_0 at flow rate q_0. The TF results in:

$$f(\mathbf{x}, t) = \frac{1}{F_0} \cdot \frac{\partial C(\mathbf{x}, t)}{\partial t} \tag{4.1}$$

Eq. 4.1 coupled with a numerical flow and transport model known from calibration or expert elicitation, allows easily to determine the TFs at a generic point $\mathbf{x}$ by processing the

concentration history (breakthrough curve) at the same location due to a stepwise tracer injection at $\mathbf{x_0}$. The choice of using an input step function and then deriving numerically the breakthrough curve rather than computing directly the aquifer response due to an impulsive injection, can be explained by the need of reducing numerical errors caused by the discrete time representation of the process, that are unavoidable in the numerical computations. The numerical description of an impulse necessarily have to develop in a small but finite time (not infinitesimal) so the aquifer response is not correct because it is due to a finite injection and not to an impulsive one. Besides, the responses of areas far from the source and less exposed to the contamination, can be underestimated. The study of the transport of a step input of infinite time length is more accurate and not affected by such kind of errors. For a given measurement point, the breakthrough curve is an output of the numerical model and it consists in a series of concentration values recorded in time. The shorter is the temporal interval between two computations, the more accurate is the computation of the numerical derivative of the TF curve; by definition, the derivative can be calculated as the rate $\frac{\Delta C}{\Delta t}$, with $\Delta t \to 0$.

The core of the method is the quasi-linear geostatistical approach developed by *Kitanidis* (1995, 1996) and *Snodgrass and Kitanidis* (1997) that is summarized in the following. The value of the concentration may be estimated by the following expression:

$$\mathbf{z} = \mathbf{h}(\mathbf{s}, \mathbf{r}) + \mathbf{v} \tag{4.2}$$

where $\mathbf{z}$ is an $m \times 1$ vector of observations, $\mathbf{s}$ is the unknown release function discretized in n time intervals, $\mathbf{r}$ is a vector that contains other parameters needed by the model function $\mathbf{h}(\mathbf{s}, \mathbf{r})$ (for instance the aquifer parameters). In this work the parameters $\mathbf{r}$ are assumed known so the Eq. 4.2 is reduced to $\mathbf{z} = \mathbf{h}(\mathbf{s}) + \mathbf{v}$. $\mathbf{h}(\mathbf{s})$ is an $m \times 1$ vector that represents the transport process. $\mathbf{v}$ is an $m \times 1$ vector of measurements errors assumed with zero mean and known covariance matrix $\mathbf{R}$. The unknown function $s(t)$ is analyzed as a stochastic random process characterized by the mean $E[\mathbf{s}] = \mathbf{X}\boldsymbol{\beta}$ and covariance matrix $\mathbf{Q}(\boldsymbol{\theta}) = E\left[(\mathbf{s} - \mathbf{X}\boldsymbol{\beta})(\mathbf{s} - \mathbf{X}\boldsymbol{\beta})^T\right]$, where $\mathbf{X}$ is a known $n \times p$ matrix and $\boldsymbol{\beta}$ are $p \times 1$ unknown drift coefficients; $\boldsymbol{\theta}$ are the unknown parameters of the covariance matrix $\mathbf{Q}$. Taking for instance the Gaussian distribution, the parameters of $\mathbf{Q}$ are the variance (σ^2) and the characteristic time length (l). For conservative solute transport the relationship between the observed concentration and the solute input is linear so the Eq. 4.2 can be simplified to

$$\mathbf{z} = \mathbf{H} \cdot \mathbf{s} + \mathbf{v} \tag{4.3}$$

where $\mathbf{H}$ is a known matrix $m \times n$ and represents the matrix of the transfer functions. The estimation procedure proposed by *Kitanidis* (1995) is divided into two parts; first

the structural parameters $\boldsymbol{\theta}$ of the chosen distribution are found then the unknown release function is estimated. The parameters $\boldsymbol{\theta}$ are estimated maximizing the probability that the process represents the observation $\mathbf{z}$, through the following equation:

$$p(\mathbf{z}|\boldsymbol{\theta}) \propto |\boldsymbol{\Sigma}|^{-1/2} \left|\mathbf{X}^T\mathbf{H}^T\boldsymbol{\Sigma}^{-1}\mathbf{H}\mathbf{X}\right|^{-1/2} \exp\left[-\frac{1}{2}\mathbf{z}^T\boldsymbol{\Xi}^{-1}\mathbf{z}\right] \tag{4.4}$$

where

$$\boldsymbol{\Sigma} = \mathbf{H}\mathbf{Q}\mathbf{H}^T + \mathbf{R} \tag{4.5}$$

($\boldsymbol{\Sigma}$ is a $m \times m$ matrix) and

$$\boldsymbol{\Xi} = \boldsymbol{\Sigma}^{-1} - \boldsymbol{\Sigma}^{-1}\mathbf{H}\mathbf{X}(\mathbf{X}^T\mathbf{H}^T\boldsymbol{\Sigma}^{-1}\mathbf{H}\mathbf{X})^{-1}\mathbf{X}^T\mathbf{H}^T\boldsymbol{\Sigma}^{-1} \tag{4.6}$$

($\boldsymbol{\Xi}$ is a $m \times m$ matrix). Maximizing Eq. 4.4 is equivalent to minimizing the negative logarithm of $p(\mathbf{z}|\boldsymbol{\theta})$:

$$L(\boldsymbol{\theta}) = \frac{1}{2}\ln|\boldsymbol{\Sigma}| + \frac{1}{2}\ln\left|\mathbf{X}^T\mathbf{H}^T\boldsymbol{\Sigma}^{-1}\mathbf{H}\mathbf{X}\right| + \frac{1}{2}\mathbf{z}^T\boldsymbol{\Xi}^{-1}\mathbf{z} \tag{4.7}$$

The minimization of Eq. 4.7 can be achieved by taking derivatives of $L(\boldsymbol{\theta})$ respect to $\boldsymbol{\theta}$ and setting them to zero. This process can be defined by:

$$g_i = \frac{\partial L}{\partial \theta_i} = \frac{1}{2}Tr\left[\boldsymbol{\Xi}\frac{\partial \boldsymbol{\Sigma}}{\partial \theta_i}\right] - \frac{1}{2}\mathbf{z}^T\left(\boldsymbol{\Xi}\frac{\partial \boldsymbol{\Sigma}}{\partial \theta_i}\boldsymbol{\Xi}\right)\mathbf{z}$$

and this equation can be solves numerically using the Gauss-Newton iterative method:

$$\boldsymbol{\theta}_{i+1} = \boldsymbol{\theta}_i - \mathbf{F}^{-1}\mathbf{g}$$

where $\mathbf{F}$ is the Fisher information matrix:

$$\mathbf{F}_{ij} = \frac{1}{2}Tr\left[\boldsymbol{\Xi}\frac{\partial \boldsymbol{\Sigma}}{\partial \theta_i}\boldsymbol{\Xi}\frac{\partial \boldsymbol{\Sigma}}{\partial \theta_j}\right]$$

Sometimes it is necessary to apply the Marquardt modification by replacing $\mathbf{F}^{-1}$ with $(\mathbf{F} + \lambda\mathbf{I})^{-1}$, where $\mathbf{I}$ is the identity matrix and λ is a positive parameter.

Once that the iterations have converged and the $\boldsymbol{\theta}$ are evaluated it is possible to obtain the best estimate of the release function $s(t)$ by solving the universal Kriging:

$$\hat{\mathbf{s}} = \boldsymbol{\Lambda} \cdot \mathbf{z}$$

The Kriging method evaluates the $\mathbf{\Lambda}$ coefficients ($n \times m$) with the constrains of unbiased mean and minimum variance of the error, solving the following system:

$$\begin{bmatrix} \mathbf{\Sigma} & \mathbf{HX} \\ (\mathbf{HX})^T & \mathbf{0} \end{bmatrix} \begin{bmatrix} \mathbf{\Lambda}^T \\ \mathbf{M} \end{bmatrix} = \begin{bmatrix} \mathbf{HQ} \\ \mathbf{X}^T \end{bmatrix} \tag{4.8}$$

where $\mathbf{M}$ is a matrix of multiplier ($p \times n$). The covariance matrix ($n \times n$) of the error of the estimate is

$$\mathbf{V} = -\mathbf{XM} + \mathbf{Q} - \mathbf{QH}^T\mathbf{\Lambda}^T \tag{4.9}$$

The transfer matrix $\mathbf{H}$, discretized in n regular time intervals Δt, results the following:

$$\mathbf{H} = \Delta t \cdot \begin{bmatrix} f\left(x_1, T-t_1\right) & \ldots & f\left(x_1, T-t_n\right) \\ f\left(x_2, T-t_1\right) & \ldots & f\left(x_2, T-t_n\right) \\ \ldots & \ldots & \ldots \\ f\left(x_m, T-t_1\right) & \ldots & f\left(x_m, T-t_n\right) \end{bmatrix} \tag{4.10}$$

The function $f\left(x_i, T-t_j\right)$ represents the transfer functions (TFs) located in the point i at time $T-t_j$. In simple cases such as 1-D or 2-D uniform flow, an analytical solution for the TF is available. This methodology (unconstrained case) is functional and fast but does not enforce the non-negativity of the concentration; then, with the aim at avoiding this kind of problem, a transformation of the unknown variable $\mathbf{s}$ has been proposed (*Kitanidis and Shen*, 1996; *Snodgrass and Kitanidis*, 1997). The new unknown becomes:

$$\tilde{\mathbf{s}} = \alpha\left(\mathbf{s}^{1/\alpha} - 1\right) \tag{4.11}$$

where α is a positive number and chosen as small as possible while ensuring that $\tilde{\mathbf{s}} > -\alpha$; (in this work $\alpha = 2$). The values of $\mathbf{s}$ are then constrained to be positive (constrained case) and they are physically compatible.

Eq. 4.2 in the transformed spaces becomes:

$$\mathbf{z} = \tilde{\mathbf{h}}\left(\tilde{\mathbf{s}}\right) + \mathbf{v} = \mathbf{h}\left[\left(\frac{\tilde{\mathbf{s}} + \alpha}{\alpha}\right)^{\alpha}\right] + \mathbf{v} \tag{4.12}$$

In this case the transfer function $\tilde{\mathbf{h}}\left(\tilde{\mathbf{s}}\right)$ is not linear with respect to the unknown $\tilde{\mathbf{s}}$ and the solution is reached iteratively (see *Kitanidis*, 1995). The procedure starts with making an

initial estimate of the unknown $\tilde{\mathbf{s}}_l$ then the derivative of $\tilde{\mathbf{h}}$ with respect to $\tilde{\mathbf{s}}$ at $\tilde{\mathbf{s}}_l$ is found:

$$\tilde{\mathbf{H}}_l = \left.\frac{\partial \tilde{\mathbf{h}}}{\partial \tilde{\mathbf{s}}}\right|_{\tilde{\mathbf{s}}=\tilde{\mathbf{s}}_l} \tag{4.13}$$

Then it is possible to find the new estimate: $\hat{\mathbf{s}}_{l\_1} = \mathbf{\Lambda} \cdot \mathbf{z}_{0l}$, where $\mathbf{z}_{0l} = \mathbf{z} - \tilde{\mathbf{h}}\left(\tilde{\mathbf{s}}_l\right) + \tilde{\mathbf{H}}_l \tilde{\mathbf{s}}_l$, and $\tilde{\mathbf{h}}\left(\tilde{\mathbf{s}}_0\right) = \int_0^t \left(\frac{\tilde{\mathbf{s}}_0+\alpha}{\alpha}\right)^{\alpha} f\,(x, t-\tau)\,d\tau$, where $\tilde{\mathbf{s}}_0$ is the initial guess. The $\mathbf{\Lambda}$ $(n \times m)$ matrix of coefficients is evaluated from the solution of the following system:

$$\begin{bmatrix} \mathbf{\Sigma} & \tilde{\mathbf{H}}_l \mathbf{X} \\ \left(\tilde{\mathbf{H}}_l \mathbf{X}\right)^T & \mathbf{0} \end{bmatrix} \begin{bmatrix} \mathbf{\Lambda}^T \\ \mathbf{M} \end{bmatrix} = \begin{bmatrix} \tilde{\mathbf{H}}_l \mathbf{Q} \\ \mathbf{X}^T \end{bmatrix}$$

where $\mathbf{\Sigma} = \tilde{\mathbf{H}}_l \mathbf{Q} \tilde{\mathbf{H}}_l^T + \mathbf{R}$ and $\mathbf{M}$ is a matrix of multiplier $(p \times n)$. The transfer function matrix $\tilde{\mathbf{H}}_l$ for the transformed variable $\tilde{\mathbf{s}}_l$ becomes:

$$\tilde{\mathbf{H}}_l = \Delta t \cdot \begin{bmatrix} \left(\frac{\tilde{\mathbf{s}}_0(t_1)+\alpha}{\alpha}\right)^{\alpha-1} f\left(x_1, T-t_1\right) & \dots & \left(\frac{\tilde{\mathbf{s}}_0(t_n)+\alpha}{\alpha}\right)^{\alpha-1} f\left(x_1, T-t_n\right) \\ \left(\frac{\tilde{\mathbf{s}}_0(t_1)+\alpha}{\alpha}\right)^{\alpha-1} f\left(x_2, T-t_1\right) & \dots & \left(\frac{\tilde{\mathbf{s}}_0(t_n)+\alpha}{\alpha}\right)^{\alpha-1} f\left(x_2, T-t_n\right) \\ \dots & \dots & \dots \\ \left(\frac{\tilde{\mathbf{s}}_0(t_1)+\alpha}{\alpha}\right)^{\alpha-1} f\left(x_m, T-t_1\right) & \dots & \left(\frac{\tilde{\mathbf{s}}_0(t_n)+\alpha}{\alpha}\right)^{\alpha-1} f\left(x_m, T-t_n\right) \end{bmatrix}$$

The structural parameters $\boldsymbol{\theta}$ are evaluated at each iteration minimizing the equation:

$$L\,(\boldsymbol{\theta}) = \frac{1}{2} \ln |\mathbf{\Sigma}| + \frac{1}{2} \ln \left|\mathbf{X}^T \tilde{\mathbf{H}}_l^T \mathbf{\Sigma}^{-1} \tilde{\mathbf{H}}_l \mathbf{X}\right| + \frac{1}{2} \mathbf{z}_{0l}^T \mathbf{\Xi}^{-1} \mathbf{z}_{0l}$$

where $\mathbf{\Xi} = \mathbf{\Sigma}^{-1} - \mathbf{\Sigma}^{-1} \tilde{\mathbf{H}}_l \mathbf{X} \left(\mathbf{X}^T \tilde{\mathbf{H}}_l^T \mathbf{\Sigma}^{-1} \tilde{\mathbf{H}}_l \mathbf{X}\right)^{-1} \mathbf{X}^T \tilde{\mathbf{H}}_l^T \mathbf{\Sigma}^{-1}$.

In the parameter estimation step $\mathbf{z}_{0l}$ and $\tilde{\mathbf{H}}_l$ are treated as constants and the minimization is obtained using the Gauss-Newton method. Once $\boldsymbol{\theta}$ is found it is used to find and update the value of $\tilde{\mathbf{s}}_l$. This iterative process is continued until $\tilde{\mathbf{s}}_l$ and $\boldsymbol{\theta}$ converge. The final value of $\tilde{\mathbf{s}}_l$ is the best estimate of the transformed function and its covariance function

is given by the equation $\mathbf{V} = -\mathbf{XM} + \mathbf{Q} - \mathbf{Q}\tilde{\mathbf{H}}^{T}\mathbf{\Lambda}^{T}$.

At the end of the process it is necessary to apply the inverse transformation of Eq. 4.11 to calculate the release function $s(t)$; the best estimate results:

$$\hat{\mathbf{s}} = \left(\frac{\tilde{\mathbf{s}}_I + \alpha}{\alpha} \right)^{\alpha} \tag{4.14}$$

For the SRSI procedure, the vector $\mathbf{s}$ of the unknown release function in (4) is made up by the collection of J sub-vectors s_j, each with dimensions $n_i \times 1$, where n_i is the number of time values used to discretize the release history. The total dimension of $\mathbf{s}$ is: $(n_1 + n_2 + ... + n_J) \times 1$:

$$\mathbf{s} = \begin{bmatrix} \mathbf{s}_1 \\ \mathbf{s}_2 \\ ... \\ \mathbf{s}_J \end{bmatrix} \tag{4.15}$$

The transfer matrix $\mathbf{H}$ is a block matrix

$$\mathbf{H} = \begin{bmatrix} \mathbf{H}_1 & \mathbf{H}_2 & ... & \mathbf{H}_J \end{bmatrix} \tag{4.16}$$

whose dimensions are $m \times (n_1 + n_2 + ... + n_J)$. The generic matrix $\mathbf{H}_j$ describes the effects of the pollutant release in the sub-area j on the measured concentration data in the m monitoring points. The covariance matrix $\mathbf{Q}$ of the $\mathbf{s}$ process, due to the lack of correlation among the release histories, is a block matrix with non-zero elements only in the diagonal blocks:

$$\mathbf{Q} = \begin{bmatrix} \mathbf{Q}_1 & 0 & 0 & 0 \\ 0 & \mathbf{Q}_2 & 0 & 0 \\ 0 & 0 & \mathbf{Q}_3 & 0 \\ 0 & 0 & 0 & \mathbf{Q}_4 \end{bmatrix} \tag{4.17}$$

The results of the geostatistical procedure described in this section provide the pollutant history in the J hypothetical source locations. The release function in the real source will be substantial, while in the other suspect locations the time histories will be negligible.

4.3 Backward probability model based on adjoint state method (BPM-ASM)

The use of backward location probability density function to identify the source location is explained in the following. At this time, this approach is evaluated from the authors only for an instantaneous point source and it is assumed that the release time τ is known. To calculate backward location PDF it is often necessary a numerical model calibrated on the experimental data. So, it is required to consider every observation point as an instantaneous source in the adjoint equation. The adjoint equations can be solved with the same flow and transport software used in forward simulation, on a domain with modified boundary conditions that produce reverse flow direction. In the test case explained in the following, one independent backward simulation (flow and transport) for each observation point was performed. The initial condition was

$$C_w(\mathbf{x}_w, 0) = \frac{1}{Q_w \cdot \Delta t} \tag{4.18}$$

where $\mathbf{x}_w$ is the position of the observation point, considered now as source, Q_w [$L^3 \cdot T^{-1}$] is the instantaneous discharge of tracer solution injected negligible respect to the background flow, and Δt [T] is the time step length. So the mass injected in the single time step, is

$$M_{injected} = C_w \cdot Q_w \cdot \Delta t = 1 \tag{4.19}$$

The evolution of the plume in the backward model provides the backward location PDF and represents the probability that the contaminant exists at that location and given backward time.

4.3.1 Single-Observation Backward Location PDF

For more details see *Neupauer and Wilson* (1999, 2002, 2003, 2004b). Let's consider Eq. 1.7; boundary and initial conditions are:

$$C(\mathbf{x}, t_0) = \frac{m_0}{\phi}\delta_0(\mathbf{x} - \mathbf{x}_0$$

$$C(\mathbf{x}, t_0) = g_1(t), \qquad on \quad \Gamma_1$$

$$\left[\mathbf{D}\frac{\partial C(\mathbf{x}, t)}{\partial x_j}\right] \cdot \mathbf{n} = g_2(t), \qquad on \quad \Gamma_2$$

$$[\mathbf{u}C(\mathbf{x}, t) - \mathbf{D}\nabla C(\mathbf{x}, t)] \cdot \mathbf{n} = g_3(t), \qquad on \quad \Gamma_3$$

where $C(\mathbf{x}, t)$ is the concentration, $\mathbf{D}$ is the dispersion tensor, $\mathbf{u}$ is the effective velocity, t_0 is the source release time, x_0 is the source location, m_0 [M] is the source mass, $\delta(\cdot)$ is the Dirac delta function, $g_i(t)$ are known boundary functions, and Γ_i are the boundaries. The adjoint of the Eq. 1.7 is given by *Neupauer and Wilson* (2002).

$$\phi\frac{\partial\psi^*}{\partial\tau} = \nabla(\phi\mathbf{D}\nabla\psi^*) + \nabla(\phi\mathbf{u}\psi^*) + q_I\psi^* \cdot \delta(\mathbf{x}-\mathbf{x}_w)\cdot\delta(\tau-\tau_w) + H(\mathbf{x},\tau) \quad (4.20)$$

$$\psi^*(\mathbf{x},0) = 0$$

$$\psi^*(\mathbf{x},\tau) = 0 \qquad on \quad \Gamma_1$$

$$\left[\mathbf{D}\frac{\partial\psi^*}{\partial x_j} + \mathbf{u}\psi^*\right]\cdot\mathbf{n} = 0, \qquad on \quad \Gamma_2$$

$$\left[\mathbf{D}\frac{\partial\psi^*}{\partial x_j}\right]\cdot\mathbf{n} = 0, \qquad on \quad \Gamma_3$$

where $[\mathrm{T}^{-1}]$ is the source inflow rate per unit volume and ψ^* $[\mathrm{L}^{-3}]$ is an adjoint state that is also (*Neupauer and Wilson*, 1999) the marginal sensitivity of the concentration to source mass. τ is backward time, $\mathbf{x}_w$ and τ_w are the observation location and sampling time, respectively. Using samples taken at monitoring wells

$$H(\mathbf{x},\tau) = \left[\frac{u_1\cdot\alpha_L}{\mid\mathbf{u}(\mathbf{x})\mid}\delta'_{x_1}(x_1-x_{1_w})\delta(x_2-x_{2_w}) + \frac{u_2\cdot\alpha_L}{\mid\mathbf{u}(\mathbf{x})\mid}\delta'_{x_2}(x_1-x_{1_w})\delta(x_2-x_{2_w})\right]\delta(\tau-\tau_w) \quad (4.21)$$

where the sample location is $\mathbf{x}_w = (x_{1_w}, x_{2_w})$, $\delta'_{x_i}(x_i - x_{i_w})$ is the derivative of the Dirac delta function with respect to x_i, vertical bars denote magnitude, and α_L [L] is the longitudinal dispersivity. The relationship between the adjoint state from Eq. 4.20 and the backward location probability density function is given by (*Neupauer and Wilson*, 2002)

$$f_{\mathbf{X}}(\mathbf{x};\tau,\mathbf{x}_w,\tau_w) = \phi\cdot\psi^*(\mathbf{x};\tau,\mathbf{x}_w,\tau_w) \quad (4.22)$$

where $f_{\mathbf{X}}(\mathbf{x};\tau,\mathbf{x}_w,\tau_w)$ is the backward location PDF concerning the position $\mathbf{x}$ at backward time τ of a contaminant particle that was observed at $\mathbf{x}_w$ at backward time τ_w, and ψ^* is the adjoint state obtained from Eq. 4.20.

4.3.2 Multiple-Observation Backward Location PDF

If several observations are available, it is possible to obtain multiple-observation backward location density function (*Neupauer and Wilson*, 2005) by first calculating the single-observation PDF for each observation, and then combining them. Each observation gives additional information to characterize the former position of contamination, thus reducing the uncertainty or variance of the location PDF. In this step only the presence of the pollutant at monitoring points is considered, and not the concentration values. Let N be the number of observations, and let $\mathbf{x}_w$ and τ_w be N-length vectors of sampling locations and sampling times, respectively. The multiple-observation backward location PDF, $f_{\mathbf{X}}(\mathbf{x}; \tau, \mathbf{x}_w, \tau_w)$, describes the possible former positions of all observed contaminant particles, given that at a previous time τ, they were at the same location, i.e. source location. It is calculated as

$$f_{\mathbf{X}}(\mathbf{x}; \tau, \mathbf{x}_w, \tau_w) = \frac{\prod_{i=1}^{N} f_{\mathbf{X}}(\mathbf{x}; \tau, \mathbf{x}_{wi}, \tau_{wi})}{\int \prod_{i=1}^{N} f_{\mathbf{X}}(\mathbf{x}; \tau, \mathbf{x}_{wi}, \tau_{wi}) \cdot d\mathbf{x}} \tag{4.23}$$

where $f_{\mathbf{X}}(\mathbf{x}; \tau, \mathbf{x}_{wi}, \tau_{wi})$ is the backward location PDF for the ith sample, obtained from Eq. 4.22. The sum of multiple-observation PDF, calculated on the whole domain, is equal to 1. An important aspect of this method is that only the presence or the absence of the pollutant is considered and the concentration values are not kept in account.

4.3.3 Conditioned Backward Location PDF

Neupauer and Lin (2006) improved the backward location probability density function conditioning on measured concentrations collected after an instantaneous release originated from a point source located in $\mathbf{x}_0$. Let $\hat{C}_i = \hat{C}(\mathbf{x}_{wi}, \tau_{wi})$, $i = 1,2,...,N$, the observed concentrations, where $\mathbf{x}_{wi}$ is the location and τ_{wi} is the backward time at which sample i was taken. $\hat{C}_i$ is considered as a random variable with true value $C(x_{wi}, \tau_{wi} \mid m_0, \mathbf{x}_0, \tau)$. So ϵ_i is the error of the ith measurement and it is normally-distributed with zero mean and variance σ_i^2. Therefore measured concentrations, $\hat{C}_i$ are normally distributed with a mean equal to the true concentration and variance σ_R^2, given by

$$f_{\hat{C}_i}(\hat{C}_i \mid m_0, \mathbf{x}_0, \tau) = \frac{1}{\sqrt{2\pi\sigma_R^2}} \cdot exp\left\{ -\frac{\left[\hat{C}_i - C(x_{wi}, \tau_{wi} \mid m_0, \mathbf{x}_0, \tau)\right]^2}{2 \cdot \sigma_R^2} \right\} \tag{4.24}$$

If ϵ_i is considered independent from any other, for a known source mass m_0 and a source location $\mathbf{x}_0$, the joint PDF on all N measured concentrations is simply the product

of the PDFs for the individual observations given by

$$f_{\hat{\mathbf{C}}}(\hat{\mathbf{C}} \mid m_0, \mathbf{x}_0, \tau) = \prod_{i=1}^{N} \frac{1}{\sqrt{2\pi\sigma_R^2}} \cdot exp\left\{ -\frac{\left[\hat{C}_i - C(x_{wi}, \tau_{wi} \mid m_0, \mathbf{x}_0, \tau)\right]^2}{2 \cdot \sigma_R^2} \right\} \quad (4.25)$$

In this problem the source mass and the source location are unknown but the measured concentrations are known. *Neupauer and Wilson* (2006) propose to use Bayes' theorem with the aim of constraining the source mass M and the random source location $\mathbf{x}_0$ on the particular measured concentrations. Assuming that the source mass is independent of source location in the absence of any concentration information, the final result is

$$f_{\mathbf{X}_0|\hat{\mathbf{C}}}(\mathbf{x}_0 \mid \hat{\mathbf{C}}; \tau) = \mathrm{B}_x \int \prod_{i=1}^{N} \left[f_{\hat{C}_i|M,X_0}(\hat{C}_i \mid m_0, \mathbf{x}_0, \tau) \cdot f_x(\mathbf{x}; \tau, \mathbf{x}_{wi}, \tau_{wi}) \right] \cdot dm_0 \quad (4.26)$$

where $f_{\hat{C}_i|M,X_0}(\hat{C}_i \mid m_0, \mathbf{x}_0, \tau)$ is the distribution of $\hat{C}_i$, calculated for each observation for a range of possible source masses and a range of possible source locations that includes the entire spatial domain of the model, $f_{\mathbf{X}}(\mathbf{x}; \tau, \mathbf{x}_{wi}, \tau_{wi})$ is the unconditioned backward location probability density function and B_x is a normalization factor.

4.4 Test case and results

The test case has been already described in section 2.12, in which were described the boundary conditions and the main features of the experiment (Table 2.2). The numerical model has been created updating that described in section 2.14.

4.4.1 Results of the geostatistical approach

The SA has been assumed upgradient from the measurement points in the region $11.25 \leq x \leq 17.25$ cm and $29.75 \leq z \leq 35.75$ cm and it was subdivided into 9 sub areas as shown in Fig. 4.1. The centroid of each area represents a possible source location. At first, the TFs relevant to the two monitoring points and the nine possible sources have been computed by means of the application of the SIF procedure, requiring nine runs of the forward flow and transport models. In this specific test case the mass rate released in time and source position are the unknowns. For each monitoring point, 32 concentration values are considered available throughout the duration of the injection with a time step equal to 70 s (Fig. 4.3). During the calibration of the device, the maximum measurement error of the concentration σ_R has been estimated in less than 3 mg/l. A Gaussian covariance

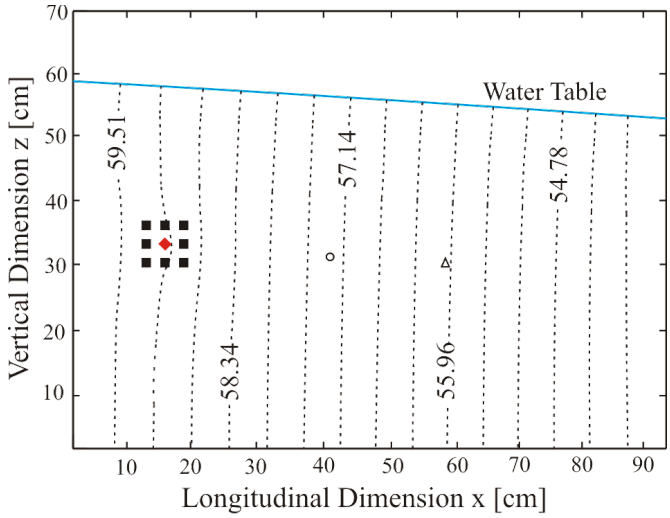

Figure 4.1: Hydraulic head distribution (in cm) from the numerical model. The red diamond is the source location. The filled squares denote the possible sources in the SA. The open circle and the triangle represent observation points P1 and P2, respectively. The experimental equipment reproduced an unconfined aquifer.

function was chosen $Q(t_i, t_j \mid \theta) = \sigma_s^2 \cdot \exp(-(t_i - t_j)/\lambda_s^2)$, so the variance σ_s^2 and the correlation length λ_s^2 for each of the nine suspected point source were estimated. Finally, the SRSI procedure was carried out and the release function for each of the nine possible sources was obtained (Fig. 4.4). In all the locations, except in $x = 14.25$ cm $z = 32.75$ cm the release history is null. This result indicates that the source is located in the sub-area with those centroid coordinates (just the ones of the actual source). The recovered release history for the source location $x = 14.25$ cm, $z = 32.75$ cm shows a good agreement between the observed and the recovered of the peak times; moreover the whole release history is included in the 5-95% confidence interval. A drawback of methodology is if the number of SA is too high the methodology could be computational ineffective, because it requires one run for each suspected source.

4.4.2 Results of backward model based on adjoint state method (BPM -ASM)

4.4.2.1 Unconditioned single-observation backward location PDF

At first, the single unconditioned backward location probability density functions were calculated, at the single observation points P1 and P2 (see Fig. 4.2). At backward time τ=0, a tracer solution discharge equal to Q_w and a concentration given by 4.18, was injected for only one time step. The travel times between the true source and observation

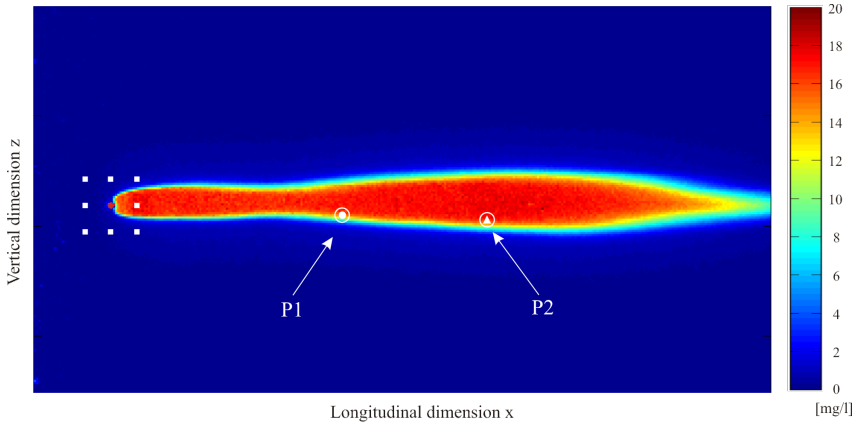

Figure 4.2: Concentration field estimated through the analysis of the image collected 690 s after the start of the injection. The concentration field depicted (85.28 × 44.15 cm) corresponds to the rectangle indicated in Fig. 4.1. The red diamond is the source location. The white filled squares denote the possible sources in the SA.

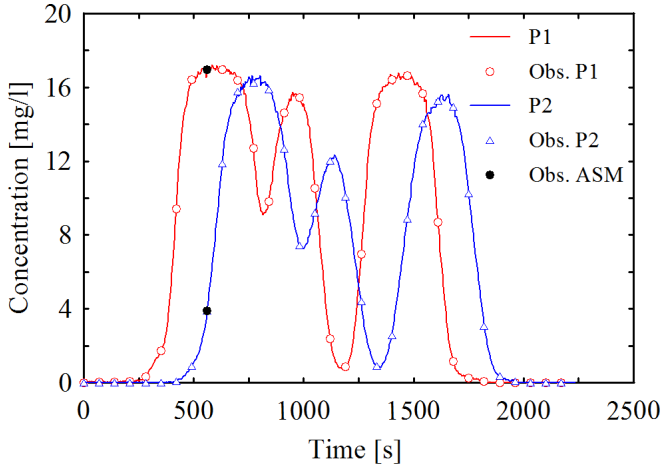

Figure 4.3: Concentration observed at the two monitoring points (solid line). Black dots are the observations used to condition the multiple observation PDF in BPM-ASM method. Time 0 s represents the time at which injection starts (t_{start}).

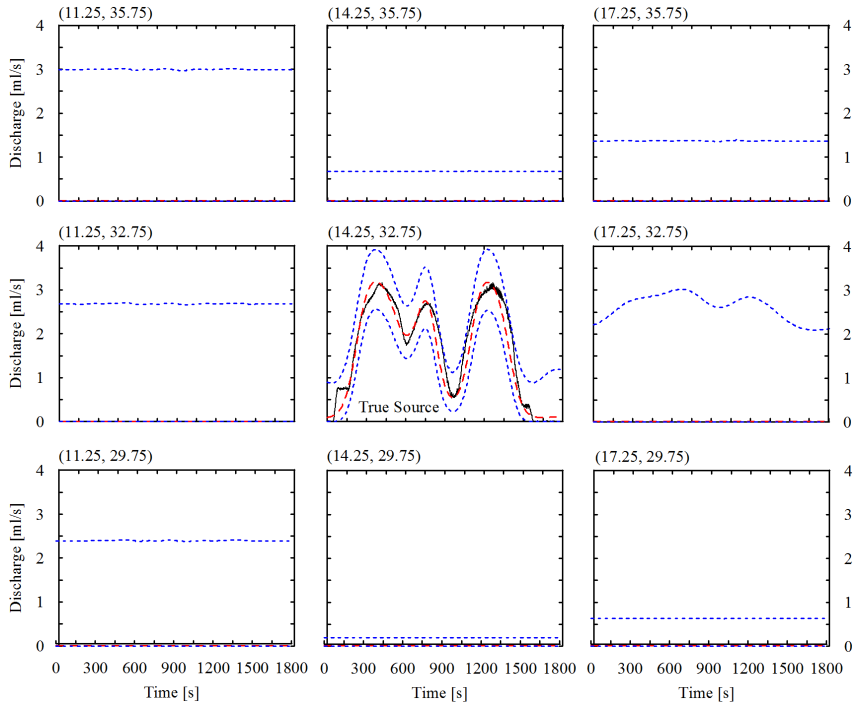

Figure 4.4: The release history recovered at the hypothesized source locations: the true solution (solid black line), best estimate (red dashed line) and 5–95 % confidence interval (blue dotted line). Coordinates of the sources in cm. Time 0 s represent the time at which injection starts (t_{start}).

points P1 and P2 are respectively $\Delta\tau_{P1} = 340$ s and $\Delta\tau_{P2} = 400$ s. So, the evolution of the backward location PDF, at backward time $\tau = 400$ s (Fig. 4.5a, b) was computed. Whereas the porous medium is homogeneous and isotropic, the shapes of the contours are symmetric as shown in Fig. 4.5a, b. Moreover, Fig. 4.5a shows that for a closer observation point, the backward location PDF is higher, as expected. This spreading out of PDF is caused by dispersion, similar to the processes that occur in a forward model.

4.4.2.2 Multiple-observation backward location PDF

In this case, two observations of contamination collected at the two observation points are used to calculate the multiple-observation location PDF, given by Eq. 4.23. It was assumed that the particles observed in P1 and P2 were originated by a unique release at the same point source location at the same backward time. As shown in Fig. 4.5c, the dispersion of the backward location is smaller than the two single-observation location PDF (Fig. 4.5a, b). This approach does not allow to consider the concentration measurement, but only the presence or the absence of the contaminant. So, one point detected in

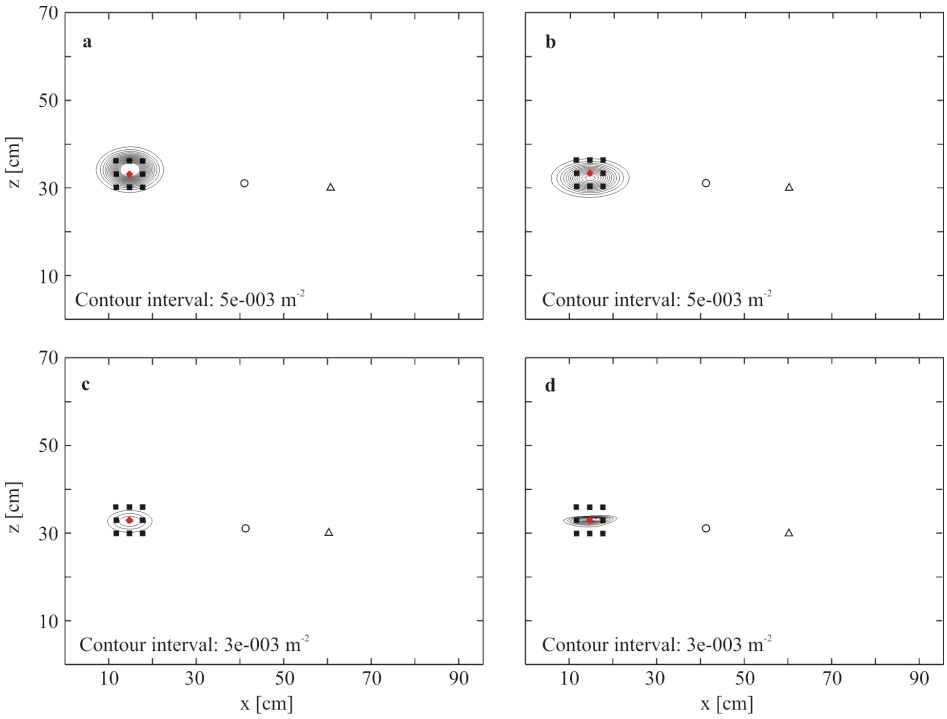

Figure 4.5: Backward location PDF at $\tau = 400$ s. **a** Unconditioned backward location PDF: observation point P1. **b** Unconditioned backward location PDF: observation point P2. **c** Multiple-observation (P1 and P2) backward location PDF. **d** Conditioned backward location PDF on concentrations.

a marginal position of the plume could compromise the result because the observations cannot identify the plume shape. In fact, in the backward model, the backward location PDF simply follows the same processes that occur in the forward model, and the resulting multiple-observation backward location PDF is not able to give a weight to observations with a higher concentration value.

4.4.2.3 Backward location PDF conditioned on measured concentrations

In the previous sections the concentration measured at the two observation points was not considered. A lot of information about the concentration in time at both points P1 and P2 was available through the images collected during the laboratory test. However the method requires only the concentration values at the monitoring points collected at a time $\bar{t}$. Several sample times were considered during preliminary studies and all yielded very similar results. In this case, the results due to the concentration sampled at $\bar{t} = 590$ s after t_{start} are shown. Since the release mass is considered unknown, as the source loca-

tion, $f_{\hat{C}_i}(\hat{C}_i \mid m_0, \mathbf{x}_0, \tau)$ was calculated for each observation for a range of possible source masses (50 mg $< m_0 <$ 70 mg) and a range of possible source locations that include the entire spatial domain. An iterative procedure was developed with Matlab (*Mathworks*, 2010) in order to change the source position in every cell, and run the flow and transport models. This approach could be computationally challenging if the number of cells is too high, due either to an excessively extensive investigated area or a high spatial resolution. This could be improved by analyzing the delineated suspected area only, as in the SRSI method. The concentrations observed at the monitoring points used to condition the backward location PDF were 16.97 mg/L for P1 and 3.88 mg/L for P2 (Fig. 4.3). As described in 4.4.1, the measurement error is taken as being constant and equal to 3 mg/L, although this value represents the maximum error, and for small concentrations it is smaller than the one considered. The source location, based on the backward location PDF, conditioned on concentrations measured, is very well identified. The conditioned backward probability PDF plume has a long and narrow shape, as shown in Fig. 4.5d. This improvement reduces the backward location variance and it allows to increase information on the source.

4.4.2.4 Backward location PDF conditioned on measured concentrations

An assumption on the release time is required when the backward probability model is used, so a study about the effect of this parameter on the results was considered. In the previous sections, the backward release time was fixed at $\tau = 400$ s. An error of 10 and 20 % of $\Delta\tau_{P2}$ was considered with the aim of studying the results with a wrong time release. Thus, backward release times $\tau_{-10\%} = 360$ s, and $\tau_{-20\%} = 320$ s were hypothesized, and the results are shown in Figs. 4.6 and 4.7. While the results obtained with a 10 % error remain acceptable, a 20 % error does not allow to identify the true source location. Moreover, by considering an error of +10 % ($\tau_{+10\%} = 440$ s) or +20 % ($\tau_{+20\%} = 480$ s), the source location will be estimated upstream the true one and it will present a larger backward location PDF plume than the one estimated with -10 or -20 %.

4.5 Discussion and conclusions

In this chapter, a comparison between two methods, simultaneous release function and source location identification (SRSI) and backward probability model based on adjoint state method (BPM-ASM), was carried out. For the application of these methodologies, experimental data collected through laboratory equipment under controlled conditions were used. This allowed to perform both methodologies in a real test case in which the true solution was known a priori. A numerical model was calibrated on experimental data with the aim of computing the transfer function TFs (*Butera et al.* 2004, 2006) and

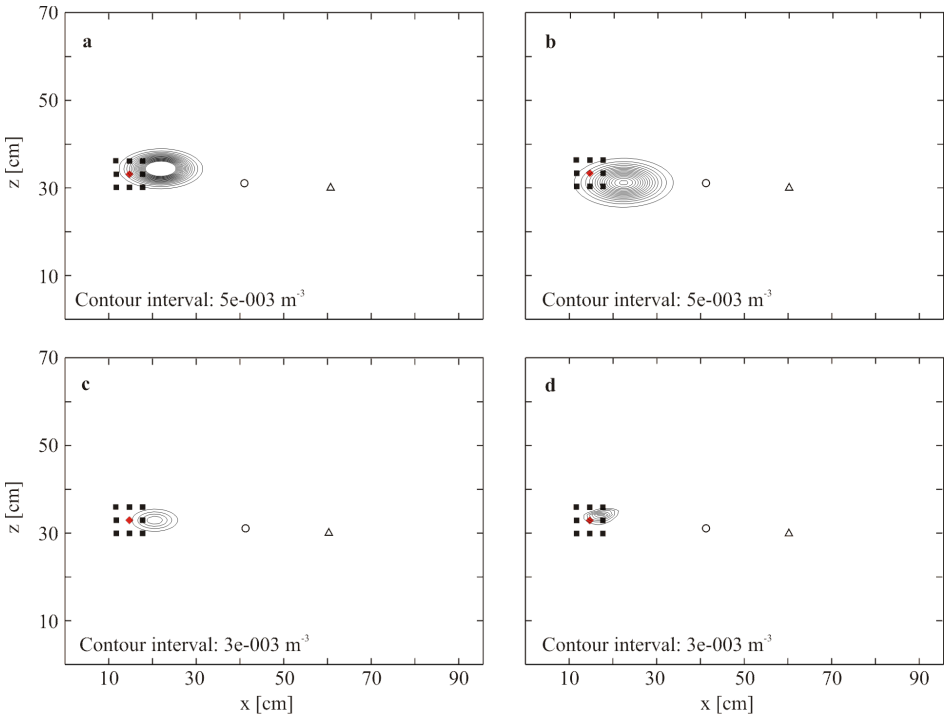

Figure 4.6: Backward location PDF at $\tau_{-10\%} = 360$ s. **a** Unconditioned backward location PDF: observation point P1. **b** Unconditioned backward location PDF: observation point P2. **c** Multiple-observation (P1 and P2) backward location PDF. **d** Conditioned backward location PDF on concentrations.

to build the backward model for the BPM-ASM (*Neupauer and Wilson* 1999, 2000). The SRSI procedure is able to simultaneously recover the release function and identify the source location, but it requires a preliminary delineation of the suspected areas and to do some weak hypothesis about the statistical structure of the unknown release function. The number of preliminary runs of the forward transport model necessary to obtain the numerical TFs is equal to the number of the suspect source locations.

The backward location PDF describes the possible former positions of the observed contamination at a fixed time in the past. Using an adjoint model, an instantaneous point source of an adjoint state (related to the backward location PDFs) is released at the observation location. Given the simplicity of the flow field, the exchange of the boundary conditions was sufficient to obtain the backward model. At first, the unconditioned backward-location PDFs were calculated for each monitoring point, considering the time release known. Then the multiple-observation PDF was calculated and finally it was conditioned on the experimental concentration measurement. This method identifies the true

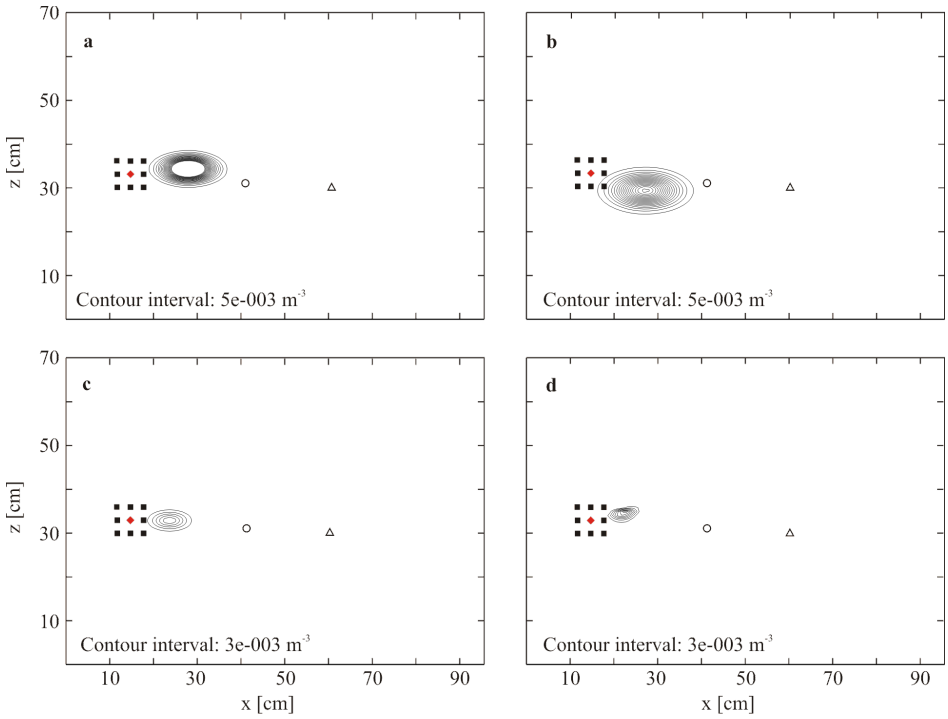

Figure 4.7: Backward location PDF at $\tau_{-20\%} = 320$ s. **a** Unconditioned backward location PDF: observation point P1. **b** Unconditioned backward location PDF: observation point P2. **c** Multiple-observation (P1 and P2) backward location PDF. **d** Conditioned backward location PDF on concentrations.+

source very well. As SRSI method, two observation points were used, but while in the SRSI multiple times were considered (32 in this test case), in the BPM-ASM only two observations at a specific time, were required.

In conclusion, both methods allow to identify the true source; the SRSI allows also to recover the release history. While SRSI method requires to define a suspected area, the BPM-ASM requires to know the release time: both hypothesis could be strong in certain cases. Finally both methodologies could be computationally inefficient, and if the SRSI requires a forward run for each suspected source, the conditioning of multiple-observation PDF requires a forward run for each grid node of the numerical model. The number of the forward runs in the BPM-ASM could be reduced analyzing only the suspected area. Another important difference between the two methods is that the SRSI works also with multiple sources, while the BPM-ASM is able to recognize only one point source. In fact the multiple-observation PDF is based on the hypothesis that all particles observed at a specific time were originated at same location from an instantaneous release. It is

important to notice that the BPM-ASM performed well also in this test case, in which the observations were originated from a complex release history.

In order to overcome the limits of the two methods, a new procedure that includes the best performance of both approaches could be developed: for instance the BPM-ASM could be preliminary used to identify the suspected areas, considering several backward times, and then the SRSI can be applied to estimate the true source location and its release function.

Part 2

Laboratory studies at University of Wisconsin

5 Application of Oscillatory Hydraulic Tomography in a 2D laboratory sandbox

§

5.1 Introduction

One of the greatest challenges in successfully managing groundwater contamination sites lies in the inherent difficulty of understanding heterogeneous subsurface properties. In groundwater contamination problems, in particular, hydraulic conductivity is a key parameter necessary for accurately describing a polluted aquifer and building predictive transport models. The traditional approach for estimating aquifer properties such as hydraulic conductivity (K) is the analysis of pumping tests with analytical formulas, in which the subsurface is assumed to be homogeneous and the obtained conductivity value is an averaged K of the aquifer over a large volume (*Butler and Liu*, 1993). In real aquifers, this assumption of a homogeneous subsurface is almost always violated, and the spatial variability of subsurface material must be understood in order to accurately make solute and contamination transport predictions.

Numerous methods have been suggested for estimating spatially variable hydraulic properties in the shallow subsurface and validated through field experiments, theoretical analysis and numerical simulations. Often, small-scale stimulations such as slug tests are used to obtain local estimates of hydraulic parameters. The data may then be processed through geostatistical analysis while incorporating geologic, hydrogeologic, and geophysical information to create images of aquifer properties (e.g., as summarized in *Kolterman and Gorelick*, 1996). The effective parameter estimation approach is computationally effective, however exhaustive sampling may be necessary to obtain accurate interpolated

maps of aquifer heterogeneity. A recently developed approach to characterize subsurface properties is hydraulic tomography, in which constant-rate pumping tests alternate at different locations and a set of pressure change data are obtained at monitoring locations for tomographic analysis.

Yeh and Liu (2000) originally performed a numerical hydraulic tomography study by applying a geostatistical inverse approach - the sequential successive linear estimator (SSLE) - to characterize 3-D spatial heterogeneity. They presented promising results, revealing more detailed aquifer heterogeneity than classical aquifer tests. The first real-world experiment evaluating hydraulic tomography is from *Liu et al.* (2002), who conducted two laboratory sandbox studies and applied the SSLE to characterizing aquifer heterogeneity. In this analysis, steady-state drawdowns due to pumping tests were used as the data for inversion, i.e., steady-state hydraulic tomography. They demonstrated that hydraulic tomography is able to reproduce the major heterogeneity patterns through comparison with the known sandbox heterogeneity patterns. *Liu et al.* (2007) then used sandbox experimentation to further verify the effectiveness of transient hydraulic tomography based on the SSLE algorithm developed by *Vargas-Guzman and Yeh* (2002). This work validated the hydraulic tomography concept when transient drawdowns are used as the tomographic data source and the SSLE algorithm is applied to transient models. *Illman et al.* (2008) conducted a series of cross-hole pumping tests in a laboratory aquifer to investigate practical issues that affects the performance of hydraulic tomography. Later, *Illman et al.* (2010 a) presented a controlled laboratory study on hydraulic tomography in characterizing a DNAPL source. To compare the hydraulic tomography performance to the kriging approach, *Illman et al.* (2010 b) performed another controlled study using laboratory experiments. Furthermore, *Yin and Illman* (2009) applied temporal drawdown data in hydraulic tomography study; *Liu and Kitanidis* (2011) looked into different inverse modeling approaches on hydraulic tomography. Overall, controlled sandbox experiments have proven to be an effective approach to validate hydraulic tomography.

Recently, testing of hydraulic tomography has also been carried out in the field. *Berg and Illman* (2011) investigated a highly heterogeneous glaciofluvial aquifer-aquitard system using transient hydraulic tomography and proved it to be a promising approach for characterizing aquifer heterogeneity. *Cardiff et al.* (2012) conducted a field test for aquifer imaging using 3-D transient hydraulic tomography and compared the heterogeneity estimates obtained against estimates from detailed slug testing. *Berg and Illman* (2013) similarly performed a field study of imaging subsurface properties using steady-state hydraulic tomography. Hydraulic tomography, as applied in the above laboratory and field studies, uses "traditional" constant-rate pumping tests and relies on extensive amounts of water extraction or injection at pumping locations, which could potentially cause spreading of subsurface contaminants if applied at a contaminant site, or lead to excess water treatment costs. Traditional pumping tests can also require significant field time before steady-state

conditions are achieved, as summarized by *Cardiff and Barrash* (2011), meaning that either long-term field effort or cumbersome transient numerical modeling is required to generate and analyze hydraulic tomography data. In the hydrology and petroleum literatures, a few other tomography approaches have been suggested to avoid mass water extraction. *Vasco et al.* (2000), and *Brauchler et al.* (2003, 2007) collected data from impulse response (i.e., slug interference tests) and inverted the pressure wave's travel time and amplitude to characterize subsurface properties. Their analysis, however, requires aquifer flow to be simulated using a physically approximate "0th order" model.

While slug tests and pumping tests represent standard methods applied for aquifer characterization, some study has been done on oscillatory pumping approaches, in which water is extracted and re-injected in a periodic fashion. This approach was first applied in the area of petroleum reservoir testing (*Kuo*, 1972). The practical advantages of oscillatory testing include: 1) no net injection or extraction of water; 2) little movement of existing contamination; 3) minimal impact of model boundary conditions; 4) easy extraction of oscillatory signals from noisy data. Soon after its application in petroleum field, *Black and Kipp* (1981) developed analytical solutions to study steady-periodic (i.e., constant amplitude and phase) pressure responses to oscillatory stimulation at a pumping location. These pumping tests have been applied only occasionally in field studies such as *Bernabe et al.* (2005), *Rasmussen et al.* (2003), *Renner and Messar* (2006), *Maineult et al.* (2008), and *Becker and Guiltinan* (2010) represent the few examples in which oscillatory or periodic testing was used to analyze subsurface properties. However, each of these analyses assumed a homogeneous aquifer and fit oscillatory data to the homogeneous model. *Lavenue and Marsily* (2001) performed a field application of the pilot point inverse method on a heterogeneous aquifer (containing both fractured and fractured features) by using sinusoidal pumping test data. This is the most representative work we known in which periodic pumping data was used to assess spatially distributed aquifer heterogeneity.

Combining the concepts of oscillatory testing with hydraulic tomography, *Cardiff et al* (2013) presented a modified hydraulic tomography approach, Oscillatory Hydraulic Tomography (OHT), for characterizing the spatial distribution of aquifer conductivity and storage properties. In this approach, several periodic pumping signals of different frequencies are used for stimulation, and responses are analyzed tomographically, using a fast, "steady-periodic" groundwater flow model. Numerical results also demonstrated that different frequencies of testing provide additional information about aquifer heterogeneity. Much like in seismological investigations, high frequency oscillations tend to be more sensitive to subsurface properties in the "near field", whereas low-frequency oscillations are sensitive to a broader region, but appear to have less resolution. To verify the physics governing propagation of oscillatory pressure waves and evaluate the practical effectiveness of OHT, we have built a laboratory sandbox and use laboratory data

collected from sandbox experimentation to validate the theoretical model for OHT.

The focus of the research presented here is to provide an experimental confirmation of the theory of OHT for testing frequencies that are reasonable in practical hydraulic application (generally <1 Hz). In our setup, we use an instrumented laboratory sandbox, filled with material of known hydraulic properties, and measure aquifer responses due to an oscillatory stimulation at a variety of frequencies. Through these tests, we experimentally verify the physical model developed for studying oscillatory flow and likewise validate the capability of OHT for characterizing heterogeneity. The remainder of this work is organized as follows: We first describe the design and instrumentation of the sandbox in Section 5.2. The pumping tests performed - which consisted of oscillatory pumping at multiple frequencies and locations - are described in Section 5.3. In Section 5.4, we discuss data processing of OHT data, in which signal properties are extracted from raw transient signals. In Section 5.5, we discuss the physical groundwater flow model in the phasor domain, the applied inversion approach, and error propagation on oscillatory data. Finally, we present and discuss the results of OHT imaging in Section 5.6. The work presented in this chapter has been published in *Zhou et al.* (submitted) and presented at 2014 AGU Fall Meeting in *Zhou et al.* (2014).

5.2 Sandbox constructions and data collection

The sandbox is designed to evaluate aquifer properties within a 2-D domain, packed with materials with known hydraulic properties. It is built to be compatible with organic solvents such as DNAPL to allow contaminant transport testing. The sandbox total size is 1.78 m wide, 0.77 m tall and 0.14 m thick (Fig. 5.1) with the actual internal volume for porous media packing being 1.5 m x 0.75 m x 0.1 m. The thickness dimension constrains the sandbox essentially to the study of 2D flow and transport. The sandbox is constructed of 2.5cm thick plexiglass (Midland Plastics), bonded by a mixture of plexiglass and chloroform. The front side of the sandbox contains ports of 1/4" diameter at 25 equally spaced locations (Fig. 5.1). Fiber optic pressure transducers can be installed to record pressure changes due to oscillatory pumping at different frequencies. To maintain the vertical stability of the sandbox, we clamped Unistrut metal support beams at the front and the back side of sandbox.

The sandbox built for current research is also designed to simulate natural fluid flow and solute transport in a confined or unconfined aquifer under a controlled environment. The sandbox has constant head boundaries maintained on two ends of the domain, with a noflux condition at the base. The constant head boundaries are maintained by constant water supply at one end of flow cell and over flow at the other end. A fine mesh barrier, 400×400 cloth, capable of filtering sands while allowing flow of water, is attached to the plexiglass that separates the water supply from the porous media domain. Towards the top

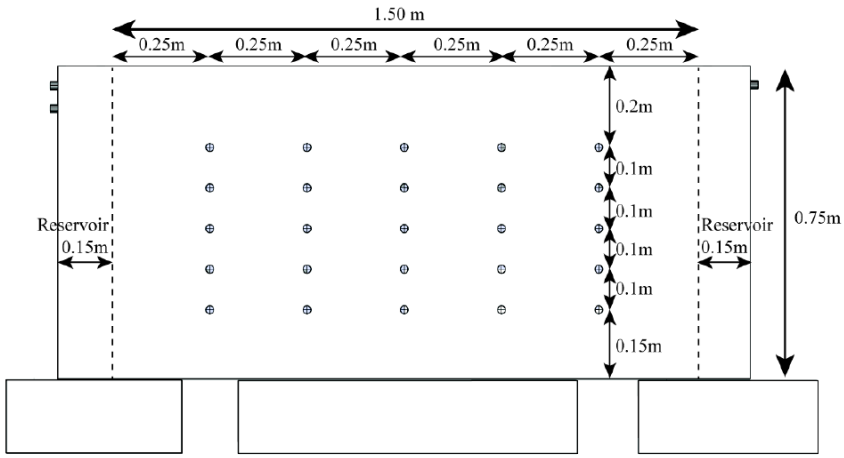

Figure 5.1: The open area of the sandbox is 1.5m x 0.75m x 0.1m. Constant head reservoirs are built on both ends of the sandbox. It is capable of supplying water throughout the porous media sufficiently. A fine mesh barrier is attached to the barrier between reservoir and sandbox open area to prevent movements of sediment into the reservoir. The constant head reservoir is equipped with outlets to adjust the water level. On the left side reservoir, we placed two outlets that are 0.05m apart that accommodates flow transportation experiments. The right side reservoir outlet has the same elevation with the top outlet on the left side.

of the reservoirs, copper connectors are installed which allow the flow system to maintain at a controlled water level. At the bottom of one reservoir, a third copper connector is installed to allow water drainage when needed. Five locations in the sandbox are setup for pumping. Each pumping location is installed with a 1" diameter air stone diffuser. The air stone diffuser acts as a stable porous media that distributes injected water throughout the thickness and also prevents sand collapse on the pumping interval. Fiber optic pressure transducers (FISO co.), with a sampling frequency of 125 Hz, are used to detect pressure variations at the observation locations. All pressure transducers are connected to a central data acquisition system, which records relative pressure changes throughout the duration of the experiment. The high-accuracy fiber-optic transducers used are able to record pressure variation to a resolution of <1mm. The described laboratory sandbox setup allows controlled testing including conventional pumping tests, cross hole pumping tests, and also oscillatory pumping tests on confined or unconfined conditions. It can further be used to test periodic signal propagation during transport of contaminants such as high-viscosity DNAPL in different types of porous media. The system is capable of controlling and monitoring the pumping site and monitoring site head responses at the same time.

5.3 Oscillatory flow testing

To study and validate the response of aquifers to periodic forcing across a range of frequencies, two experiments with an oscillating pump are investigated. The first experiment was performed using a homogeneous aquifer, in which the sandbox is filled with homogeneous commercial silica sand with a hydraulic conductivity of 1.1e-4 m/s, as measured from falling-head permeameter testing. The second experiment is performed in a heterogeneous aquifer (Fig. 5.2) with a higher K (2.7e-3 m/s) gravel distributed among the lower K (1.1e-4 m/s) background sand. A series of oscillatory pumping tests are performed at pumping ports at nominal periods of 2s, 5s, 10s, and 20s. During each test, oscillatory pumping is continued until steady-periodic conditions are observed at data collection locations. The pumping location is varied throughout the domain while observation locations remain the same (Fig. 5.3). During the pumping test and data collection, we tested a few pumping volumes to ensure linear (Darcian) response. Each data collection starts with a zero pressure change and generally after 5-6 periodic cycles (see Fig. 5.4), it transitions to steady-periodic motion, in which the amplitude and phase of all signals are consistent. Oscillatory pumping tests were performed on both the homogeneous and heterogeneous sandbox using the same set of pumping volumes, pumping locations, and observation locations.

When the system reaches steady-periodic, the head variation at each observation location appears to be oscillatory with constant amplitude and phase, relative to the pumping well pressure (Fig. 5.5, left). General trends observed in raw data are as follows: the frequencies of the head responses are consistent with the oscillatory pumping frequencies. The amplitude of the head response at each location is dependent on its distance to the pumping port. Observation locations that are closer to the pumping port achieve stronger amplitudes in head change and vice versa. Using a constant volume oscillator, low frequency oscillatory pumping tests produce signals that have lower amplitude of head responses, and the amplitude attenuation with distance is also less significant than in higher frequency oscillatory pumping tests. An interesting feature of OHT tests is the phase lag, i.e., the peak of each sinusoidal signal occurs at delayed times. For the homogeneous aquifer, the phase lag is mostly dependent on the distance between the observation location and pumping location, and may also be affected by boundary conditions. The farther the sinusoidal signal propagates away from the pumping port, the larger the phase lag. In the heterogeneous case, variations in the amplitude and phase of signals obtained during the two testing rounds suggest sensitivity to local heterogeneity (Fig. 5.5, right).

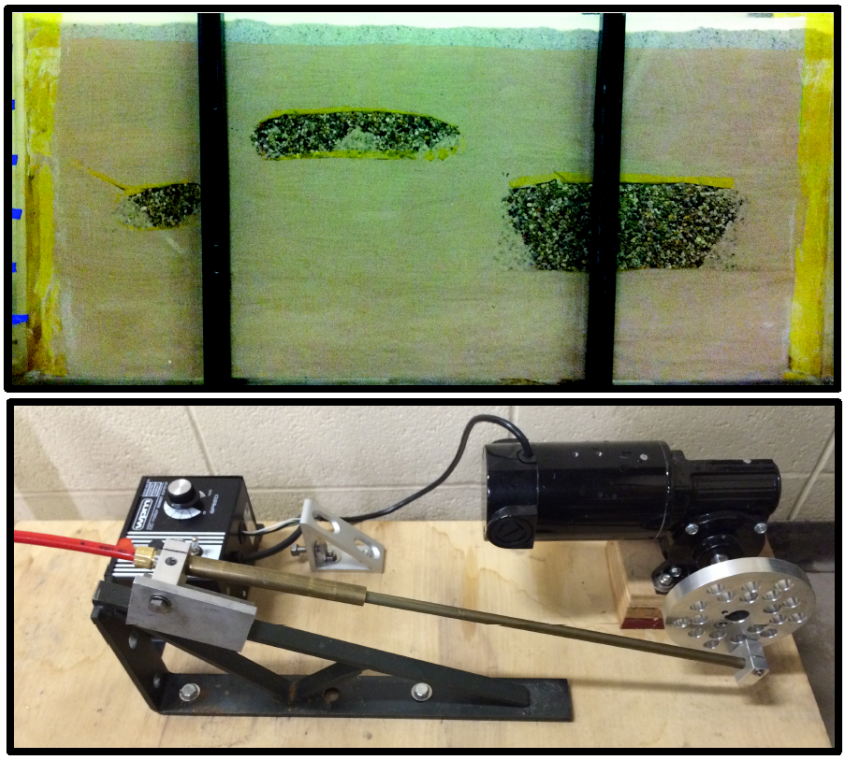

Figure 5.2: The top picture shows the heterogeneous sandbox packing, front view. The background material is sand and the heterogeneities are gravels. The bottom picture shows the design of oscillating signal generator. The stroke length of the generator can be adjusted to control desired pumping volumes.

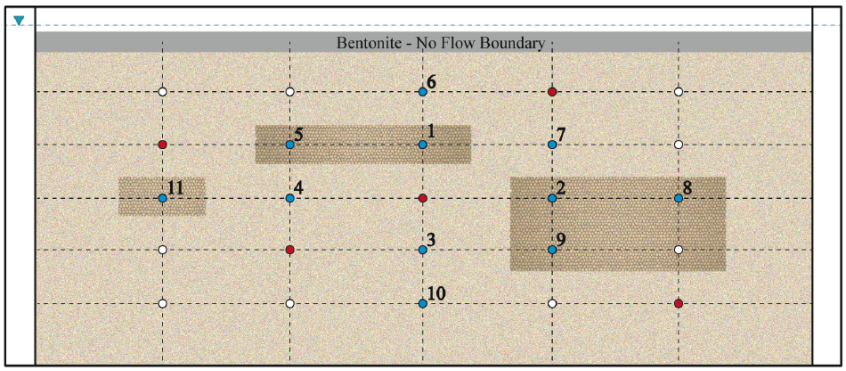

Figure 5.3: Red points are pumping locations, and blue points are observation locations. Center red source point is defined as row 3, column 3. Dark brown color patterns represent the gravel distribution that highly resembles the actual sandbox packing.

5.4 Data processing

During each oscillatory pumping test, a sinusoidal pressure wave of a given period, i.e., either 2s, 5s, 10s, or 20s, is induced in an aquifer at a source location and pressure changes are recorded at an array of observation locations. The collected time series data is sinusoidal and has several components associated with it including sensor noise, and sensor drift. Spectral analysis is performed on the pressure changes collected at each observation location and the pumping location to extract the signal amplitudes and phases associated with the given pumping frequency. Fast Fourier transform (FFT) algorithm is used to analyze the time series data to obtain Fourier coefficients, which store information about the oscillation frequencies as well as their amplitude and phase shift. In our testing, each oscillatory pumping test produced 12 datasets, with one dataset representing the pumping port pressure, and the rest of the datasets representing monitoring location responses. Fig. 5.6 shows one example of a dataset collected during oscillating pumping at a nominal 10-second period, and the corresponding frequency domain power.

In the frequency spectrum plot, the highly dominant frequency component is about 0.1 Hz (10 second period). While we show only one example, almost all of the datasets recorded (including those at the pumping location) contain a single dominant frequency component, and in all cases, we found that the sandbox response appeared to be highly linear, i.e. the observation locations have the same dominant frequency component as the pumping location. In order to apply the steady-periodic numerical model (discussed in the following section), each observation is represented by the Fourier coefficients measured at the corresponding point in the sandbox, which describes the amplitude and phase of the steady-periodic signal. To ensure that the dominant signal components are represented by the obtained Fourier coefficients, we can convert the coefficients back to the time domain and fit to the real data (Fig. 5.7). In all cases analyzed, the standard deviation between the computed curve and the real data is in the order of 10^{-3} m to 10^{-4} m. The result provides confidence that Fast Fourier Transform captures the majority of the response observed in the transient pressure signals.

5.5 Imaging approach

5.5.1 Physical Model

The phasor-based groundwater flow model is used to describe propagation of oscillations at given frequency. A detailed description of the phasor model derivation can be found at *Cardiff et al.* (2013). By replacing hydraulic head with $\Phi_\omega(\mathbf{x})$, a complex-valued field variable, the standard groundwater flow model can be expressed as follows:

$$i\omega S_S \Phi_\omega = \nabla \cdot (K \nabla \Phi_\omega) + Q \quad \forall\, \mathbf{x} \in \Omega$$

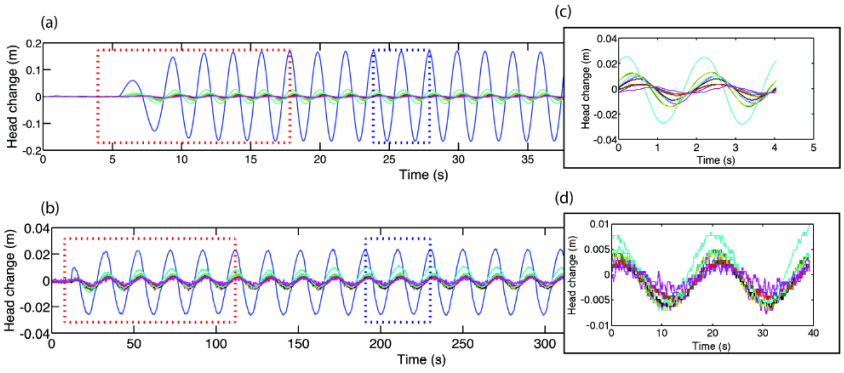

Figure 5.4: Pressure responses measured during oscillatory testing with nominal 2-second period (a) and 20-second (b), red dashed box show the transition from zero pressure to steady periodic response with a consistent amplitude and phase. (c) and (d) present magnified views of steady-periodic pressure responses at observation locations from testing with nominal 2-second period and 20-second period.

$$\Phi_\omega = 0 \quad \forall\, \mathbf{x} \in \Gamma_d$$

$$\nabla\Phi_\omega \cdot \mathbf{n} = 0 \quad \forall\, \mathbf{x} \in \Gamma_n$$

$$K\nabla\Phi_\omega \cdot \mathbf{n} = i\omega S_S \Phi_\omega \quad \forall\, \mathbf{x} \in \Gamma_w$$

where Ω is the domain of interest; $\mathbf{x}$ is a vector of spatial coordinates [L]; Γ_d, Γ_n and Γ_w represent Dirichlet, Neumann, and linearized water table boundaries, respectively; $Q(\mathbf{x})$ is a scalar field giving peak volume flow rates [$(L^3T^{-1}L^{-3}$] and ω is the angular frequency of the oscillation [radians$\cdot T^{-1}$]; $S_S(\mathbf{x})$ is a scalar field of specific storage values [L^{-1}]; $K(\mathbf{x})$ is a scalar field of hydraulic conductivity values [LT^{-1}] (assumed isotropic). This model can solve for steady-periodic response within in the aquifer, after initial transient response has dissipated. Measured responses from lab or field tests (Fourier coefficients extracted from steady periodic hydraulic heads) can be inverted using this fast-running model to simulate aquifer response.

5.5.2 Inverse Model

OHT data can be inverted using any standard method for ill-posed (tomographic) inverse problems. In our approach, we utilize the quasi-linear geostatistical theory developed by *Kitanidis* (1995). We utilize this algorithm to map the spatial distribution of both K and S_s in the laboratory sandbox aquifer, by inverting the Fourier Coefficients of the pressure response (as discussed in detail in *Cardiff et al.* (2013)). To obtain K and S_s tomograms from multiple oscillatory pumping tests, we solve an inverse problem for os-

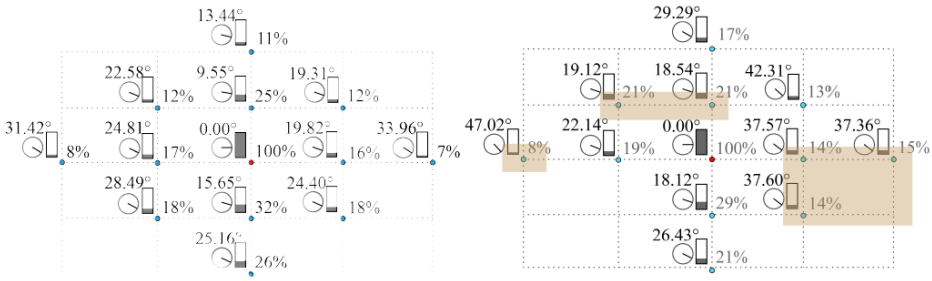

Figure 5.5: Phase and amplitude summary from testing with nominal 20-second period for homogeneous (left) and heterogeneous aquifer (right). The clock indicator represents the phase change and the bar indicator represents the amplitude change. The shaded areas on heterogeneous aquifer represent the gravel pattern in the background sand.

cillatory flow conditions. The sandbox was discretized into 1800 cells with each cell of 0.025m × 0.025m × 0.1m. Input data to the inverse model includes ''measured'' sinusoidal and cosinusoidal coefficients (i.e., the real and imaginary parts of the Fourier coefficients) at each stimulation frequency along with the covariance matrix of the errors of these coefficients. The objective function optimized is:

$$min_{\mathbf{s},\beta} \frac{1}{2}(\mathbf{y}-\mathbf{h}(\mathbf{s}))^T R^{-1}(\mathbf{y}-\mathbf{h}(\mathbf{s}) + \frac{1}{2}(\mathbf{s}-\mathbf{X}\beta)^T Q^{-1}(\mathbf{s}-\mathbf{X}\beta)$$

where $\mathbf{s}$ is the vector of parameter values (K and S_S in each grid cell), $\mathbf{y}$ is the vector of data (real and imaginary parts of the Fourier coefficients measured at each location and each frequency), $\mathbf{h}()$ is the physical forward model described above, $\mathbf{R}$ is the covariance matrix of data errors (derived from the covariance matrix of Fourier coefficient errors from the normal equations – see e.g., *Bakhos et al.*, 2013), $\mathbf{X}$ is a vector of drift function values, β is a vector of drift coefficients, and $\mathbf{Q}$ is the expected parameter covariance. In this example, as in *Cardiff et al.* (2013), we assumed the sandbox heterogeneity can be modeled as a stationary, constant-mean random field. Therefore, $\mathbf{X}$ is a vector of ones, and $\mathbf{Q}$ represents the spatial covariance calculated given a known variogram. The variance and correlation length of K and S_s (variogram) are computed based on the permeameter tested parameter (K and S_s) values and prior knowledge of the parameter field distribution in sandbox. All inverse modeling runs were executed using a MacBook Pro with 2.6 GHz Intel Core i7 processor and 16GB of RAM. Individual inversion runtime increases with increasing amount of data input. However, the total maximum run time is less than 10 minutes for any individual imaging result.

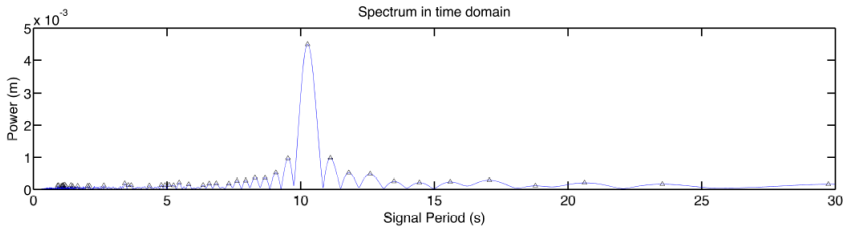

Figure 5.6: Time domain spectrum plot for one of the 10-second period oscillatory data.

5.5.3 Error propagation

Oscillation response of known frequency, in practice, is contaminated with noise, which results error in the Fourier coefficients. *Bakhos et al.* (2013) used linear regression to recover signal from a set of noisy measurement. In specific, they looked into the effectiveness of linear regression on four common types of noise observed in practice: white noise, white noise with a jump in the signal, white noise with a linear drift and correlated noise. Data error is quantified by data covariance matrix assuming data noise (ϵ) is Gaussian, $\epsilon \sim N(0, \sigma^2)$. For instance, a time series hydraulic head data can be expressed as (*Cardiff et al.*, 2013):

$$\mathbf{d} = A_\omega \sin(\omega \mathbf{x}) + B_\omega \cos(\omega \mathbf{x}) + \epsilon$$

where $\mathbf{d}$ represents the data vector at a particular measurement point and frequency; $\mathbf{t}$ is the vector of measurement times; A_ω and B_ω represent the sinusoidal and cosinusoidal coefficients, respectively. If the time interval between data measurement Δt is small and total sampling time T_S is a multiple of the signal period, the covariance matrix of data error ($\mathbf{R}$) can be expressed as (*Bakhos et al.*, 2013):

$$cov(\mathbf{d}) \approx 2\sigma^2 \frac{\Delta t}{T_S} \begin{pmatrix} 1 & 0 \\ 0 & 1 \end{pmatrix}$$

For all the four cases analyzed in their paper, true signal is recovered from noisy measurement. This provides confidence that the sinusoidal and cosinusoidal coefficients extracted from oscillation tests is able to represent the actual physics in aquifer system.

5.6 Results and Discussion

In this section, we analyze OHT imaging as applied to the laboratory sandbox, and investigate the influence of different factors on the obtained tomograms. In Section 5.6.1 we

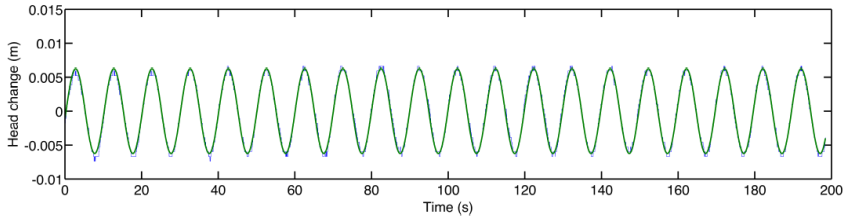

Figure 5.7: Comparison between observed data (blue) and representation using a single-component sinusoid (green).

look into signal length's effect on Fourier coefficients computation. In Section 5.6.2, we discuss signal frequency influence on K tomogram by comparing single frequency and multi-frequency inversion results. In Section 5.6.3, we discuss the improvement on K tomogram using multi-source location compare to single source location. Finally in Section 5.6.4, we analyze receiver locations' influence on K tomogram followed with error quantification on K tomogram in Section 5.6.5. Note that in each inversion, we estimate both spatially distributed K and S_s in all grid blocks of the numerical model.

5.6.1 Signal lenght effect on Fourier coefficients

One key benefit of using oscillatory signals (with a known frequency) for aquifer stimulation is that the signal is easily extractable from real data in the presence of significant noise and even sensor drift. Additionally, error estimates of signal Fourier coefficients can be reduced through increased signal lengths of time-series measurements. To study the robustness of signal processing routines for extracting known-frequency oscillation from noisy data at different signal lengths, we compare the mean and variance of estimated errors for 2 periods and 10 periods of oscillatory data, respectively. We find that the difference in estimated Fourier coefficients is fairly small and use shorter periods does not significantly affect the Fourier coefficients computation in this study. For all inversions presented in the following sections (5.6.2, 5.6.3, 5.6.4), we use 10 periods of steady-periodic data to determine the Fourier coefficients.

5.6.2 Signal frequency influence on K tomogram

One key aspect of OHT - which has been shown theoretically - is that different frequencies of aquifer stimulation provide different sensitivities to heterogeneity within a volume. Thus, a single pumping location can be used to obtain different sets of information about aquifer heterogeneity by altering the pumping frequency. To demonstrate this impact, in our analysis, we provide results of inversion in which a single pumping location is utilized, but progressively larger numbers of testing frequencies are inverted. Our results

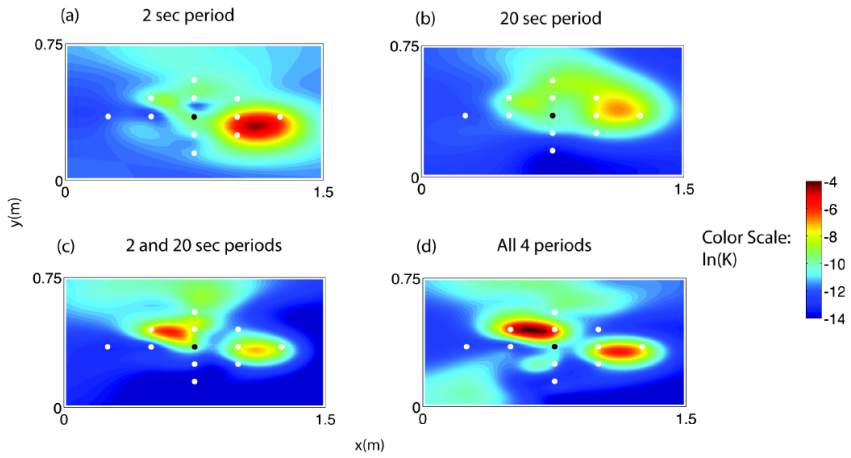

Figure 5.8: Comparison of inversion results using a single pumping location (center: row 3, column 3, as indicated by the black point), as the number of testing frequencies is increased. White points show the observation locations.

show two single frequency inversions (2s and 20s), a joint inversion of 2s and 20s oscillations, and a joint inversion of 2s, 5s, 10s and 20s oscillations (Fig. 5.8). These experimental results agree with numerical simulations presented in *Cardiff et al.* (2013), i.e., the high frequency oscillations are more sensitive to "near field" parameters and low frequency oscillations produce more diffusive sensitivities throughout aquifer. The results also demonstrate that progressive improvement in aquifer imaging results are obtained by jointly inverting multiple frequencies' response.

5.6.3 Source location influence on K tomogram

To obtain truly tomographic results, we implemented multiple source and receiver combinations using 2-second frequency data. In Fig. 5.9, the receiver locations remain the same while source locations (i.e., additional pumping tests) are gradually added. By adding more source locations, we are able to obtain improved resolution of both finescale and large-scale aquifer features in the K tomogram. When using 2 sources for imaging, we can already obtain a K tomogram that well represents the true sandbox pattern. The K tomogram incorporating 5 sources provides a even more detailed characterization of the heterogeneous feature. This is also true when we look at the S_s tomogram. We also notice that the K tomograms are not significantly correlated with S_s tomograms. This is likely due to the fact that Ss varies less from one type of sand to the other, as discussed in *Yin and Illman* (2009). Note that improvement in imaging with multiple pumping tests is comparable to improvement of using multiple testing frequencies for a single pumping

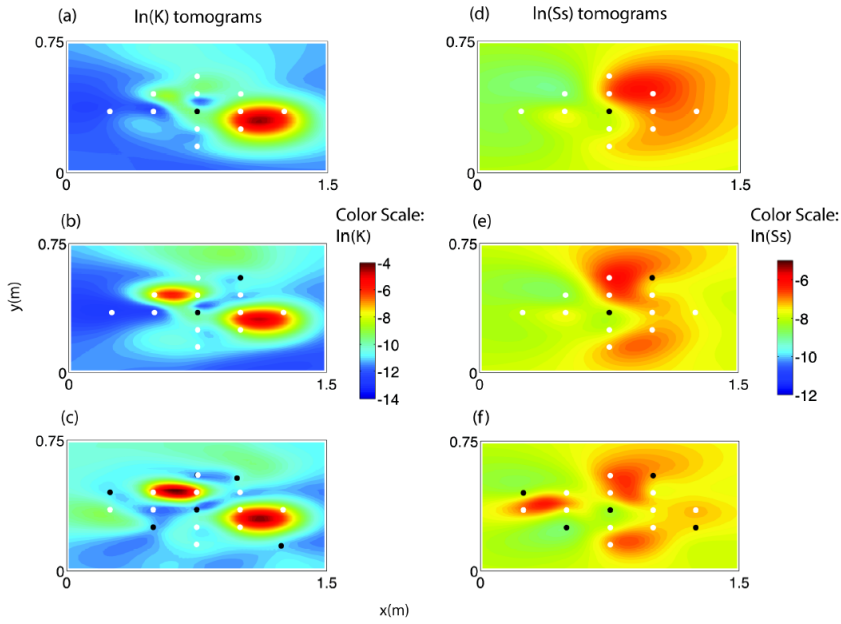

Figure 5.9: Improvements in K and S_s tomograms as more pumping tests are included. Black points represent pumping locations inverted. White points are observation locations. Note that case (c) is the best K tomogram among estimations using 2-second data from all the pumping tests.

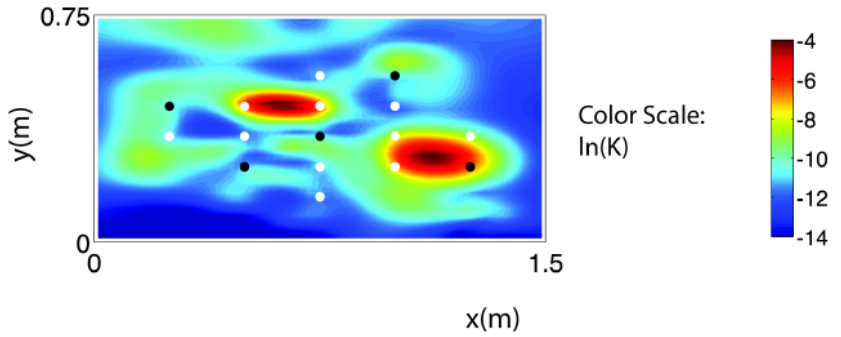

Figure 5.10: Best K tomogram inverted when using all frequency data from all pumping tests.

test (e.g., Fig. 5.8 vs. Fig. 5.9). Furthermore, a best K tomogram can be obtained when using all frequencies data (2s, 5s, 10s and 20s) from all pumping tests (Fig. 5.10).

5.6.4 Receiver location influence on K tomogram

In this section, we looked into receiver locations' influence on K tomogram while keeping the number of source locations constant (3 pumping tests). We specified receivers to 3 arrays, with the inner array indicated by white solid points on Fig. 5.10b, middle array are white solid points on Fig. 5.10d, and outer array are white solid points on Fig. 5.10f. We assume receiver data from these white points are available in each corresponding tomogram. It is surprising that when using only the inner or the middle array of receiver data, we can also obtain a K tomogram that clearly represents the sandbox K pattern, see Fig. 5.10b and Fig. 5.10d. When using only the outer array of receiver data, the K tomogram does not provide as clear of a description of aquifer heterogeneity. This is likely due to the fact that the distance between source and outer array of receivers is further; therefore the transmitted signal dissipates more and contains less information for aquifer characterization. Another interesting finding is that if we excluding the each array of receiver one at a time, we are able to obtain K tomograms with improved resolution compare to using single receiver array. Overall, using two arrays of receiver in inversion provides better imaging results than using single array, though single array of receiver (such as the inner and middle array) data is able to detect aquifer K field patterns. A direct comparison between K tomograms with varied receivers (Fig. 5.9) and the best K tomogram (Fig. 5.10) is also presented in Fig. 5.11.

5.6.5 Error quantification on K tomogram and oscillatory data

We next validate the OHT by comparing the geometric mean of log scale K ($\ln K$), variance of $\ln K$, data and model misfit. In Table 5.1, we find that the geometric mean K computed from varies K tomograms is relatively smaller than effective K of -9.1, computed from constant rate pumping test. Previously, we have shown that using one pumping location (column3 row 3, i.e., c3r3 on Table 5.1) while gradually input additional frequencies data visually improves K tomogram (Fig. 5.8), although statistical comparison on Table 5.1, row 1 to row13, is not in complete agreement with visual comparison. K tomograms from single frequency with 5 pumping tests have low misfit in both data and model (Table 5.1, row 14 to row 17). When all the pumping frequencies are used in inversion, K tomogram improves with increasing pumping test locations (Table 5.1, row 18 to row 22). When using only partial observation locations' data in inversion, model and data misfit is surprisingly small.

5.7 Conclusions

This is the first comprehensive validation of oscillatory hydraulic tomography applied to a real (laboratory scale) aquifer. To process and invert the collected data efficiently,

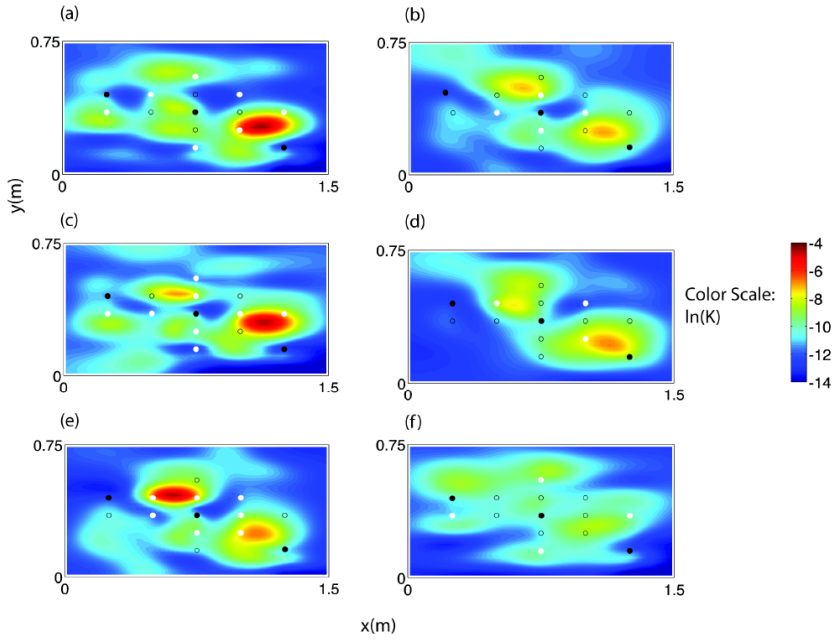

Figure 5.11: *K* tomogram of testing receiver influence on inversion, black solid points represent source location, white solid points represent receiver location, and black empty points represent non-active receiver locations (meaning data from these locations is not used in inversion).

we convert the groundwater flow equation to a phasor domain (see *Cardiff et al.*, 2013) and represented the oscillatory head data using Fourier coefficients. Data collected from the sandbox was likewise processed using the Fast Fourier transform in order to obtain the dominant signal components. This approach allows estimation of both heterogeneous conductivity and storage coefficients, with drastically improved modeling efficiency compared to a fully transient hydraulic tomography analysis, and comparable imaging results. We experimentally validated that multi-frequency joint inversion is able to improve K tomograms compare to a single frequency inversion. To better recover the K distribution in the sandbox, we tried different source and receiver combinations. From the laboratory test results, we have following suggestions for field applications of OHT:

1. For single source and multi-receiver OHT, locating the source at the center of the receiver array will help to obtain the best characterization of the K field;

2. When the number of pumping and/or measurement locations is limited, additional information about heterogeneity can be obtained by performing OHT at a range of frequencies.

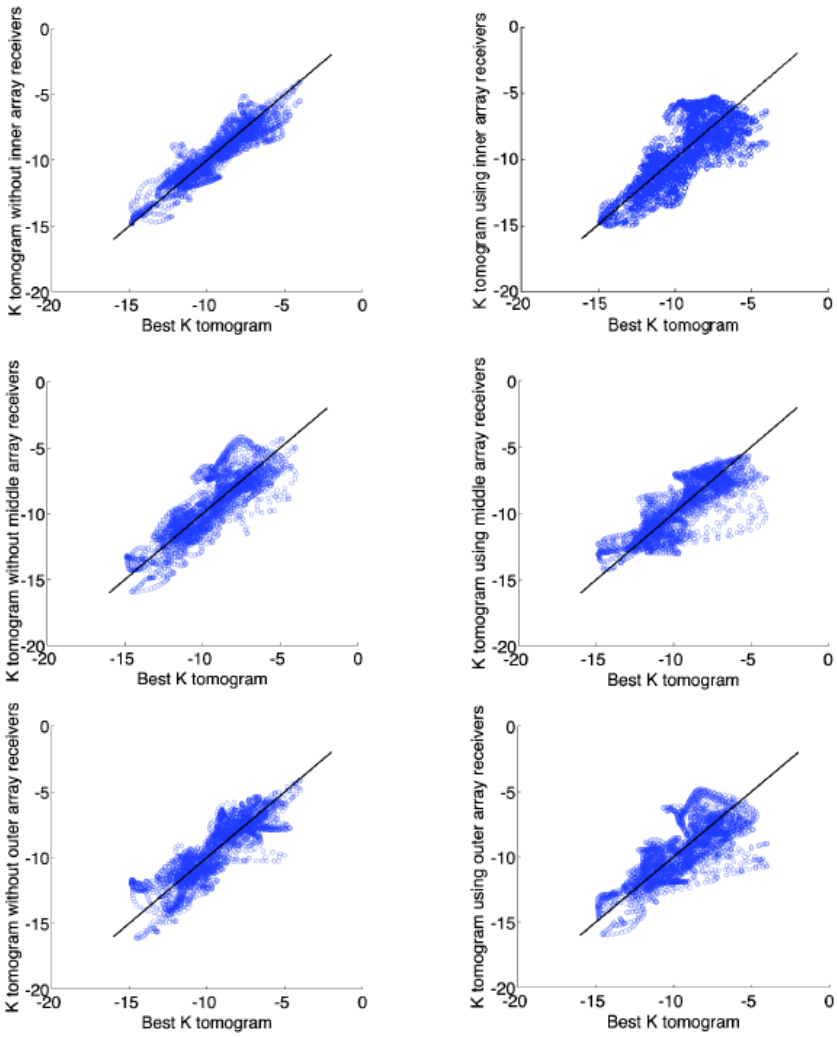

Figure 5.12: Scatter plot of K tomogram with respect to the best K tomogram for Fig. 5.11.

We believe OHT, if applied in the field, is more reliable than constant rate pumping test, which is often easily affected by noises and more difficult to separate from other background signals that may occur during pumping tests (e.g., evapotranspiration, other nearby pumping wells, etc.). It is also a promising technique for characterizing contaminated sites, in that OHT minimally impacts groundwater flow fields during the process of testing.

Table 5.1: A list of log scale geometric mean K value ($\ln K$), variance of $\ln K$, data misfit (difference between all of the observed Fourier coefficients and simulated Fourier coefficients), and model misfit (difference between the best K tomogram and other K tomograms) are presented. Here we assume the best K tomogram represents the true parameter field because its data misfit with respect to the observed data is less than 0.05%. The first column listed pumping frequencies included in analysis. The second column listed pumping locations, i.e., observation location data collected from these pumping tests are used in inversion. Here, for example, c3r3 represents pumping location is at column 3 row 3, and so on. The third column listed observation locations used in inversion (e.g. see Fig. 5.3).

	Data Periods Included	Pumping Location	Observation Location	$\ln K$	$\sigma^2_{\ln K}$	Data RMSE	Model RMSE
1	2s	c3r3	$1 \rightarrow 11$	-10.68	2.32	$2.95 \cdot 10^{-3}$	1.54
2	5s	c3r3	$1 \rightarrow 11$	-10.64	1.50	$2.07 \cdot 10^{-3}$	1.57
3	10s	c3r3	$1 \rightarrow 11$	-11.02	2.48	$3.40 \cdot 10^{-3}$	2.15
4	20s	c3r3	$1 \rightarrow 11$	-11.48	2.88	$4.98 \cdot 10^{-3}$	1.96
5	2s, 5s	c3r3	$1 \rightarrow 11$	-11.48	4.23	$8.56 \cdot 10^{-3}$	2.08
6	2s, 10s	c3r3	$1 \rightarrow 11$	-11.31	3.52	$4.26 \cdot 10^{-3}$	1.76
7	2s, 20s	c3r3	$1 \rightarrow 11$	-12.17	5.36	$1.48 \cdot 10^{-2}$	2.57
8	5s, 10s	c3r3	$1 \rightarrow 11$	-10.93	1.86	$2.01 \cdot 10^{-3}$	1.65
9	10s, 20s	c3r3	$1 \rightarrow 11$	-11.00	1.80	$2.37 \cdot 10^{-3}$	1.70
10	2s, 5s, 10s	c3r3	$1 \rightarrow 11$	-11.32	3.57	$3.40 \cdot 10^{-3}$	1.71
11	2s, 5s, 20s	c3r3	$1 \rightarrow 11$	-11.78	4.39	$4.91 \cdot 10^{-3}$	2.26
12	5s, 10s, 20s	c3r3	$1 \rightarrow 11$	-10.96	1.97	$1.63 \cdot 10^{-3}$	1.69
13	2s, 5s, 10s, 20s	c3r3	$1 \rightarrow 11$	-10.93	3.79	$8.34 \cdot 10^{-3}$	1.53
14	2s	c1r2, c2r4, c3r3, c4r1, c5r5	$1 \rightarrow 11$	-10.29	1.91	$1.11 \cdot 10^{-3}$	1.56
15	5s	c1r2, c2r4, c3r3, c4r1, c5r5	$1 \rightarrow 11$	-10.58	1.95	$9.25 \cdot 10^{-4}$	1.42
16	10s	c1r2, c2r4, c3r3, c4r1, c5r5	$1 \rightarrow 11$	-10.79	1.90	$1.13 \cdot 10^{-3}$	1.31
17	20s	c1r2, c2r4, c3r3, c4r1, c5r5	$1 \rightarrow 11$	-11.41	2.94	$2.58 \cdot 10^{-3}$	1.58
18	2s, 5s, 10s, 20s	c1r2	$1 \rightarrow 11$	-11.84	2.84	$4.99 \cdot 10^{-3}$	1.78
19	2s, 5s, 10s, 20s	c1r2, c2r4	$1 \rightarrow 11$	-11.34	2.88	$3.49 \cdot 10^{-3}$	1.58
20	2s, 5s, 10s, 20s	c1r2, c2r4, c3r3	$1 \rightarrow 11$	-11.44	3.46	$2.08 \cdot 10^{-3}$	2.08
21	2s, 5s, 10s, 20s	c1r2, c2r4, c3r3, c4r1	$1 \rightarrow 11$	-10.92	3.61	$4.85 \cdot 10^{-4}$	1.28
22	2s, 5s, 10s, 20s	c1r2, c2r4, c3r3, c4r1, c5r5	$1 \rightarrow 11$	-10.91	4.38	$4.46 \cdot 10^{-4}$	0.00
23	2s, 5s, 10s, 20s	c1r2, c3r3, c5r5	$5 \rightarrow 11$	-11.17	3.18	$2.97 \cdot 10^{-3}$	1.70
24	2s, 5s, 10s, 20s	c1r2, c3r3, c5r5	$1 \rightarrow 4, 6, 8, 10, 11$	-10.96	2.95	$1.48 \cdot 10^{-3}$	1.54
25	2s, 5s, 10s, 20s	c1r2, c3r3, c5r5	$1 \rightarrow 5, 7, 9$	-11.29	3.83	$1.16 \cdot 10^{-3}$	1.94
26	2s, 5s, 10s, 20s	c1r2, c3r3, c5r5	1, 2, 3, 4	-10.86	1.89	$2.21 \cdot 10^{-3}$	1.53
27	2s, 5s, 10s, 20s	c1r2, c3r3, c5r5	5, 7, 9	-11.23	2.70	$4.98 \cdot 10^{-3}$	1.84
28	2s, 5s, 10s, 20s	c1r2, c3r3, c5r5	6, 8, 10, 11	-11.07	1.73	$1.80 \cdot 10^{-3}$	1.81

Part 3

Field studies

6 The DiFeST research site

§

6.1 Introduction

In this part, the field activities and the analysis carried out at the well field of the Department of Physics and Geosciences (DiFeST) are shown. The well field was created for educational purposes, but it represents a very good research site for its location. It consists of eight wells of small diameter; it is provided by electrical supply. Initially, traditional aquifer tests have been performed and compared; then, the Multi-Frequency Oscillatory pumping test (M-OHT) (*Cardiff et al.*, 2013), which represents an innovative procedure, was applied. The traditional equipment is not sufficient for carrying out this new approach, so it was implemented creating a cheap and easy configuration, able to stress the aquifer and collect reliable data. In order to verify goodness of the experimental data and of the data estimated by means of traditional analysis (Theis, Bierchenk, Hantush) a numerical model has been performed. The work presented in this part has been presented at 42^{nd} IAH Congress in *Cupola et al.* (2015e).

6.2 The well field

6.2.1 Location

The test site is located in an alluvial deposit between Parma and Baganza rivers (with a mean elevation of 82 m asl). The eight wells are labeled with S and P. The S are screened between 8 and 11 meters below the ground surface, meanwhile the P are screened over the entire extension of the studied aquifer, which is comprised between 21 and 24 meters. In Appendix D the geologic sections around the site are shown. The two aquifers intercepted are joined upstream, in fact they present very similar water level. The studied aquifer is semi-confined and 3 meters thick (between 21 and 24 meters below the ground surface);

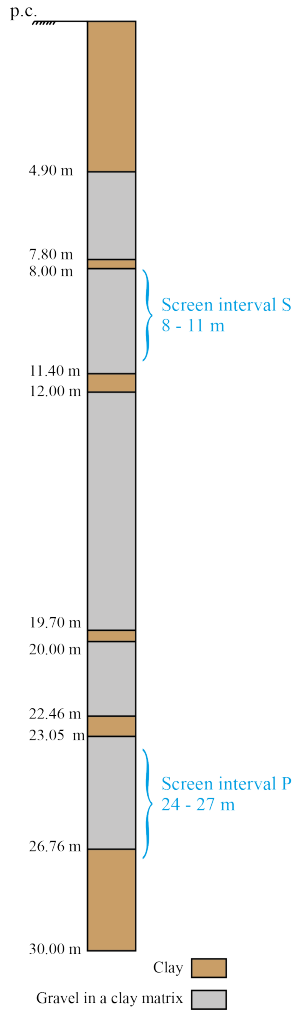

Figure 6.1: Stratigraphy of the well field caught at well P4.

it is mainly constitute by sand comprised between two sandy clay layers. A stratigraphic column showing the vertical sequence of underground materials has been obtained during the drillings at the location P4 (Fig. 6.1). The locations of the wells in the field (in the UTM ED 50 reference system) and their mutual distances, are reported in Figs. 6.2, 6.3, 6.4 and Tables and 6.2.

Figure 6.2: Satellite view of the well field.

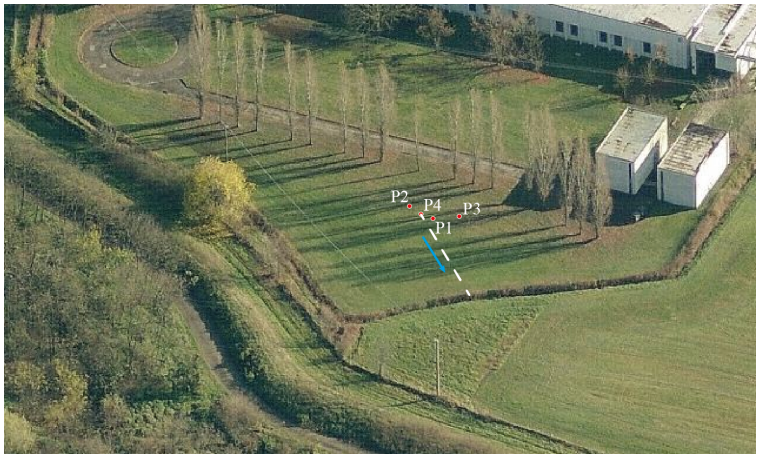

Figure 6.3: View of the well field.

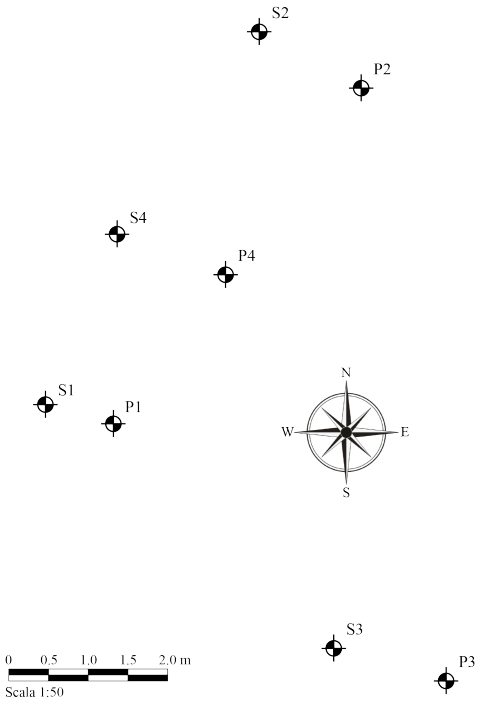

Figure 6.4: Sketch of the well field.

Table 6.1: Wells coordinates.

Point	North [m]	East [m]	Elevation [m a.s.l.]
P1	4957849	603080	82.28
P2	4957853	603083	82.34
P3	4957846	603084	82.38
P4	4957851	603081	82.54
S1	4957849	603079	82.40
S2	4957854	603082	82.28
S3	4957846	603082	82.43
S4	4957851	603080	82.48

Table 6.2: Mutual distances from the wells.

	Distances [m]							
	P1	P2	P3	P4	S1	S2	S3	S4
P1	0.00	5.26	5.30	2.35	0.89	5.28	3.96	2.39
P2		0.00	7.56	2.91	5.63	1.47	7.08	3.58
P3			0.00	5.83	6.13	8.52	1.47	1.46
P4				0.00	2.80	3.09	4.91	1.46
S1					0.00	5.42	4.76	2.33
S2						0.00	7.84	3.12
S3							0.00	5.90
S4								0.00

Table 6.3: Coordinates of the monitoring wells used for recovering the water surface of Fig. 6.6 (in UTM ED 50 reference system). The water level have been collected in May 2012.

RER Code	X [m]	Y [m]	Water table elevation [m a.s.l.]
PR38-00	596340	4961400	49.90
PR47-01	605635	4954195	93.40
PR55-01	611920	4960350	43.32
PR61-05	606730	4949000	130.14
PR69-00	611110	4954445	63.49
PR93-02	606540	4956380	66.36
PRA1-00	602795	4951160	109.80
PRA2-00	596678	4949770	189.96
RE71-00	613499	4948103	92.30

6.2.2 Regional hydrology

With the aim of investigating the groundwater flow in the area where the well field is located, the piezometric data collected by ARPA (Agenzia Regionale Protezione Ambiente), during May 2012, have been used. The location and the data used for recovering the water surface are shown in Fig. 6.5 and Table 6.3. As shown in Fig. 6.6 the flow direction is reasonable, in fact it goes from upstream to downstream, following the flow of Parma and Baganza Rivers. This study has been carried out, also for defining the boundary conditions in the numerical model developed using the software MODFLOW 2005 (Harbaugh, 2005), explained in Chapter 8.

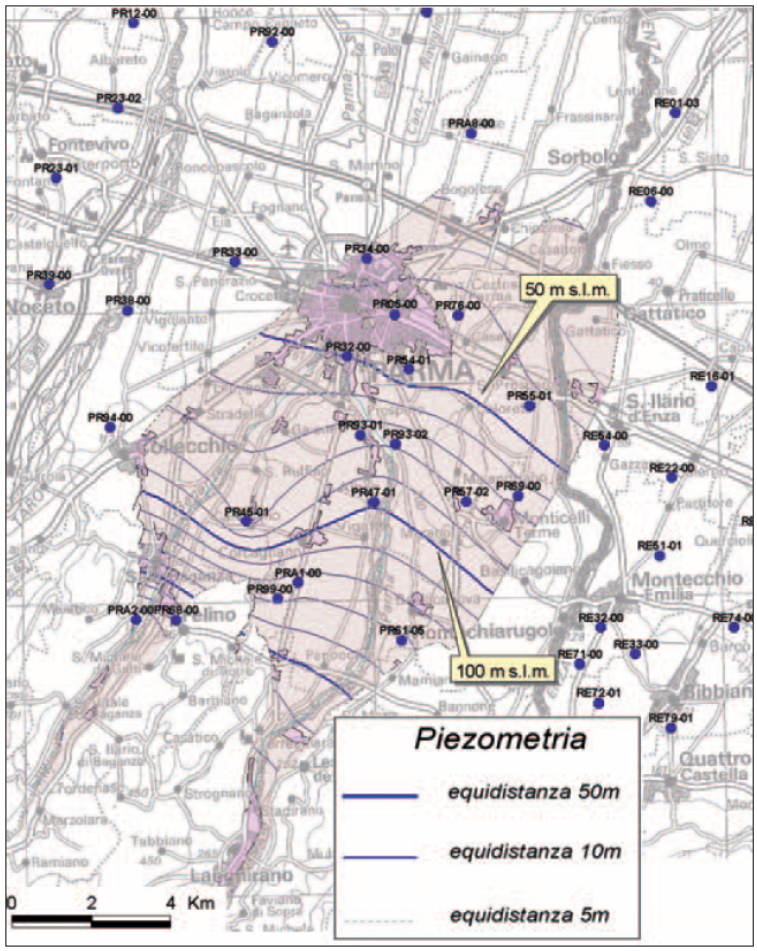

Figure 6.5: Location of the monitoring wells of ARPA. Some of these have been used for estimating the gradient of the groundwater flow. Source: ARPA Emilia Romagna - Conoide del Parma-Baganza

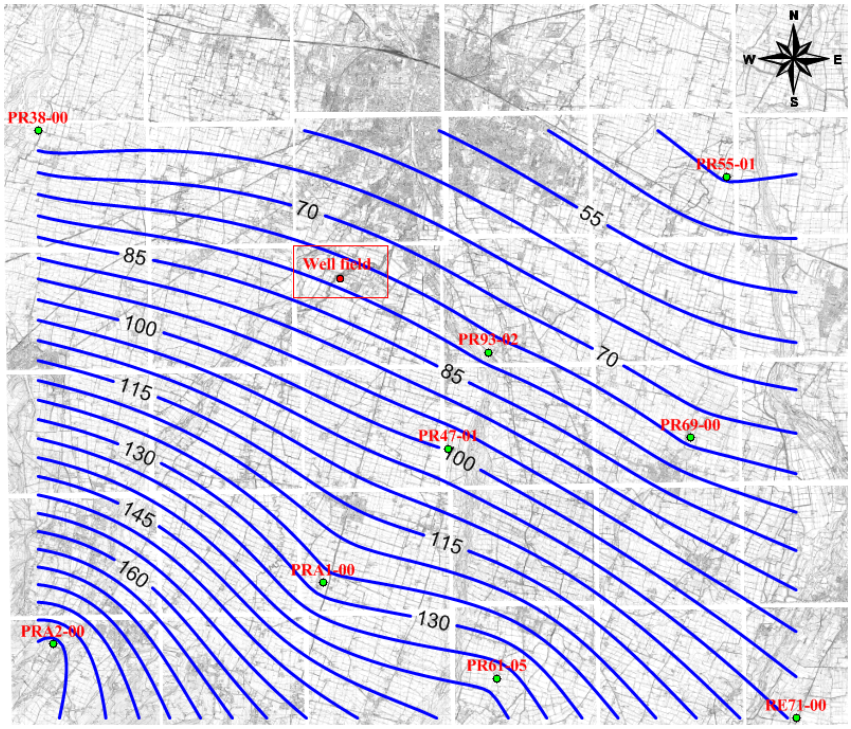

Figure 6.6: Groundwater head (May 2012) based on data of Table 6.3. Unit: m a.s.l..

6.3 Available instruments and capabilities

The well field was equipped with the following instruments:

- 1 submersible pump (*Groundfos SP7-40* with 1.2 kW of power and small diameter (74 mm) able to extract a maximum flow rate of 0.15 m^3/min;
- 5 submersible pressure and temperature probes with integrated data logging;
- 1 magnetic flow meter;
- 1 manual water level meter (contact gauge);

For the Multi Frequency Oscillatory Tomography, other instruments and materials were necessary:

- 1 volumetric pump *Euromatic PVC 500* with 0.37 kW of power and a flow rate of 0.04 m^3/s;

- 1 tank with a volume of about 350 L;

With the above described instruments, in the well field there are the capabilities to conduct traditional pumping tests and sequential tests too (in oscillatory tomographic way). The five pressure probes are permanently installed one for each *P* well (and in one *S* well) and the water levels can be measured and stored with a very small time (up to 1 s) and with settable sampling intervals during the tests. The collected data can be downloaded from the probes via infrared interface (IrDA) or by cable, powered by means of a laptop without the removal of the sensors. The pump *Groundfos SP7-40* has been installed in different locations for collecting data from different points, even if the most meaningful test have been carried out pumping water from well P4. The manual water level meter is useful to set the reference level values of the pressure sensors and to verify their proper operation. More information and data sheets about the instruments are provided in Appendix C.

7 Aquifer characterization

§

7.1 Introduction

Pumping tests are the most common methods involved in the hydraulic characterization of aquifers. Usually a constant rate of water is extracted from a well and the changes in water level (drawdowns) are monitored in one or more observation wells and in the extraction well itself. The hydraulic parameters are then estimated by matching the collected data with analytical solutions developed under several approximation. One of the most important was developed by *Theis* (1935) under transient conditions. In Table 7.2 the tests carried out at DiFeST research site are summarized.

7.2 Traditional aquifer analyses

In Fig. 7.1 an aquifer of thickness b, hydraulic conductivity equal to K and confined by an aquitard of thickness b' and hydraulic conductivity k' is represented. The goal of the aquifer analysis is of estimating K [LT^{-1}], k'[LT^{-1}] and the storativies S[-] and S'[-]. In this first part, the data collected for applying traditional tests (Theis, Hantush and Bierschenk) are reported. For applying these methods several pumping tests have been carried out.

Before starting the tests, the link between the shallow and the main aquifer was not clear and known. So, initially the Theis method was applied, supposing the hydraulic conductivity of the aquitard equal to zero, but then, after some tests, the beahviour of the drawdown in time has made it clear that the studied aquifer is semi-confined and that the hydraulic conductivity K' is not negligible. In Fig. 7.2 the behaviour of three different kind of aquifers is shown.

Table 7.1: Tests summary

Date	Graph	Processing	Numerical model
February 26^{th}, 2015	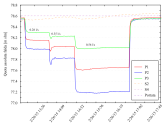		
March 5^{th}, 2015	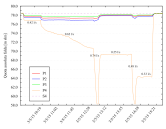		
March 12^{th}, 2015	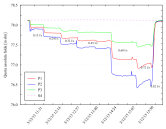		
March 19^{th}, 2015	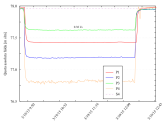		
March 31^{th}, 2015	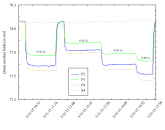		
May 5^{th}, 2015	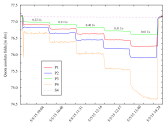	Theis, Biershenk	
May 18^{th}, 2015	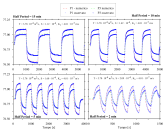	Oscil. pumping test	•
May 25^{th}, 2015	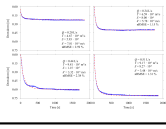	Hantush	•

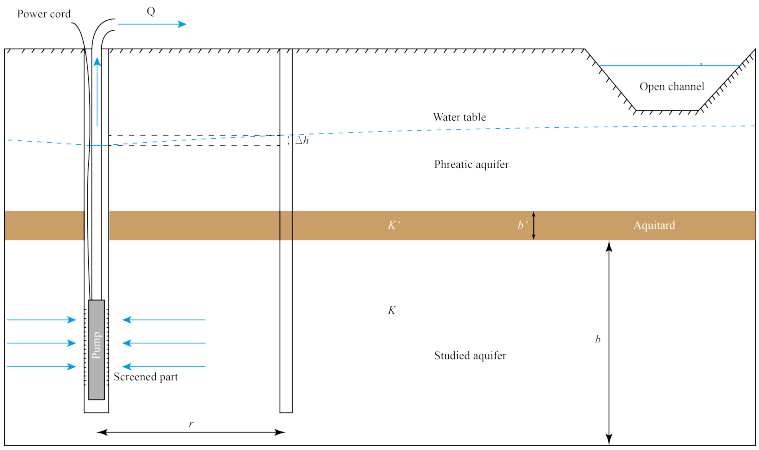

Figure 7.1: Sketch of an aquifer and the meaningful parameter. K is the hydraulic conductivity, K' is the hydraulic conductivity of the aquitard, b and b' are the thickness of the aquifer and of the aquitard. r is the distance between the well and the monitoring well.

7.2.1 Theis method

Theis (1935) was the first that had quantified the drawdown in a confined aquifer due to a pumping test as function of the extracted constant flow rate Q [L^3T^{-1}], the distance r [L] between observation and extraction well and the time t [T]:

$$s(r,t) = \frac{Q}{4\pi T}\int_{r^2 S/4Tt}^{\infty}\left(\frac{e^{-\tau}}{\tau}\right)d\tau \tag{7.1}$$

T[L^2T^{-1}] and S[-] are the transmissivity and the storativity, which represent a measure of how much water can be transmitted horizontally and the volume of water released from storage per unit decline in hydraulic head in the aquifer, per unit area of the aquifer, respectively. The integral expression is known as exponential integral and it is usually indicated as well function $W(u)$. The explicit form of the well function is given by an infinite series:

$$W(u) = \int_{u}^{\infty}\left(\frac{e^{-\tau}}{\tau}\right)d\tau = -0.5572 - \ln u + u - \frac{u^2}{2\cdot 2} + \frac{u^3}{2\cdot 3} + o(u^4)$$

where

$$u = \frac{r^2 S}{4Tt}$$

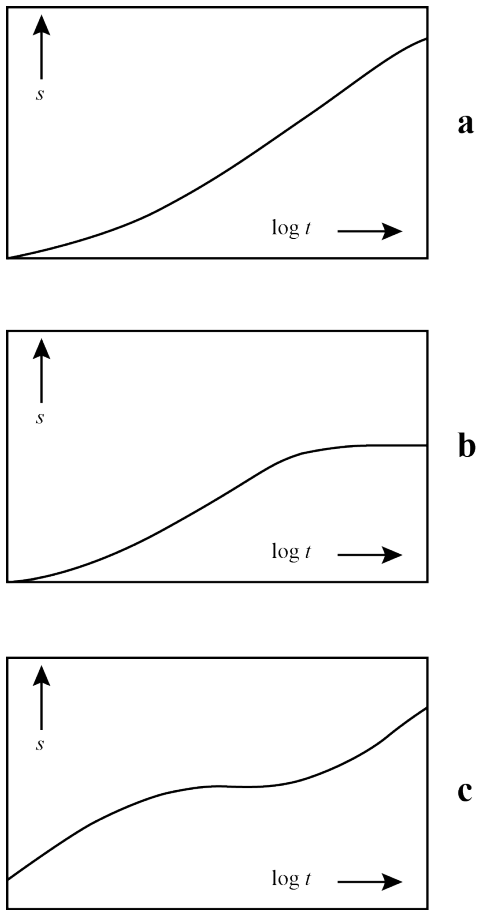

Figure 7.2: Drawdown-log t curves for *a*) confined, *b*) semi-confined and *c*) unconfined aquifer.

is dimensionless and the drawdown can be consequently expressed as:

$$s(r,t) = \frac{Q}{4\pi T} W(u)$$

and $W(u)$ is dimensionless too. The Theis solution (Eq. 7.1) is valid under these assumptions:

1. the aquifer is homogeneous and isotropic;
2. the aquifer has infinite areal extent;
3. the well is fully penetrating

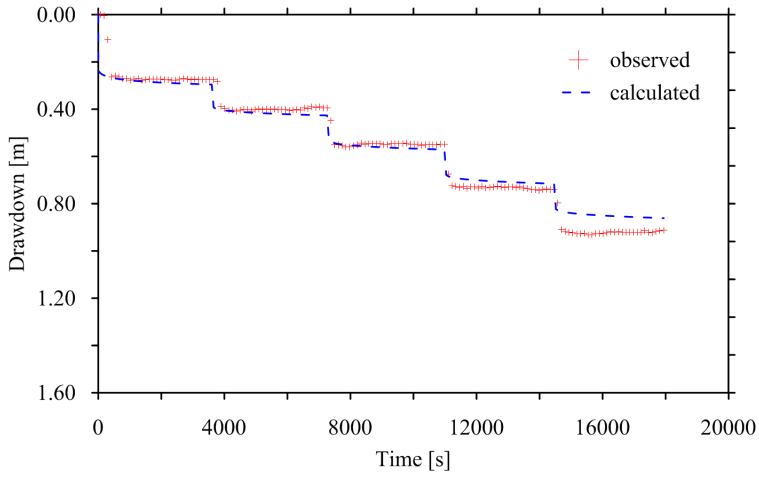

Figure 7.3: Comparison between observed and theoretical drawdown at observing well P1 for all discharges.

4. the diameter of the well is infinitesimal

5. T is constant in time and space

Despite these restrictions, the Theis formula is successfully applied to many groundwater problems.

Assuming that the drawdowns due to a pumping test are known for a given distance from the pumping well and at several times, transmissivity and storativity can be determined through a least square approach that minimize the sum of square differences between observed and theoretical drawdowns:

$$f(t) = \sum_{i=1}^{m} [\bar{s}(r, t_i) - s(r, t_i)]^2 = min$$

where $\bar{s}(r, t_i)$ is the observed drawdown at distance r from pumping well and at time t_i; $s(r, t_i)$ is the theoretical drawdown at same location and time of the observed one, calculated by means of the Theis formula; m is the total number of drawdown data recorded in the observation interval during which the pumping rate remains constant.

As example, in the follow, the application of Theis theory is shown for the test carried out on May 5^{th} (see 7.1). Initially, Theis has been applied for all the duration and for all the pumping rates using the superposition theory (Figs. 7.3 to 7.5); then it has been used for the first step only with a discharge equal to 0.22 L/s (Figs. 7.6 to 7.8).

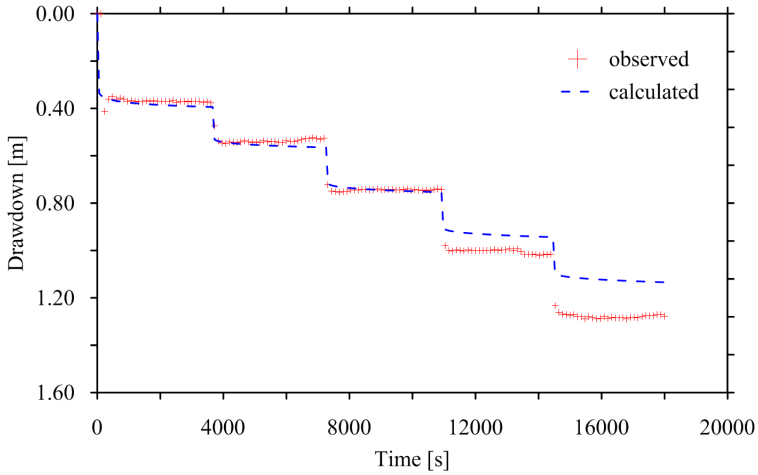

Figure 7.4: Comparison between observed and theoretical drawdown at observing well P2 for all discharges.

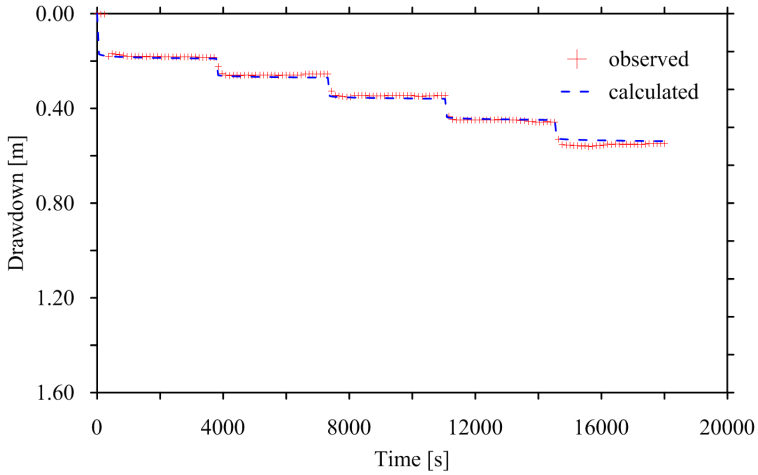

Figure 7.5: Comparison between observed and theoretical drawdown at observing well P3 for all discharges.

Table 7.2: Parameters estimated by Theis method using all discharges. It is clear like the storativity values are not reliable.

	P1	P2	P3
T [m^2/s]	$1.23 \cdot 10^{-3}$	$1.23 \cdot 10^{-3}$	$3.91 \cdot 10^{-3}$
S [-]	$1.78 \cdot 10^{-9}$	$1.16 \cdot 10^{-12}$	$3.83 \cdot 10^{-19}$

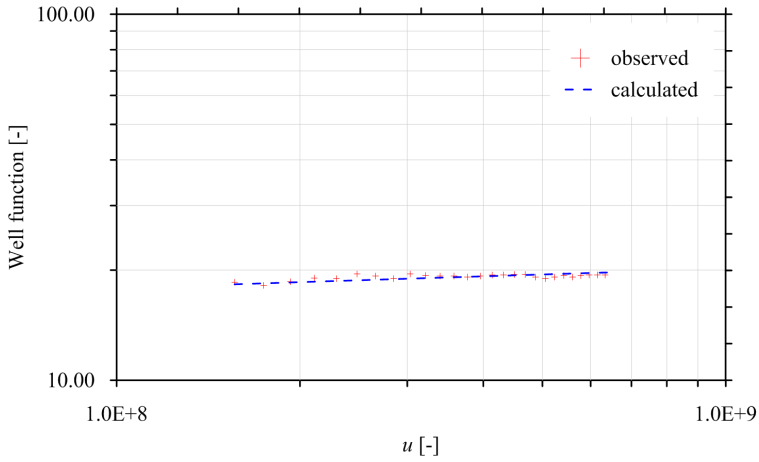

Figure 7.6: Comparison between observed and theoretical drawdown at observing well P1 for the first step only.

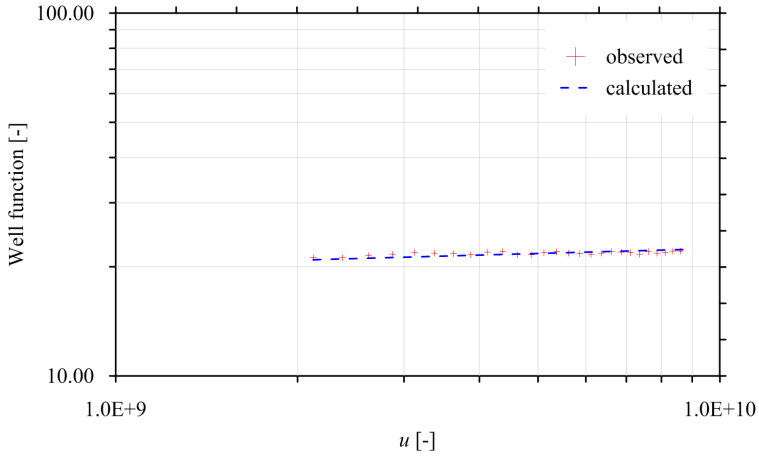

Figure 7.7: Comparison between observed and theoretical drawdown at observing well P2 for the first step only.

Table 7.3: Parameters estimated by Theis method using the first discharge only. Even here, like in Table 7.2, the storativity values are not reliable.

	P1	P2	P3
T [m^2/s]	$1.23 \cdot 10^{-3}$	$1.03 \cdot 10^{-3}$	$2.41 \cdot 10^{-3}$
S [-]	$5.81 \cdot 10^{-9}$	$2.34 \cdot 10^{-10}$	$4.30 \cdot 10^{-12}$

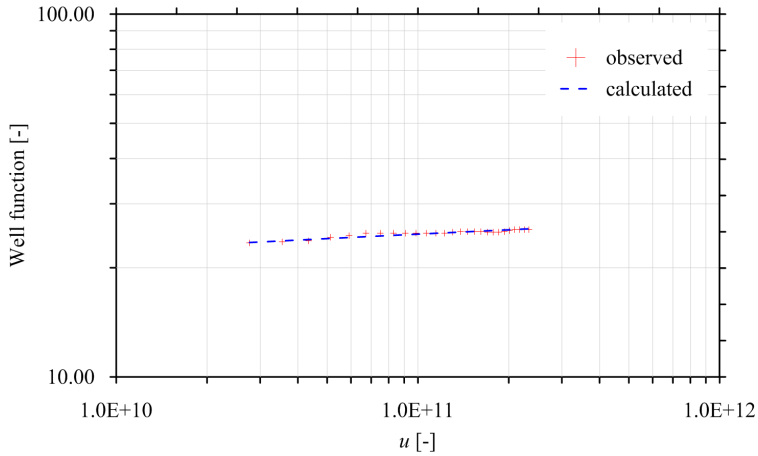

Figure 7.8: Comparison between observed and theoretical drawdown at observing well P3 for the first step only.

7.2.2 Bierschenk method

Some tests have been carried out, pumping different flow rates, for estimating the efficiency of the well. At this aim the Bierschenk method (Bierschenk and William, 1963) has been applied. In such analyses the discharge is incremented step by step, measuring simultaneously the water level. Ideally, the stationary condition has to be reached: however, often this can not be done, due to the slow response of the aquifer. In Fig. 7.9 the test (in term of drawdown) carried out intentionally for applying the Bierschenk method is shown. In general, the total drawdown of an aquifer, due to a well, can be estimated as:

$$s_T = s + s_{wL} + s_p + s_d + s_b - s_r \tag{7.2}$$

where s_T [L] is the total drawdown, s [L] is the head loss due to the laminar flow in the aquifer, s_{wL} is the head loss due to the turbulent flow, s_p is the head loss due to the partial penetration of the well in the aquifer, s_d is the head loss due to the dewatering, s_b takes in the account the finited dimensions of the aquifer and s_r represents the recharge of the aquifer. In the practical applications, the only significant terms of Eq. 7.2 are s (linearly dependent from Q) and s_{wL} (quadratic respect Q) which can be calculated respectively as:

$$s = BQ$$

and

$$s_{wL} = CQ^2$$

where Q [L^3T^{-1}] is the pumping rate, B [$L^{-2}T$] and C [$L^{-5}T^2$] are two parameters dependent from the characteristic of the aquifer and the well). So, Eq. 7.2 becomes

$$s_T = BQ + CQ^2 \tag{7.3}$$

where BQ represents the drawdown due to formation loss and CQ^2 represents the drawdown due to the well loss. The efficiency of the well may be defined as BQ/s_T. The efficiency of a well is governed largely by the magnitude of a well loss and thus falls rapidly as discharge is increased. The efficiency of a well in an aquifer having an high transmissivity is affected by well loss to a greater degree than the efficiency of a well in an aquifer having a low transmissivity, and it is least affected by partial penetration of aquifers having a large transmissivity. Eq. 7.3 can be rewritten as

$$s_T/Q = B + CQ^2$$

If the data collected during a pumping test are plotted in the space s_T/Q vs Q, the slope and the intercept with the y axis represent the C and B respectively. According with Walton (1962) if:

- $C < 1900$ s^2/m^5 the well is good
- $1900 < C < 3800$ s^2/m^5 the well is partially obstructed or damaged
- $3800 < C < 15000$ s^2/m^5 the well is very obstructed or damaged
- $C > 14400$ s^2/m^5 the well is obstructed and no more useful

Once, B and C are calculated, the efficiency of the well can be estimated as

$$e = \frac{BQ}{(BQ + CQ^2)} \cdot 100 \tag{7.4}$$

In the follow the graphical and numerical results for the tests carried out on May 5^{th} are reported. In this test four different pumping rates have been used: this has allowed to test the well in different situations.

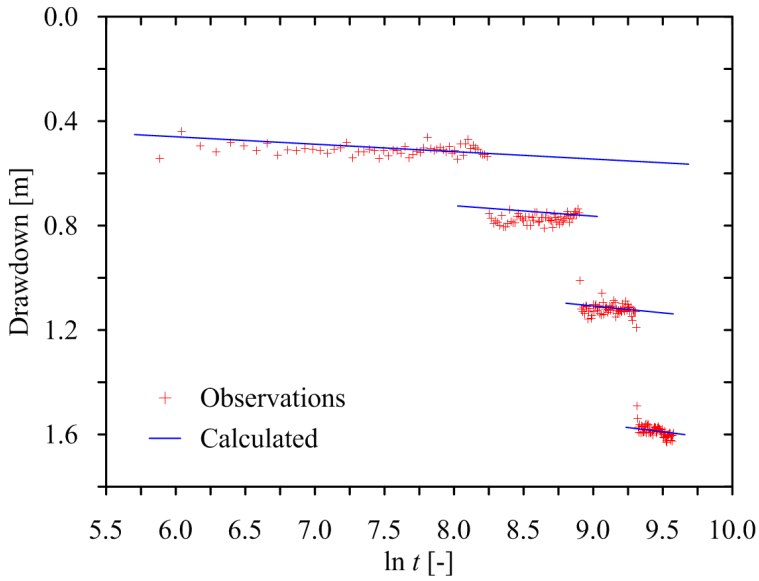

Figure 7.9: Drawdown *vs* ln(t).

Table 7.4: Data used for applying Bierschenk method.

Discharge [L/s]	Water table elevation [m a.s.l]	Δs_i [m]	Drawdown s_T	s_T/Q [s/m^2]
0.22	77.16	0.52	0.52	2349
0.31	76.64	0.22	0.73	2365
0.41	76.40	0.35	1.08	2634
0.51	76.03	0.46	1.54	3012

Looking at Fig. 7.10, the coefficients B and C of Eq. 7.4 are respectively $B = 2348419.32$ [s^2/m^5] and $C = 1738.29$ [s/m^2]. The calculation B and C has allowed the estimation of the efficiency of the well for the different pumping rates adopted during the test (Eq. 7.4).

Looking at Table 7.5 one can notice that the efficiency is low, even using the lowest pumping rate. This means that the behavior of the well is reliable only for small values of discharges.

7.2.3 Hantush

One of the most important hypothesis of Theis solution is that the water pumped is removed from storage within the aquifer. But this can not be true in several situations,

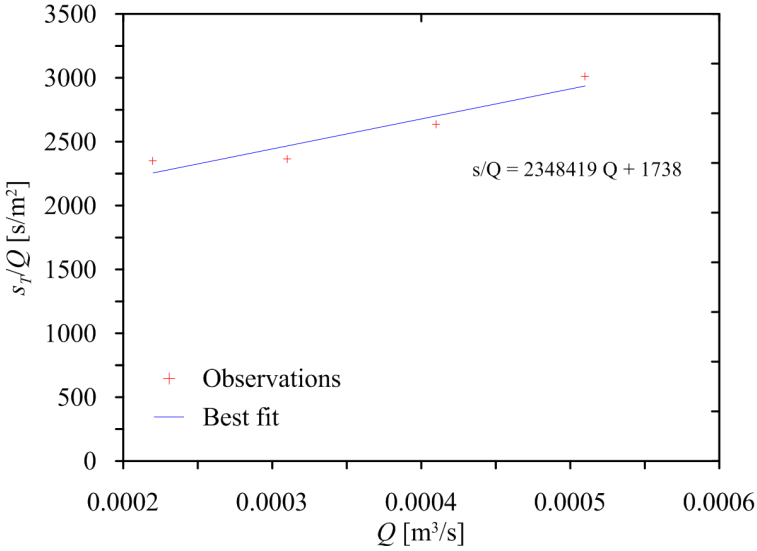

Figure 7.10: Graph used for estimating the parameters for the estimation of the efficiency of the well.

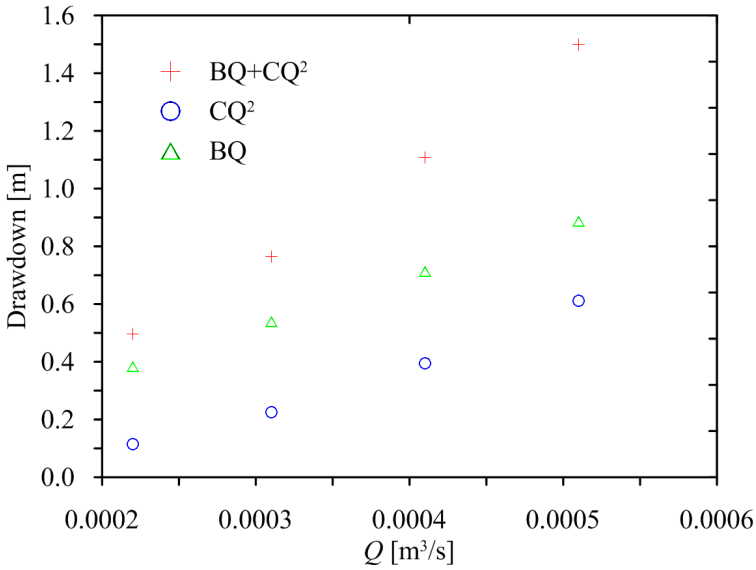

Figure 7.11: Behaviour of the different components used for the calculation of the efficiency.

Table 7.5: Calculation of the efficiency of the well.

Q [L/s]	s/Q	BQ [m]	CQ^2 [m]	$BQ + CQ^2$	e [%]
0.22	2349.16	0.382	0.113	0.496	77
0.31	2364.82	0.539	0.225	0.769	70
0.41	2634.41	0.712	0.394	1.114	64
0.51	3012.38	0.886	0.610	1.658	59

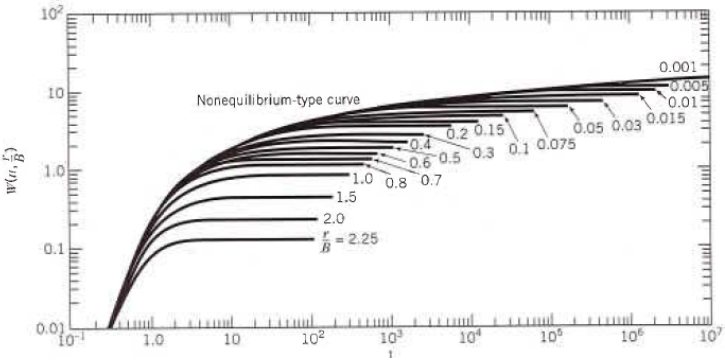

Figure 7.12: Type curve for leaky aquifers (from Domenico and Schwartz (1990)).

such as direct recharge to the aquifer from streams, direct recharge across bounding low-permeability materials etc.. The problem of leakage has been extensively investigated by *Hantush and Jacob* (1955) and *Hantush* (1956, 1960, 1964). The typical response at an observation well in a leaky aquifer in which water can be transmitted across the low-permeability boundaries is represented in Fig. 7.2b. A method for analyzing the drawdown curve in leaky aquifers requires a curve-matching procedure where the drawdown for all time is given by

$$s = \frac{Q}{4\pi T} W\left(u, \frac{r}{H}\right) \tag{7.5}$$

where $W(u, r/B)$ is the tabulated well function for leaky aquifers.

The family of curves (Fig. 7.12) converges on the non-leaky curve for small values of $1/u$ (which correspond to small values of time) and small of r/H. Moreover, the coefficient

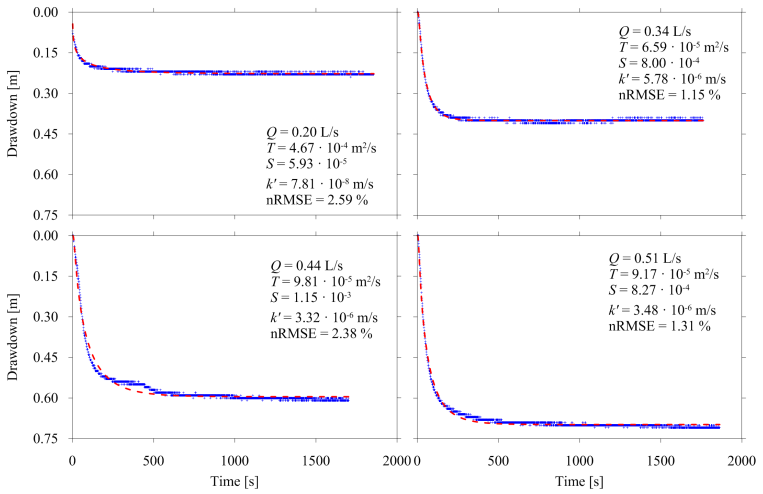

Figure 7.13: Observed (blue cross) and analytical (red dotted line) drawdown at monitoring well P1 through Hantush theory.

of vertical hydraulic conductivity can be determined from the relationship

$$\frac{1}{H} = \left(\frac{k'/m'}{T}\right)^{1/2} \tag{7.6}$$

where H [L] is the thickness of the aquifer, m' [L] is the thickness of the bounding low-permeability formation, and k' [LT^{-1}] is the vertical hydraulic conductivity of the aquitard.

This method has been applied to the test carried out on May 25^{th}. The estimation of the transmissivity, of the storage and, in this case, of the vertical hydraulic conductivity of the aquitard has been made, initially at each observation well and then, combining together the data collected at every location for every different discharge. One can notice (see Figs. from 7.13 to 7.19) that the calculated drawdown fits very well the observed one and then the magnitude of the transmissivity and of the storage is consistent with the materials. Regarding the value of k', the order of magnitude is three order lower than the aquifer (see Tables 7.6 and 7.7), which is not negligible: its value supports the hypothesis that the aquifer is recharged across the boundaries.

7.3 Multi Frequency oscillatory pumping test

The multi frequency oscillatory pumping tests (*Cardiff et al.*, 2013) represent a new approach which allows to stimulate the aquifer with different stress signals. In particular,

Table 7.6: Parameters estimated by Hantush method at each monitoring well and using every discharge.

	$T \cdot 10^{-4}$ [m^2/s]			$S \cdot 10^{-4}$ [-]			$c \cdot 10^{5}$ [s]			$k' \cdot 10^{-6}$ [m/s]		
Q [L/s]	P1	P2	P3	P1	P2	P3	P1	P2	P3	P1	P2	P3
0.20	4.67	2.80	3.59	0.59	0.54	1.21	76.8	50.8	25.9	0.78	1.18	2.31
0.34	0.66	0.99	1.69	8.00	2.13	2.11	1.04	4.01	6.21	57.9	15.0	9.66
0.44	0.98	1.17	1.91	11.5	3.34	2.98	1.81	7.71	9.15	33.2	7.78	6.56

Table 7.7: Parameters estimated by Hantush method at each monitoring well grouping data from different discharges.

$T \cdot 10^{-4}$ [m^2/s]			$S \cdot 10^{-4}$ [-]			$k' \cdot 10^{-6}$ [m/s]			nRMSE		
P1	P2	P3	P1	P2	P3	P1	P2	P3	P1	P2	P3
1.02	1.31	1.99	9.00	2.13	2.43	3.42	0.67	0.66	0.05	0.05	0.03

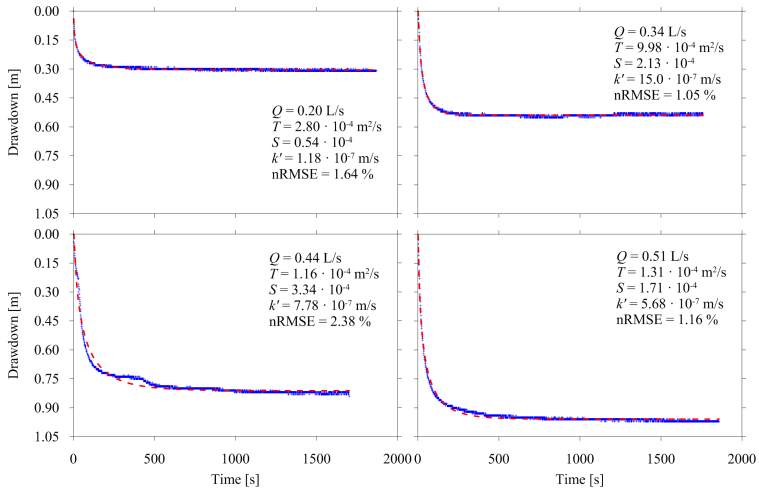

Figure 7.14: Observed (blue cross) and analytical (red dotted line) drawdown at monitoring well P2 through Hantush theory.

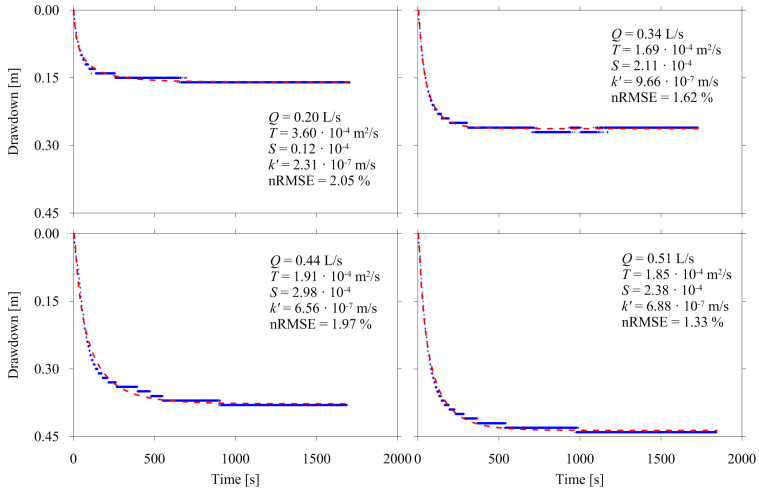

Figure 7.15: Observed (blue cross) and analytical (red dotted line) drawdown at monitoring well P3 through Hantush theory.

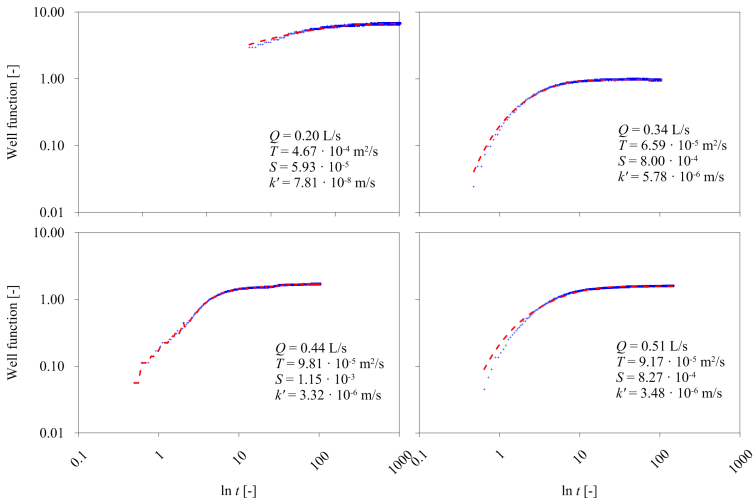

Figure 7.16: Experimental (blue cross) and analytical (red dotted line) well function at monitoring well P1 through Hantush theory.

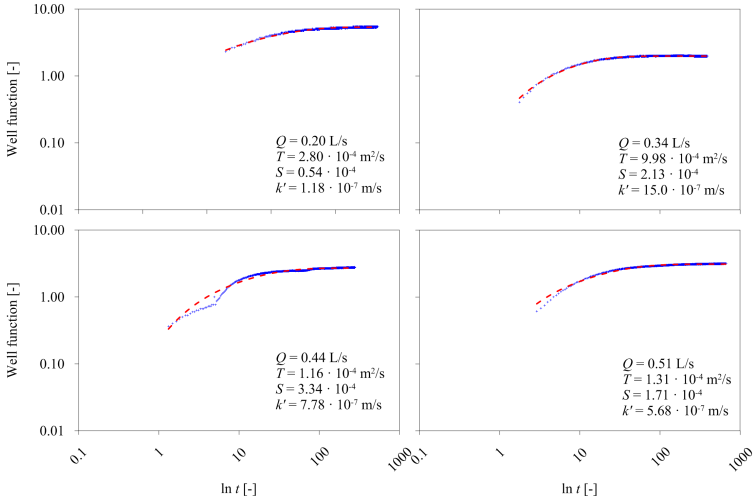

Figure 7.17: Experimental (blue cross) and analytical (red dotted line) well function at monitoring well P2 through Hantush theory.

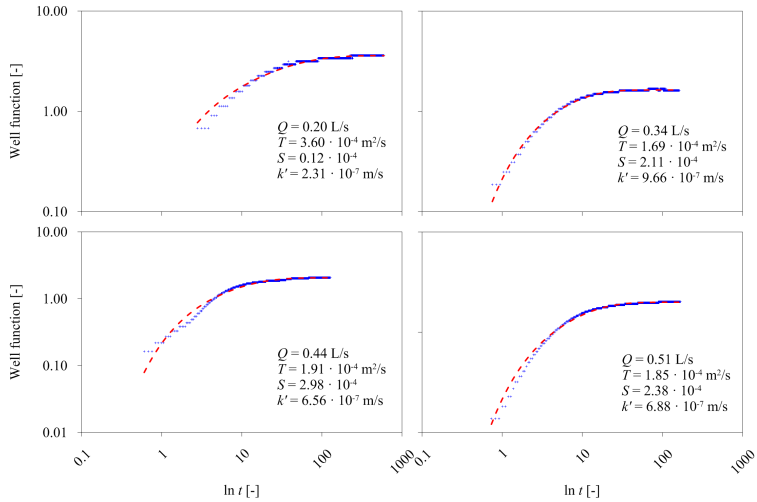

Figure 7.18: Experimental (blue cross) and analytical (red dotted line) well function at monitoring well P3 through Hantush theory.

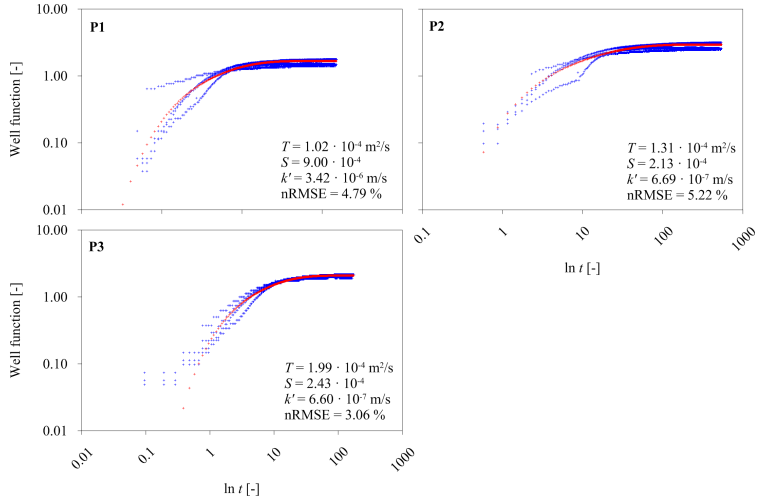

Figure 7.19: Experimental (blue cross) and analytical (red dotted line) well function grouping data from different discharges.

stimulating the aquifer with a periodic signals, the data in term of amplitude and phase offset at the different monitoring points can give an information about the hydraulic structure. Different square waves have been used at the research site of the DiFeST, thus the head has been recorded at the well and at the monitoring points. The difference of amplitude and phase between the well and the receivers depend by the distance and by the hydraulic properties of the aquifer.

For doing these kind of tests the water has been injected and extracted in a periodic way. For injecting the water the pump EUROMATIC PVC 500 has been used (see Appendix C). During these tests there is the necessity to store the water: at this aim a tank (Fig. 7.20) of about 400 L has been used and the water level inside has been recorded by using a pressure probe of the same kind of those installed at the monitoring wells. All the variable have been acquired with a frequency of 1 Hz, which can be considered an high frequency for pumping tests. In Fig. 7.21 the scheme of the equipment used during the oscillatory pumping tests is shown.

In Fig. 8.5 the data collected during the test carried out on May 18^{th} are reported with those simulated with the numerical model. The semi-periods of 15, 10, 5 and 2 minutes have been tested. During the experiments it was noticed that the period of 1 minute is too short for ensuring a good accuracy in the operations of closing and opening of the valves.

Figure 7.20: Tank used for storing the water during the oscillatory pumping tests.

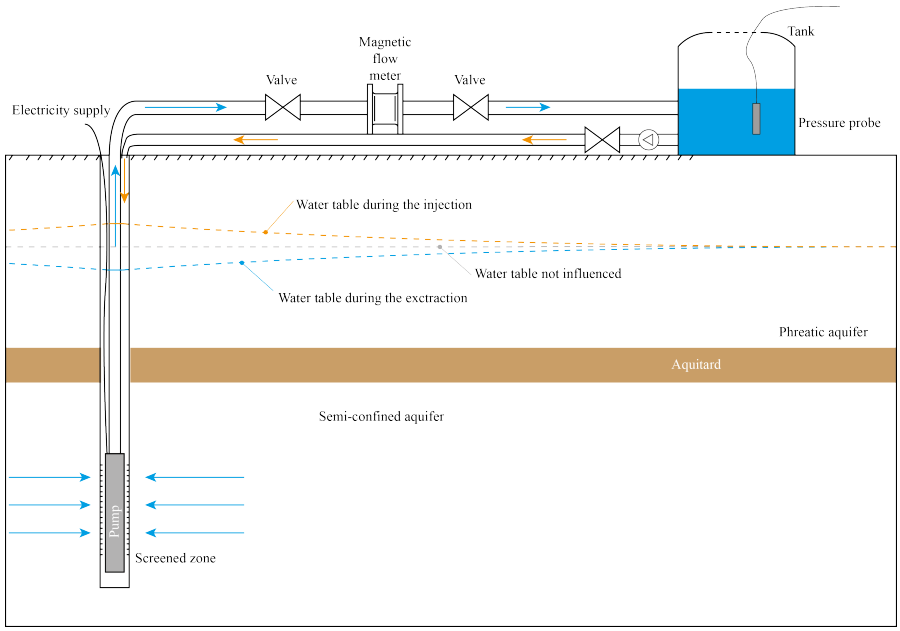

Figure 7.21: Scheme of the uipment used during the oscillatory pumping tests.

8 Forward model

§

8.1 Model grid

A numerical model able to reproduce the observed values at the same locations and times for each pumping tests is often necessary. In these studies the forward model is MODFLOW 2005 (*Harbaugh*, 2005). The dimension of the model was based on the study about the regional groundwater head shown in Fig. 6.6. So, the model is oriented along the flow direction and it is centered in the well P4. A constant head was considered at the North-East and South-West boundaries in such a way that the gradient respects the one estimated in Fig. 6.6. At the other boundaries a no-flow condition was imposed. The dimension of the grid is 530 m $\times$ 350 m; initially a smaller dimension was tested, but, in that case, the boundary conditions influenced the results in an unacceptable way. The use of a fine grid over the entire domain was computationally heavy so a mesh refinement procedure was used to better detail the model in the area of the well field. Figs. 8.1 and 8.2 show the extent of the model and a detail around the well field where the grid is regular and refined (20 cm $\times$ 20 cm). The model has three layers (Fig. 8.3). The first one is 22.46 m thick (from 82.2 to 59.74 m a.s.l.), the aquitard is 0.6 m thick and the main aquifer is 3.71 m thick with the bottom level at 55.44 m a.s.l.. A summary of the characteristics of the model is tabulated in Table 8.1.

In the next sections will be presented the main results for two different tests (May 18^{th} and 25^{th}).

8.2 Numerical results: May 25^{th}

In order to verify the reliability and the goodness of the numerical model, the data of May 25^{th} were reproduced. An analysis of those data through Hantush theory is presented in

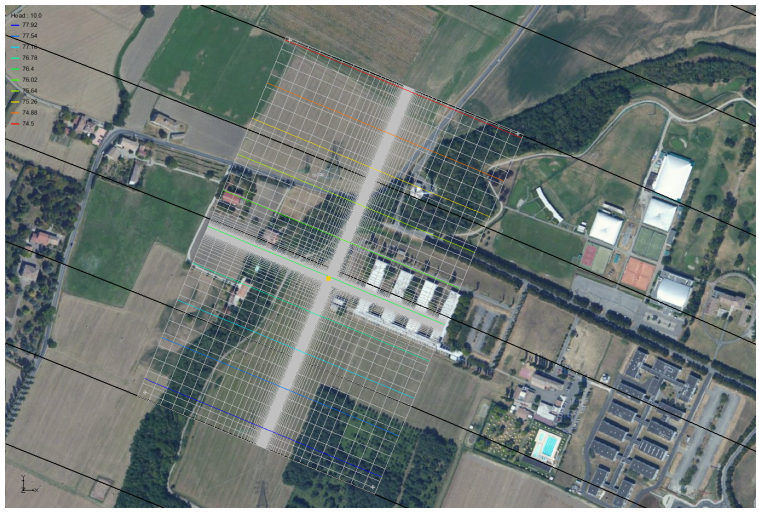

Figure 8.1: Extent of the model.

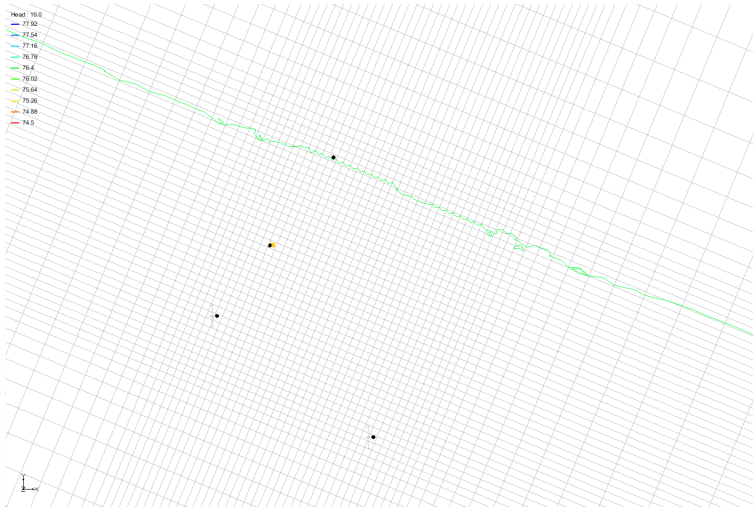

Figure 8.2: Grid around the well field.

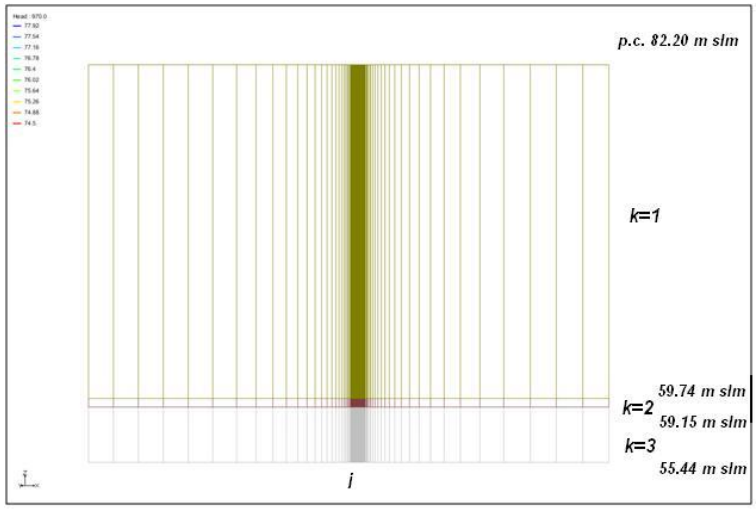

Figure 8.3: Vertical section of the numerical model.

Table 8.1: Characteristics of regional model and local model.

Longitudinal extent x [m]	530
Transversal extent y [m]	350
Vertical extent z [m]	26.76
Numbers of cells in x-direction	105
Numbers of cells in y-direction	93
Number of cells in z-direction	3
Minimum grid spacing [m]	0.20
Maximum grid spacing [m]	20
Hydraulic gradient [%]	0.75

Section 7.2.3. During the different tests (not shown here for brevity) it was clear how the data collected at well P2 were not reliable, probably for construction problems. So in this analysis only the data collected at well P1 and P3 were used. All the forward runs were performed in two stress periods: the first steady and the second transient with a duration of 1200 s (with a time step of 10 s). The hydraulic conductivity values of the confined aquifer were estimated by means of PEST (Parameter ESTimation) (*Doherty*, 2008), starting from an initial value given by the Hantush analysis. As shown in Fig. 8.4, the numerical curves reproduce very well the observed data for every flow rate. A summary of the parameter values estimated for the test carried out on May 25th is tabulated in Table 8.2.

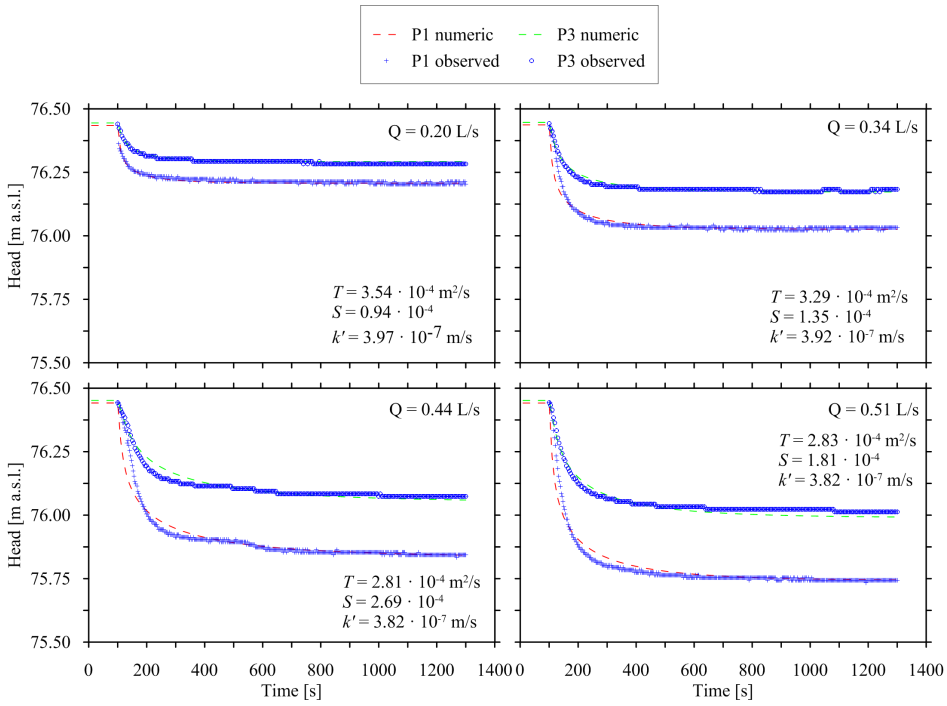

Figure 8.4: Comparison between numerical and observed data.

Table 8.2: Parameters estimated through PEST for the test of May 25^{th}.

Q [L/s]	$T \cdot 10^{-4}$ [m^2/s]	$S \cdot 10^{-4}$ [-]	$k' \cdot 10^{-7}$ [m/s]
0.20	3.54	0.94	3.97
0.34	3.29	1.35	3.92
0.44	2.81	2.69	3.82
0.51	2.83	1.81	3.82
Mean value	**3.12**	**1.70**	**3.88**

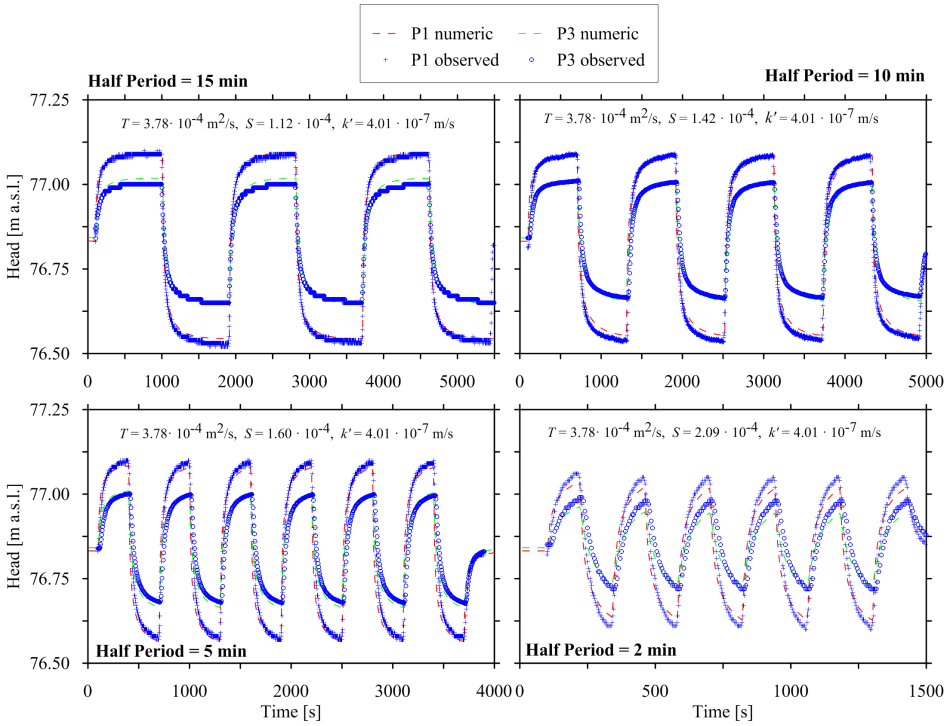

Figure 8.5: Comparison between numerical and observed data for the oscillatory pumping test.

Table 8.3: Parameters estimated through PEST for the test of May 18th.

Half period [min]	$T \cdot 10^{-4}$ [m^2/s]	$S \cdot 10^{-4}$ [-]	$k' \cdot 10^{-7}$ [m/s]
15	3.78	1.12	4.01
10	3.78	1.42	4.01
5	3.78	1.60	4.01
2	3.78	2.09	4.01
Mean value	**3.78**	**1.56**	**4.01**

8.3 Numerical results: May 18th

A second simulation has been performed considering the oscillatory pumping test carried out on May 18th. In particular, all the periodic signals were simulated with very good results. In this case, the simulation has been divided in several stress periods, one for each semi-period. Like in Sec. 8.2, the first stress period was in steady state condition. Fig. 8.5 shows the good agreement between numerical and observed data.

9 Conclusions

The work reported in this part allowed to estimate the hydraulic parameters of the DiFeST research site. The well field consists of eight wells, but only those screened in the deeper part have been considered. After some tests and some traditional analysis, the initial hypothesis of confined aquifer proved wrong; instead, the Hantush analysis showed that the aquifer is semi-confined. Some oscillatory pumping tests were performed extracting and re-injecting the water, stressing the aquifer with a square wave with a semi-period equal to 20, 15, 10, 5 and 2 minutes. An easy and cheap equipment has been configured for carrying out these activities. In order to reproduce the observed data, a numerical model has been performed. It covers an area of 530 m $\times$ 350 m and it has an irregular grid, finer around the well field. It presents three layers, in which the deepest one has been investigated during the field activities. It is able to well reproduce even the data collected during the oscillatory pumping tests. The value of transmissivity and storativity estimated in the different tests are similar to each other and they are consistent with those estimated through the numerical model ($T = 3.00 \cdot 10^{-4}$ m^2/s and $S = 1.90 \cdot 10^{-4}$). It is important to note that the Hantush analysis have allowed to estimate also the vertical permeability of the aquitard which separates the superficial and the investigated aquifer ($k' = 3.88 \cdot 10^{-4}$ m/s). During the tests, the data collected at well P2 were not consistent with the others, revealing an abnormal behavior. The Bierschenk analysis has allowed to calculate the efficiency of the well, which is very low (77% with a pumping rate of 0.20 L/s).

Part 4

Numerical studies

10 Application and extension of the Minimum Relative Entropy Method

§

10.1 Introduction

The interest in approaches that allow the estimation of pollutant source release in groundwater has increased exponentially over the last decades. This is due to the large number of groundwater reclamation procedures that have been carried out and the related costs that can easily be shared among the different actors if the release history is known. Moreover a reliable release history can be a useful tool for predicting the plume evolution, its concentration and the potential natural attenuation. Several methodologies were developed in the '90s to estimate the release history of a pollutant source for simple cases (1-D homogeneous aquifer) through a maximum likelihood (*Wagner*, 1992), the Thikonov regularization (*Skaggs and Kabala*, 1994), a minimum relative entropy method (*Woodbury and Ulrych* 1993, 1996), and a geostatistical approach (*Snodgrass and Kitanidis*, 1997). All these methods recover the release history of a pollutant at a certain source location starting from the observation of several concentrations in the groundwater at a specific sampling time T.

The principle of minimum relative entropy (MRE) was introduced by *Kullback* (1959) and was used in several different fields (from geophysics to information theory). *Woodbury and Ulrych* (1993, 1996) applied the MRE approach to recovering the contaminant release history in aquifers. *Woodbury et al.* (1998) then extended the MRE approach to recovering a three-dimensional plume source within a constant velocity field and constant dispersivity value using the analytical solution of the transport equation developed by *Domenico and Schwartz* (1990). *Neupauer et al.* (2000) made a comparison between the

MRE approach and the Thikonov regularization proposed by *Skaggs and Kabala* (1994). *Neupauer and Borchers* (2001) developed a Matlab code which applies the MRE method on a 1-D synthetic field, also investigating the sensitivity of the results to the input parameters. *Ulrych and Woodbury* (2003) verified the approach by using noisy data.

Due to the linearity of the governing differential equations of the transport problem, the afore mentioned methods adopt the convolution integral approach (*Jury and Roth*, 1990), in which the concentration at a time and at a point of the domain is due to the integral of the mass release history at the source location multiplied by the transfer functions (TFs) that describe the effect in time, at a certain location of the aquifer, of an impulse release of a pollutant at its source. The TF can be analytically determined if the flow field is very simple (*Skaggs and Kabala*, 1994; *Woodbury and Ulrych*, 1996; *Snodgrass and Kitanidis*, 1997; *Butera and Tanda*, 2003), but in many practical applications, the characteristics of the groundwater flow field (conditioned on local heterogeneities, pumping wells, complex boundary conditions, etc.) do not allow an analytical formulation of the TF (*Butera et al.*, 2006, 2013). At this aim, numerical procedures to compute the TF have to be developed (*Neupauer et al.*, 2000; *Michalak and Kitanidis*, 2004; *Butera and Tanda*, 2006; *Sun et al.*, 2006); among these the stepwise input function (SIF) procedure, introduced by *Butera et al.* (2006, 2013), has been adopted in the present study. The SIF procedure was successfully applied to compute the TFs considering 2-D synthetic homogeneous and heterogeneous aquifers (*Butera et al.*, 2006, 2013), using data obtained from a laboratory device (*Cupola et al.*, 2015a) and using field data (*Gzyl et al.*, 2014).

The objectives of the present work are to:

1. extend the application of the MRE approach to contaminant release identification, developed by *Woodbury and Ulrych* (1993, 1996), to 2-D heterogeneous aquifers using as observations several concentration values at different observation points at a given time;

2. extend the application of the MRE approach to contaminant release identification to heterogeneous multidimensional aquifers with availability of concentration values in few observation points at several monitoring times;

3. analyze the performance of the MRE method, applied to contaminant release estimation, varying the prior information.

Before analyzing the heterogeneous cases we have verified the procedure by investigating case studies in a 2-D aquifer characterized by homogeneous hydraulic conductivity and uniform flow field, and in this paper we report the results of the application of the proposed method in four case studies: two homogeneous (HO1 and HO2) and two heterogeneous synthetic aquifers (HE1 and HE2). The results provide an evaluation of the influence of the heterogeneities on the solution of the inverse problem.

The work presented in this chapter has been published in *Cupola et al.* (2015b) and presented at 2014 AGU Fall Meeting in *Cupola et al.* (2014).

10.2 Mathematical Statements

The study of the flow and transport phenomenon in aquifers has been already reported in Chapter 1. All the symbols refer to that chapter.

10.2.1 Minimum relative entropy theory

The core of the method is the Minimum relative entropy (MRE) inversion developed by *Woodbury and Ulrych* (1993, 1996), which is briefly summarized in the following. Considering $p(\mathbf{y})$ as a priori estimation of $q(\mathbf{y})$, which is the multivariate probability density function (pdf) of occurrence of event $\mathbf{y} = (y_1, ..., y_j, ..., y_N)$, the entropy of $q(\mathbf{y})$ relative $p(\mathbf{y})$ can be calculated as

$$E(q, p) = \int q(\mathbf{y}) \cdot \ln \left[\frac{q(\mathbf{y})}{p(\mathbf{y})} \right] \cdot d\mathbf{y} \tag{10.1}$$

The goal is to calculate the posterior pdf $q(\mathbf{y})$ considering:

$$\int q(\mathbf{y}) \cdot d\mathbf{y} = 1 \tag{10.2}$$

where the integration is over the full range of the random variable $\mathbf{y}$ and information given in the form of expected value

$$\int q(\mathbf{y}) \cdot w_i(\mathbf{y}) \cdot d\mathbf{y} = \bar{w}_i \tag{10.3}$$

where $w_i(\mathbf{y})$ and $\bar{w}_i$ are known and the index i goes from 1 to M which represents the number of known data (in this case is the number of observations). So, posterior estimate $q(\mathbf{y})$ assumes the form (for more details about mathematical statement, see *Woodbury and Ulrych*, 1993)

$$q(\mathbf{y}) = p(\mathbf{y}) \cdot \exp \left[-1 - \mu - \sum_{i=1}^{M} \lambda_i w_i(\mathbf{y}) \right] \tag{10.4}$$

where μ and λ_i are Lagrange multipliers determined by Eqs. 10.2 and 10.3. Therefore, the calculation of the multipliers is essential to estimate the posterior pdf.

10.2.2 Inverse problem

For the case of a non-sorbing, non-reactive solute, the relationship between the concentrations observed at monitoring points and the release history is linear

$$\mathbf{z} = \mathbf{H} \cdot \mathbf{s} \tag{10.5}$$

where $\mathbf{z}$ ($M\times 1$ is an M known vector of observations, $\mathbf{s} = (s_1, ..., s_j, ...s_N)$ is the $(N\times 1)$ vector of unknown, and $\mathbf{H}$ $(M \times N)$ is the transfer matrix which describes the relation between unknowns and observations and it is defined as Eq. 4.10. For the calculation of the Transfer functions has been adopted the SIF procedure described in Section 4.2. The goal is to obtain an estimate $\hat{\mathbf{s}}$ $(N \times 1)$ of $\mathbf{s}$ that satisfies Eq. 10.5. Eq. 10.5 can also be written in discretization form

$$z_i = \sum_{j=1}^{N} f_{ij} \cdot s_j \tag{10.6}$$

where $j = 1,...,N$ is the index of the j-th unknown and f_{ij} is the shortened form of $f(\mathbf{x}_i, T-j\Delta t)$. Let $\hat{\mathbf{s}}$ be the expected value of random vector $\mathbf{s}$; it can be calculated as: $\hat{\mathbf{s}} = \int_M \mathbf{s} \cdot q(\mathbf{s})d\mathbf{s}$; consequently Eq. 10.6 becomes

$$z_i = \int_M q(\mathbf{s}) \left[\sum_{j=1}^{N} f_{ij} \cdot s_j \right] \tag{10.7}$$

where $q(\mathbf{s})$ is the pdf of $\mathbf{s}$ and the integration is over all the allowed values of $\mathbf{s}$. Eq. 10.7 can be rewritten in the form of 10.3, where z_i corresponds to the known observation $\bar{w}_i$ and $\sum_{j=1}^{N} f_{ij} \cdot s_j$ corresponds to $w_i(\mathbf{y})$. *Woodbury and Ulrych* (1996) constrained the value of $\mathbf{s}$ in the range ($\mathbf{L}$, $\mathbf{U}$). This knowledge a priori is used to define a joint Boxcar pdf (uniform distribution between an upper and lower bound). The Boxcar pdf, $b(\mathbf{s})$, is defined as

$$\begin{cases} b(s_j) = (U_j - L_j)^{-1}\ ,\ L_j \le s_j \le U_j \\ b(s_j) = 0\ ,\ otherwise \end{cases} \tag{10.8}$$

where L_j and U_j are the individual lower and upper bounds. In this work the lower and upper bounds are considered constant for each j. Let $\mathbf{r}$ be the expected value vector of a pdf $p(\mathbf{s})$ which is chosen in such a way that it has minimum relative entropy to a Boxcar pdf, subject to the expected value constraints, $\hat{\mathbf{r}} = (\hat{r}_1, ..., \hat{r}_j, ...\hat{r}_N)$. *Woodbury and Ulrych*

(1993) showed that the a priori estimation $p(\mathbf{s})$ has the form

$$p(\mathbf{s}) = \prod_{j=1}^{N} \frac{-\beta_j}{\exp(-\beta_j U_j) - 1} \cdot \exp(-\beta_j \hat{r}_j \tag{10.9}$$

which is a multivariate truncated exponential. β_j are Lagrange multipliers which can be estimated from the upper and lower bounds and the expected value constraints. By definition, $p(\mathbf{s})$ satisfies the expected value constraints

$$\int p(\mathbf{s}) \cdot \mathbf{s} \cdot d\mathbf{s} = \hat{\mathbf{r}} \tag{10.10}$$

Finally, the posterior pdf $q(\mathbf{s})$) is determined by minimizing its entropy relative to $p(\mathbf{s})$ (subjected to the constraints of Eqs. 10.2 and 10.7). As demonstrated by *Woodbury and Ulrych* (1993), the posterior pdf has expression:

$$q(\mathbf{s}) = \prod_{j=1}^{N} \frac{-a_j}{\exp(-a_j U_j) - 1} \cdot \exp(-s_j a_j) \tag{10.11}$$

where

$$a_j = \beta_j + \sum_{i=1}^{M} \lambda_i f_{ij} \tag{10.12}$$

in which $\boldsymbol{\lambda}$ is a Lagrange multipliers vector ($M \times 1$). The expected value of the vector of unknowns is given by

$$\hat{s}_j(\boldsymbol{\lambda}) = \frac{\exp(-a_j U_j) \cdot a_j U_j + \exp(-a_j U_j) - 1}{a_j[\exp(-a_j U_j) - 1]} \tag{10.13}$$

Substituting Eq. 10.13 in Eq. 10.6, we obtain

$$\hat{z}_i = \sum_{j=1}^{N} f_{ij} \cdot \hat{s}_j(\boldsymbol{\lambda}) \tag{10.14}$$

where $\hat{z}_i$ are the estimated concentrations. Minimizing the objective function

$$F(\boldsymbol{\lambda})_i = z_i - \hat{z}_i = z_i - \sum_{j=1}^{N} f_{ij} \cdot \hat{s}_j(\boldsymbol{\lambda}) \tag{10.15}$$

the appropriate multipliers λ can be determined using the Newton-Raphson algorithm (*Johnson et al.*, 1987) (see *Woodbury and Ulrych* (1996), for more details).

10.2.3 Determination of Confidence Intervals

As expressed by Eq. 10.11, the posterior pdf $q(\mathbf{s})$ is non-Gaussian and confidence intervals cannot be easily derived in the classic way. However, they can be calculated starting from the cumulative distribution function (cdf) for $\mathbf{s}$, defined as

$$\int_0^{\mathbf{s}} p(\mathbf{x}) \cdot d\mathbf{x} = P(\mathbf{s}) \tag{10.16}$$

which, integrating terms by terms, gives

$$P(s_j) = \frac{\exp(-a_j s_j) - 1}{\exp(-a_j U_j) - 1} \quad 0 \le s_j \le U \ , \ \forall \ j = 1, ..., N \tag{10.17}$$

The goal is to define s_j corresponding to the defined probability P:

$$s_j = -\frac{\log[P \cdot (\exp(-a_j U_j) - 1) + 1]}{a_j}$$

Assuming for instance $P = 0.95$, s_j results:

$$s_j = -\frac{\log[0.95 \cdot (\exp(-a_j U_j) - 1) + 1]}{a_j} \tag{10.18}$$

10.3 Study cases

The method proposed by *Woodbury and Ulrych* (1996) for a 1-D uniform flow field was extended to 2-D uniform and non-uniform flow fields. Both cases are based on numerical flow and transport models. The flow model, developed with MODFLOW (*Harbaugh et al.*, 2000), reproduces a 2-D confined aquifer (1 layer) having rectangular shape (400 m long, 100 m wide) and 10 m thickness (Figs. 10.2 and 10.3). The computational grid is discretized into 2 m×2 m×10 m cells, obtaining 200×50 computational nodes. The boundary conditions are no flow boundaries at the North and South boundaries, constant head on the upstream (West) side $h_U = 24$ m and on the downstream (East) side $h_D = 20$ m (see Fig. 10.2). The hydraulic conductivity of the uniform flow field case (HO) is homogeneous and equal to $2.31 \cdot 10^{-4}$ m/s, and the resulting flow through the aquifer is $2.3 \cdot 10^{-3}$ m^3/s. The transport model, developed with MT3D (*Zheng and Wang*, 1999), uncoupled from the flow model, considers a solute non-sorbing, non-reactive release lo-

cated in a point source at $\mathbf{x}_0$ (x=49.0 m and y =49.0 m, see Fig. 10.2). The longitudinal and transverse dispersivities and the porosity are assumed constant and equal to α_L=1.0 m, α_T =0.1 m, and $\phi = 0.20$. The pollutant release at $\mathbf{x}_0$ is simulated as an injection with a constant water discharge and variable tracer concentration over time. The amount of the conservative pollutant per time unit injected into the aquifer at the source is given by:

$$s(\mathbf{x}_0, t) = Q_{in}(\mathbf{x}_0, t) \cdot C_{in}(\mathbf{x}_0, t)$$

where Q_{in} [$\mathrm{L}^3 \cdot \mathrm{T}^{-1}$] is the constant water discharge and C_{in} [$\mathrm{M} \cdot \mathrm{L}^{-3}$] is the concentration release history, variable in time, of the injected solution. A unit value was adopted for $Q_{in}(\mathbf{x}_0, t)$. Following the works of *Skaggs and Kabala* (1994), *Woodbury and Ulrych* (1996), *Snodgrass and Kitanidis* (1997), *Neupauer and Borchers* (2001) and *Butera et al.* (2013), we considered a concentration release history with the expression:

$$C_{in}(\mathbf{x}_0, t) = \exp\left(\frac{-(t/\Delta t - 130)^2}{50}\right) + 0.3 \cdot \exp\left(\frac{-(t/\Delta t - 150)^2}{200}\right) + 0.5 \cdot \exp\left(\frac{-(t/\Delta t - 190)^2}{98}\right) \tag{10.19}$$

Since $Q_{in}(\mathbf{x}_0, t)$ is of unit value, the identification of the release history $s(\mathbf{x}_0, t)$ is equivalent to the identification of the concentration history $C_{in}(\mathbf{x}_0, t)$. The total time of the test is $T = 600$ days and the release history is discretized in 300 intervals with a time step of $\Delta t = 2$ days. According to previous works the results are made dimensionless dividing the concentration by $C_0 = 1$ mg/L and the time by the time step Δt. Two scenarios were studied: the first (HO1) recovered the release history by means of the observations collected at 20 monitoring points (black dots in Fig. 10.2) at time T, whilst the second (HO2) recovered the release history by means of the observations collected at 2 monitoring points (P1 with coordinates 65.0 m, 49.0 m and P2 with coordinates 115.5 m, 49.0 m in Fig. 10.2) at 15 sampling times (see Table 10.1 for the summary of the study cases).

The non-uniform flow field (HE) was realized considering the heterogeneous hydraulic conductivity field proposed by *Butera et al.* (2013). We have chosen the same hydraulic conductivity field as *Butera et al.* (2013) in order to allow the reader to easily compare the results of different methodologies in complex cases. The conductivity field is characterized by a mean value of $3.2 \cdot 10^{-4}$ m/s, a standard deviation of $4.2 \cdot 10^{-4}$ m/s and a correlation length equal to 20 m. The hydraulic conductivity has a very broad range from $2.6 \cdot 10^{-6}$ m/s to $5.5 \cdot 10^{-3}$ m/s. Fig. 10.3 shows the normalized log conductivity field $Z = (Y - \mu_Y)/\sigma_Y$ where $Y = \log K$ with mean μ_Y and standard deviation σ_Y. The log conductivity field variance is $\sigma_Y^2 = 1.32$ and the resulting flow through the aquifer is about $1.20 \cdot 10^{-3}$ m^3/s.

The assumption of a known hydraulic conductivity field is rather unrealistic; in fact,

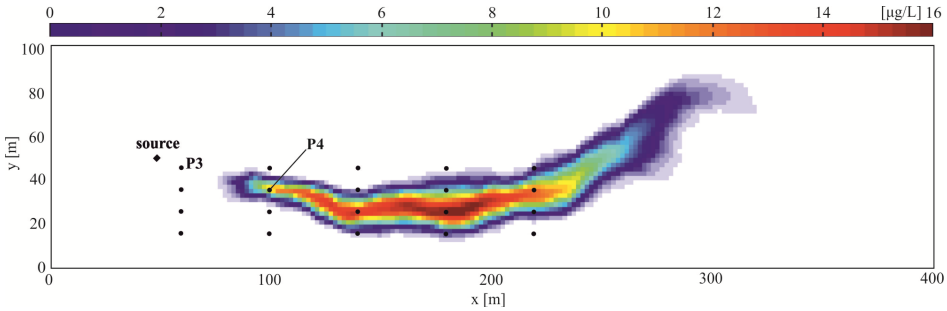

Figure 10.1: Plume at $T = 300\Delta t$. The black dots indicate the measurement points of Cases HE1; P3 and P4 are the measurements points of Case HE2. The black diamond is the source location.

in field condition it is difficult to obtain detailed information on hydraulic parameters and for this reason there is a huge collection of literature on estimating hydraulic conductivity variability (for example see *Fienen et al.*, 2009, *Zanini and Kitanidis*, 2009 and *Cardiff et al.*, 2013). The present paper has the goal of testing the goodness of the MRE procedure applied to contaminant release history identification, assuming known the conductivity field and transport parameters.

The transport parameters and the source location are the same as the previous case. As for the HO case, two scenarios were studied: the first (HE1) recovered the release history by means of the observations from 20 monitoring points (black dots in Fig. 10.3) at time T, whilst the second (HE2) recovered the release history by means of the observations from 2 monitoring points (P3 with coordinates 60.0 m, 45.0 m and P4 with coordinates 100.0 m, 35.0 m in Fig. 10.3) with 25 samples at different times (see Table 10.1 for the summary of the study cases). Fig. 10.1 shows the concentration distribution due to the heterogeneities at time T. The tests were carried out in the following sequence

1. the numerical flow and transport models were used to estimate the TFs at each monitoring points by using the SIF procedure developed by *Butera et al.* (2013);

2. the numerical models were used to compute the concentrations at the monitoring points due to the release function described by Eq. 10.19;

3. the observations collected at the monitoring points were used in the inverse procedure aimed at recovering the release history at the source location.

The MRE approach requires information on the prior distribution of the release history; for this purpose in this work we tested the method under the two alternatives of a Gaussian

(Eq. 10.20) and a Boxcar (Eq. 10.21) function.

$$\bar{r}(t) = \alpha_g \cdot \exp\left(- \frac{(t - \mu_g)^2}{2 \cdot \sigma_g^2} \right) \quad \forall\, t \in [0, T] \tag{10.20}$$

$$\begin{cases} \bar{r}(t) = \bar{r}_{b,max} & t_s \leq t \leq t_e \\ 0 \quad elsewhere \end{cases} \tag{10.21}$$

in which $t_s, t_e \in [0, T]$. α_g, μ_g, σ_g^2 are the parameters of the Gaussian function, $\bar{r}_{b,max}$ is the height of the Boxcar function used as expected value constraints, and t_s and t_e are the temporal limits of the Boxcar function. The parameters of the prior information were different in each case, and they were manually adjusted in order to obtain the best agreement between the observed and computed concentrations. The knowledge of this information requires some hypothesis about the release history, such as the hypothetical start and end of the injection, its magnitude expressed by the expected value function and its upper value **U**.

10.3.1 Case HO1 - Analysis with concentration data collected at 20 locations at the same time

20 observations collected at 20 positions (Fig. 10.2) at time $T = 300\Delta t$ were considered in the recovery process (Fig. 10.4) in order to determine the release history at 300 time intervals (unknowns), i.e. the **s** vector with dimension (300×1). The above described 10.20 and 10.21 expressions for the expected value of the prior distribution of the release history have been considered; the results obtained are shown in Fig. 10.5a,b. Initially, the processed data were considered error free, and then they were corrupted with a random error with mean value equal to 10^{-3} mg/L; in Figs. 10.4 and 10.5 the results obtained using corrupted observations are shown.

The results of the procedure, using a Gaussian function as expected value (Fig. 10.5a), are very satisfactory. The recovered release history is very similar to the true one. Moreover, the concentrations estimated at the monitoring point (due to the recovered release history) are very close to the one observed (Fig. 10.4). The maximum nRMSE computed between the recovered and true release history results 2.20 % (see Table 10.1), while the one maximum computed between the estimated and observed concentration at the monitoring points is 1.52 %. Considering a Boxcar function as expected value (Fig. 10.5b), the estimated release history is even better than the previous one; that is confirmed by the nRMSE computed, in the worst case, between the recovered and true release history

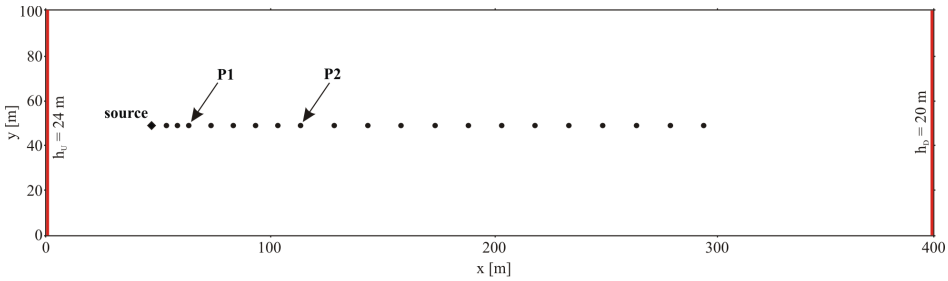

Figure 10.2: Sketch of the numerical model, in red the constant head boundary conditions. The black dots indicate the measurement points of Case HO1, while P1 and P2 are the measurement points of Case HO2. The black diamond denotes the source location.

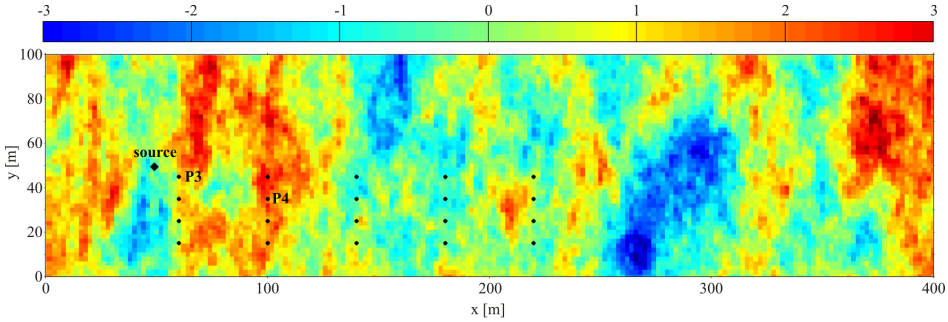

Figure 10.3: Normalized log-conductivity field (σ^2_Y=1.32). The black dots indicate the measurement points of Cases HE1; P3 and P4 are the measurements points of Case HE2. The black diamond is the source location.

in 1.34 % (see Table 10.1), while the one computed between the estimated and observed concentration at the monitoring points is 1.16 %.

The results are very sensitive to the prior information required by the method, in particular to upper value **U** and to the parameters of the expected value function. The knowledge of these parameters requires a rough idea of the true release history, so the goodness of the results is conditioned by some strong, in a certain sense arbitrary, hypothesis. Several tests, not reported here for briefness, were carried out to investigate the sensitivity of the MRE method to the expected value functions and to the upper value. Basically, the results showed that the solutions are relatively insensitive to the kind of previously expected value functions, while it is more sensitive to the upper value. In particular, if the maximum of the expected value function is greater than the upper value, the method is not able to converge to a solution. Moreover, the results worsen as the value (assumed constant) of the upper bound **U** increases.

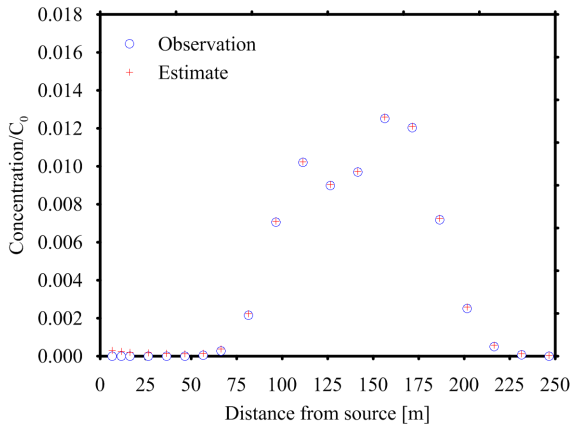

Figure 10.4: Observed and estimated concentrations at time T for Case HO1. These data were collected at 20 monitoring points depicted in Fig. 10.2. The estimated concentrations shown here were calculated by using the Gaussian function as prior estimate.

10.3.2 Case HO2 - Analysis with concentration data collected at 2 locations at different times

The goal of this second application is to investigate the reliability of the MRE method using several pieces of information collected at few locations at different times. This case is very realistic, as it is common to have only few monitoring points and several sampled concentration values for each point at different times. The test case is the same as case HO1, but only two observation points (P1 and P2 of Fig. 10.2) were used. At these points 15 concentration values are considered available in 600 days, with a time step equal to $20\Delta t$ (Fig. 10.6). The transfer functions for the two observation points were the same as the previous case but the $\mathbf{H}$ matrix becomes $\mathbf{H} = \Delta t[\mathbf{H}_{P1}\mathbf{H}_{P2}]^T$ where $\mathbf{H}_{Pi}$ are the matrices that contains the TF of each monitoring point evaluated at the specified sampling time; the vector of the observations can be written as: $\mathbf{z} = [\mathbf{z}_{P1}\mathbf{z}_{P2}]^T$ so Eq. 10.5 is still valid.

Figs. 10.5c and 10.5d show the results once again using two different expected value functions (Gaussian and Boxcar). In these cases the results do not appear to be as good as the previous case; in particular neither of the release histories recovered is totally included in the 5-95% confidence interval, although both the peaks values and times are well estimated. By considering the nRMSE (Table 10.1) it is clear that the results are less accurate than the ones obtained in case HO1.

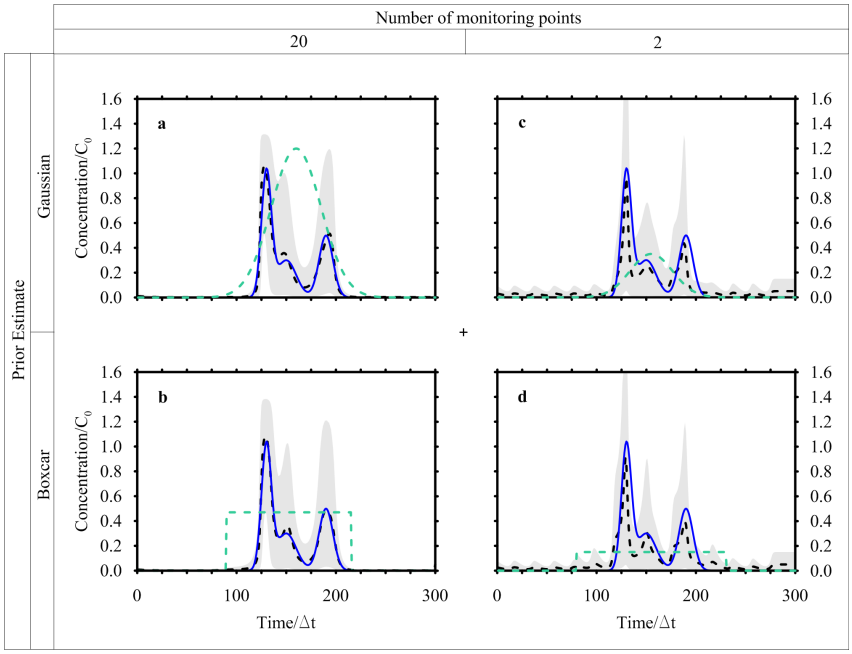

Figure 10.5: True solution (blue line), best estimate (dashed line), prior estimate (green dashed line) and 5-95% confidence interval (gray band). a) Case HO1 with Gaussian prior estimate; b) Case HO1 with Boxcar prior estimate; c) Case HO2 with Gaussian prior estimate; d) Case HO2 with Boxcar prior estimate.

10.3.3 Case HE1 - Analysis with concentration data collected at 20 locations at same time

The tests were carried out in the sequence described above for the cases HO1 and HO2. In these cases (HE1 and HE2), the monitoring points cannot be the same as the ones used in the cases HO1 and HO2, since the plume evolution is very different: in fact the local heterogeneities increase the complexity of the recovering process originating a plume evolution that involves the monitoring points of Fig. 10.3 to a negligible extent.

The monitoring points, depicted in Fig. 10.3, are located in the nodes of a grid covering the region $60 \leq x \leq 220$ m and $15 \leq y \leq 45$ m. After the calculation of the TFs at each point, the MRE method has been applied at first without considering any measurement error, with good results: then the observations have been corrupted by a random error normally distributed with $\sigma R = 10^{-3}$ mg/L. Fig. 10.7 shows the observations (corrupted by errors) collected at $T = 600$ days in each monitoring point and those estimated through the inverse procedure. Two prior expected functions have been considered, the Gaussian and the Boxcar expression. The results are shown in Fig. 10.8a, b and Table 10.1. Con-

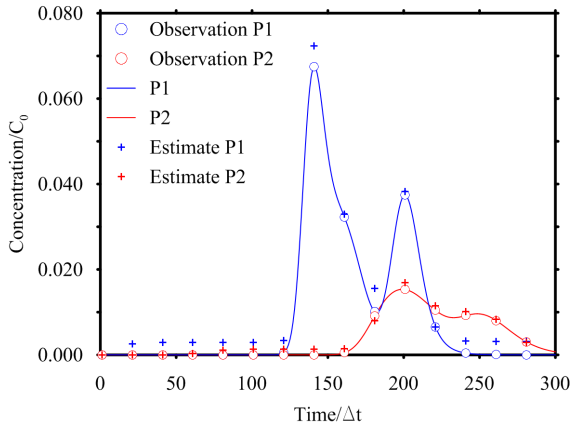

Figure 10.6: The sampled time-concentration data for Case HO2. The estimated concentrations shown here were calculated by using the Gaussian function as prior estimate.

sidering the Gaussian function (Fig. 10.8a) the MRE procedure estimates the true release history reasonably for both with and without error cases (see Fig. 10.8; Table 10.1). The nRMSE, computed between the true and the estimated (with the Gaussian prior pdf and in presence of measurement errors) release history is close to 9 %. While, analyzing the release history obtained through the boxcar expression (Fig. 10.8b), even if it is overestimated, it seems acceptable for $t/\Delta t > 100$ only and this misfit is quantified in an nRMSE of about 39 %. The nRMSE between the computed and observed concentrations shows, in all cases, values below 7 % that indicates an acceptable estimation of the observations.

10.3.4 Case HE2 - Analysis with concentration data collected at 2 locations at different times

In this scenario, only two monitoring points (P3 and P4 depicted in Fig. 10.3) are considered and 25 concentration values are taken as observations in 600 days, with a time step equal to $12\Delta t$ (Fig. 10.9). Like in HE1, two different conditions have been considered: the first assumes noisefree data, while the second considers an error with a standard deviation equal to 10^{-3} mg/L. The processing of the error free data has provided very encouraging results, with nRMSE values between the computed and observed data and the true and estimated release histories close to 4 %. In presence of measurement errors, both the Gaussian (Fig. 10.8c) and Boxcar functions (Fig. 10.8d) have resulted in good release histories (nRMSE about 5 %) and in a satisfactory reproduction of the observed concentrations (see Fig. 10.7 for the Gaussian expression and Table 10.1).

Both graphical (Figs. 10.8, 10.7) and numerical (Table 10.1) results show that, in this scenario, the release history is better recovered and presents a smaller confidence interval

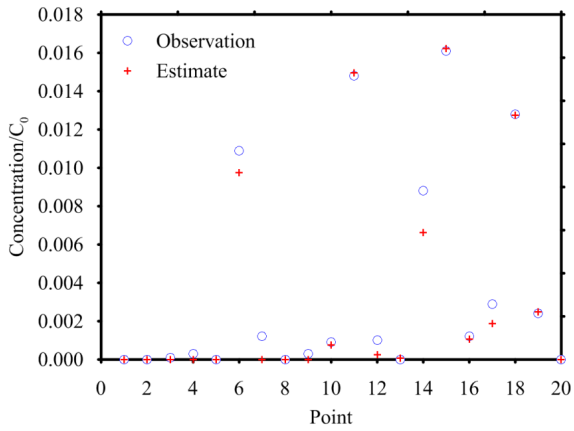

Figure 10.7: Observed and estimated concentrations at time T for Case HE1. These data were collected at 20 monitoring points depicted in Fig. 10.3. The estimated concentrations shown here were calculated by using the Gaussian function as prior estimate.

than in HE1; surely this is due to the high values of the TF at the monitoring points P3 and P4, which provide very reliable information. Moreover, 50 observations (as a total) are available instead of only 20 (HE1). It is important to remark that considering information in few points at several times allows to capture the leading and the trailing edge of the plume and provides information about the entire release history. Whereas considering information at several monitoring points at a specific time does not allow to capture the leading edge of the plume and consequently the data do not contains information about the early times of the release history distribution. That demonstrates the need for either good spatial coverage or good temporal coverage or both.

10.4 Comparison to other approach

Butera et al. (2006, 2013) have presented an improvement of the geostatistical approach to contaminant release history identification developed by *Snodgrass and Kitanidis* (1997) and have tested the method on several cases. The Case HE1, discussed in this chapter, is the same of Case 1 presented by *Butera et al.* (2013); this allows a comparison of the results between the two methodologies. Figs. 10.8a and 10.8b show the estimated release histories using two different prior estimates. It is evident that the Gaussian prior provides better results than the Boxcar one. Comparing Fig. 10.8a to Fig. 2 of *Butera et al.* (2013), it seems that both methods recover well the two main peaks of the release function and do not identify the middle one. The MRE reproduces better the magnitude and the timing of the peaks, but on the downside it presents non zero values on the first part of the release. This problem seems reduced in the geostatistical approach but instead

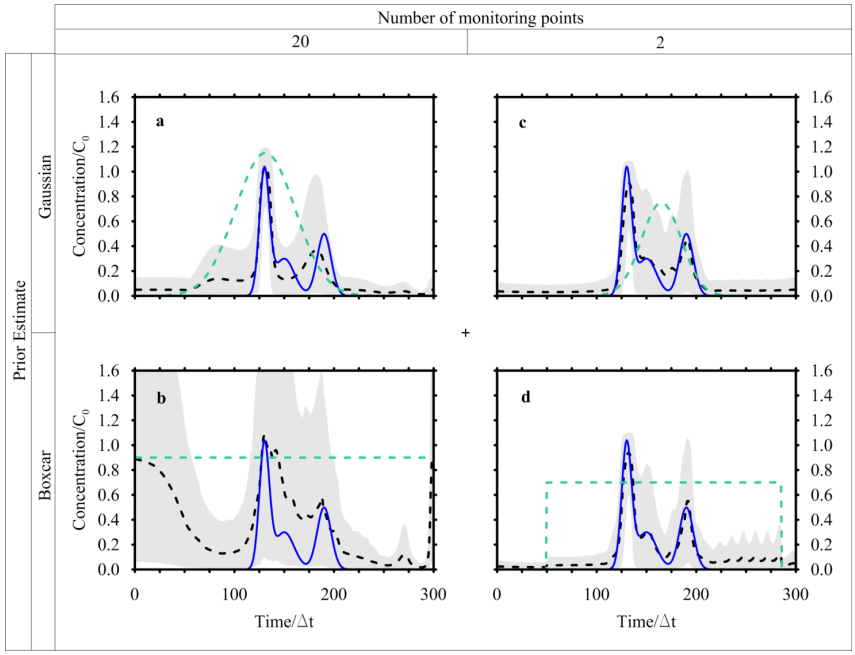

Figure 10.8: True solution (blue line), best estimate (dashed line), expected value function (green dashed line) and 5-95% confidence interval (grey band). a) Case HE1 with Gaussian prior estimate; b) Case HE1 with Boxcar prior estimate; c) Case HE2 with Gaussian prior estimate; d) Case HE2 with Boxcar prior estimate.

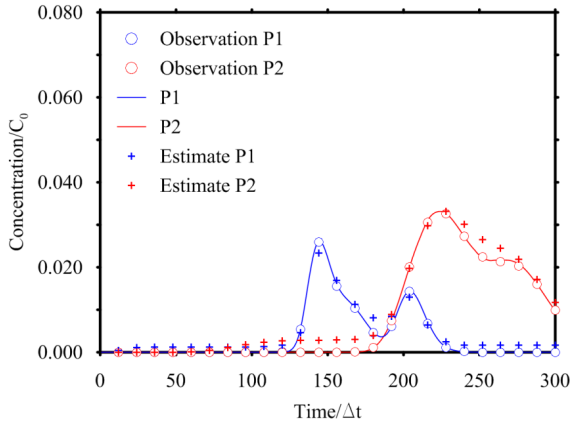

Figure 10.9: The sampled time-concentration data for Case HE2. The estimated concentrations shown here were calculated by using the Gaussian function as prior estimate.

Table 10.1: Summary of the study cases and numerical results.

Case	Sampling times	N. Obs.	Measurement error σ_R [mg/L]	nRMSE [%] Released History Prior estimate		nRMSE [%] Observed/Estimated Prior estimate	
				Gaussian	Boxcar	Gaussian	Boxcar
HO1	$T = 300\Delta t$	20	none	1.85	1.20	1.40	1.09
			10^{-3}	2.20	1.34	1.52	1.16
HO2	15 collected every $20\Delta t$ up to T	30	none	5.37	5.72	2.43	2.10
			10^{-3}	6.12	7.01	3.42	2.95
HE1	$T = 300\Delta t$	20	none	7.49	34.91	2.07	5.22
			10^{-3}	9.06	38.72	4.38	6.71
HE2	25 collected every $12\Delta t$ up to T	50	none	4.59	4.88	4.57	3.84
			10^{-3}	4.78	5.34	4.87	4.30

a larger confidence interval is present. The Case HE2 (Figs. 10.8c and 10.8d) can be compared to the results obtained in Case 3 (true source location in Fig. 7) of *Butera et al.* (2013). The geostatistical approach estimates a large confidence interval at the head and at the tail of the estimated release function; while MRE at the same times estimates non zero concentration values but it presents a narrow confidence interval. However, both methods are able to reproduce the three peaks of the release history, their magnitude and timing that in the reclamation and forensic activities are the most important issues (*Atmadja and Bagtzoglou*, 2001).

10.5 Discussion and Conclusions

In this chapter the minimum relative entropy method for recovering the contaminant release history in 2-D homogeneous and heterogeneous aquifers involved in a pollutant event has been applied. In the applications here referred, the SIF numerical method (*Butera et al.*, 2006) has been applied for the computation of the TFs. The performances of the MRE have been tested in uniform and non-uniform flow field, considering different scenarios, and with different prior information. They have been quantified by the nRMSE calculated between the true source release and the estimated ones, and between the concentration observed and the computed ones; the nRMSE quantities are summarized in Table 10.1.

Two scenarios have been considered: the first uses 20 observations collected at different locations at the same time while the second processes several observations collected at different times at two monitoring points only. For each scenario, the method has been applied using two different expected value functions: the Gaussian and the Boxcar expression. The results show that in the homogeneous case (HO) the methodology works very well; this is clearly shown by the nRMSE, which is lower than 2.2% in all tests. The release function is well recovered in the two cases studied with the two different expected value functions. It is important to remark that in this case the release function presents 300 unknowns (N) and it is recovered with 20 observations (M) (HO1, with a ratio M/N of 0.067) or 30 observations (HO2, with a ratio M/N of 0.100), while *Woodbury and Ulrych* (1996) estimated 200 unknowns with 61 observations with a ratio M/N of 0.305. The results have demonstrated that the method is efficient with few observations too.

Regarding the non-uniform flow field, the presented cases have a heterogeneous hydraulic conductivity field with a log conductivity variance of $\sigma_Y^2 = 1.32$; the results obtained in these cases are not as good as in the homogeneous ones but still appreciable and meaningful. The method performs better using several observations collected in few monitoring points rather than one observation at different points. However, in HE1, 300 unknowns (N) were estimated by using 20 observations (ratio equal to 0.067), while in HE2 50 observations collected at two different points at different times (ratio equal to

0.167) have been used. The observations have been compared with the ones reproduced by the forward transport model by using the estimated release history as source term: the results show that the agreement is acceptable in both cases. Note again that the ratio of the number of observations on the unknowns (M/N) is very low (0.067) in comparison with the ratio $M/N = 0.305$ used by *Woodbury and Ulrych* (1996) in their applications to homogeneous 1-D aquifers. The present results have demonstrated that the method is efficient with few observations too and the less performance can be ascribed to the non-uniformity of the flow field rather than to the amount of available data.

Another important issue, in a non-uniform context, is the monitoring point location: it is crucial to have available information in spots with high peak TF values; in HE1, several monitoring points have TFs with a very low peak value which means that monitoring locations provide very poor information about the pollutant event development and numerically they generated a matrix **H** that is ill-conditioned. This **H** matrix causes failing in the convergence procedure and consequently errors on the results. During the design of a monitoring network we suggest to consider the monitoring points that present the higher peak values of the TF. It is important to note that a monitoring point can have a high peak TF value and a zero concentration; this information is very important and allows to bound the plume.

The comparison between the different cases shows that, while in the homogeneous case the spatial data are more informative and the methodology performs better, in the heterogeneous case, the temporal data allow a better estimation of the release history. Basically, they give opposite indications. This is due to the position of the monitoring points respect the shape of the plume. In fact, in the case HO1 all the points are interested by the pollution phenomenon and all of them give information different from the others. All together, they provide a very good framework of the evolution of the plume. In case HO2, the information given by two points is not as comprehensive as those provided in case HO1. Moreover, since the field is homogeneous, the concentration data at P1 and P2 cannot be so different (considering their position). Looking at the case HE1, instead, several monitoring points have TFs with a very low peak value. For sure, they provide information, but globally, the quantity of data is less than the case HO1.

In case HE2 the two monitoring points are along the plume and they provide very good information about the concentration evolution. This proves, once again, how much a good reconstruction of the flow field is important, in order to design a monitoring network. It is worth to add some considerations about the prior information that the MRE method requires. If the assumed prior is very far from the right posterior and the TF is poor at the point or in time, the Newton-Raphson method cannot converge to a solution. The method requires a prior expected value of the unknown release history and a guess of the collocation in time. By using a Gaussian expression, this means to choose the mean and the variance of the Gaussian curve, while, for the Boxcar, a rough idea of the concentration

maximum value and the start and the end time of the injection are necessary. The MRE prior should reflect what is known before the new information is considered and should be maximally uncommitted with respect to unknown information (*Woodbury and Ulrych* 1993, 1998). For this reason the prior information are not subjective to the user; a useful guidance on their selection was given in *Woodbury and Ulrych* (1996) and *Woodbury* (2011).

The MRE approach, thanks to the lower limit **L** (that in this work is set to zero), does not require the transformation of variables, as other methods do, to constrain the unknown function (for instance the concentrations) to only positive values. This fact avoids the increase of unknowns (parameters of the transformation) in the inverse procedure and does not affect the stability of the procedure that can happen choosing the wrong transformation. In conclusion, the MRE approach developed by *Woodbury and Ulrych* (1993, 1996) integrated with the SIF procedure (*Butera et al.*, 2006) works fine in simple study cases (such as 1-D and 2-D with uniform flow field), even with few observations, and in complex cases, the reliability of the results depends on the number of the available observations and the location of the monitoring points. However, the procedure is considered satisfactory; all three peak times have been detected, and the best estimate falls in the 5-95% confidence interval for all cases. Thanks to the numerical modeling and the SIF procedure, the MRE can be applied to field cases, using the data that normally are spread in space and time.

Future studies will use the experimental data collected in laboratory (*Cupola et al.*, 2015a), where different transport processes can be realized in controlled conditions. Another interesting subject is to test the MRE procedure for the simultaneous identification of the source location and release history and compare the results with the ones obtained by *Butera et al.* (2013) by using a geostatistical approach.

11 The recovering of the contaminant release history in heterogeneous and partially known flow field

§

11.1 Introduction

The topic of the contaminant source identification and release history reconstruction is very important in groundwater reclamation. Since the 90's the literature presented a large number of methods that were based on analytical formulation (for instance *Gorelick et al.* (1983), *Wagner* (1992), *Bagtzoglou et al.* (1994), *Skaggs and Kabala* (1994), *Woodbury and Ulrych* (1993, 1996), *Snodgrass and Kitanidis* (1997)), of the flow and transport process or on numerical models (*Neupauer et al.* (1999), *Michalak* (2003), *Butera et al.* (2013), *Gzyl et al.* (2014), *Cupola et al.* (2015a)) .

The knowledge of the flow field is of main importance to determine the relationships between the sources and the monitoring points. But very often this perfect knowledge is only an unattainable hope: few boreholes and pumping tests are usually available and realizing new ones can lead to unacceptable costs. An evaluation of the reliability of the results obtained with the procedures for the recovering of the release history in heterogeneous and partially known flow field can be a very useful subject under the point of view of researchers and the practitioners. In fact the different methods can be more or less sensitive to the problem or give information that includes or not an uncertainty evaluation; moreover it can be possible to quantify the adequate amount of the site characterization actions.

This work has the goals to answer to the following questions:

1. Can the methods, aimed at identifying the source position and/or the release history reconstruction, be applied in the real practice?

2. Which is the minimum information required to recover reliable data?

3. What is the relevance of the magnitude of the heterogeneity about the possibility of obtaining a reliable estimation of the release history?

Regarding the first question, *Butera et al.* (2013), *Gzyl et al.* (2014) and *Cupola et al.* (2015a, 2015b) showed that through a simple procedure (*Butera et al.*, 2006) it is possible to extend all the methods available in literature to keep into account non-linear flow field due to heterogeneous porous media, presence of wells, recharge etc., even in laboratory or field cases.

For answering the other questions a numerical model of a 2-D confined aquifer with rectangular shape characterized by a heterogeneous hydraulic conductivity field was built. The conductivity field was estimated through a kriging interpolation starting from values sampled on a regular grids of different density. Starting from that partially known field the pollutant release history was estimated.

Preliminary results are shown in *Cupola et al.* (2015d).

11.2 Procedure

With the aim of estimating the importance of the knowledge of the conductivity field for recovering the release history of a contaminant, we built three different numerical model with different magnitude of heterogeneity. All of them are based on MODFLOW (*Harbaugh et al.*, 2000) and they reproduce a 2-D confined aquifer (1 layer) having rectangular shape (400 m long, 100 m wide) and 10 m thickness. The computational grid is discretized into 2 m×2 m×10 m cells, obtaining 200×50 computational nodes. The boundary conditions are no flow boundaries at the North and South boundaries, constant head on the upstream (West) side $h_U = 24$ m and on the downstream (East) side $h_D = 20$ m. Three transmissivity fields were built considering different log-conductivity variance (Case 1 $\sigma_Y^2 = 1.32$, Case 2 $\sigma_Y^2 = 0.01$ and Case 3 $\sigma_Y^2 = 3.6{\cdot}10^{-5}$) and a correlation lenght equal to 20% of the field width. Fig. 11.1 shows the normalized log conductivity field $Z = (Y - \mu_Y)/\sigma_Y$ where $Y = \log K$ with mean μ_Y and standard deviation σ_Y.

The transport model, developed with MT3D (*Zheng and Wang*, 1999), uncoupled from the flow model, considers a solute non-sorbing, non-reactive release located at a point source at $\mathbf{x}_0$ (x=49.0 m and y =49.0 m). The longitudinal and transverse dispersivities and the porosity are assumed constant and equal to α_L=1.0 m, α_T =0.1 m, and $\phi = 0.20$. The pollutant release at $\mathbf{x}_0$ is simulated as an injection with a constant water discharge and variable tracer concentration over time. The amount of the conservative pollutant per time unit injected into the aquifer at the source is given by:

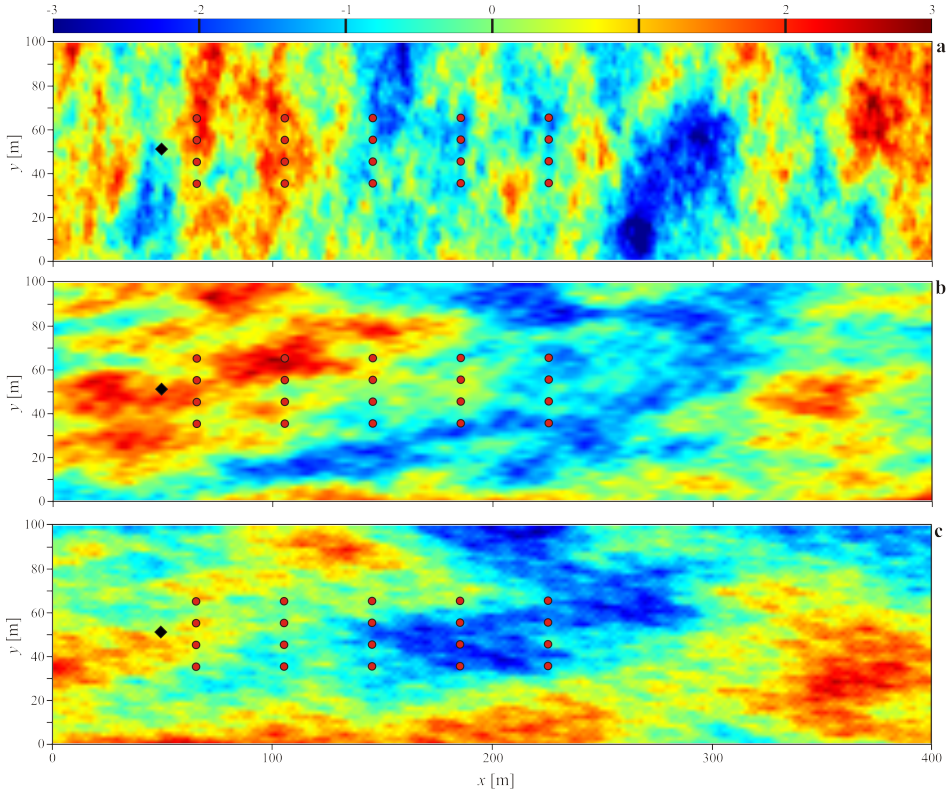

Figure 11.1: Three normalized log conductivity field studied in this chapter. a) $\sigma_Y^2 = 1.32$, b) $\sigma_Y^2 = 0.01$, c) $\sigma_Y^2 = 3.6{\cdot}10^{-5}$. The dots indicate the concentration monitoring points. The diamond is the source location.

$$s(\mathbf{x}_0, t) = Q_{in}(\mathbf{x}_0, t) \cdot C_{in}(\mathbf{x}_0, t)$$

where Q_{in} [$L^3 \cdot T^{-1}$] is the constant water discharge and C_{in} [$M \cdot L^{-3}$] is the concentration release history, variable in time, of the injected solution. A unit value was adopted for $Q_{in}(\mathbf{x}_0, t)$. Following the works of *Skaggs and Kabala* (1994), *Woodbury and Ulrych* (1996), *Snodgrass and Kitanidis* (1997), *Neupauer and Borchers* (2001) and *Butera et al.* (2013), we considered a concentration release history with the expression of Eq. 10.19.

Each true transmissivity field has been sampled at the nodes of a grid with different dimension: 10×10, 20×20, 30×30, 40×40, 50×50 and 100×100 m^2, which, respectively, mean 400, 100, 44, 25, 16 and 4 known hydraulic conductivity values. Starting from those observed values, the interpolation of the conductivity field has been carried

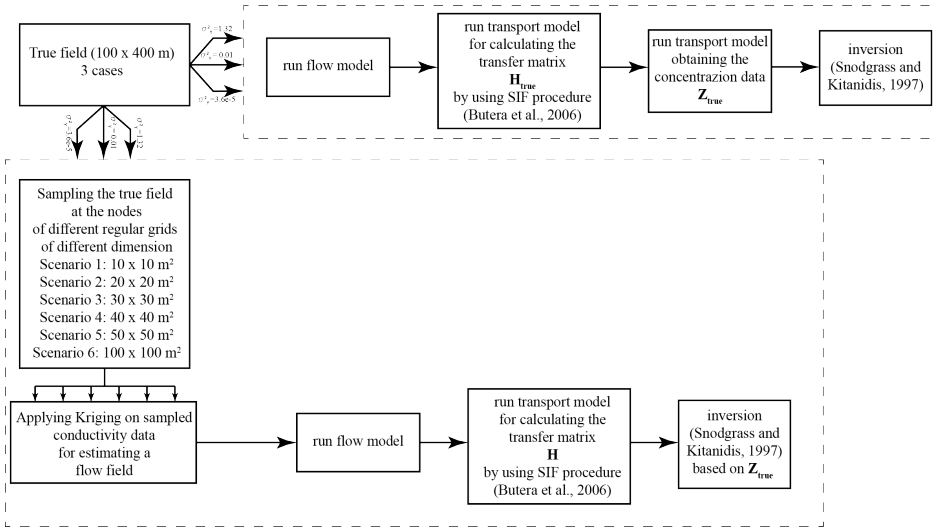

Figure 11.2: Flowchart of the procedure.

out through the Kriging, obtaining six conductivity fields. Preliminary, the experimental semi-variogram of the observed hydraulic conductivity values has been evaluated. A transport forward run has been performed for each flow field estimated: this allowed to calculate the transfer function of the 20 monitoring points depicted in Fig. 11.1 in the different cases.

All the inversions are based on the same observations, collected at the 20 monitoring points of Fig. 11.1 of the true field. In Fig. 11.2 the procedure is summarized for a better comprehension. Even if some cases sound unrealistic, they represent a good study for understanding the minimum efforts necessary for doing a reliable inversion.

11.3 Results

As discussed in the previous section, six scenarios with different degree of information have been investigated. In particular, each of the three different conductivity field has been sampled by using six different grids. So, the total number of cases studied in this work is $3 \cdot 6 = 18$. For each kind of conductivity field, the following studies have been carried out:

1. the transfer function calculated using the true field have been compared with those calculated in the conductivity field estimated through the Kriging;

2. the release history estimated in each case has been compared with the true one;

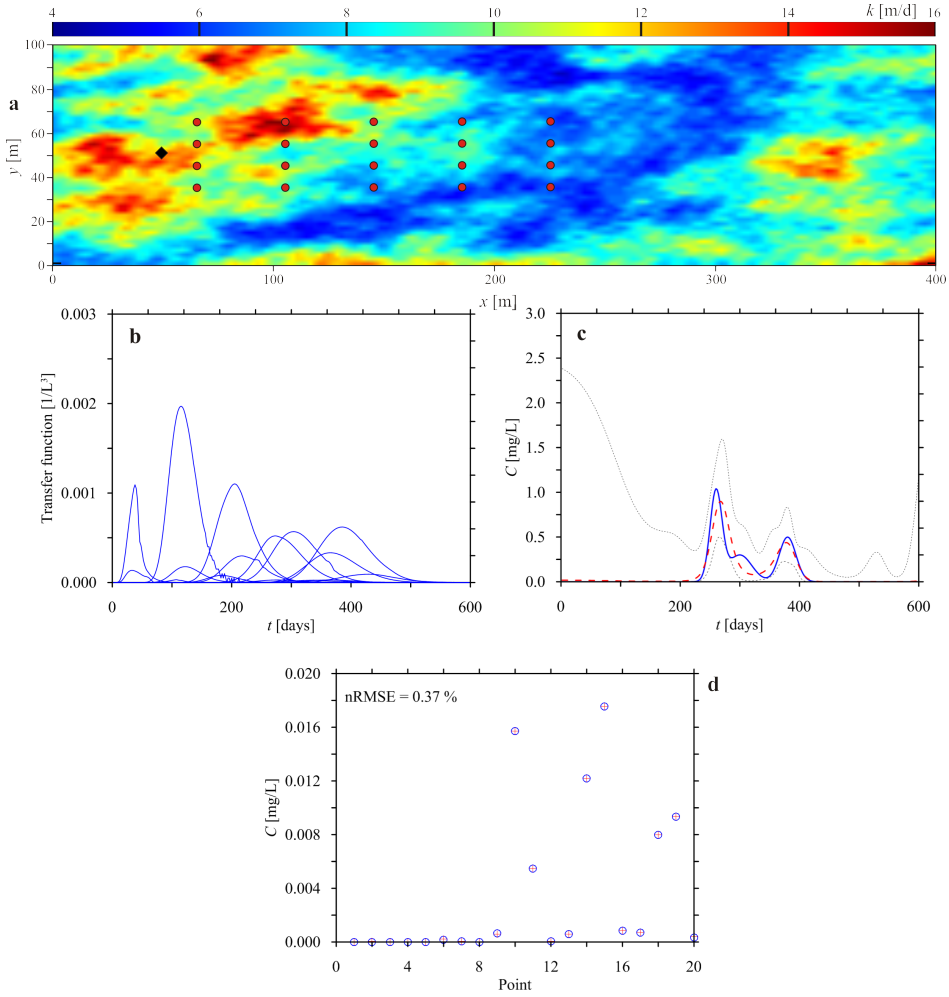

Figure 11.3: True case. a) Conductivity field, b) Transfer functions, c) true and estimated release history, d) observed and computed concentration values.

3. the concentration data obtained using the true release history have been compared with those computed considering the estimated release history through the geostatistical approach

For brevity, only the results obtained considering Case 2 with conductivity field with a normalized log conductivity standard deviation equal to 0.01 are shown graphically (from Fig. 11.3 to Fig. 11.9). The results obtained in the other cases are reported in Table 11.1.

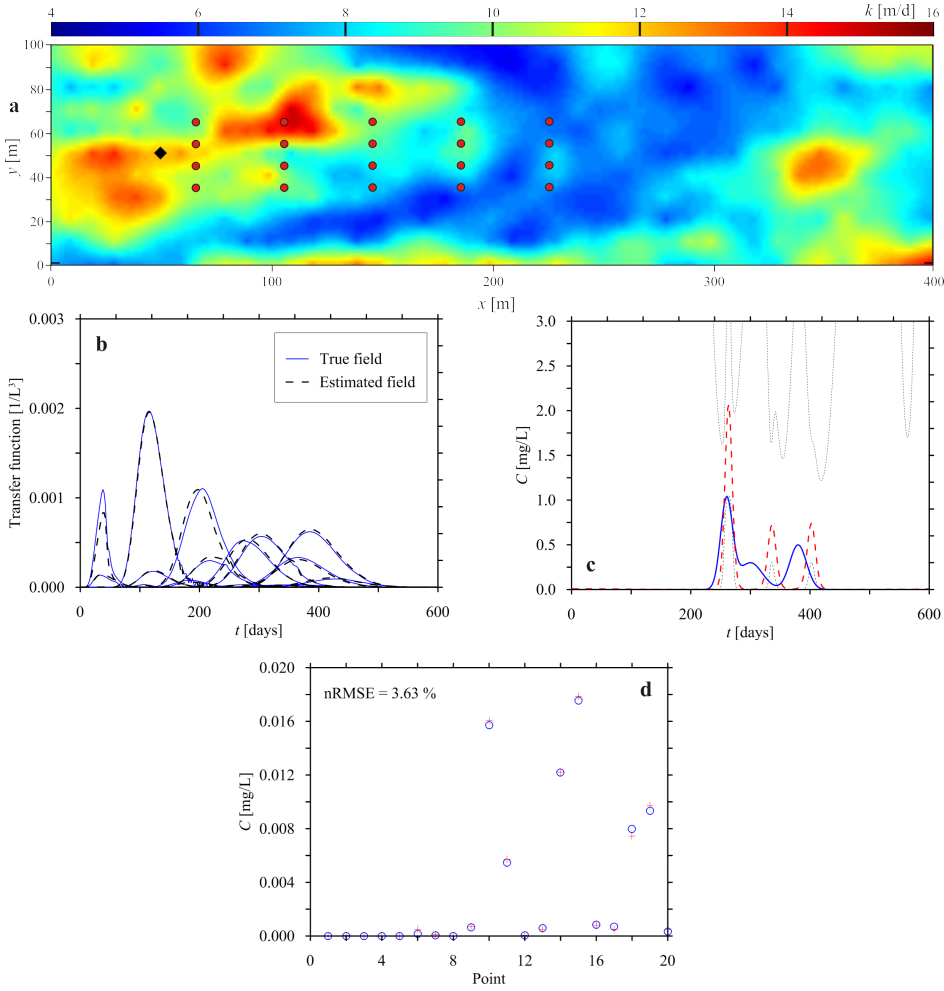

Figure 11.4: Case 2, Scenario 1: grid size equal to 10 m. a) Conductivity field, b) Transfer functions, c) true and estimated release history, d) observed and computed concentration values.

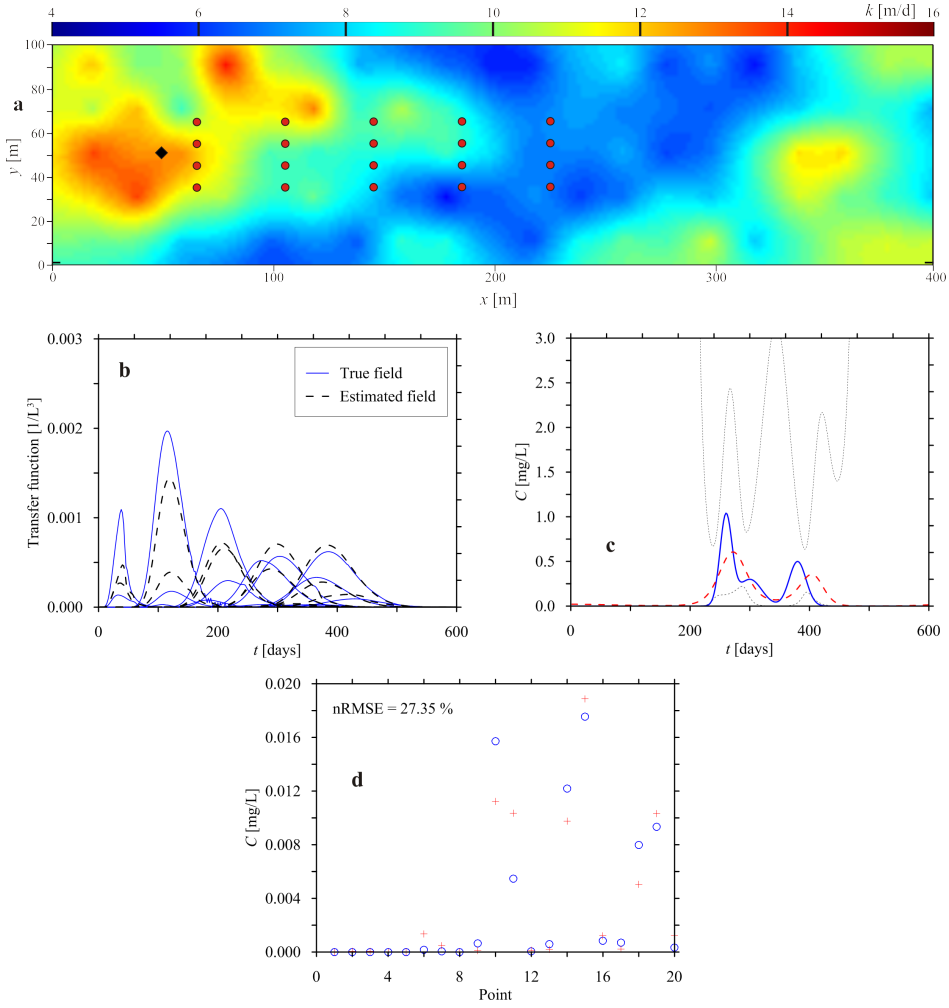

Figure 11.5: Case 2, Scenario 2: grid size equal to 20 m. a) Conductivity field, b) Transfer functions, c) true and estimated release history, d) observed and computed concentration values.

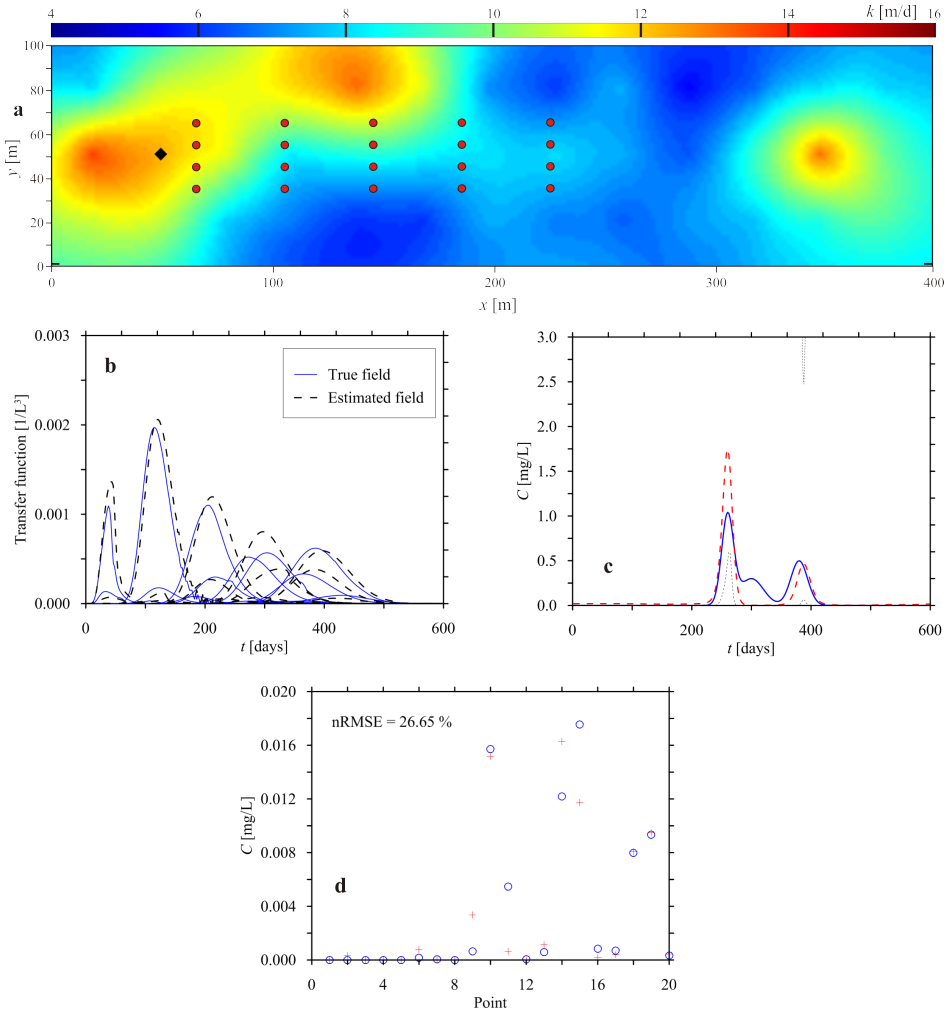

Figure 11.6: Case 2, Scenario 3: grid size equal to 30 m. a) Conductivity field, b) Transfer functions, c) true and estimated release history, d) observed and computed concentration values.

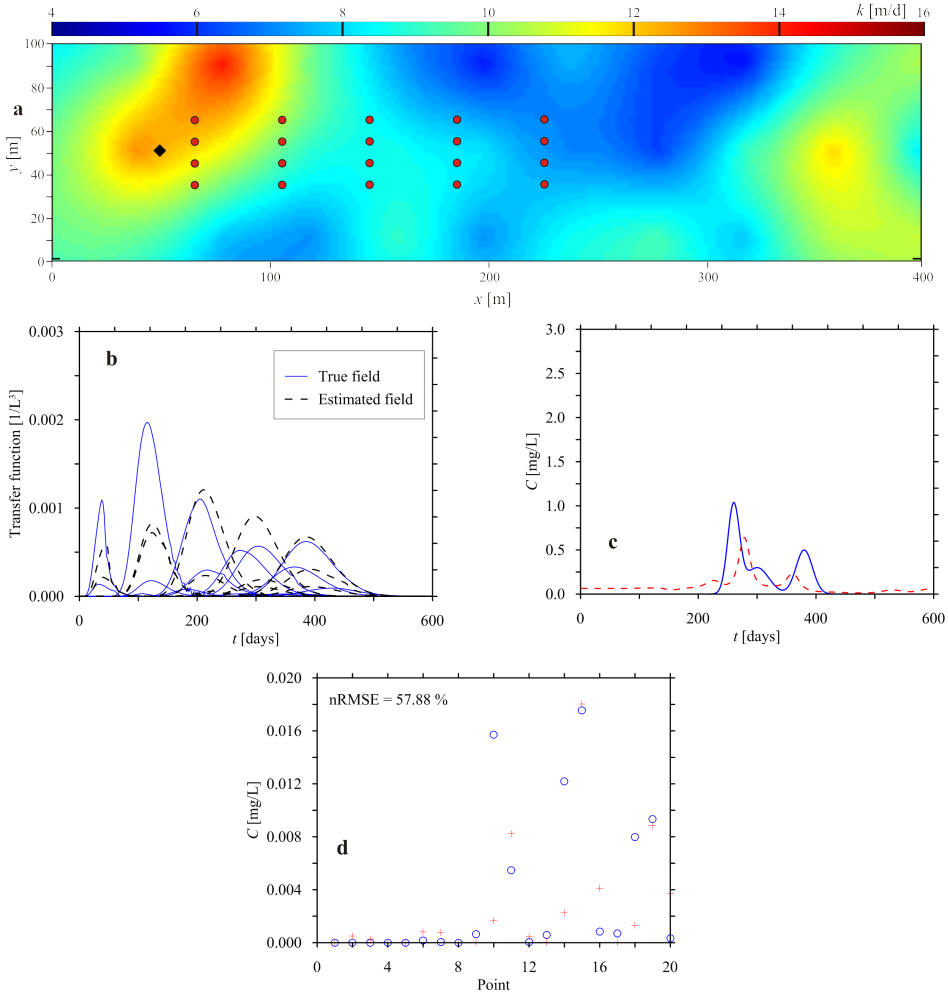

Figure 11.7: Case 2, Scenario 4: grid size equal to 40 m. a) Conductivity field, b) Transfer functions, c) true and estimated release history, d) observed and computed concentration values.

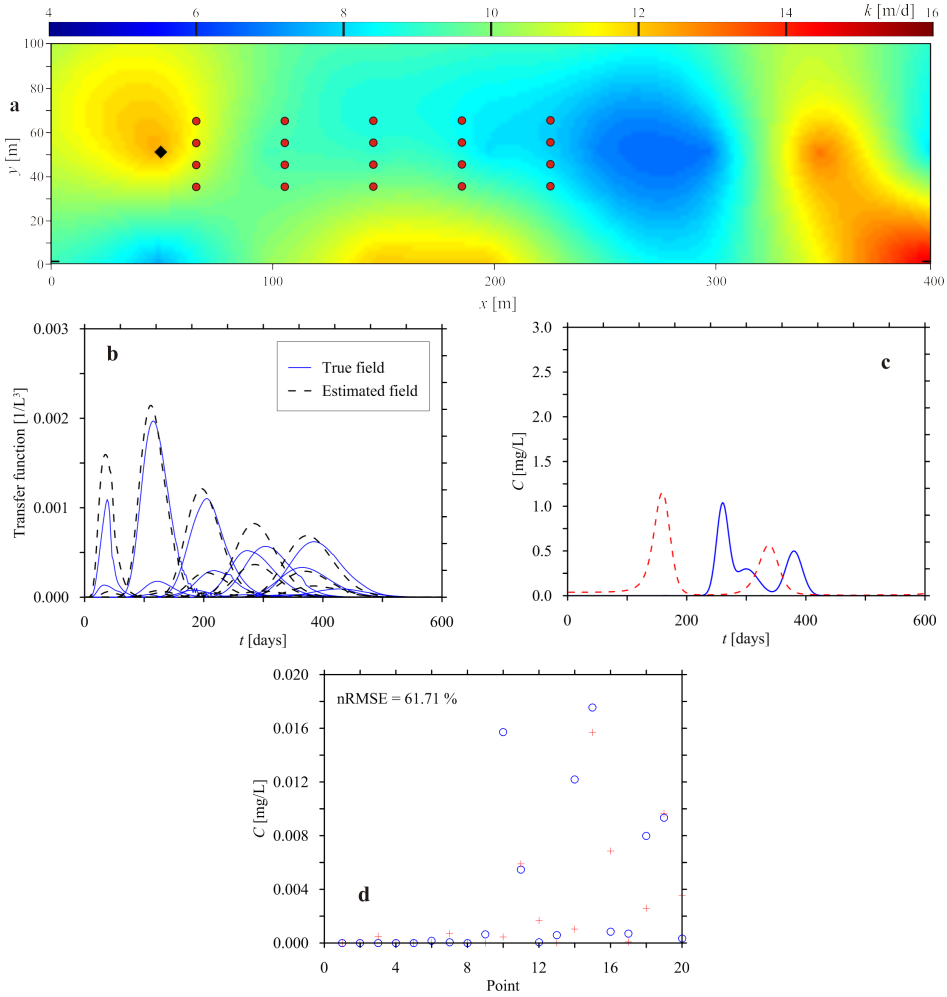

Figure 11.8: Case 2, Scenario 5: grid size equal to 50 m. a) Conductivity field, b) Transfer functions, c) true and estimated release history, d) observed and computed concentration values.

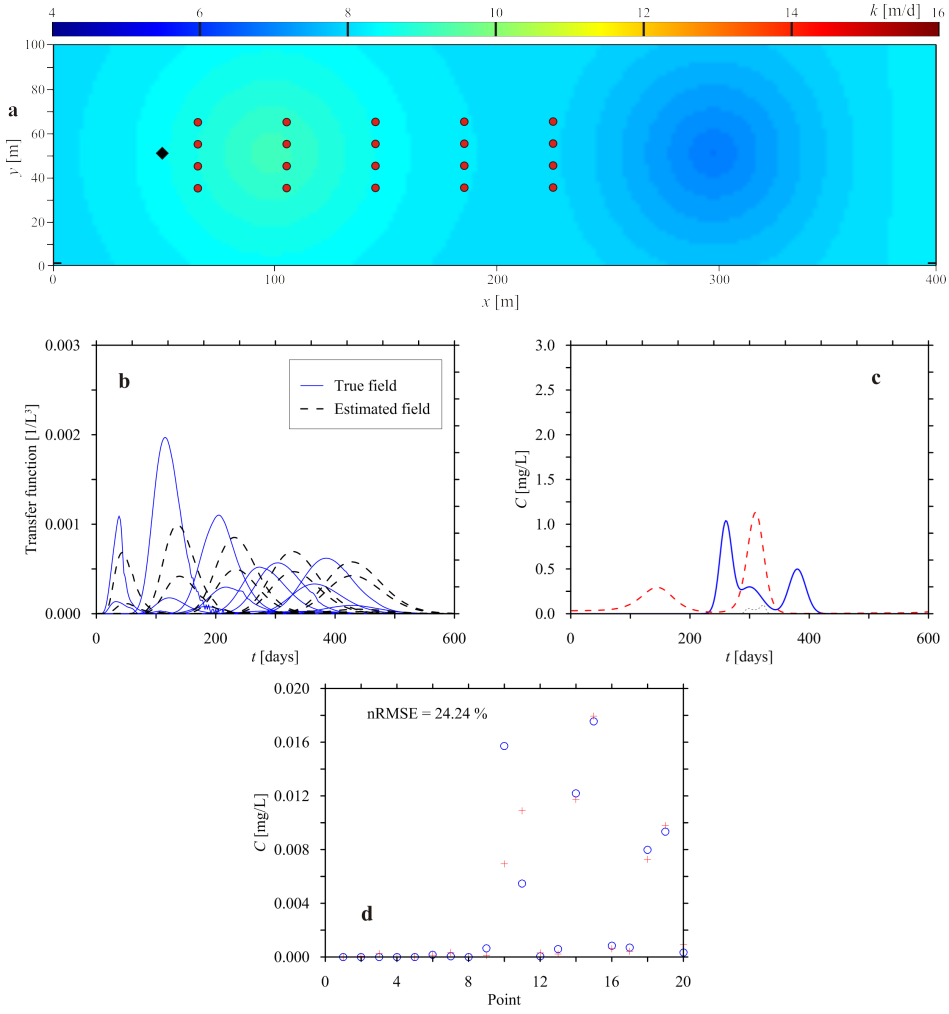

Figure 11.9: Case 2, Scenario 6: grid size equal to 100 m. a) Conductivity field, b) Transfer functions, c) true and estimated release history, d) observed and computed concentration values.

Table 11.1: Summary of the study cases and numerical results.

Case #	σ_Y	Scenario #	Sampled grid dimension	nRMSE measurements [%]
1	$\sigma_Y = 1.32$	true field	-	13.31
		1	10×10 m^2	21.56
		2	20×20 m^2	25.89
		3	30×30 m^2	31.48
		4	40×40 m^2	39.16
		5	50×50 m^2	45.09
		6	100×100 m^2	48.75
2	$\sigma_Y = 0.01$	true field	-	0.37
		1	10×10 m^2	3.63
		2	20×20 m^2	27.35
		3	30×30 m^2	26.65
		4	40×40 m^2	57.88
		5	50×50 m^2	61.71
		6	100×100 m^2	24.24
3	$\sigma_Y = 3.6{\cdot}10^{-5}$	true field	-	0.07
		1	10×10 m^2	0.23
		2	20×20 m^2	3.27
		3	30×30 m^2	1.88
		4	40×40 m^2	5.77
		5	50×50 m^2	0.90
		6	100×100 m^2	1.27

11.4 Discussion and conclusions

In the field of hydrology, several problems must be solved under high degree of uncertainty. In particular, recovering the release history of a pollutant in an aquifer requires to know the conductivity properties of the field which determines the faith of the contamination. In this chapter the importance of the knowledge of the conductivity field for recovering the release history has been investigated. Three different fields with a different magnitude of heterogeneity have been considered. For each of them, the reconstruction of the flow field has been based on the observations collected at the node of a grid with cells of different dimensions. A grid too fine is unrealistic, but if the number of the observations is too small the flow field recovered could be unacceptably different from the true one. Starting from the sampled conductivity values, different fields have been estimated by the Kriging method: on them, the geostatistical inverse procedure (*Kitanidis*, 1995) has been applied. Increasing the log conductivity variance, or decreasing the number of the points in which the conductivity is known, the transfer functions become too different from the true ones. As shown in the previous section, a lack of information have severe consequence on the ability of estimating the actual transfer matrix, and so, to properly describe the model that link the release history and the concentration measurements. In

Table 11.1, one can note that the nRMSE increases by increasing the heterogeneity. As expected, the performance declines by decreasing the size of the sampling grid of the hydraulic conductivity. Looking at Case 2, the nRMSE value in Scenario 6 is lower than in Scenario 5: this is due to the temporal shift between the true and the estimated release history. The time shift and the possibility of correctly using the information given by the concentration values collected at the monitoring points are strictly linked at the transfer functions available. Decreasing the number of sample of hydraulic conductivity, the difference between the true and the estimated field is bigger, influencing the goodness of the transfer functions. In conclusion, the answers to the questions raised in Section 11.1:

1. As stated above, all the methods, available in literature, to identify the contaminant source location and/or its release history, can be applied on real field by means of a simple procedure developed by *Butera et al.* (2006) that allows to keep into account non-linear flow field due to heterogeneous porous media, presence of wells, recharge etc.;

2. analyzing the obtained results, both analytical and numerical, it was noticed that, using a sampling grid smaller than 50% of the correlation length of the hydraulic conductivity field, the geostatistical approach (used in this work to recover the release history) was able to estimate quite well the magnitude and the timing of the two main peaks of the true release function; while considering a sampling grid larger than 50% the approach brings to unreliable results. Consequently, considering hydraulic conductivity fields with medium/small heterogeneity, this study indicates that the sampling grid of the hydraulic conductivity has not to exceed the 50% of the correlation length of the field;

3. In general, the number of information required for obtaining a satisfactory release history depends strictly on the heterogeneity magnitude and on the geometry of the problems. All this aspects and the goodness of the conductivity field estimated have consequence to the transfer functions, which express the link between the release history and the concentration values at the monitoring points. Considering hydraulic conductivity field too heterogeneous, the reliability of the transfer functions is not satisfactory, even using small sampling grids. In these cases (for instance Case 1), the efforts in sampling the conductivity field has to be unrealistic. This work confirmed the necessity of reliable and accurate procedures for estimating the hydraulic parameters and their spatial distribution.

Part 5

Appendices

MatLab Scripts

§

A.1 Elaboration of images collected using the sandbox at DICATeA

A.1.1 Script which converts a .RAW image in a .m matrix. `trasforma.m`

```
clear all
clc

% path RAW photo
percorsoPROVA = 'C:\Dottorato\prove_aprile_2013\prova_16apr13\RAW\';
addpath(percorsoPROVA)

% list RAW files
lista = dir(strcat(percorsoPROVA,'*.CR2'));
% number of photos
Nfoto = numel(lista);
cd RAW
A1 = '!dcraw -D -4 '; % RAW a 14 bit
%A1 = '!dcraw -w -o0 -j ';


% Calculation of transformation matrix
      Nfile = 1;
      nomefileCR2 = lista(Nfile).name;
      lunghezza_nomefile = size(nomefileCR2,2);
```

```
21      A = [A1 nomefileCR2];
22      eval(A)
23      disp(A)
24      nomefilePGM = nomefileCR2;
25      nomefilePGM(lunghezza_nomefile-2:lunghezza_nomefile) = 'pgm';
26      PGM = imread(nomefilePGM);
27      RGB = demosaic(PGM,'rggb');
28
29
30      risp = input('vuoi effettuare il cp select?  s / n  \n','s')
31      COObase=[       0       0
32                      289     0
33                      580     0
34                      868     0
35                      0       520
36                      290     519
37                      580     519
38                      869     520];%[mm]
39
40       if (risp == 's')
41          foto = RGB*16;
42
43                      B = checkerboard(1,5,9);
44                      cooapprox = 1000*[
45                       0.2241     0.3244
46                       1.3456     0.2894
47                       2.4804     0.2553
48                       3.6191     0.2257
49                       0.2568     2.3667
50                       1.4219     2.3112
51                       2.5537     2.3112
52                       3.6744     2.2946];
53
54      [coolastra,base_points] = cpselect(foto,B,cooapprox,COObase,'Wait',true);
55
56      save(strcat(percorsoPROVA,'Clastra'),'coolastra');
57
58      clear foto
59
60      else
61          load(strcat(percorsoPROVA,'Clastra'), 'coolastra')
62      end %if
63
64      TFORM = cp2tform(coolastra, COObase,'projective'); % transformation matrix
65
66
67      clear A
68      clear Nfile
69      delete(nomefilePGM)
```

```
70      clear PGM
71      clear RGB
72      clear lunghezza_nomefile
73      clear nomefileCR2
74      clear nomefilePGM
75      clear risp
76
77  % End calculation transformation matrix
78
79
80
81      for Nfile = 1:Nfoto
82
83          nomefileCR2 = lista(Nfile).name;
84          lunghezza_nomefile = size(nomefileCR2,2);
85          A = [A1 nomefileCR2];
86          eval(A)
87          disp(A)
88          nomefilePGM = nomefileCR2;
89          nomefilePGM(lunghezza_nomefile-2:lunghezza_nomefile) = 'pgm';
90          PGM = imread(nomefilePGM);
91          RGB = demosaic(PGM,'rggb');
92
93
94
95
96          %  Cutting image  %
97          sr = 0;
98          sc = 0; % sbordo
99          r1 = coolastra(1,2)+sr;
100         r2 = coolastra(5,2)-sr;
101         c1 = coolastra(1,1)-sc;
102         c2 = coolastra(4,1)+sc;
103         fr = RGB(r1:r2,c1:c2,:);
104         clear RGB
105         Frc = imtransform((fr),TFORM,'size',[2034  3396]);
106         clear fr
107
108          taglio_sup =  97;
109          taglio_inf = 1846;
110
111          Frc = Frc(taglio_sup:taglio_inf,10:3389,:);
112
113
114          save(strcat('C:\Dottorato\prove_aprile_2013\prova_16apr13\mat\',...
115          num2str(Nfile)),'Frc');
116          clear Frc
117          delete(nomefilePGM)
118
```

```
119 end
```

A.1.2 Script used for calibrating the image acquisition system. `calibra_2013.m`

```
1  clear
2  clc
3  close all
4
5  %% Start calibration
6  cd C:\Dottorato\prove_aprile_2013\prova_15apr13\cal\cal_media
7  load 0.mat
8  Frc = uint16(Frc(1:1750,1:3380,1:3));
9  [righe colonne colori] = size(Frc);
10 clear Frc
11
12 intorno = 10;
13 row = floor(righe/intorno);
14 col = floor(colonne/intorno);
15 % Dimension of pixel
16 dim_pixel = 0.8568/3396; % m
17 area_pixel = dim_pixel^2; % m^2
18 spessore = 0.1; % m
19 porosita = 0.37;
20
21 area_intorno = area_pixel*intorno^2; % m^2
22 volume_intorno = area_intorno*spessore*1000; % litri
23 volume_intorno_liquido = volume_intorno*porosita; % litri
24
25 area_tot = area_pixel*row*col; % m^2
26 volume = area_tot*spessore*1000; % litri
27 volume_liquido = volume*porosita; % litri
28
29 %++++++++++++++++++++++++++++++++++++++++++++++++++++++++++++++++++++++
30
31 % Reading images
32 M = {'0.mat','2.mat','5.mat','10.mat','20.mat', '25.mat',...
33   '30.mat', '35.mat', '40.mat', '50.mat'}; % Foto concentrazioni
34 C = [0 2 5 10 20 25 30 35 40 50]; % Concentration in mg/l
35
36 m = size(M,2);
37 m1 = size(C,2);
38
39
40
41 filename = char(M(1,1));
42 load(filename)
43
```

```
Frc = uint16(Frc(1:1750,1:3380,1:3));

fondo = ridimensiona(Frc,intorno,row,col,3);
gr_ridim = rgb2gray(Frc);
fondo_grigio = ridimensiona(gr_ridim,intorno,row,col,1);

clear Frc gr_ridim

R = zeros(row,col,m);
G = zeros(row,col,m);
B = zeros(row,col,m);
grigio_cal = zeros(row,col,m);

    for i = 1:m

        filename = char(M(1,i));
        load(filename)

        Frc = uint16(Frc(:,:,1:3));

        ridim2 = ridimensiona(Frc,intorno,row,col,3);

        gr_ridim = rgb2gray(Frc);
        gr = ridimensiona(gr_ridim,intorno,row,col,1);

        % background depuration
        R(:,:,i) = (ridim2(:,:,1)-fondo (:,:,1));
        G(:,:,i) = (ridim2(:,:,2)-fondo (:,:,2));
        B(:,:,i) = (fondo(:,:,3)-ridim2(:,:,3));
        grigio_cal(:,:,i) = gr - fondo_grigio;

        clear Frc ridim ridim2 gr gr_ridim

    end % for m

   % End calibration

    clear fondo fondo_grigio

   % Start elaboration images of test %%%%

    cd C:\Dottorato\prove_aprile_2013\prova_16apr13\mat


    lista = dir(strcat('*.mat'));
    N_foto = numel(lista);
    clear lista

   % lettura fondo
```

```
93      load 1.mat
94      fondo = ridimensiona(Frc,intorno,row,col,3);
95      gr_ridim = rgb2gray(Frc);
96      fondo_grigio = ridimensiona(gr_ridim,intorno,row,col,1);
97
98      clear Frc
99
100     rosso =  zeros(row,col,N_foto);
101     verde =  zeros(row,col,N_foto);
102     blu   =  zeros(row,col,N_foto);
103     grigio = zeros(row,col,N_foto);
104
105     massaR = zeros(N_foto,1);
106     massaG = zeros(N_foto,1);
107     massaB = zeros(N_foto,1);
108     massa_grigio = zeros(N_foto,1);
109
110
111     for foto = 1:N_foto
112
113
114      clc, disp([num2str(foto) ' di ' num2str(N_foto)])
115      nomefile = [int2str(foto) '.mat'];
116      load (nomefile);
117
118      immagine0 = (ridimensiona(Frc,intorno,row,col,3));
119      gr_ridim = rgb2gray(Frc);
120      gr0 = (ridimensiona(gr_ridim,intorno,row,col,1));
121
122      % background depuration
123      for colore = 1:2
124         immagine(:,:,colore) = (immagine0(:,:,colore)-(fondo(:,:,colore)));
125      end
126         immagine(:,:,3) = (fondo(:,:,3)-immagine0(:,:,3));
127         gr = (gr0-(fondo_grigio));
128
129     clear Frc ridim gr0 immagine0
130
131
132
133         for riga = 1:row
134             for colonna = 1:col
135
136                 vettR = (reshape(R(riga,colonna,:),1,m));
137                 vettG = (reshape(G(riga,colonna,:),1,m));
138                 vettB = (reshape(B(riga,colonna,:),1,m));
139                 vettgrigio = (reshape(grigio_cal(riga,colonna,:),1,m));
140
141               for u = 1:m
```

```
142                     for y = 1:m
143                      if vettG(u) == vettG(y)
144                         vettR(u) = vettR(u)+rand(1);
145                      end
146                      if  vettG(u) == vettG(y)
147                          vettG(u) = vettG(u)+rand(1);
148                      end
149                      if  vettB(u) == vettB(y)
150                          vettB(u) = vettB(u)+rand(1);
151                      end
152                      if  vettgrigio(u) == vettgrigio(y)
153                          vettgrigio(u) = vettgrigio(u)+rand(1);
154                      end
155                    end
156                end
157
158
159
160                 ConcR = interp1(double(vettR),C,double(immagine(riga,colonna,1)),...
161                 'linear','extrap'); % in mg/l
162                 ConcG = interp1(double(vettG),C,double(immagine(riga,colonna,2)),...
163                 'linear','extrap'); % in mg/l
164                 ConcB = interp1(double(vettB),C,double(immagine(riga,colonna,3)),...
165                 'linear','extrap'); % in mg/l
166
167                 Conc_grigio = interp1(double(vettgrigio),C,double(gr(riga,colonna)),...
168                 'linear','extrap'); % in mg/l
169
170                 if ConcR > 0
171                     rosso(riga,colonna,foto) = ConcR;
172                 else
173                     ConcR = 0;
174                     rosso(riga,colonna,foto) = 0;
175                 end
176
177                 if ConcG > 0
178                     verde(riga,colonna,foto) = ConcG;
179                 else
180                     ConcG = 0;
181                     verde(riga,colonna,foto) = 0;
182                 end
183
184                 if ConcB > 0
185                     blu(riga,colonna,foto) = ConcB;
186                 else
187                     ConcB = 0;
188                     blu(riga,colonna,foto) = 0;
189                 end
190
```

```
191                 if Conc_grigio > 0
192                     grigio(riga,colonna,foto) = Conc_grigio;
193                 else
194                     Conc_grigio = 0;
195                     grigio(riga,colonna,foto) = 0;
196                 end
197
198
199                 if ConcR < 25
200                     rosso(riga,colonna,foto) = ConcR;
201                 else
202                     rosso(riga,colonna,foto) = 25;
203                 end
204
205                 if ConcG < 25
206                     verde(riga,colonna,foto) = ConcG;
207                 else
208                     verde(riga,colonna,foto) = 25;
209                 end
210
211                 if ConcB < 25
212                     blu(riga,colonna,foto) = ConcB;
213                 else
214                     blu(riga,colonna,foto) = 25;
215                 end
216
217                 if Conc_grigio < 25
218                     grigio(riga,colonna,foto) = Conc_grigio;
219                 else
220                     grigio(riga,colonna,foto) = 25;
221                 end
222
223
224
225
226             end % for colonna
227         end % for riga
228
229         massaR (foto) = sum(sum(rosso(:,:,foto)))*volume_intorno_liquido; % mg
230         massaG (foto) = sum(sum(verde(:,:,foto)))*volume_intorno_liquido; % mg
231         massaB (foto) = sum(sum(blu  (:,:,foto)))*volume_intorno_liquido; % mg
232         massa_grigio (foto) = sum(sum(grigio(:,:,foto)))*volume_intorno_liquido; % mg
233
234     end
235
236 plot(10:10:N_foto*10,massaR(1:N_foto),'*r',10:10:N_foto*10,massaG(1:N_foto),'og',...
237 10:10:N_foto*10,massaB(1:N_foto),'+b',10:10:10*N_foto,massa_grigio(1:N_foto),'y')
238
239 save elab_16apr13
```

A.1.3 Script used for elaborating the images acquired in the .m format. ridimensiona.m

```
function [ridotta] = ridimensiona(immagine,intorno,righe,colonne,COL)
% downsampling of the images

ridotta = uint16(zeros(righe,colonne,COL));
somma = 0;

for colore = 1:COL
    for i = 1:righe
        for j = 1:colonne

            somma = sum(sum(immagine(1+intorno*(i-1):intorno*(i-1)+intorno,...
            1+intorno*(j-1):intorno*(j-1)+intorno,colore)))/(intorno^2);

            ridotta(i,j,colore) = uint16(somma);

            somma = 0;
        end
    end
end
```

A.1.4 Script used for verifyng the reliability of the results. portate.m

```
clear
clc
close all

%% Data management
% file txt of acquisition
load prova_2.txt
load massa_modello.txt % mass balance MT3D

% data from experiment
load elab_16apr13_prova2


% analogic data from sand box
tempoo = prova_2(:,1); % s
tensione_vaso = prova_2(:,2);
tensione_Qfondo = prova_2(:,3);


m_tempoo = size (tempoo,1);

% sampling frequency
```

```
23 f = 10; %Hz
24 DT = 1/f; %s
25
26 % data of the test
27 inizio1 = 30; %second
28 fine1 = 950; %second
29
30 inizio2 = 1800; %second
31 fine2 = 2480; %second
32
33 clear prova_2
34
35 % Calibration Mariotte's bottle
36 a = 760.88;
37 b = -939.9;
38
39 % smoothing acquisition
40 arrotondamento = 300;
41
42 %  Volume inside Mariotte's bottle
43 Volume_vaso = a*smooth(tensione_vaso,arrotondamento) + b; % ml
44
45 % Background discharge
46 Q_fondo = smooth(tensione_Qfondo,arrotondamento) * 10;
47
48
49 % volumetric discharhe injected in the sandbox
50 tempo = tempoo(2:end);
51 Q_inj = -diff(Volume_vaso)/DT; % ml/s
52
53
54 % taking into account a recharge of the Mariotte's Bottle
55
56 for i = 1:fine1*f
57     Q_inj(i,1) = Q_inj(i);
58 end
59
60 for i = fine1*f+1:inizio2*f
61     Q_inj(i,1) = 0;
62 end
63
64 for i = inizio2*f+1:fine2*f
65     Q_inj(i,1) = Q_inj(i);
66 end
67
68 for i = fine2*f+1:m_tempoo-1
69     Q_inj(i,1) = 0;
70 end
71
```

```
% Concentration of the tracer
C0 = 30; % mg/l

% Mass rate injected in the sandbox
QM_inj = Q_inj*C0/1000; % mg/s

% Mass rate in a DT
M_inj = QM_inj*DT; %mg

% Cumulative mass injected
Mcum_inj = cumsum(M_inj); % massa totale immessa in mg

% Time axis

Delta_scatto = 5; %second
Inizio_scatto = 10; %second

tempo_scatto = 0:Delta_scatto:(N_foto-1)*Delta_scatto;
tempo_scatto = tempo_scatto + Inizio_scatto;

% Analyses along a vertical cross section
h = size(verde,1);

% Position
distanza = input('Distance from the injector (in cm) of the vertical ...
cross section (from 0 to 75 cm)?', 's');
distanza = fix(str2num(distanza)/(dim_pixel*intorno*100));
riga = 200 - distanza;

% Porosity
n = 0.37;
istante = 150;

p1 = 4;
p2 = 197;
g1 = reshape(verde(64,p1,:),1,N_foto);
g2 = reshape(verde(64,p2,:),1,N_foto);

Delta_xx = (p2-p1)*dim_pixel*15;
figure(99)
plot(g1,'-r')
hold on
plot(g2,'-b')

t1 = input('Tempo arrivo 1 =', 's');
t2 = input('Tempo di arrivo 2=', 's');

t1 = str2num(t1);
t2 = str2num(t2);
```

```
121
122 Deltat_arrivo = abs(t1-t2)*Delta_scatto; %s
123
124 Delta_x = abs(p2-p1)*dim_pixel*intorno*100; %cm
125
126 % Calculated effective velocity
127 v_eff = Delta_x/Deltat_arrivo; %cm/s
128
129 clear Delta_x
130
131 Delta_striscia = intorno*100 * dim_pixel; %cm
132 Delta_tt = Delta_striscia/v_eff; %s
133
134
135 for foto = 1:N_foto
136
137     % Mass resident in the vertical cross section
138     for i = 1:h
139         Deltam_rosso(i) = 0.1*dim_pixel*intorno*rosso(i,riga,foto)*...
140         n*dim_pixel*intorno*1000;  %mg
141         Deltam_verde(i) = 0.1*dim_pixel*intorno*verde(i,riga,foto)*...
142         n*dim_pixel*intorno*1000; %mg
143         Deltam_blu(i) = 0.1*dim_pixel*intorno*blu(i,riga,foto)*...
144         n*dim_pixel*intorno*1000; %mg
145         Deltam_grigio(i) = 0.1*dim_pixel*intorno*grigio(i,riga,foto)*...
146         n*dim_pixel*intorno*1000; %mg
147     end
148
149     M_rosso(foto) = sum(Deltam_rosso); %mg
150     M_verde(foto) = sum(Deltam_verde); %mg
151     M_blu(foto) = sum(Deltam_blu); %mg
152     M_grigio(foto) = sum(Deltam_grigio);
153
154     Q_m_foto_rosso(foto) = M_rosso(foto)/Delta_tt; %mg/s
155     Q_m_foto_verde(foto) = M_verde(foto)/Delta_tt;
156     Q_m_foto_blu(foto) = M_blu(foto)/Delta_tt;
157     Q_m_foto_grigio(foto) = M_grigio(foto)/Delta_tt;
158
159     Q_iniettore_r(foto) = Q_m_foto_rosso(foto) / C0;
160     Q_iniettore_g(foto) = Q_m_foto_verde(foto) / C0;
161     Q_iniettore_b(foto) = Q_m_foto_blu(foto) / C0;
162     Q_iniettore_grigio(foto) = Q_m_foto_grigio(foto) / C0;
163
164
165 end
166
167 %% PLOT
168
169 close all
```

```
170
171 massa_modello(:,2) = massa_modello(:,2)/1000;
172
173 figure(1)
174 subplot(2,2,1)
175 plot(tempo_scatto,massaR(1:N_foto)*fattore_elab,'*r',tempo_scatto,...
176 massaG(1:N_foto)*fattore_elab,'og',tempo_scatto,massaB(1:N_foto)*fattore_elab,'+b',...
177 tempo_scatto,massa_grigio(1:N_foto)*fattore_elab,'y')
178 hold on
179 plot (tempoo(1:m_tempoo-1),Mcum_inj*fattore_mis,'k')
180 plot(massa_modello(:,1),massa_modello(:,2),'--k')
181 title('Comparison between mass injected and resident')
182 xlabel('Time (s)')
183 ylabel('Mass injected/Mass resident(mg)')
184 grid on
185
186 subplot(2,2,2)
187 A = [0 0; inizio1 0;
188     inizio1 max(Q_fondo)+1;
189     fine1 max(Q_fondo)+1;
190     fine1 0;
191     inizio2 0;
192     inizio2 max(Q_fondo)+1;
193     fine2 max(Q_fondo)+1;
194     fine2 0;
195     tempoo(m_tempoo) 0];
196 h = area(A(:,1),A(:,2));
197 set(h,'FaceColor',[0.2 0 0])
198 hold on
199 plot(tempoo,Q_fondo,'-m')
200 title('Background discharge')
201 xlabel('Time (s)')
202 ylabel('Background discharge (ml/s)')
203 ylim([23 27])
204
205 subplot(2,2,3)
206 plot(tempo, Q_inj)
207 title('Volumetric discharge injected')
208 xlabel('Tempo (s)')
209 ylabel('Volumetric discharge injected (ml/s)')
210 grid on
211
212 subplot(2,2,4)
213 plot(tempo, QM_inj*1/fattore_elab)
214 title('Mass rate injected')
215 xlabel('Time (s)')
216 ylabel('Mass rate injected (mg/s)')
217 grid on
218 hold on
```

```
tempo_percorrenza = 220; %s
plot(tempo_scatto-tempo_percorrenza,Q_m_foto_verde,'--g')
plot(tempo_scatto-tempo_percorrenza,Q_m_foto_rosso,'--r')
plot(tempo_scatto-tempo_percorrenza,Q_m_foto_blu,'--b')
plot(tempo_scatto-tempo_percorrenza,Q_m_foto_grigio,'--y')
```

A.2 SRSI method

A.2.1 Script for building the transfer matrix and the data vector from raw data. `costruzione_FF_2.m`

```
% ********************************************************************
% Script for building the transfer matrix from the numerical model data and
% data from the experimental data

% dt: time interval data from numerical model
% n:  size vector of data from numerical model
% qo: discharge injected in the numerical model
% nn: size fdt
% m_tot: number of concentration data available (number of photo)
% numero_punti: how many concentration data we want
% m: number of concentration data we use at the end

% RISULTATI                                                dimensione

% FF: TF                                                    m+1 x nn
% tempoZ: observation sampling time                           m x 1
% Z: data vector                                            m x 1
% ********************************************************************

clear
clc
close all

dati_prova3

% breakthrough curve from numerical model
txt_curvaS_modello_numerico = '35_81_P1.txt';

% experimental concentration data
txt_misure_Sandbox = 'Cp8.txt';

% file output
nomefile_output = '35_81_P1.mat';

%% Building a fdt

C_modello = load(txt_curvaS_modello_numerico);
```

A.2.1. Script for building the transfer matrix and the data vector from raw data.

costruzione_FF_2.m

```
38
39 dt = C_modello(4,1) - C_modello(3,1);
40
41 % cutting time before injection
42 Cc = C_modello(Inizio_iniezione_modello/5+1:end,:);
43
44 % time correction
45 Cc(:,1) = Cc(:,1) - Inizio_iniezione_modello;
46 n = size(Cc,1);
47
48 qo = 3; %ml/s in the numerical model
49
50 t_durata_fdt = 3000;  % (s)
51 nn = t_durata_fdt/dt; %
52
53 fdt = zeros(nn,2);
54
55 fdt(:,1) = dt:dt:nn*5;
56 fdt(2:n,2) = diff(Cc(:,2))/dt/qo;
57
58 % data < 0 imposed to 0
59 glizero = find(fdt(:,2)<0);
60 fdt(glizero,2) = fdt(glizero,2) * 0;
61
62 figure
63 plot(fdt(:,1),fdt(:,2))
64 title('Funzione di trasferimento')
65 xlabel('Tempo (s)')
66 ylabel('Fdt')
67
68 conc = load (txt_misure_Sandbox);
69 m_tot = size(conc,1); %numero totale di misure, cio il numero di foto scattate
70
71 % downsampling
72 numero_punti = 30; % circa  perch poi c' l'approssimazione
73 step = floor(m_tot/numero_punti);
74
75 sottocamp = 1:step:m_tot;
76
77 tempoZ = conc(sottocamp,1);
78 Z = conc(sottocamp,2);
79
80 % size data vector
81 m = size(Z,1);
82
83
84 %% BUILDING THE TRANSFER MATRIX FROM THE SINGULAR fdt
85
86
```

```
F_nocamp = zeros(m_tot,nn);
F_nocamp(1,1:nn) = fdt(:,2)';

for i=2:m_tot
    F_nocamp(i,i:nn) = fdt(1:nn-i+1,2)';
end

FF = zeros(m+1,nn);
FF(1,:) = fdt(:,1)';
FF(2:m+1,:) = F_nocamp(sottocamp,:);

figure
for j = 2:m+1
    plot(FF(1,:),FF(j,:))
    hold on
    title('Plottaggio di tutte le funzioni di trasferimento')
    xlabel('Tempo (s)')
    ylabel('Fdt')
end

%% SAVE data
FF_35_81_P1 = FF;
save(nomefile_output, 'FF_35_81_P1')
```

A.2.2 *Script for building the transfer matrix and the data vector from raw data for N potential sources.* `costruzione_F_N_SOR.m`

```
%             Variable                                  Dimension

%          number of sources                             N_SOR
% observation at single point                           m = mp
%          size fdt                                       n
%      number observation points                          p
%       transfer matrix                              p*m x n x N_SOR
%       data vector Z                                  p*m x 2

clc
clear all
close all

Inizio_acquisizione = 0;
Inizio_scatto = 240;
Inizio_iniezione = 310;
Tempo_taglio = 2310;
Inizio_iniezione_modello = 300; %s

% TF single point
```

A.2.2. Script for building the transfer matrix and the data vector from raw data for N potential sources. `costruzione_F_N_SOR.m`

```
filenameP1 = {'23_69_P1.mat',...
              '23_75_P1.mat',...
              '23_81_P1.mat',...
              '29_69_P1.mat',...
              '29_75_P1.mat',...
              '29_81_P1.mat',...
              '35_69_P1.mat',...
              '35_75_P1.mat',...
              '35_81_P1.mat'};


filenameP2 = {'23_69_P2.mat',...
              '23_75_P2.mat',...
              '23_81_P2.mat',...
              '29_69_P2.mat',...
              '29_75_P2.mat',...
              '29_81_P2.mat',...
              '35_69_P2.mat',...
              '35_75_P2.mat',...
              '35_81_P2.mat'};


% ********************************************************************
% point location
%          1                   4                   7
%       (-3,+3)             (+0,+3)             (+3,+3)
%          +                   +                   +
%       (23,69)             (29,69)             (35,69)
%
%
%          2                   5                   8
%       (-3,+0)             (+0,+0)             (+3,+0)
%          +                   +                   +
%       (23,75)             (29,75)             (35,75)
%
%
%          3                   6                   9
%       (-3,-3)             (+0,-3)             (+3,-3)
%          +                   +                   +
%       (23,81)             (29,81)             (35,81)
%
% ********************************************************************


punti = [-3     3;
         -3     0;
         -3    -3;
          0     3
          0     0  % true source
```

```
70              0    -3
71              3     3
72              3     0
73              3    -3];
74  N_SOR = size(filenameP1,2);
75
76  load 23_69_P1.mat
77  m = size(FF,1)-1;
78  n = size(FF,2);
79  p = 2;
80  clear FF_23_69_P1
81
82  F = zeros(2*m+1,n,N_SOR);
83
84  % P1
85  for sorgenti = 1:N_SOR
86
87      filein = char(filenameP1(sorgenti));
88      load(filein)
89
90      F(1,:,sorgenti) = FF(1,:);
91      F(1:m,:,sorgenti) = FF(2:end,:);
92
93  end
94
95  % P2
96  for sorgenti = 1:N_SOR
97
98      filein = char(filenameP2(sorgenti));
99      load(filein)
100
101     F(m+1:2*m,:,sorgenti) = FF(2:end,:);
102
103 end
104
105 % Building Z vector
106
107 % Z1
108 conc = load('Cp7.txt');
109
110 m_tot = size(conc,1); %numero totale di misure, cio il numero di foto scattate
111
112 % downsampling
113 numero_punti = 30; % circa  perch poi c' l'approssimazione
114 step = floor(m_tot/numero_punti);
115
116 sottocamp = 1:step:m_tot;
117
118 tempoZ_P1 = conc(sottocamp,1);
```

A.2.2. Script for building the transfer matrix and the data vector from raw data for N potential sources. `costruzione_F_N_SOR.m`

```
Z_P1 = conc(sottocamp,2);

mp = size(Z_P1,1);

Z = zeros(2*mp,2);
Z(1:mp,1) = tempoZ_P1;
Z(1:mp,2) = Z_P1;


% Z2

conc = load('Cp8.txt');

m_tot = size(conc,1);

% downsampling
numero_punti = 30;
step = floor(m_tot/numero_punti);

sottocamp = 1:step:m_tot;

tempoZ_P2 = conc(sottocamp,1);
Z_P2 = conc(sottocamp,2);

mp = size(Z_P2,1);

Z(mp+1:2*mp,1) = tempoZ_P2;
Z(mp+1:2*mp,2) = Z_P2;

osservazioni = Z;
T_osservazioni = Z(:,1);
clear Z
Z = osservazioni(:,1);

% Reading true release history

portata = load ('portata_3.txt');

% downsampling
sottocamp_portata = 10:10:size(portata,1);
QQ = portata(sottocamp_portata,:);
Q_misurata(:,1) = QQ(Inizio_scatto+1:Tempo_taglio,1)-Inizio_scatto;
Q_misurata(:,2) = QQ(Inizio_scatto+1:Tempo_taglio,2);

figure
plot(Q_misurata(:,1),Q_misurata(:,2))
title('Portata di fluorescina immessa')
xlabel ('Tempo(s)')
ylabel ('q immessa (ml/s)')
```

```
168
169 obs = Q_misurata;
170
171 %% Save data
172 save('FDT_dp.m','F','Z','T_osservazioni','osservazioni','obs','punti')
```

A.3 BPM-ASM method

A.3.1 Script for changing the source position in MODFLOW and MT3D and running the simulation. `cambio_pos_neup.m`

```
1  clear
2  clc
3
4  TIME_STEP = 200;
5
6  KK = 140;
7  JJ = 192;
8
9  C1 = zeros(KK,JJ);
10 C2 = zeros(KK,JJ);
11
12 row_min = 65;
13 row_max = 65;
14
15 col_min = 10;    col_max = 60;
16
17 for row = row_min:row_max;%2:KK-1
18     for col = col_min:col_max;%2:JJ-1
19
20         cd C:\modello\BPM_MODFLOW\Out_Mf2k
21
22         fidMOD = fopen('BPM.wel','wt');
23         rigaMOD = '%u 1 %u 3.0 0 0.0 -1';
24         strMOD = sprintf(rigaMOD,row,col);
25         fprintf(fidMOD,'1 740 AUX IFACE AUX QFACT AUX CELLGRP\n 1
   0 0\n');
26         fprintf(fidMOD,strMOD);
27         for y = 1:TIME_STEP
28             fprintf(fidMOD,'  -1  0  0\n');
29         end
30
31         ! mf2k.exe BPM.mfn
32
33         cd C:\modello\BPM_MT3DMS
34
35         fidMUL = fopen('BPM.ssm','wt');
```

```
36
37          riga = '        %u          1        %u 20.000000          2 20.000000\n';
38          str = sprintf(riga,row,col);
39          fprintf(fidMUL,' T F F F T F\n        229\n');
40          for h = 1:TIME_STEP
41              fprintf(fidMUL,'          1\n');
42              fprintf(fidMUL,str);
43          end
44
45
46          ! mt3dms52.exe BPM.mts
47
48          % lettura concentrazioni
49          fidCON = fopen('BPM.ocn','rt');
50
51          for i = 1:25936    % prime righe
52              fline = fgetl(fidCON);
53          end
54
55          riga_C1 = fgetl(fidCON);
56          riga_C2 = fgetl(fidCON);
57
58          C1(row,col) = str2num(riga_C1(65:69));
59          C2(row,col) = str2num(riga_C2(65:69));
60
61          fclose(fidCON);
62          clc
63      end % col
64  end % row
```

A.4 Application of Hantush to field data

A.4.1 Script used for applying the Hantush formula to the experimental data. `calcola_s.m`

```
1  % ********************************************************************* %
2  % Hantush method
3  % ********************************************************************* %
4
5  % ************************  VARIABILI  ************************** %
6  % s_obs: observed drawdown
7  % s_P  : t,observed drawdown
8  % r    : distance from the well
9  % t    : time vector
10 % Q    : discharge from the well
11 % m    : thickness aquitard
12 % c    : [T] --> lambda = sqrt(T * c)
13 % X0   : [T0 S0 c0], starting values from optimization
```

```
% X_min: low value allowed for X
% X_max: upper value allowed for X
% X_opt: optimized value X = [T S c]
% s_est: drawdown estimated
% ********************************************************************* %

clear
clc
close all

% ****************** Dati del campo pozzi ************************** %
% Distance from well P4                                                %
% P1: 2.35 m                                                           %
% P2: 2.91 m                                                           %
% P3: 5.83 m                                                           %
% ********************************************************************* %

% ******************  Value to change    ************************** %
file = 's_P3_25mag15_Q051';
r = 5.83;      % m
Q = 0.00051;  % m3/s
m = 0.6;       % m

%        [  T    S   c ]
X0 =     [1e-4 1e-7 1e7];
X_min = [1e-5 1e-7 5e4];
X_max = [1e-2 1e-2 1e8];
% ********************************************************************* %

nome_file_in = strcat(file,'.txt');
nome_file_out = strcat(file,'_out.txt');
nome_file_par = strcat(file,'_par.txt');

s_P = load(nome_file_in);
t = s_P(:,1)'; % tempo in secondi
s_obs = s_P(:,2)';
N = size(s_obs,2);

% optimization
X_opt = fminsearchbnd(@(X)sum((s_obs-Hantush(X,r,t,Q)).^2), X0,X_min,X_max);

s_est = Hantush(X_opt,r,t,Q);

W_est = s_est.*(4*pi*X_opt(1))/Q;
u = r^2*X_opt(2)./(4*X_opt(1)*t);
W_obs = s_obs.*(4*pi*X_opt(1))/Q;

RMSE = sqrt(sum((s_obs - s_est).^2)/N);
nRMSE = RMSE/(max(s_obs)-min(s_obs));
```

A.4.1. Script used for applying the Hantush formula to the experimental data. `calcola_s.m`

```
63
64 % ******************          Figures      ************************** %
65 subplot(2,1,1)
66 loglog(1./u(10:end),W_obs(10:end),'or')
67 hold on
68 loglog(1./u(10:end),W_est(10:end))
69
70 subplot(2,1,2)
71 plot(t,s_est*100)
72 hold on
73 plot(s_P(:,1),s_P(:,2)*100,'*r')
74 xlabel('Tempo(s)')
75 ylabel('Abbassamento (cm)')
76 legend('Abb. stimato','Abb. osservato')
77
78 lambda = sqrt(X_opt(1)*X_opt(3));
79 kv = m/X_opt(3);
80
81 d1 = strcat('T = ',num2str(X_opt(1)),'m2/s');
82 d2 = strcat('S = ',num2str(X_opt(2)));
83 d3 = strcat('kv = ',num2str(kv),'m/s');
84 d4 = strcat('c = ',num2str(X_opt(3)),'s');
85 d5 = strcat('nRMSE = ',num2str(nRMSE*100),'%');
86 disp(d1)
87 disp(d2)
88 disp(d3)
89 disp(d4)
90 disp(d5)
91
92 % ******************* save results      ******************* %
93
94 export(:,1) = t';
95 export(:,2) = s_obs';
96 export(:,3) = s_est';
97 export(:,4) = 1./u;
98 export(:,5) = W_obs;
99 export(:,6) = W_est;
100 save(nome_file_out,'export','-ascii');
101
102 fidMOD = fopen(nome_file_par,'wt');
103 fprintf(fidMOD,'%s\n',d1);
104 fprintf(fidMOD,'%s\n',d2);
105 fprintf(fidMOD,'%s\n',d3);
106 fprintf(fidMOD,'%s\n',d4);
107 fprintf(fidMOD,'%s',d5);
108 fclose(fidMOD);
```

A.5 Analytical calculation of sandbox deformation

A.5.1 Script for estimating analytically the deformation of sandbox walls. `calcolo_distanza.m`

```
clear all
clc

load marker.txt

x = marker(:,2);
y = marker(:,3);
z = marker(:,4);

n_marker = size(marker,1);

% points in the plane

p1 = 1;
p2 = 4;
p3 = 5;

% creation of the two vectors

v1 = marker(p2,2:4) - marker(p1,2:4);
v2 = marker(p3,2:4) - marker(p1,2:4);

% vectorial product

pvet = cross(v1,v2)

% estimating plane equation
%           ax + by +cz +d = 0

a = pvet(1);
b = pvet(2);
c = pvet(3);

d = -1*pvet(1)*marker(p1,2)-1*pvet(2)*marker(p1,3)-1*pvet(3)*marker(p2,4);

spanciamento = zeros(n_marker,2);
spanciamento(:,1) = marker(:,1);

for i = 1:n_marker
    spanciamento(i,2) = abs(a*marker(i,2)+b*marker(i,3)+c*marker(i,4)+d)/sqrt(a^2+b^2+c
end

plot3(x,y,z,'*r')
```

```
44 hold on
45 grid on
46 title('Marker nello spazio e spanciamento in mm')
47
48 for j = 1:n_marker
49     text(x(j)+0.01,y(j)+0.1,z(j),num2str(spanciamento(j,2)))
50 end
```

Permeameter tests at University of Wisconsin

B

§

At the laboratory of the Department of Geoscience (UW - Madison) several constant and falling head permeability tests were carried out in order to estimate the permeability of different materials used in the sand box; they were useful even to understand a reasonable pattern of material to investigate with the M-OHT procedure. In Fig. B.1 is represented a permeameter like the one used during the tests. The results of the tests are summarized in Fig. B.2

B.1 Constant head permeabilty test

The procedure used consists of the following steps:

- mix sufficient water into the sample to prevent segregation of particle sizes during placement into permeameter. Enough water should be added to allow the mixture to flow freely, forming layers
- remove both the chamber cap and upper chamber from the unit by unscrewing the three knurled cap nuts and lifting them off the tie rods
- position one porous stone on the inner support ring in the base of the chamber
- using a scoop or funnel, pour the prepared specimen into the lower chamber, using a circular motion to fill the lower chamber to a depth of 1.5 cm. A uniform layer should be formed
- use an appropriate tamping device to compact the layer of soil to the desired density. Repeat the compacting procedure until the sample is within 2 cm of the top of the lower chamber section

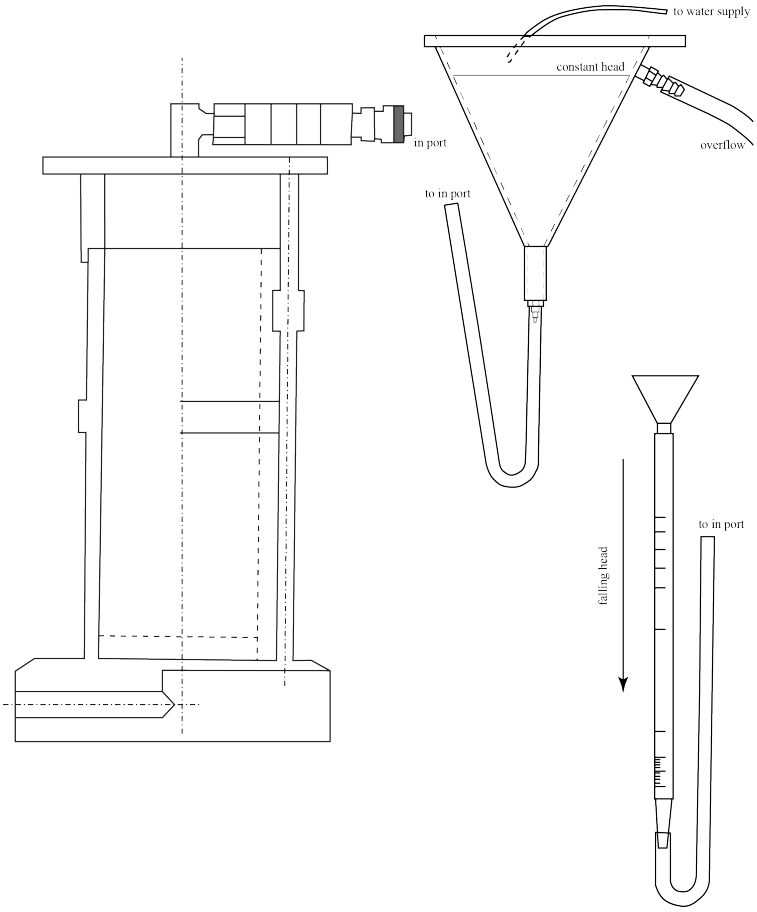

Figure B.1: Permeameter used during the test and the equipment for constant and falling head tests.

- replace the upper chamber section, placing the rubber gasket between the chamber sections. It is important to not disturb the test specimen. Continue the sample placement operation until the level of compacted material is about 2 cm below the rim of the upper chamber. Carefully level the surface of the specimen and place the upper porous stone on it

- Place the compression spring on the porous stone. Replace the chamber cap and sealing gasket, securing it firmly with the cap nuts. The spring will restrict upward sample movement

- measure and record the sample lenght

- assemble the constant head funnel, rod and meter stick. Use the rod clamp the funnel's lower portion
- adjust the level of the funnel to allow the constant water level in it to remain a few cm above the top of the specimen
- connect the flexible tube from the tail of the funnel to the bottom outlet of the permeameter. Keep the valves on the top of the permeameter open
- place a receiver at the top outlet to collect any water that may come out
- if preferred, a piece of tubing may be connected to the outlet, leading the water to a sink
- open the bottom outlet valve and allow water to flow into the permeameter
- as soon as water begins to flow out of the top control (deairing) valve, close the control valve, letting the water flow out the outlet for a time
- close the bottom outlet valve and disconnect the flexible tubing at the bottom. Connect the constant head funnel to the top side port
- open the bottom outlet valve and raise the constant level head (funnel) to a convenient height to get a reasonable steady flow of water
- accurately measure the vertical distance between the funnel overflow level and the chamber outflow level
- measure and record the lenght of the specimen
- allow adequate time for the flow pattern and/or specimen to stabilize
- after equilibrium flow has benn established, measure the time taken to have specified volume of water flowing out. Use a measuring cylinder and a stop watch. Repeat three or more times, calculating the average time

The equation used for calculating the permeability k is:

$$k = \frac{VL}{Aht} \tag{B.1}$$

where V [L^3] is the collected volume of water, L [L] is the lenght of soil column, A [L^2] is the area of the soil column, h [L] is the head difference and t [T] is the time required to get the volume V.

B.2 Falling head permeability test

The procedure used consists of the following steps:

- compact the sample in the lower chamber section of the permeameter, in layers approximately 1.5 cm deep, to within about 2 cm of the lower chamber rim. Use an appropriate tamping device to compact the sample to the desired density
- remove the upper section of the chamber tie rods and place the upper porous stone on the specimen, securing the upper section of the chamber with spring to the unit
- measure and record the length of the specimen
- use the clamp to attach the falling head burette to the support rod. Position the burette as high as is possible for practicality. Place the meter stick directly behind the burette, so the height of water in the burette above the chamber outflow port may be read
- saturate the specimen, following the steps outlined above
- measure the height of the two levels from the outflow level

In this case, the equation used for calculating the permeability is:

$$k = \frac{aL}{At} \ln \frac{h_0}{h_1} \tag{B.2}$$

where a [L^2] is the area of the burette, L [L] is the length of soil column, A [L^2] is the area of the soil column, h_0 [L] is the initial height of water, h_1 [L] is the final height of water ($h_0 - \Delta h$) and t [T] is the time.

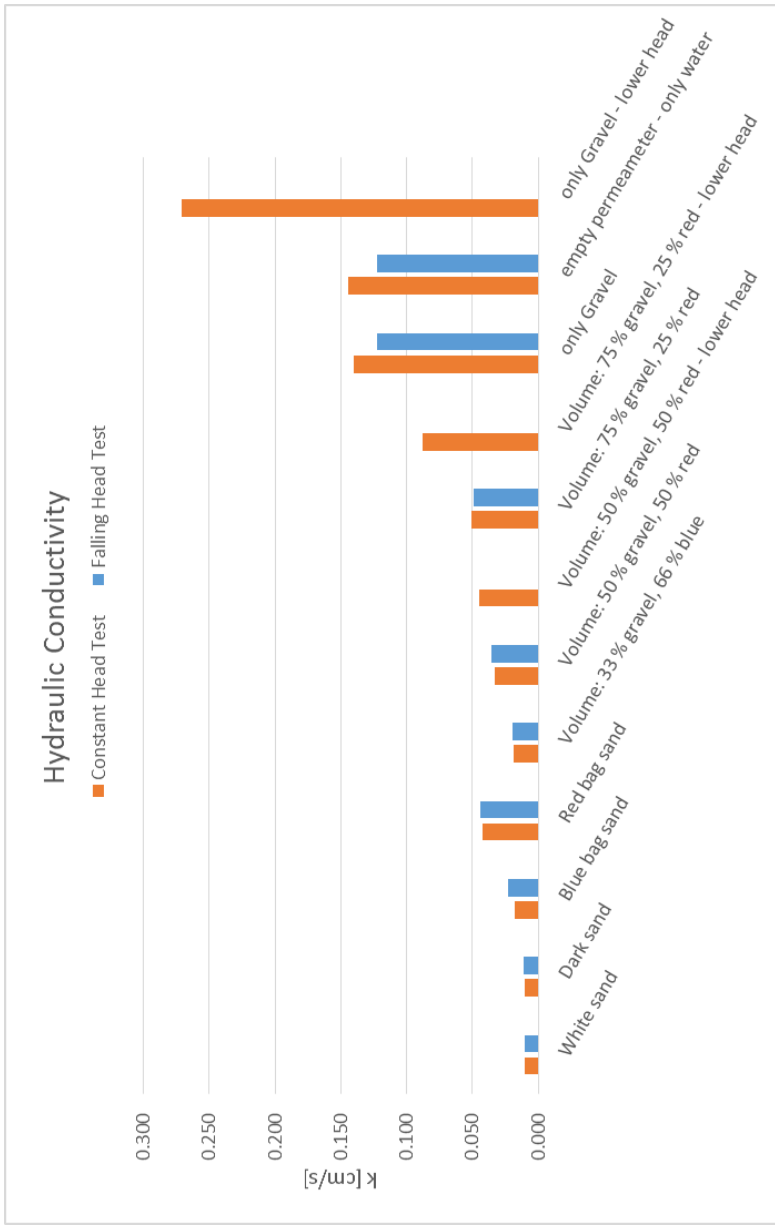

Figure B.2: Summary of the permeameter tests.

C

Well field instruments

§

C.1 Pressure and temperature probes

The pressure and temperature probes are the submersible OTT Orpheus Mini and AquiLite Kompaktsonde ATP00; they have been designed for the reliable monitoring and storage of water level and temperature. The main application of such kind of probes is the installation in groundwater pipes and wells. Looking at the most recent OTT Orpheus Mini, it is equipped with a rugged, ceramic-capacitive measuring cell and a precise temperature sensor. A data logger, which can be configured individually, stores and manages the monitored measured values in a 4 MB non-volatile memory (corresponds to approximately 500,000 measured values). The connexion for data retrieval and start-up and the power supply of the OTT Orpheus Mini are provided by the communication unit. The kevlar-reinforced pressure probe cable with pressure compensation capillary in combination with a dessicant cartridge prevents reliably measuring errors by compensating barometric pressure fluctuations.

C.2 Contact gauge

The manual water meter available in the well field is the OTT Contact Gauge. The electric contact gauges are used for fast and accurate measurements of water level in groundwater areas. They are suitable for both control measurements as well as for continuous monitoring of pump tests. Fig. C.2 shows the OTT Contact Gauge and Table C.3 reports its main characteristics.

Figure C.1: Pressure and temperature probe OTT Orpheus Mini.

Table C.1: Main characteristics of the OTT Orpheus Mini.

Measuring range	0-40 m water column
Resolution pressure	0.01 % FS
Accuracy pressure	± 0.05 % FS
Resolution temperature	0.1 °C
Accuracy temperature	± 0.5 °C
Interface	Infrared (IrDA)
Memory	4 MB
Number of measured values	approx. 500000
Reading interval	1 second 24 hours
Storage interval	1 second 24 hours

Table C.2: Main characteristics of the AquiLite sensor.

Measuring range	1-10 bar
Resolution pressure	0.1 % FS
Accuracy pressure	± 0.005 % FS
Reading interval	1 second 24 hours
Storage interval	1 second 24 hours
Storage temperature	-20°C to +50°C

Figure C.2: OTT Contact Gauge.

Table C.3: Main characteristics of the OTT Contact Gauge.

Measuring range	0-50 m
Measuring accuracy	0.1% of the measured value
Measuring tape type	2-stranded
Labelling	Meter scale: black; cm divisions and dm numbers

C.3 Magnetic flow meters

The two magnetic flow meters (*Mag-Flow*) used in the well field are *Fischer & Porter* production. The electromagnetic flow meter can be used to accurately measure the flow rate of liquids which have an electrical conductivity bigger than 5 μS/cm. The flow meters are the model COPA-XM and present a linear and accurate flow rate metering independent of flow profile. Fig. C.3 shows the flow meters and Table C.4 reports its main characteristics.

C.4 Pumps

C.4.1 Pump SQ 7-40

Pump in Fig. C.4 has been used for extracting water from the well.

Figure C.3: *Fischer & Porter* magnetic flow meters.

Table C.4: Main characteristics of the *Fischer & Porter* magnetic flow meters available in the Boretto well field.

DN	100 mm	50 mm
Warm-Up time	30 min	30 min
$Q_{max}DN$	240 m^3h^{-1}	60 m^3h^{-1}
Accuracy	Q > 0.05 $Q_{max}DN$; ± 0.05 % VM	Q < 0.05 $Q_{max}DN$; ± 0.0002 % $Q_{max}DN$

C.4.2 Pump Euromatic PVC 500

Pump in Fig. C.5 has been adopted for injecting the water in the well during the multi-oscillatory pumping tests.

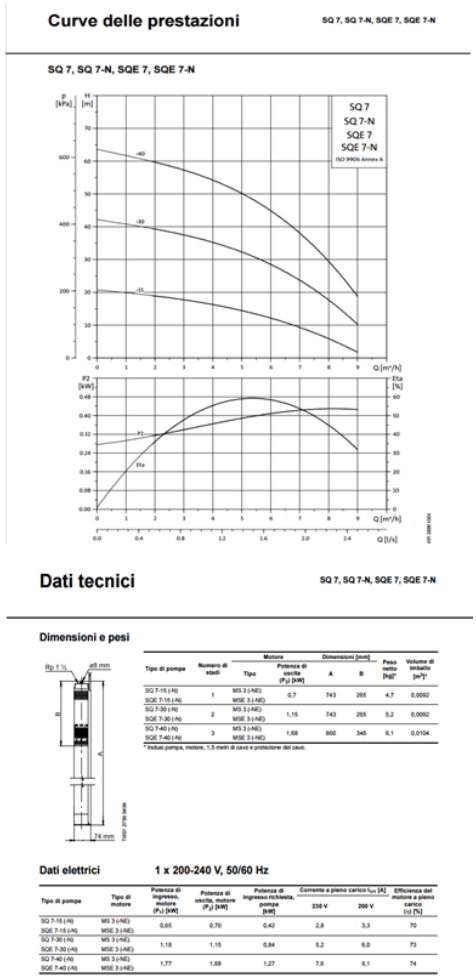

Curve delle prestazioni

SQ 7, SQ 7-N, SQE 7, SQE 7-N

SQ 7, SQ 7-N, SQE 7, SQE 7-N

Dati tecnici

SQ 7, SQ 7-N, SQE 7, SQE 7-N

Dimensioni e pesi

Tipo di pompa	Numero di stadi	Motore		Dimensioni [mm]		Peso netto [kg]*	Volume di imballo [m³]*
		Tipo	Potenza di uscita (P_2) [kW]	A	B		
SQ 7-15 (-N) SQE 7-15 (-N)	1	MS 3 (-NE) MSE 3 (-NE)	0,7	743	265	4,7	0,0092
SQ 7-30 (-N) SQE 7-30 (-N)	2	MS 3 (-NE) MSE 3 (-NE)	1,15	743	265	5,2	0,0092
SQ 7-40 (-N) SQE 7-40 (-N)	3	MS 3 (-NE) MSE 3 (-NE)	1,68	860	346	6,1	0,0104

* Indusi pompa, motore, 1,5 metri di cavo e protezione del cavo.

Dati elettrici **1 x 200-240 V, 50/60 Hz**

Tipo di pompa	Tipo di motore	Potenza di ingresso, motore (P_1) [kW]	Potenza di uscita, motore (P_2) [kW]	Potenza di ingresso richiesta, pompa [kW]	Corrente a pieno carico $I_{1/1}$ [A]		Efficienza del motore a pieno carico (η) [%]
					230 V	200 V	
SQ 7-15 (-N)	MS 3 (-NE)	0,85	0,70	0,42	2,8	3,3	70
SQE 7-15 (-N)	MSE 3 (-NE)						
SQ 7-30 (-N)	MS 3 (-NE)	1,18	1,15	0,84	5,2	6,0	73
SQE 7-30 (-N)	MSE 3 (-NE)						
SQ 7-40 (-N)	MS 3 (-NE)	1,77	1,68	1,27	7,6	9,1	74
SQE 7-40 (-N)	MSE 3 (-NE)						

Figure C.4: Pump SQ 7-40 used for exctracting water from the well.

EUROMATIC

ELETTROPOMPE VOLUMETRICHE
VOLUMETRIC PUMPS

LIMITI D'IMPIEGO
- Temperatura liquido fino a 60°C
- Temperatura ambiente fino a 40°C
- Altezza d'aspirazione manometrica fino a 7 mt.
- Servizio continuo

MOTORE
- Motore elettrico ad induzione a 2 poli (n = 2850 r.p.m.)
- Isolamento Classe F
- Protezione IP 44

MATERIALI

- Corpo pompa	Ghisa
- Supporto motore	Ghisa
- Girante	Ottone
- Albero motore	Acciaio Inox
- Tenute meccaniche	Ceramica/Grafite

OPERATING CONDITIONS
- *Liquid temperature up to 60°C*
- *Ambient temperature up to 40°C*
- *Total suction lift up to 7 mt.*
- *Continuous duty*

MOTOR
- *Two-Pole induction motor (n = 2850 r.p.m.)*
- *Insulation Class F*
- *Protection IP 44*

MATERIALS

- *Pump body*	*Cast Iron*
- *Motor Support*	*Cast Iron*
- *Impeller*	*Brass*
- *Shaft with rotor*	*Stainless/Steel*
- *Mechanical seal*	*Ceramic/Graphite*

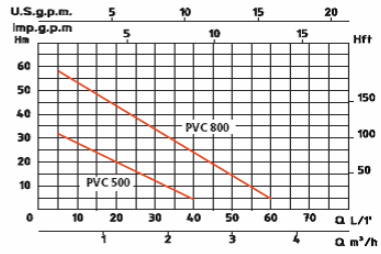

TIPO - *TYPE*	PVC 500	PVC 800
P2	0,5 HP	0,8 HP
Voltage	230 V	230 V
Frequency	50 Hz	50 Hz
Ampere	2,9 A	3,8 A
Q max.	40 l/1'	60 l/1'
H max.	35 m	60 m
Dnm - Dna	1"-1"	1"-1"

2

Figure C.5: Pump Euromatic PVC 500 used for injecting water in the well.

Stratigraphic sections for DiFeST research site

D

215

§

During the last decades some geologic sections have been produced by Emilia-Romagna region. In this chapter some of these are reported in order to have an idea of which materials are present in the research site.

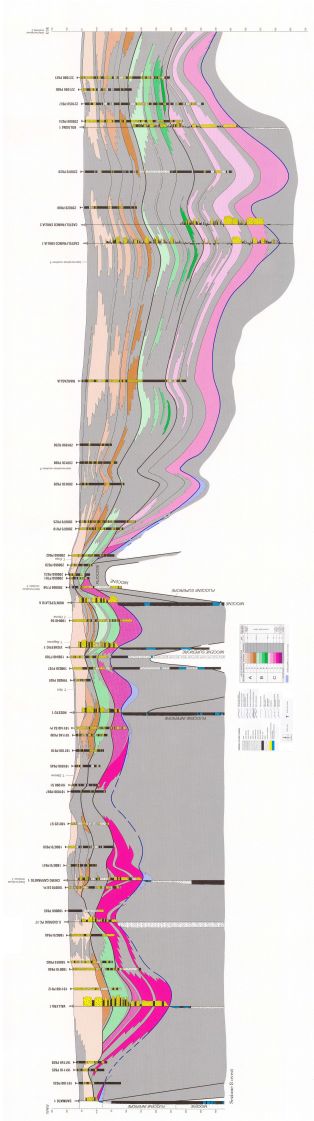

Figure D.1: Section 31. From *WEB GIS Emilia Romagna*.

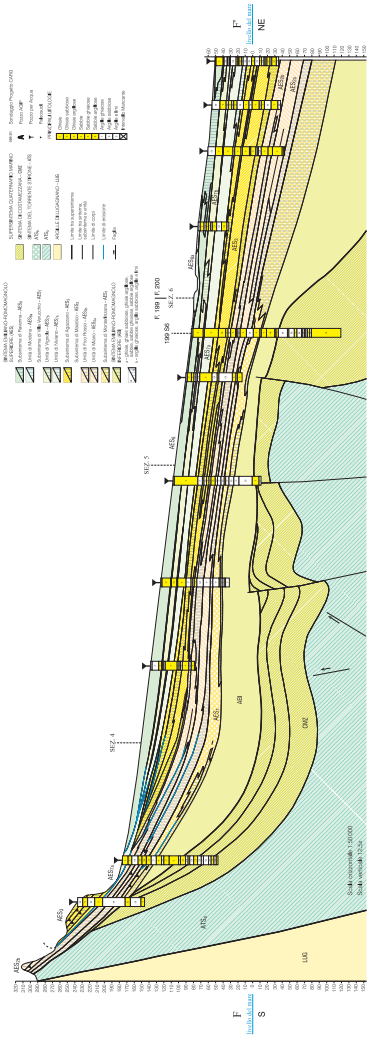

Figure D.2: Section 40. From *WEB GIS Emilia Romagna*.

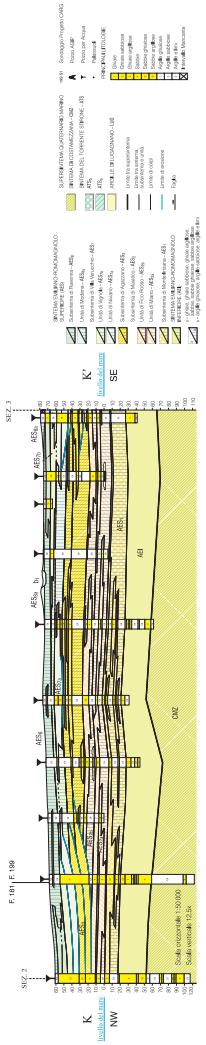

Figure D.3: Section 43. From *WEB GIS Emilia Romagna*.

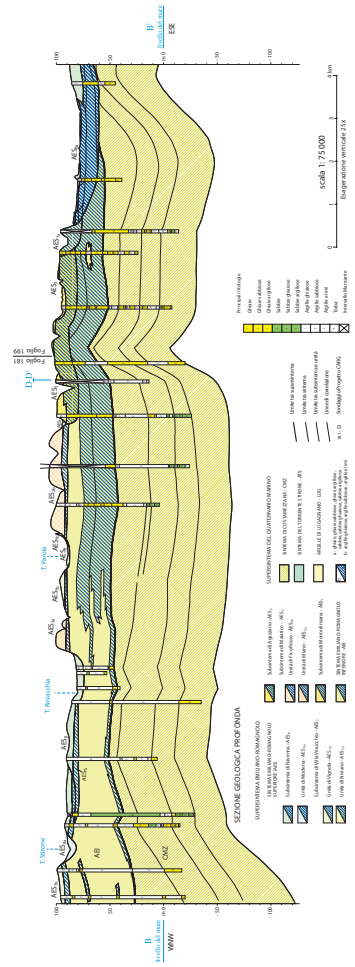
SEZIONE GEOLOGICA PROFONDA
scala 1:75000
Esagerazione verticale 2.5x
T. Stirone
T. Rovacchia
T. Riglia
Foglio 181
Foglio 199
DUY
B
Bacino del Mare
WNW
F
Bacino del mare
ESE
AES
AES1
AES2
AES3
AES4
AES5
AES6
AES7
AES8
AEI
AEI1
AEI2
AEI3
AEI4
AEI5
AEI6
AEI7
AEI8
AEI9
AEI10
AEI11
AEI12
AEI13
AEI14
AEI15
AEI16
AEI17
AEI18
AEI19
AEI20
AEI21
AEI22
AEI23
AEI24
AEI25
AEI26
AEI27
AEI28
AEI29
AEI30
AEI31
AEI32
AEI33
AEI34
AEI35
AEI36
AEI37
AEI38
AEI39
AEI40

List of symbol

E

§

Table E.1: Chapter 1. Experimental installation.

Symbol	Dimension	Description
C	[ML^{-3}]	concentration
C_{inj}	[ML^{3}]	concentration injected
F	[-]	luminosity in term of R, G or B
H	[L]	height of the sandbox
H_D	[L]	Upstream constant head
H_U	[L]	Downstream constant head
i	[-]	index
j	[-]	index
k	[-]	index
K	[LT^{-1}]	hydraulic conductivity
L	[L]	lenght of the sandbox
l	[L]	dimension of the pixel
$\dot{M}$	[MT^{-1}]	mass rate injected
n	[-]	side of ApA
q	[$L^{2}T^{-1}$]	specific discharge per unit width
Q_{inj}	[$L^{3}T^{-1}$]	injected flow rate
Q_S	[$L^{3}T^{-1}$]	discharge flowing across the sandbox
T_H	[L]	sandbox thickness
V	[L^{3}]	volume
v	[LT^{-1}]	Darcy's velocity
$\bar{v}$	[LT^{-1}]	mean velocity
Z	[L]	lenght of the cross section
α_L	[L]	longitudinal dispersivity coefficient
α_T	[L]	transverse dispersivity coefficient
Δx	[L]	dimensione of a pixel
Δz	[L]	dimensione of a pixel
ϕ	[-]	effective porosity

Table E.2: Chapter 2. Fundamentals of Hydraulics od Groundwater.

Symbol	Dimension	Description
A	$[L^2]$	cross-sectional area
C	$[ML^{-3}]$	concentration
C_0	$[ML^3]$	concentration injected at the source
$\mathbf{D}(\mathbf{x})$	$[L^2T^{-1}]$	dispersion tensor
D^*	$[L^2T^{-1}]$	effective molecular diffusion coefficient
h	[L]	hydraulic head
K	$[LT^{-1}]$	hydraulic conductivity
L	[L]	characterictic lenght
Pe	[-]	Peclet number
Q	$[L^3T^{-1}]$	discharge
q	$[T^{-1}]$	source/sink per unit volume
q_0	$[L^3T^{-1}]$	discharge injected at the source
ρ	$[ML^{-3}]$	density
R_n	$[MT^{-1}]$	reactive factor
$s(\mathbf{x_0}, t)$	$[MT^{-1}]$	mass rate injected at the source
S_S	$[L^{-1}]$	specific storativity
u	$[LT^{-1}]$	effective velocity
v	$[LT^{-1}]$	Darcy's velocity
$\mathbf{x_0}$	[L]	source location
α_L	[L]	longitudinal dispersivity coefficient
α_T	[L]	transverse dispersivity coefficient
δ	[-]	Dirac delta function
ϕ	[-]	effective porosity

Table E.3: Chapter 3. Recovery of the source position and of the contaminant release history.

Symbol	Dimension	Description
$\mathbf{b}$	[-]	unknown coefficients
$C(\mathbf{x}, t)$	$[\mathrm{ML}^{-3}]$	concentration at point $\mathbf{x}$ anf time t
C_0	$[\mathrm{ML}^{-3}]$	solution concentration
$\hat{C}_i$	$[\mathrm{ML}^{-3}]$	observed concentration
C_w	$[\mathrm{ML}^{-3}]$	initial condition in backward model
$\mathbf{D}$	$[\mathrm{L}^2\mathrm{T}^{-1}]$	dispersion tensor
$F(t)$	$[\mathrm{ML}^{-3}]$	concentration of the water injected at the source
F_0	$[\mathrm{MT}^{-1}]$	constant and known mass rate input function
$f_{\hat{C}_i}$	[-]	measured concentrations PDF
$\mathbf{H}$	[-]	sensitivity matrix
$\mathbf{h}(\mathbf{s})$	[]	vector that describes the transport process
$H_L(\mathbf{x}, t)$	[]	load term
$H_{SF}(t)$	[-]	heaviside step function
h_D	[L]	head level downstream
h_U	[L]	head level upstream
J	[-]	generic sub-areas
K	$[\mathrm{LT}^{-1}]$	hydraulic conductivity
m	[-]	number of observations
m_0	[M]	release source mass
M	[M]	random source mass
$\mathbf{M}$	[-]	multipliers
n	[-]	number of unknowns
$\mathbf{n}$	[-]	normal versor
p	[-]	number of unknown coefficients
$\mathbf{Q}(\boldsymbol{\theta})$	[-]	matrix covariance of the unknown process
Q_{in}	$[\mathrm{L}^3\mathrm{T}^{-1}]$	injected flow rate
Q_w	$[\mathrm{L}^3\mathrm{T}^{-1}]$	initial condition in backward model
q_0	$[\mathrm{L}^3\mathrm{T}^{-1}]$	injected solution discharge
q_I	$[\mathrm{T}^{-1}]$	source inflow rate per unit volume
$\mathbf{R}$	[]	error covariance matrix
$\mathbf{s}$	$[\mathrm{MT}^{-1}]$	unknowns
$s(t)$	$[\mathrm{MT}^{-1}]$	unknown release function
$\tilde{s}$	[]	transformed unknown function
$\hat{\mathbf{s}}$	$[\mathrm{MT}^{-1}]$	vector of estimated release function
t	[T]	time

Table E.4: Chapter 3. Recovery of the source position and of the contaminant release history.

	... from last page	
$\bar{t}$	[T]	sampling time
t_{start}	[T]	starting time
t_{end}	[T]	ending time
$\mathbf{u}$	[LT^{-1}]	velocity tensor
$\mathbf{v}$	[ML^{-3}]	measurement errors
$\mathbf{V}$	[]	matrix covariance of the estimate of the errors
$\mathbf{x}$	[L]	position of the domain
$\mathbf{x}_0$	[L]	source location
x_{inj}	[L]	longitudinal coordinate of injector
$\mathbf{X}_0$	[L]	random source location
$\mathbf{X}$	[]	matrix mean of the unknown process
$\mathbf{x}_w$	[L]	observation location
$\mathbf{z}$	[ML^{-3}]	observations
z_{inj}	[L]	vertical coordinate of injector
α	[-]	positive number
α_L	[L]	longitudinal dispersivity coefficient
α_T	[L]	transverse dispersivity coefficient
β_x	[-]	normalization factor
Γ_i	[-]	boundaries
δ	[-]	Dirac delta function
Δt	[T]	numerical model time step
Δx	[L]	longitudinal size of the numerical cell grid
Δy	[L]	transversal size of numerical cell grid
Δz	[L]	vertical size of numerical cell grid
ϵ_i	[ML^{-3}]	ith measurement error
η	[T]	time
$\boldsymbol{\theta}$	[-]	structural parameters of the covariance function
λ_s	[T]	correlation time lenght of the unknown release function $s(t)$
Λ	[-]	kriging coefficients
Θ	[-]	dummy matrix
σ_R^2	[M^2L^{-6}]	variance of the measurement error
σ_S^2	[M^2T^{-2}]	variance of the unknown release function
Σ	[]	dummy matrix
τ	[T]	backward time
τ_w	[T]	backward sampling time
ϕ	[-]	porosity
ψ^*	[-]	adjoint state
∇	[]	Nabla operator

Table E.5: Chapter 4. Evaluation of dispersivity coefficients by means of a laboratory image analysis.

Symbol	Dimension	Description
$C(\mathbf{x}, t)$	$[ML^{-3}]$	concentration at point **x** anf time t
C_{inj}	$[ML^{-3}]$	concentration injected
$\mathbf{D}$	$[L^2T^{-1}]$	dispersion tensor
Q_{inj}	$[L^3T^{-1}]$	injected flow rate
$s(\mathbf{x_0}, t)$	$[MT^{-1}]$	mass rate injected at the source
$\mathbf{u}$	$[LT^{-1}]$	velocity tensor
$\bar{v}$	$[LT^{-1}]$	mean velocity
x	[L]	longitudinal coordinate
z	[L]	vertical coordinate
α_L	[L]	longitudinal dispersivity coefficient
α_T	[L]	transverse dispersivity coefficient
δ	[-]	Dirac delta function
Δx	[L]	longitudinal size of ApA
Δz	[L]	vertical size of ApA
ϕ	[-]	porosity
∇	[]	Nabla operator

Table E.6: Chapter 5. Application of Oscillatory Hydraulic Tomography in a 2D laboratory sandbox.

Symbol	Dimension	Description
i	[-]	complex number
A_ω	[L]	sinusoidal coefficient
B_ω	[L]	cosinusoidal coefficient
$\mathbf{d}$	[L]	data vector
Δt	[T]	time interval between data measurement
K	$[LT^{-1}]$	hydraulic conductivity
Φ_ω	[-]	complex-valued field variable
Q	$[L^3T^{-1}]$	exctracted/injected flow rate
S_S	$[L^{-1}]$	specific storativity
T_S	[T]	sampling time
$\mathbf{x}$	[L]	space location

Table E.7: Chapter 6-7. Aquifer characterization.

Symbol	Dimension	Description
b	[L]	aquifer thickness
b'	[L]	aquitard thickness
e	[-]	efficiency
K	[LT^{-1}]	aquifer hydraulic conductivity
k'	[LT^{-1}]	aquitard hydraulic conductivity
r	[L]	distance from the well
S	[-]	aquifer storativity
S'	[-]	aquitard storativity
$s(r,t)$	[L]	drawdown
t	[T]	time
T	[L^2T^{-1}]	transmissivity
u	[-]	dimensionless variable
$W(u)$	[-]	well function

Table E.8: Chapter 10. Application and extension on the Minimum Relative Entropy.

Symbol	Dimension	Description
$\mathbf{a}$	[-]	function of Lagrange multipliers
$b(\mathbf{s})$	[-]	boxcar pdf
$C(\mathbf{x}, t)$	$[\mathrm{ML}^{-3}]$	concentration at point $\mathbf{x}$ and time t
E	[-]	entropy
$f(\mathbf{x}, t)$	$[\mathrm{T}^{-p}]$	transfer function at point $\mathbf{x}$ and time t
$\partial\mathbf{F}/\partial\lambda$	[-]	Frechèt matrix
h_D	[L]	head level downstream
h_U	[L]	head level upstream
$\mathbf{H}$	$[\mathrm{T}^{-p}]$	transfer matrix
$H(t)$	[-]	heaviside function
K	$[\mathrm{LT}^{-1}]$	hydraulic conductivity
L	$[\mathrm{MT}^{-1}]$	lower expected value bound
M	[-]	number of observations
N	[-]	number of unknowns
$p(\mathbf{s})$	[-]	prior pdf
$q(\mathbf{s})$	[-]	posterior pdf of release history
Q_{in}	$[\mathrm{L}^3\mathrm{T}^{-1}]$	injected flow rate
$\mathbf{r}$	[-]	expected value of prior pdf
$\bar{\mathbf{r}}$	[-]	expected value constraints vector
$\mathbf{s}$	$[\mathrm{MT}^{-1}]$	unknowns
$s(t)$	$[\mathrm{MT}^{-1}]$	unknown release function
$\hat{\mathbf{s}}$	$[\mathrm{MT}^{-1}]$	expected value of the posterior pdf $q(\mathbf{s})$
$S(t)$	$[\mathrm{ML}^{-3}]$	concentration of the water injected at the source as function of time t
S_0	$[\mathrm{MT}^{-1}]$	constant and known mass rate input function
t	[T]	time
U	$[\mathrm{MT}^{-1}]$	upper expected value bound
$w_j(\mathbf{x})$	$[\mathrm{ML}^{-3}]$	known data
$\mathbf{x}$	[L]	position in the domain
$\mathbf{x}_0$	[L]	source location
$\mathbf{y}$	[]	generic statistical event

Table E.9: Chapter 10. Application and extension on the Minimum Relative Entropy.

		... from last page
Y	[-]	logarithm of the hydraulic conductivity
$\mathbf{z}$	[ML^{-3}]	observations
Z	[-]	normalized log-conductivity
α_L	[L]	longitudinal dispersivity coefficient
α_T	[L]	transverse dispersivity coefficient
$\boldsymbol{\beta}$	[-]	Lagrange multipliers vector
$\boldsymbol{\lambda}$	[-]	Lagrange multipliers vector
μ_g	[MT^{-1}]	mean of the Gaussian function
μ_y	[-]	mean of the log-conductivity field
μ	[-]	Lagrange multiplier
σ_g^2	[M^2T^{-2}]	variance of Gaussian function
σ_Y^2	[-]	variance of the log-conductivity field
τ	[T]	time

Bibliography

[1] Aeby P, Schultze U, Braichotte D, Bundt M, Moser-Boroumand F, Wydler H, Fluhler H (2001) Fluorescence Imaging of Tracer Distributions in Soil Profiles. Environ Sci Technol 35:753-760. doi:10.1021/es000096x

[2] Aksoy A, Guney MS (2010) Experimental determination of three-dimensional dispersivities in homogeneous porous medium. Environ Earth Sci 60 (2):383-393. doi:10.1007/s12665-009-0182-6

[3] Aureli F, Maranzoni A, Mignosa P, Ziveri C (2011) An image processing technique for measuring free surface of dam-break flow. Experiments in Fluids 50:665-675. doi:10.1007/s00348-010-0953-6

[4] Atmadja J., Bagtzoglou AC (2000), Groundwater pollution source identification using the backward beam equation method, in: *Computational methods for Subsurface Flow and Transport*, 397-404, A.A. Balkema, Rotterdam, The Netherlands.

[5] Bakhos T, Cardiff M, Barrash W, Kitanidis PK (2014) Data processing for oscillatory pumping tests. Journal of Hydrology 511:310-319. doi:http://dx.doi.org/10.1016/j.jhydrol.2014.01.007

[6] Barrero LS, Capilla Roma JE, Sanchez Fuster I (2010) Modeling of anomalous transport effects in an artificial heterogeneous porous medium in a laboratory tank. In: IAHR International Groundwater Symposium, Valencia (E), 22-24 September 2010 2010.

[7] Bear J (1972) Dynamics of fluids in porous media. American Elsevier Pub. Co., New York,

[8] Bear J, Verruijt A (1987) Modeling Groundwater Flow and Pollution. Springer,

[9] Becker M, Guiltinian E (2010) Cross-hole periodic hydraulic testing of inter-well connectivity, in Stanford Geothermal Workshop, SGP-TR-188, Stanford University, Stanford CA, USA

[10] Benekos ID, Cirpka OA, Kitanidis PK (2005) Experimental determination of transverse dispersivity in a helix and a cochlea. Water Resour Res 42 (W07406):10. doi:10.1029/2005WR004712

[11] Berg SJ, Illman WA (2011) Three-dimensional transient hydraulic tomography in a highly heterogeneous glaciofluvial aquifer-aquitard system. Water Resour Research 47 (W10507):25. doi:10.1029/2011WR010616

[12] Berg SJ, Illman WA (2013) Field Study of Subsurface Heterogeneity with Steady-State Hydraulic Tomography. Ground Water 51 (1):29-40. doi:10.1111/j.1745-6584.2012.00914.x

[13] Bernabe Y, Mok U, Evans B (2005) A note on the oscillating flow method for measuring rock permeability. Intl. J. Rock Mech. Min. Sci., 43, 311-316

[14] Bernard RA, Wilhelm RH (1950) Turbulent diffusion in fixed beds of packed solids. Chemical Engineering Progress 46:233–240

[15] Black JH, Kipp KL (1981) Determination of hydrogeological parameters using sinusoidal pressure tests: A theoretical appraisal. Water Resources Research 17 (3):686-692. doi:10.1029/WR017i003p00686

[16] Brauchler R, Liedl R, Dietrich P (2003) A travel time based hydraulic tomographic approach. Water Resour Research 39 (12). doi:10.1029/2003WR002262

[17] Bruch JC (1970) Two-dimensional dispersion experiments in a porous medium. Water Resources Research 6 (3):791-800

[18] Butera I, Tanda MG (2003) A geostatistical approach to recover the release history of groundwater pollutants. Water Resour Research 39 (12):1372. doi:10.1029/2003WR002314

[19] Butera I, Tanda MG, Zanini A (2004) La ricostruzione della storia del rilascio di inquinanti in acquiferi sede di moto non uniforme mediante approccio geostatistico. In: XXIX Convegno di Idraulica e Costruzioni Idrauliche, Trento, 7-10 Settembre 2004 2004. Bios, Cosenza

[20] Butera I, Tanda MG, Zanini A (2006) The recovering of the pollutant release function in unsaturated aquifers. In: XXX Convegno di Idraulica e Costruzioni Idrauliche, Roma, 10-15 Settembre 2006. Casa Editrice La Sapienza, Roma

[21] Butera I, Tanda MG, Zanini A (2013) Simultaneous identification of the pollutant release history and the source location in groundwater by means of a geostatistical approach. Stochastic Environmental Research and Risk Assessment 27 (5):1269-1280. doi:10.1007/s00477-012-0662-1

[22] Butler JJ, Liu W (1993) Pumping Test in Nonuiform Aquifers: The Radially Asymmetric Case. Water Resour Research 29 (2):259-269

[23] Capilla Roma J, Sanchez Fuster I (2012) Modeling the local effective dispersivity to deal with the limitations of the Advection-Dispersion Equation. Groundwater

Modeling and Management under Uncertainty. In: Hadi K, Copty N (eds) Sixth IAHR International Groundwater Symposium, Kuwait, 19 - 21 November, 2012.

[24] Cardiff M, Barrash W, Kitanidis PK (2012) A field proof-of-concept of aquifer imaging using 3-D transient hydraulic tomography with modular, temporarily-emplaced equipment. Water Resources Research 48 (5):n/a-n/a. doi:10.1029/2011WR011704

[25] Cardiff M, Barrash W, Kitanidis PK (2013) Hydraulic conductivity imaging from 3-D transient hydraulic tomography at several pumping/observation densities. Water Resources Research 49 (11):7311-7326. doi:10.1002/wrcr.20519

[26] Castro-Alcala E, Fernaǹdez-Garcia D, Carrera J, Bolster D (2012) Visualization of Mixing Processes in a Heterogeneous Sand Box Aquifer. environ sci technol 46:3228-3235. doi:10.1021/es201779p

[27] Catania F, Massabo‘ M, Valle M, Bracco G, Paladino O (2008) Assessment of quantitative imaging of contaminant distributions in porous media. Experiments in Fluids 44:167-177. doi:10.1007/s00348-007-0388-x

[28] Chiogna G, Eberhardt C, Grathwohl P, Cirpka OA, Rolle M (2010) Evidence of Compound-Dependent Hydrodynamic and Mechanical Transverse Dispersion by Multitracer Laboratory Experiments. Environ Sci Technol 44 (2):688-693. doi:10.1021/es9023964

[29] Cirpka OA, Olsson Å, Ju Q, Rahman MA, Grathwohl P (2006) Determination of Transverse Dispersion Coefficients from Reactive Plume Lengths. Ground Water 44 (2):212-221. doi:10.1111/j.1745-6584.2005.00124.x

[30] Citarella D, Tanda MG, Zanini A (2010) Setup and calibration of an experimental device aimed at the validation of geostatistical procedures. In: IAHR International Groundwater Symposium, Valencia (E), 22-24 September 2010.

[31] Citarella D, Cupola F, Tanda MG, Zanini A (2015) Evaluation of dispersivity coefficients by means of a laboratory image analysis. Journal of contaminant hydrology 172:10-23

[32] Citarella D. (2012). Experimental study on pollutant transport in a laboratory sandbox by means of fluorescent tracer. Ph.D thesis. 122 pp

[33] Cupola F, Tanda M, Zanini A (2015a) Laboratory sandbox validation of pollutant source location methods. Stochastic Environmental Research and Risk Assessment:1-14. doi:10.1007/s00477-014-0869-4

[34] Cupola F, Tanda MG, Zanini A (2015b) Contaminant release history identification in 2-D heterogeneous aquifers through a minimum relative entropy approach. SpringerPlus 4 (1):1-19

[35] Cupola F, Tanda M, Zanini A (2015c) Laboratory Estimation of Dispersivity Coefficients. Procedia Environmental Sciences 25:74-81

[36] Cupola F, Tanda M, Zanini A (2015d) The recovering of the contaminant release history in heterogeneous and partially known flow field. AGU Fall meeting Abstracts H13E-1586

[37] Cupola F, Tanda MG and Zanini A (2014) Laboratory estimation of dispersivity coefficients, 7th Groundwater Symposium of the Int. Association for Hydraulic Research (IAHR), Perugia, 22-24 settembre 2014

[38] Cupola F, Tanda MG and Zanini A (2014) Ricostruzione della posizione della sorgente e della storia di rilascio in mezzi porosi utilizzando dati di laboratorio, XXXIV Convegno nazionale di Idraulica e Costruzioni Idrauliche, Bari, 8-10 settembre 2014

[39] Cupola F, Tanda MG and Zanini A (2014) Stima dei coefficienti di dispersività mediante prove sperimentali condotte in vasche di filtrazione, XXXIV Convegno nazionale di Idraulica e Costruzioni Idrauliche, Bari, 8-10 settembre 2014

[40] Cupola F., Cardiff M. and Zanini A. (2015e), Application of Multi-frequency Oscillatory Hydraulic Tomography for estimating the transmissivity on a well field, 42nd IAH Congress, Rome, 13-18 September 2015

[41] Cupola F, Tanda M, Zanini A (2014) Identification of the release history of a groundwater contaminant in non-uniform flow field through the minimum relative entropy method. AGU Fall Meeting Abstracts 1:0560

[42] Dai Z, Ritzi Jr. R.W., Dominic DF (2005) Improving permeability semivariograms with transition probability models of hierarchical sedimentary architecture derived from outcrop analog studies. Water Resource Research 41 (W07032). doi:10.1029/2004WR003515

[43] Doherty J (2008) PEST, Model Independent Parameter Estimation. Addendum to User Manual: 5th Edition. http://www.sspa.com/PEST/. Watermark Numerical Computing, Brisbane, Queensland Australia

[44] Domenico PA, Robbins G, A. (1985) A new method of contaminant plume analysis. Ground Water 23 (4):476-485

[45] Domenico PA, Schwartz FW (1998) Physical and chemical hydrogeology. 2nd edn. Wiley, New York

[46] Fienen M, Muffels C, Hunt R (2009) On constraining pilot point calibration with regularization in PEST. Ground Water. doi:10.1111/j.1745-6584.2009.00579.x

[47] Gelhar LW, Welty C, Rehfeldt KR (1992) A Critical Review of Data on Field-Scale Dispersion in Aquifer. Water Resour Res 28 (7):1955-1974

[48] Gimmi T, Ursino N (2004) Mapping Material Distribution in a Heterogeneous Sand Tank by Image Analysis. Soil Sci Soc Am J 68:1508-1514

[49] Goswami RR, Clement TP (2007) Laboratory-scale investigation of saltwater intrusion dynamics. Water Resources Research 43:W04418. doi:10.1029/2006WR005151

[50] Gorelick, S. M., B. Evans, and I. Remson (1983), Identifying sources of groundwater pollution: An optimization approach, Water Resources Research, 19(3), 779-790.

[51] Grane FE, Gardner GHF (1961) Measurements of Transverse Dispersion in Granular Media. Journal of chemical and engineering data 6 (2):283-287

[52] Gzyl G, Zanini A, Frączek R, Kura K (2014) Contaminant source and release history identification in groundwater: A multi-step approach. Journal of Contaminant Hydrology 157 (0):59-72. doi:http://dx.doi.org/10.1016/j.jconhyd.2013.11.006

[53] Hantush MS (1956) Analysis of data from pumping tests in leaky aquifers. Eos, Transactions American Geophysical Union 37 (6):702-714. doi:10.1029/TR037i006p00702

[54] Hantush MS (1960) Modification of the theory of leaky aquifers. Journal of Geophysical Research 65 (11):3713-3725. doi:10.1029/JZ065i011p03713

[55] Hantush MS (1964) Hydraulics of wells. Advances in hydroscience 1:281-432

[56] Hantush MS, Jacob CE (1955) Non-steady radial flow in an infinite leaky aquifer. Eos, Transactions American Geophysical Union 36 (1):95-100. doi:10.1029/TR036i001p00095

[57] Harbaugh AW, Banta EW, Hill MC, McDonald MG (2000) MODFLOW-2000, the U.S. Geological Survey Modular Ground-Water Model–User Guide to Modularization Concepts and the Ground-Water Flow Process. United States Geological Survey: Open File Report 00-92,

[58] Harbaugh AW (2005) MODFLOW-2005, the U.S. Geological Survey modular ground-water model – the Ground-Water Flow Process. U.S. Geological Survey Techniques and Methods: 6-A16, Reston, Virginia

[59] Huang W, Smith C, Lerner D, Thornton S, Oram A (2002) Physical modelling of solute transport in porous media: evaluation of an imaging technique using UV excited fluorescent dye. Water Research 36:1843-1853

[60] Illman WA, Craig AJ, Liu X (2008) Practical Issues in Imaging Hydraulic Conductivity through Hydraulic Tomography. Ground Water 46 (1):120-132. doi:10.1111/j.1745-6584.2007.00374.x

[61] Illman WA, Liu XY, Craig A (2007) Steady-state hydraulic tomography in a laboratory aquifer with deterministic heterogeneity: Multi-method and multiscale validation of hydraulic conductivity tomograms. Journal of Hydrology 341 (3-4):222-234. doi:10.1016/j.jhydrol.2007.05.011

[62] Illman WA, Zhu J, Craig AJ, Yin D (2010) Comparison of aquifer characterization approaches through steady state groundwater model validation: A controlled laboratory sandbox study. Water Resour Res 46 (W04502). doi:10.1029/2009WR007745

[63] Illman WA, Zhu J, Craig AJ, Yin D (2010) Comparison of aquifer characterization approaches through steady state groundwater model validation: A controlled laboratory sandbox study. Water Resources Research 46 (4). doi:10.1029/2009WR007745

[64] Johnson R (1987) Relative-Entropy Minimization with Uncertain Constraints: Theory and Application to Spectrum Analysis. In: Smith CR, Erickson G (eds) Maximum-Entropy and Bayesian Spectral Analysis and Estimation Problems, vol 21. Fundamental Theories of Physics. Springer Netherlands, pp 57-73. doi:10.1007/978-94-009-3961-5

[65] Jose SC, Cirpka OA (2004) Measurement of Mixing-Controlled Reactive Transport in Homogeneous Porous Media and Its Prediction from Conservative Tracer Test Data. Environ Sci Technol 38 (7):2089-2096. doi:10.1021/es034586b

[66] Jury WA, Roth K (1990) Transfer Functions and Solute Movement through Soil: Theory and Applications. Birkhäuser Verlag, Basel; Boston

[67] Kim S-B, Jo K-H, Kim D-J, Jury WA (2004) Determination of two-dimensional laboratory-scale dispersivities. Hydrological Processes 18 (13):2475-2483. doi:10.1002/hyp.1475

[68] Kitanidis PK (1995) Quasi-linear geostatistical theory for inversing. Water Resources Research 31 (10):2411-2419. doi:10.1029/95WR01945

[69] Kitanidis PK (1996) On the geostatistical approach to the inverse problem. Advances in Water Resources 19 (6):333-342. doi:10.1016/0309-1708(96)00005-X

[70] Klenk ID, Grathwohl P (2002) Transverse vertical dispersion in groundwater and the capillary fringe. Journal of Contaminant Hydrology 58 (1–2):111-128. doi:http://dx.doi.org/10.1016/S0169-7722(02)00011-6

[71] Koltermann CE, Gorelick SM (1996) Heterogeneity in Sedimentary Deposits: A Review of Structure-Imitating, Process-Imitating, and Descriptive Approaches. Water Resources Research 32 (9):2617-2658. doi:10.1029/96WR00025

[72] Kullback S (2012) Information Theory and Statistics. Dover Publications,

[73] Kuo CH Determination of Reservoir Properties from Sinusoidal and Multirate Flow Tests in One or More Wells. doi:10.2118/3632-PA

[74] Lakowicz JR (2006) Principles of Fluorescence Spectroscopy. Third edn. Springer US. doi:10.1007/978-0-387-46312-4

[75] Lavenue M, de Marsily G (2001) Three-dimensional interference test interpretation in a fractured aquifer using the pilot point inverse method. Water Resources Research 37 (11):2659-2675

[76] Liu SY, Yeh TCJ, Gardiner R (2002) Effectiveness of hydraulic tomography: Sandbox experiments - art. no. 1034. Water Resources Research 38 (4):1034

[77] Liu X, Illman WA, Craig AJ, Zhu J, Yeh TCJ (2007) Laboratory sandbox validation of transient hydraulic tomography. Water Resources Research 43 (5). doi:10.1029/2006WR005144

[78] Liu X, Kitanidis PK (2011) Large-scale inverse modeling with an application in hydraulic tomography. Water Resour Research 47 (W02501). doi:10.1029/2010WR009144

[79] Maineult A, Strobach E, Renner J (2008) Self-potential signals induced by periodic pumping tests. Journal of Geophysical Research: Solid Earth 113 (B1):n/a-n/a. doi:10.1029/2007JB005193

[80] Mathworks (2010) MATLAB 7.10.0. 7.10.0 edn. The MathWorks Inc., Natick, MA

[81] McCarthy EL (1934) Mariotte's Bottle. Science 80 (100)

[82] McNeil JD, Oldenborger GA, Schincariol RA (2006) Quantitative imaging of contaminant distributions in heterogeneous porous media laboratory experiments. Journal of Contaminant Hydrology 84:36-54. doi:10.1016/j.jconhyd.2005.12.005

[83] Michalak AM (2002) Environmental Contamination with Multiple Potential Sources and the Common Law: Current Approaches and Emerging Opportunities Fordham Environmental Law Journal

[84] Michalak AM (2003) Using Geostatistics to Constrain Source Identificationity CEE newsletter Fall 2003

[85] Michalak AM, Kitanidis PK (2004a) Application of geostatistical inverse modeling to contaminant source identification at Dover AFB, Delaware. Journal of Hydraulic Research 42 EXTRA ISSUE:9-18

[86] Michalak AM, Kitanidis PK (2004b) Estimation of historical groundwater contaminant distribution using the adjoint state method applied to geostatistical inverse modeling. Water Resources Research 40 (8):W08302. doi:10.1029/2004wr003214

[87] National Instruments (2011) LabView. National Instruments, Austin, Texas USA

[88] Neupauer RM (2002) Probabilistic Identification of Groundwater Contamination Sources.

[89] Neupauer RM, Borchers B (2001) A MATLAB implementation of the minimum relative entropy method for linear inverse problems. Computers Geosciences 27 (7):757-762. doi:http://dx.doi.org/10.1016/S0098-3004(01)00009-7

[90] Neupauer RM, Lin R (2006) Identifying sources of a conservative groundwater contaminant using backward probabilities conditioned on measured concentrations. Water Resour Research 42:W03424. doi:10.1029/2005WR004115

[91] Neupauer RM, Lin R, O'Shea H (2007) Conditioned Backward Probability Modeling to Identify Sources of Reactive Groundwater Contaminants. Water Resour Research 43:W11403. doi:10.1029/2006WR005580

[92] Neupauer RM, Wilson JL (1999) Adjoint method for obtaining backward-in-time location and travel time probabilities of a conservative groundwater contaminant. Water Resources Research 35 (11):3389-3398

[93] Neupauer RM, Wilson JL (2001) Adjoint-derived location and travel time probabilities for a multidimensional groundwater system. Water Resources Research 37 (6):1657-1668

[94] Neupauer RM, Wilson JL (2004) Forward and backward location probabilities for sorbing solutes in groundwater. Advances in Water Resources 27 (7):689-705. doi:http://dx.doi.org/10.1016/j.advwatres.2004.05.003

[95] Neupauer RM, Wilson JL (2004) Numerical Implementation of a Backward Probabilistic Model of Ground Water Contamination. Ground Water 42 (2):175-189. doi:10.1111/j.1745-6584.2004.tb02666.x

[96] Neupauer RM, Wilson JL (2005) Backward probability model using multiple observations of contamination to identify groundwater contamination sources at the Massachusetts Military Reservation. Water Resour Research 41:W02015. doi:10.1029/2003WR002974

[97] Neupauer RM, Wilson JL, Bhaskar A (2009) Forward and backward temporal probability distributions of sorbing solutes in groundwater. Water Resources Research 45 (1):n/a-n/a. doi:10.1029/2008WR007058

[98] Olsson Å, Grathwohl P (2007) Transverse dispersion of non-reactive tracers in porous media: A new nonlinear relationship to predict dispersion coefficients. Journal of Contaminant Hydrology 92 (3–4):149-161. doi:http://dx.doi.org/10.1016/j.jconhyd.2006.09.008

[99] Persson M (2005) Accurate Dye Tracer Concentration Estimations Using Image Analysis. Soil Sci Soc Am J 69 (4):967-975. doi:10.2136/sssaj2004.0186

[100] Photomodeler, Eos System Company Photomodeler Product [EB]. http://www.photomodeler.com

[101] Rahman MA (2005) Experimental Investigations on Transverse Dispersive Mixing in Heterogeneous Porous Media. PhD Thesis, Universität Stuttgart

[102] Rasmussen T, Haborak K, Young M (2003) Estimating aquifer hydraulic properties using sinusoidal pumping at the Savannah River site, South Carolina, USA. Hydrogeology Journal 11 (4):466-482. doi:10.1007/s10040-003-0255-7

[103] Renner J, Messar M (2006) Periodic pumping tests. Geophysical Journal International 167 (1):479-493. doi:10.1111/j.1365-246X.2006.02984.x

[104] Rolle M, Hochstetler D, Chiogna G, Kitanidis P, Grathwohl P (2012) Experimental Investigation and Pore-Scale Modeling Interpretation of Compound-Specific Transverse Dispersion in Porous Media. Transport in Porous Media 93 (3):347-362. doi:10.1007/s11242-012-9953-8

[105] Sanchez Fuster I (2011) Modelación de parámetros físicos de la ecuación de advección-dispersión utilizando un tanque de experimentación de escala intermedia. Universidad Politécnica de Valencia, Valencia, Spain

[106] Sanchez Fuster I, Lopez Chacon L, Capilla JE (2008) Investigacion del flujo y transporte mediante experimentacion a escala intermedia. Ingenieria del Agua 15 (3)

[107] Scheidegger AE (1961) General theory of dispersion in porous media. Journal of Geophysical Research 66 (10):3273-3278. doi:10.1029/JZ066i010p03273

[108] Silliman SE, Konikow LF, Voss CI (1987) Laboratory investigation of longitudinal dispersion in anisotropic porous media. Water Resources Research 23 (11):2145-2151. doi:10.1029/WR023i011p02145

[109] Silliman SE, Simpson ES (1987) Laboratory Evidence of the Scale Effect in Dispersion of Solutes in Porous Media. Water Resources Research 23 (8):1667-1673

[110] Silliman SE, Zheng L (2001) Comparison of Observations from a Laboratory Model with Stochastic Theory: Initial Analysis of Hydraulic and Tracer Experiments. Transport in Porous Media 42:85-107

[111] Skaggs TH, Kabala ZJ (1994) Recovering the release history of a groundwater contaminant. Water Resources Research 30 (1):71-79. doi:10.1029/93WR02656

[112] Smart PL, Laidlaw IMS (1977) An evaluation of Some Fluorescent Dyes for Water Rracing. Water Resources Research 13 (1):15-33

[113] Snodgrass MF, Kitanidis PK (1997) A geostatistical approach to contaminant source identification. Water Resources Research 33 (4):537-546. doi:10.1029/96WR03753

[114] Sternberg SPK (2004) Dispersion Measurements in Highly Heterogeneous Laboratory Scale Porous Media. Transport in Porous Media 54:107-124

[115] Sudicky EA (1986) A natural-gradient experiment on solute transport in a sand aquifer: Spatial variability of hydraulic conductivity and its role in the dispersion process. Water Resource Research 22 (13):2069–2082

[116] Taylor EMK, Uppal HL (1934) An investigation of the pressures on works on sand foundations I. Punjab Irrigation Research Institute,

[117] Tidwell VC, Gutjahr AL, Wilson A (1999) What does an instrument measure? Empirical spatial weighting functions calculated from permeability data sets

measured on multiple sample supports. Water Resource Research 35 (1):43-54. doi:10.1029/1998WR900011

[118] Ulrych TJ, Woodbury AD (2003) Extensions to minimum relative entropy inversion for noisy data. Journal of Contaminant Hydrology 67 (1–4):13-25. doi:http://dx.doi.org/10.1016/S0169-7722(03)00093-7

[119] Ursino N, Gimmi T, Fluhler H (2001) Combined effects of heterogeneity, anisotropy, and saturation on steady state flow and transport: A laboratory sand tank experiment. Water Resources Research 37 (2):201-208

[120] Vargas-Guzmán JA, Yeh TCJ (2002) The successive linear estimator: a revisit. Advances in Water Resources 25 (7):773-781. doi:http://dx.doi.org/10.1016/S0309-1708(02)00066-0

[121] Vasco DW, Keers H, Karasaki K (2000) Estimation of reservoir properties using transient pressure data: An asymptotic approach. Water Resources Research 36 (12):3447-3465. doi:10.1029/2000WR900179

[122] Wagner B (1992) Simultaneous parameter estimation and contaminant source characterization for coupled groundwater flow and contaminant transport modelling. journal of hydrology 135 (1-4):275-303. doi:doi:10.1016/0022-1694(92)90092-A

[123] Woodbury AD, Sudicky EA (1991) The geostatistical characteristics of the Borden aquifer. Water Resources Research 27 (4):553-546

[124] Woodbury AD, Ulrych TJ (1993) Minimum relative entropy - Forward probabilistic modeling. Water Resources Research 29 (8):2847-2860

[125] Woodbury AD, Ulrych TJ (1996) Minimum relative entropy inversion: Theory and application to recovering the release history of a groundwater contaminant. Water Resources Research 32 (9):2671-2681

[126] Woodbury AD, Ulrych TJ (1998) Minimum relative entropy and probabilistic inversion in groundwater hydrology. Stochastic Hydrology and Hydraulics 12 (5):317-358

[127] Yeh T, Liu S (2000) Hydraulic tomography: Development of a new aquifer test method. Water Resources Research 36 (8):2095-2105. doi:10.1029/2000WR900114

[128] Yeh TCJ, Liu S (2000) Hydraulic tomography: Development of a new aquifer test method. Water Resources Research 36 (8):2095-2105. doi:10.1029/2000WR900114

[129] Yin D, Illman WA (2009) Hydraulic tomography using temporal moments of drawdown recovery data: A laboratory sandbox study Water Resources Research 45 (W01502). doi:10.1029/2007WR006623

[130] Zanini A, Kitanidis PK (2009) Geostatistical Inversing for Large-Contrast Transmissivity Fields. Stochastic Environmental Research and Risk Assesment 23:565-577. doi:10.1007/s00477-008-0241-7

[131] Zanini A, Cupola F. (2013) Recovery the release history and source location of a pollutant in groundwater using data collected in laboratory. In: AGU FALL MEETING, 2013.

[132] Zheng C, Wang PP (1999) MT3DMS: A modular three-dimensional multispecies transport model for simulation of advection, dispersion, and chemical reactions of contaminants in groundwater systems; Documentation and user's guide. U.S. Army Engineer Research and Development Center No. SERDP-99-1, Vicksburg, MS

[133] Zhou Y, Lim D, Cupola F, Cardiff M (2014) Oscillatory Flow Testing in a Sandbox-Towards Oscillatory Hydraulic Tomography. AGU Fall Meeting Abstracts 1:0607